



**HAL**  
open science

# Harmonic and electron generation from laser-driven plasma mirrors.

Maimouna Bocoum

► **To cite this version:**

Maimouna Bocoum. Harmonic and electron generation from laser-driven plasma mirrors.. Plasma Physics [physics.plasm-ph]. Université Paris Saclay (COMUE), 2016. English. NNT : 2016SACLX023 . tel-01458082

**HAL Id: tel-01458082**

**<https://theses.hal.science/tel-01458082>**

Submitted on 3 Mar 2017

**HAL** is a multi-disciplinary open access archive for the deposit and dissemination of scientific research documents, whether they are published or not. The documents may come from teaching and research institutions in France or abroad, or from public or private research centers.

L'archive ouverte pluridisciplinaire **HAL**, est destinée au dépôt et à la diffusion de documents scientifiques de niveau recherche, publiés ou non, émanant des établissements d'enseignement et de recherche français ou étrangers, des laboratoires publics ou privés.

NNT : 2016 SACLX023

THESE DE DOCTORAT  
DE  
L'UNIVERSITE PARIS-SACLAY  
PREPAREE A  
"L'ÉCOLE POLYTECHNIQUE "

ÉCOLE DOCTORALE N° 288  
Ondes et Matière

Spécialité: Physique des plasmas

Par

**Maimouna BOCOUM**

HIGH-ORDER HARMONICS AND ELECTRON BEAMS FROM  
PLASMA MIRRORS

**Thèse présentée et soutenue à « Palaiseau», le « 24/06/2016» :**

**Composition du Jury :**

M. JOFFRE Manuel, Professeur à l'Ecole Polytechnique, Président  
M. MARJORIBANKS Robin, Professeur à l'Université de Toronto, Rapporteur  
M. DORRER Christophe, Professeur à l'Université de Rochester, Rapporteur  
M. AUDEBERT Patrick, Professeur à l'école Polytechnique, Examineur  
M. QUERE Fabien, Chargé de recherche au CEA, Examineur  
M. LOPEZ-MARTENS Rodrigo, Chargé de recherche à l'école Polytechnique, Directeur de thèse

*À mon grand-père*

# Remerciements

*Difficile de savoir dans quel ordre commencer ces remerciements, difficile de n'oublier personne, je tenterai toutefois d'être la plus exhaustive possible et m'excuse d'avance des oublis inévitables et involontaires. Je commence donc par les personnes qui m'ont le plus entourée au laboratoire pendant cette période très enrichissante, à savoir mon groupe PCO et nos amis APPLI: merci donc à Fred, Aurélie, Benoit, Aline et Magalie et Jean-Philippe pour leur soutien sans faille en salle de manip, merci à Maxence pour sa contribution aux simulations et sa disponibilité, merci à Greg et Denis pour leur soutien technique, ainsi que Stephan, Diego, Dominikas et Hermance. Enfin un merci tout particulier Rod et Jérôme pour m'avoir permis de travailler dans les meilleurs conditions. Un gros merci au secrétariat pour son dynamisme et sa bonne humeur: Sandrine, Lucie, Octavie, Carole et Patricia. Enfin, un merci bien mérité à la méca, et en particulier à Charlie pour sa bonne humeur et son professionnalisme. Merci également à toutes les autres personnes du Laboratoire, à nos partenaires au CEA, la liste est longue mais merci à tous d'avoir été aussi disponibles, ce sont des années que je n'oublierai pas de si tôt!*

*Je tiens dans un second temps à remercier mes amis, les anciennes ENSTA qui savent ce que c'est de faire une thèse: un gros bisous à Manue, Ananas, Dianou ainsi que Camille et Yves, partis pour le nouveau monde, pour leur soutien! Merci également aux anciennes Saint-Mauriennes qui se seront perdues dans les méandres d'une carrière dans la finance ou le droit des affaires: une grosse pensée pour Camillou, Laura, Ludie et Paula! Finally, a big thank you to my friends from DC and the Thanks-Giving squad: Juanita thank you for being always here ! Ririne, mountains of love all the way to New-Zealand ! Juliette, pleins de bonnes choses pour les années qui arrivent! Merci à toutes et à tous d'être là!*

*Enfin, un gros merci à ma famille, ma mère qui m'a toujours soutenue et encouragé tout le long de mes études, mon père, pas peu fier, mais à qui je précise tout de même que ma thèse est en physique et non en mathématiques, Laurent qui m'a également toujours soutenu et encouragé. Merci également à mes frères et sœurs pour toujours être restés eux mêmes, ainsi que mon amie d'enfance Valérie qui à toujours été là. J'embrasse toute ma famille au Sénégal et les remercie pour l'accueil chaleureux que j'ai*

*reçu lors de ma dernière visite, merci à toute la famille Bocoum dont je suis fier de faire partie. Enfin, une énorme pensée pour mon grand-père et ma grand-mère qui m'ont également beaucoup soutenu. Je dédie d'ailleurs cette thèse à mon grand-père: "ça-y-est, je suis r'çue papi"...*

*Merci à tous*

# Résumé

Les rayonnements électromagnétiques ou de particules énergétiques sont d'excellents outils pour sonder la matière qui nous environne. On pense par exemple à l'utilisation des rayons X pour la radiographie ou encore la diffraction pour la compréhension de la structure atomique des cristaux. Toutefois, lorsqu'il s'agit d'étudier la matière à des échelles de temps atomiques (typiquement sub-femtoseconde,  $1 \text{ fs} = 10^{-15} \text{ s}$ ), les seules sources de rayonnement disponibles restent des installations de grande envergure comme des synchrotrons, avec une résolution temporelle de l'ordre de la picoseconde, ou les lasers à électrons libres, sources parmi les plus intenses, avec des résolutions de l'ordre de la femtoseconde. Depuis une cinquantaines d'années, de nombreux travaux ont été menés pour proposer un jour une alternative reposant sur l'interaction laser-plasma. En effet, lorsqu'un plasma interagit avec une impulsion optique intense ( $> 10^{16-17} \text{ W/cm}^2$ ), il en résulte l'accélération de particules (ions, électrons) et l'émission de rayonnement électromagnétique énergétique (X-UV) cohérent. Dans le cadre de cette thèse, on étudiera la réponse d'un plasma de densité solide lorsqu'il est stimulé par une impulsion d'une dizaine de femtosecondes.

Un plasma est créé sur une cible solide avec une première impulsion de quelques  $10^{14} \text{ W/cm}^2$ , dite impulsion pompe. Ce plasma possède une interface avec le vide de qualité optique, si bien qu'il réfléchit en grande partie une seconde impulsion laser, dite impulsion sonde, d'intensité bien plus élevée ( $\sim 10^{17-18} \text{ W/cm}^2$ ): on parle alors de miroir plasma. C'est la partie non réfléchi de la sonde qui interagira non-linéairement avec ce plasma pour émettre du rayonnement X-UV ou bien libérer les particules accélérées comme des électrons. Le plasma créé avec la pompe se détend dans le vide à la vitesse du son, si bien qu'il est important de contrôler le délai pompe-sonde de manière précise. En effet, le mécanisme d'interaction avec un plasma peu détendu ( $\sim \lambda/100$ , donc délai pompe-sonde nul) facilitera l'émission de rayonnement X-UV, alors qu'une fois détendu d'une fraction de la longueur d'onde ( $\sim \lambda/10$ , donc augmentation du délai pompe-sonde), c'est l'accélération d'électrons qui prédominera.

Dans le premier Chapitre, nous revenons sur le mécanisme de "Brunel" décrivant l'interaction d'une impulsion laser avec un miroir plasma. Nous pourrions ainsi expliquer comment le plasma peut émettre une impulsion attoseconde dans la gamme X-UV à chaque cycle op-

tique du laser incident. Ces impulsions optiques interfèrent spectralement pour donner les harmoniques de la fréquence centrale du laser incident: c'est ce qu'on appelle "génération d'harmoniques". Les résultats sur la génération contrôlée d'harmoniques seront présentés au chapitre 4. En particulier, on montrera comment l'introduction de couplages spatio-temporels dans le champs laser incident permet de faire ressortir des informations sur le profil temporel du train d'impulsion attosecondes issu de l'interaction. Nous effectuerons un parallèle avec des mesure type FROG (*Frequency-Resolved Optical Gating*), technique de mesure bien connue pour les impulsions laser ultracourtes, fondé sur un algorithme de reconstruction.

Au chapitre 6, nous exposons un des résultats majeur de cette thèse: en changeant la longueur caractéristique du plasma avec lequel notre laser interagit, il est possible de façon sélective ou bien de générer des harmoniques, ou bien d'accélérer des électrons. Nous expliquons, en s'appuyant sur des simulations numériques comment la charge d'espace en surface du plasma permet d'expliquer cette observation. Cela nous conduira à nous focaliser sur le mécanisme d'accélération d'électrons au chapitre 7, notamment à travers l'observation de la distribution angulaire d'émission des électrons, ainsi que leur spectre en énergie.

La longueur caractéristique plasma étant de quelques fractions de longueur d'onde, aussi nous présentons au chapitre 5 une technique de mesure de l'expansion du plasma développé pendant cette thèse, basé sur l'interférométrie spatiale, et qui nous à permis de calibrer la vitesse d'expansion de notre plasma. Le principe est le suivant: un masque troué périodiquement est inséré dans le trajet de l'impulsion principale, si bien que plusieurs tâches de diffraction s'observent dans le plan focale de la parabole. Uniquement l'ordre 0 de diffraction est réfléchi par le miroir plasma, les autres étant réfléchis sur la surface du solide, si bien qu'au cours de la détente, les modulation du profil d'intensité du champs laser réfléchi, directement lié à un déphasage de l'ordre 0, permettent de remonter à l'expansion du plasma.

Nous décrirons au Chapitre 2, le système laser utilisé pour réaliser ces expériences sur cible solide, délivrant des impulsions de quelques millijoules,  $< 30$  fs au kHz. La compréhension et le développement de cette chaine à représenté un grande partie du travail de thèse, comme par exemple l'identification d'un processus de conversion de post-pulse en pré-pulse par non linéarité. Toutefois, un seul chapitre sera consacré au laser, l'exposé de cette thèse visant à décrire de la manière la plus exhaustive possible la physique de l'interaction laser-miroir plasma.

# Table of contents

<b>1</b>	<b>Introduction</b>	<b>11</b>
1.1	Why do we study plasmas ? . . . . .	11
1.2	Laser-plasma physics: historical context . . . . .	13
1.2.1	Plasmas: different time scales . . . . .	13
1.2.2	Lasers: different time scales . . . . .	14
1.3	Plasma mirrors . . . . .	15
1.3.1	What is a plasma mirror ? . . . . .	15
1.3.2	Lifetime of a plasma mirror . . . . .	16
1.3.3	Plasma mirrors for temporal contrast cleaning . . . . .	17
1.3.4	X-UV emission from plasma mirrors . . . . .	18
1.3.5	Electron acceleration from plasma mirrors . . . . .	20
1.4	Brief description of the different chapters . . . . .	23
<b>2</b>	<b>Laser-solid-plasma interaction: overview</b>	<b>25</b>
2.1	Laser absorption in plasmas . . . . .	25
2.1.1	Resonant absorption . . . . .	26
2.1.2	Neutral plasma response equations . . . . .	26
2.1.3	Geometrical representation of resonant absorption . . . . .	28
2.2	Brunel absorption mechanism . . . . .	29
2.2.1	Modeling . . . . .	30
2.2.2	Physical interpretation . . . . .	31
2.3	Harmonic response of an overdense plasma . . . . .	33
2.3.1	Plasma perturbative approach . . . . .	33
2.3.2	Coherent Wake Emission . . . . .	35
2.3.3	Influence of spatial spreading of the perturbation . . . . .	38
2.3.4	Landau damping in a homogeneous plasma . . . . .	38
2.3.5	Landau damping in an inhomogeneous plasma . . . . .	40
2.4	Conclusion . . . . .	41
<b>3</b>	<b>Double-CPA laser architecture</b>	<b>43</b>
3.1	Global architecture . . . . .	44

3.1.1	Overview of the laser chain . . . . .	44
3.1.2	XPW contrast cleaning . . . . .	45
3.1.3	Spectral clipping . . . . .	48
3.1.4	Prepulse generation from post-pulses . . . . .	48
3.2	Post-compression and beam shaping . . . . .	54
3.3	Solid-target experimental setup . . . . .	56
3.3.1	Experimental chamber and beam profile . . . . .	56
3.3.2	Beam temporal profile . . . . .	57
3.3.3	kHz solid target . . . . .	58
3.4	Conclusion . . . . .	60
<b>4</b>	<b>Attosecond pulses from plasma mirrors</b>	<b>61</b>
4.1	HHG on plasma mirrors . . . . .	62
4.1.1	Experimental setup for HHG measurement . . . . .	62
4.1.2	From harmonic emission time to CWE basic properties . . . . .	63
4.1.3	Harmonic coherence properties . . . . .	67
4.1.4	Influence of gradient scale length on HHG . . . . .	70
4.1.5	Reconstruction of harmonics in the far field . . . . .	72
4.2	Attosecond chirp experiment . . . . .	73
4.2.1	Definition of Wavefront rotation (WFR) . . . . .	73
4.2.2	Analytical model to evaluate WFR at focus . . . . .	75
4.2.3	WFR measurement . . . . .	77
4.3	Basic principle of attosecond FROG retrieval . . . . .	82
4.4	Conclusion . . . . .	86
<b>5</b>	<b>Measuring the plasma expansion</b>	<b>87</b>
5.1	Spatial Domain Interferometry (SDI) . . . . .	87
5.1.1	Introduction . . . . .	87
5.1.2	Basic principle . . . . .	88
5.1.3	Illustration with a step-like density profile . . . . .	90
5.1.4	Plasma expansion model . . . . .	90
5.1.5	Experimental setup . . . . .	93
5.1.6	Experimental results . . . . .	94
5.2	Sensitivity to beam alignment . . . . .	95
5.2.1	Single-order phase shift and experimental limitations . . . . .	95
5.2.2	Break of symmetry . . . . .	99
5.3	Perspectives for phase retrieval . . . . .	101
5.3.1	Inversion problem . . . . .	101
5.3.2	One-dimension retrieval . . . . .	102
5.3.3	Modifying the reference probes to break the symmetry . . . . .	107

5.3.4	Two-dimensional retrieval ambiguities . . . . .	109
5.4	Conclusion and perspectives . . . . .	110
<b>6</b>	<b>Harmonics and electrons from plasma mirrors</b>	<b>111</b>
6.1	Review of electron acceleration mechanisms . . . . .	112
6.1.1	Resonant absorption . . . . .	112
6.1.2	Vacuum heating . . . . .	112
6.1.3	$J \times B$ heating . . . . .	113
6.1.4	Laser channel . . . . .	113
6.1.5	Surface plasmon resonance . . . . .	114
6.1.6	Stochastic heating . . . . .	114
6.1.7	Conclusion . . . . .	115
6.2	Simultaneous HHG and electron detection . . . . .	116
6.2.1	Description of the experiment . . . . .	116
6.2.2	CWE/electron anticorrelation vs plasma scale length . . . . .	118
6.2.3	PIC simulations . . . . .	121
6.3	Electron angular emission . . . . .	125
6.3.1	LANEX detection plane: stereographic losses . . . . .	125
6.3.2	LANEX imaging: non isotropic emission losses . . . . .	127
6.3.3	Spatial distribution of ejected electrons . . . . .	131
6.3.4	Gyromagnetic confinement for short gradient scale length . . . . .	136
6.4	Electron spectra . . . . .	139
6.4.1	Electron spectrometer . . . . .	139
6.4.2	Experimental results . . . . .	140
6.5	Conclusion . . . . .	141
<b>7</b>	<b>Laser-electron interaction in vacuum</b>	<b>142</b>
7.1	Ponderomotive force and electron motion in vacuum . . . . .	142
7.1.1	Classical ponderomotive force derivation . . . . .	143
7.1.2	Relativistic ponderomotive force derivation . . . . .	144
7.1.3	Non-ponderomotive laser acceleration . . . . .	147
7.1.4	Strong focusing field decomposition . . . . .	149
7.2	Hole formation and spectral shaping in vacuum . . . . .	151
7.2.1	Two regimes of acceleration . . . . .	151
7.2.2	Application to the relativistic case . . . . .	152
7.2.3	Application to the sub-relativistic case . . . . .	154
7.2.4	Effect of interference field . . . . .	156
7.2.5	Non-axis-symmetrical components of the interference field . . . . .	159
7.3	Conclusion . . . . .	161

<b>8 Conclusion and perspectives</b>	<b>162</b>
<b>List of Figures</b>	<b>165</b>
<b>List of Tables</b>	<b>176</b>
<b>A Normalization conventions</b>	<b>I</b>
A.0.1 Constant and physical parameters . . . . .	I
A.1 Maxwell's equations . . . . .	II
A.1.1 General Maxwell's equations . . . . .	II
A.1.2 Energy conservation . . . . .	III
A.1.3 Maxwell's equations in vacuum . . . . .	III
A.1.4 Intensity profile of a Gaussian pulse . . . . .	IV
A.1.5 Maxwell's equations in plasmas . . . . .	IV
A.1.6 Charge conservation . . . . .	V
A.2 Equation and scaling laws . . . . .	V
A.2.1 Propagation of the electromagnetic fields . . . . .	V
A.2.2 Charge screening . . . . .	VI
A.2.3 Charge conservation . . . . .	VII
A.3 Electron equation of motion . . . . .	VII
A.4 Vlasov equation . . . . .	VIII
<b>B Green function</b>	<b>X</b>
<b>C Relativistic formulations</b>	<b>XIII</b>
C.1 A few definitions . . . . .	XIII
C.2 Relativistic equation of motion for a charged particle . . . . .	XIV
C.3 Gauge invariance . . . . .	XV
<b>D Interferences between coherent sources</b>	<b>XVI</b>
<b>E Publications</b>	<b>XX</b>
<b>Bibliography</b>	<b>XLI</b>

# Chapter 1

## Introduction

For over a century, the scientific community has invested efforts into developing energetic particle and X-ray sources. This research was driven by the need to study matter on the atomic scale, or even below, with the investigation of elementary particle behavior. The fluence, duration, or spectral emission range of these sources have to be controlled to guarantee the success of an experiment. A particle beam can be composed of simple atoms or molecules (neutrals) or most commonly electrons or ions. On the scale of a nucleus, we can also find products of nuclear reactions (protons, neutrons) and fundamental particles (quarks, leptons..) as studied at CERN. The study of nuclear and fundamental reactions goes beyond the scope of this work because it requires large-scale accelerators ( $\sim$ TeV energies), unaccessible to an average laser facility. At the Laboratoire d'Optique Appliquée (LOA), our efforts are directed towards the comprehension and development of laser-driven generators of electromagnetic sources (X-UV<sup>1</sup> in our case) and particle accelerators (electrons in our case) through laser-plasma interaction schemes.

### 1.1 Why do we study plasmas ?

A plasma is a state of matter where atoms are dissociated into electrons and positively charged ions either completely or partially. Although natural plasmas are rarely encountered on Earth, it is however the most abundant state in the universe and represents 99.9% of visible state of matter. Therefore, the study of plasmas allows a better comprehension of our universe. A plasma is characterized by various parameters among which its electron density and its temperature, provided it has reached thermal equilibrium. A common property of plasmas is their ability to emit electromagnetic and/or particle radiations. This is why astrophysical plasmas can be observed from the Earth. The spectral content of this emission is strongly related to their thermodynamical properties and chemical constituents. For instance, interstellar regions are low-density plasmas

---

1. Extreme Ultraviolet: wavelengths between 10 and 130 nm

with less than 1 electron/cm<sup>3</sup> and temperatures between 0.1 and 100 eV. Most of the spectral emission is in the far infrared. Dense plasmas ( $\sim 10^{20-25}$  electron/cm<sup>3</sup>) are encountered in the core of stars like the Sun, where strong thermonuclear reactions prevent the whole structure from collapsing under its own weight. Stars are classified according to their emission spectra going from infrared (cold stars) to gamma rays (hot and turbulent stars). In addition, very intense particle jets (electrons, protons, nuclear reaction products) coming from stars are directly or indirectly observed to describe the core plasma dynamics on various geological time scales. To generate energetic electromagnetic and particle radiation in a laboratory, we use lasers to create plasmas with micrometer-sized volumes and with densities and temperatures approaching those found in the core of stars. The lifetime of these plasmas is on the order of 10<sup>-8</sup> second.

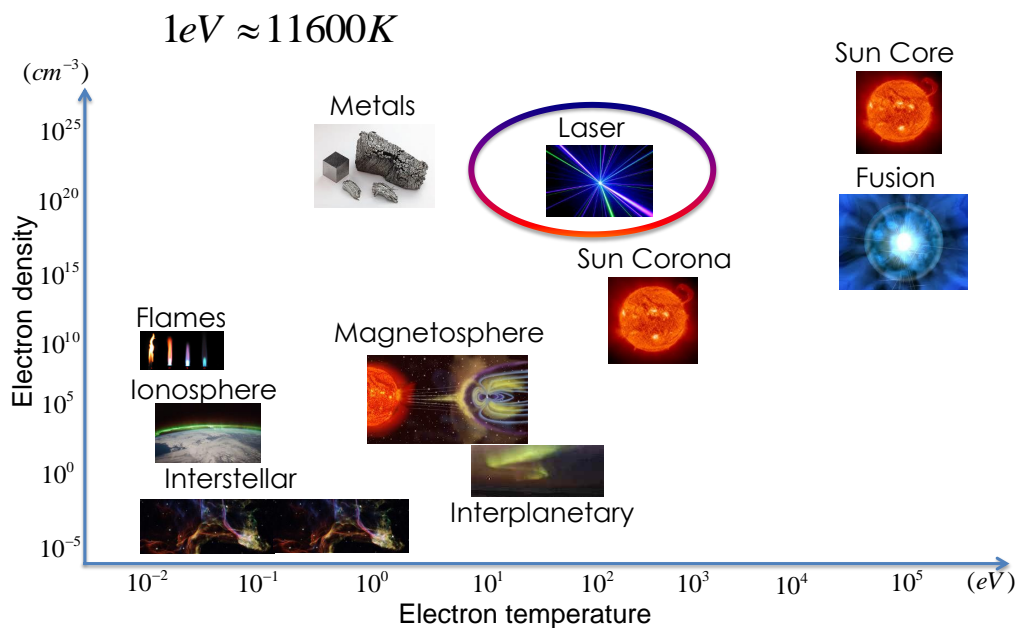


Figure 1.1 – Examples of plasmas sorted by density and temperature

In the attempt to recreate astrophysical plasmas in a laboratory, we have progressively realized that in addition to understanding better the nature of the radiation coming from space, we are also paving the way towards table-top energetic radiation with countless applications (imaging, spectroscopy, medical therapy, nuclear physics...). Over a century, the scientific community has gone from the study of the universe over geological time scale to the study of micrometric systems over proportionally short time scales.

## 1.2 Laser-plasma physics: historical context

Before the 50's, the geophysical and astrophysical community essentially studied plasmas doing spectroscopy of partially ionized gas through electric discharges. Langmuir and Tonks were the first to conduct a parametric investigation of partially ionized mercury in the 1920's [1, 2], attractive because of its low ionization potential. But in 1960, the first ruby laser would quickly open the door to laser-driven plasma physics. The first efforts were directed towards the creation of high-density plasmas in order to provoke nuclear fusion reactions. However, controlling fusion reactions was not a new idea in the 60's. Between 1936 and 1939, Atkinson, Bethe and Houtermans [3–5] had come up with a classification of light elements eligible for fusion to explain the reactions in the core of stars. With no surprise, these scientists were also part of the Manhattan project in the 1940's. In the 1950's, studies on the control of nuclear reactions using magnetically confined plasmas lead to the conception of reactors called Tokamaks [6–8]. Finally, Dawson explained in 1964 [9] how a short ( $\sim \text{ns}$ )<sup>2</sup> intense ( $\sim \text{TW}$ )<sup>3</sup> laser pulse [10, 11] was an eligible candidate to initiate thermonuclear reactions inside a solid pellet target. These intensities and durations were precisely accessible to state-of-the-art lasers in the 70's [12]. In 1974, the Lawrence Livermore National Laboratory (LLNL) conducted the first experiment part of the “inertial confinement fusion program” to demonstrate Deuterium/Tritium ignition, using a 20J,  $\sim 10 \text{ ns}$  Nd: glass, 1.06 micron laser. After decades of experimental investigation, it appeared that carefully shaping the laser pulse would reduce the energy necessary to trigger nuclear reactions. More insight into the different times scales involved in the plasma dynamics, from nanosecond to femtosecond (and most recently attosecond) has been gained.

### 1.2.1 Plasmas: different time scales

In Physics, the same system can be studied on different time scales. For instance, one uses thermodynamics to predict the final state of a gas. However, on a time scale much shorter than the collision time between two atoms, one should turn to classical kinematics instead. This is of course also true in plasma physics, where the adequate set of equations used to describe the motion of both ion and electron populations inside the plasma will be radically different depending on the time scale of the interaction. Thermonuclear plasmas inside Tokamaks, for instance, are confined during several seconds. Diffusion, convection and turbulences occur on time scales varying between  $\sim \text{ns}$  to  $< 1 \text{ s}$  [8]. Rayleigh instabilities [13] grow by  $\sim 1 \mu\text{m}$  in  $\sim 1 \text{ ns}$  [14] at the surface of laser-compressed pellets and prevent the ignition of fusion reactions [15]. Note that in the latter example,

---

2.  $1 \text{ ns} = 10^{-9} \text{ s}$

3.  $1 \text{ TW} = 10^{12} \text{ W}$ , power provided by  $\sim 500$  nuclear plants

$1\mu\text{m}/1\text{ns} = 1\text{nm}/\text{ps}$ , which is the sound velocity inside plasmas [16]. Therefore a fluid model is well suited to describe the plasma on a ns time scale over several microns, or on the picosecond time scale over several nanometers. However, using a fluid approach to predict the plasma evolution during one femtosecond over one picometer no longer makes sense. In this case, we reach the dimension of an atom and the time scale of electron collisions in a dense plasma: collisions can be neglected and the physics is now described by the equation of motion of a single electron. The study of plasmas on femtosecond time scales requires the use of femtosecond laser pulses, and a control of the plasma conditions with nanometer resolution.

### 1.2.2 Lasers: different time scales

The comprehension of plasma dynamics is strongly related to the rapid evolution of laser technologies. The temporal duration<sup>4</sup> of the laser pulse available from continuous (milliseconds) to ultrashort (femtoseconds) depends on the spectral bandwidth and the phase relation between each spectral component. This is directly influenced by the properties (losses, dimension) of the laser cavity. The temporal duration of a laser, and simultaneously its maximum peak power<sup>5</sup> can be boosted by two techniques, namely Q-switching and mode-locking.

- **1960: Q-switching:** By a temporal modulation of the losses, the lasing cavity is successively turned on or off. Many round trips occur in the cavity such that the final energy contained in the pulse exceeds by orders of magnitude that of continuous wave operation.
- **1960-1970: Laser mode-locking:** Used in the generation of ultrashort ( $\sim$  fs to a few ps) pulses. The gain medium inside the cavity has a large bandwidth and all the amplified frequencies superimpose coherently inside the cavity. As a result, they interfere constructively, and the cavity generates a continuous train of very short pulses.

In Table 1.1, we provide an incomplete list of laser systems with different temporal durations. When energetic pulses are required for a given application, the pulse will in general undergo chirped-pulse amplification (CPA) [17]. However, the world record in laser power today which simultaneously combines (i) an ultrashort (6fs) pulse duration and (ii) a very energetic pulse ( $\sim 100$  mJ) [18] is based on OPCPA [19].

---

4. The temporal duration of a laser pulse is defined by the Full Width of Half Maximum (FWHM) of the pulse in power. For a Gaussian pulse, this power is  $\propto \exp(\frac{-4 \ln(2)t^2}{\tau_{fwhm}^2})$

5. Peak power for a pulse of energy  $E_0$  and temporal duration  $P \approx E_0/\tau_{fwhm}$

Technology	year	temporal duration
Ruby	1960	$\sim$ ms
Nd:YAG	1964	$\sim 200\mu\text{s}$
Nd:YAG - Q-switched	1965	$< 1\text{ns}$
Nd:YAG - mode locked	1968	$\sim 30\text{ps}$
Nd:YLF- Q-switched	1992	$\sim 100\text{ns}$
Nd:YLF- mode locked	1992	$\sim 10\text{ps}$
He-Ne	1960	continuous
CO <sub>2</sub>	1964	1 – 100ns
CO <sub>2</sub> - Q-switched	1964	$< 1\text{ns}$
Ti:sapphire	1982	$\sim 500\text{ns}$
Ti:sapphire - mode locked	1989	$< 10\text{fs}$

Table 1.1 – Example of different laser performances

Q-switched lasers are today widely used for industrial applications involving laser processing of metal and medical applications. However, the first experiments on the generation of coherent X-UV light from plasmas were performed using nanosecond CO<sub>2</sub> [20,21] in the 80's. Those results were attributed to the formation of plasma mirrors and reproduced with shorter and more intense laser pulses in recent years [22–25].

## 1.3 Plasma mirrors

### 1.3.1 What is a plasma mirror ?

A plasma mirror (PM) is by definition a plasma, which is highly reflective for electromagnetic radiation, depending of its spectral content. The lower the laser wavelength  $\lambda$ , the higher the plasma density  $n_e$  needs to be. This is illustrated in Fig 1.2, where we plot the plasma critical density <sup>6</sup>  $n_c[\text{cm}^{-3}] = (1.1 \times 10^{21})/(\lambda[\mu\text{m}])^2$  as a function of laser wavelength. To be reflective, just like a mirror, the plasma needs an optical surface quality, which means the surface depth fluctuations should remain  $< \lambda$ . There are however two fundamental differences between a PM and a standard metallic mirror: the first is the "switchability" of the PM. Because most materials submitted to a very intense electric field ( $\gtrsim 10^{13}\text{W}/\text{cm}^2$ ) will ionize on a very short time scale ( $\sim fs$ ), most materials can be "switched" into a mirror, during a time corresponding to the PM lifetime. The second fundamental difference concerns the damage threshold: since the plasma is in ionized form, there is no intrinsic limitation in laser intensity that can be reflected on a PM.

6. Density at which radiation of wavelength  $\lambda$  is reflected by the plasma

Because of these properties, non-linear interactions take place, and with them a new field of intense laser-plasma interaction physics.

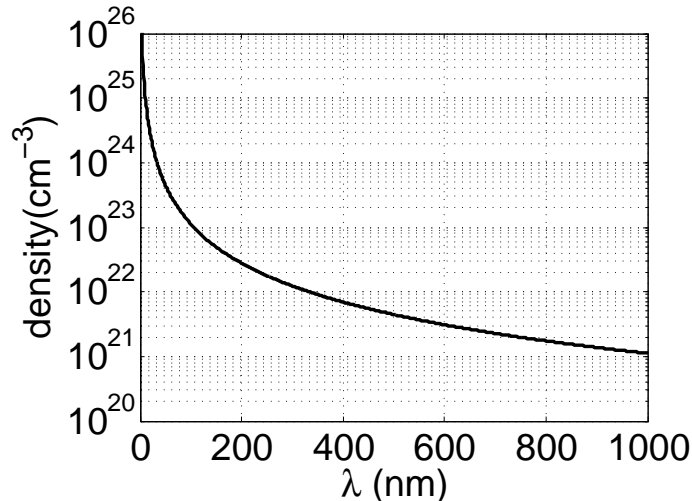


Figure 1.2 – Critical density as a function of wavelength

In 1990, Manheimer [26] proposed using plasma mirrors for radar systems to replace phase arrays. Two years later, Robson et al. [27] realized a plasma mirror for microwaves creating a partially ionized plane in a magnetic field and measured a reflectivity comparable to that of a metallic plane. These experimental proofs of principle have quickly been reproduced at lower wavelengths (near infrared, visible) [28–33] as laser technologies evolved and can now be easily created using table-top compact laser systems.

### 1.3.2 Lifetime of a plasma mirror

Laser-plasma interactions are usually performed under vacuum to prevent non-linear degradation of the laser. Therefore, the PM is created under vacuum using an auxiliary pulse we call prepulse, arriving on the solid target prior to the main laser pulse. Its intensity is high enough to ionize the target. For prepulse intensities of the order of  $\sim 10^{13-14}$  W/cm<sup>2</sup>, the plasma temperature is  $\sim 100$  eV [34]. The plasma inertia is dominated by the ions and its pressure by the free electrons, who transmit their energy to the ions. As a result, the plasma expands towards vacuum, at a velocity of the order of several nm/ps. Unfortunately, the plasma density is not a step-like function, but rather decays exponentially towards vacuum. Two consequences will therefore result from this expansion: (i) The density quickly drops, and the plasma transitions from "overdense" to "underdense". (ii) The expansion induces distortions of the critical surface, and the optical quality of the plasma-vacuum interface degrades in time. For those reasons, the plasma no longer reflects the main incident pulse if it arrives too late (few ps) after the

PM has been triggered.

That being said, one would simply need to reduce the delay between the prepulse and main pulse such that the plasma does not have time to expand. However, this is in general not possible. Indeed, a laser is a complex system made of several sub-units, and many components can introduce unwanted prepulses, with delays and durations spanning from less than a picosecond to several nanoseconds. In this case, we say the laser "temporal contrast" is degraded. For example, spontaneous emission in an amplifier [30] and scattering on gratings [35] generate incoherent light of nanosecond duration copropagating with the main laser pulse. As a consequence, if no precaution is taken, a sufficient amount of energy is temporally spread before the main pulse, and is enough to ionize any surface through tunnel ionization for moderate electric fields, or over-the-barrier ionization for intense electric fields. Electrons are stripped from all atoms at the surface of the solid, creating a plasma. This plasma expands in time and as a result of this expansion, the PM is destroyed before the main pulse arrives.

### 1.3.3 Plasma mirrors for temporal contrast cleaning

The well-recognized use of plasma mirrors so far is to improve the temporal contrast of short and intense pulses [29]. The working principle is illustrated in Fig 1.3. The underlying idea of using a plasma mirror to clean the temporal contrast of a short (fs to ps) laser pulses is precisely to take advantage of the poor laser contrast by creating a plasma mirror.

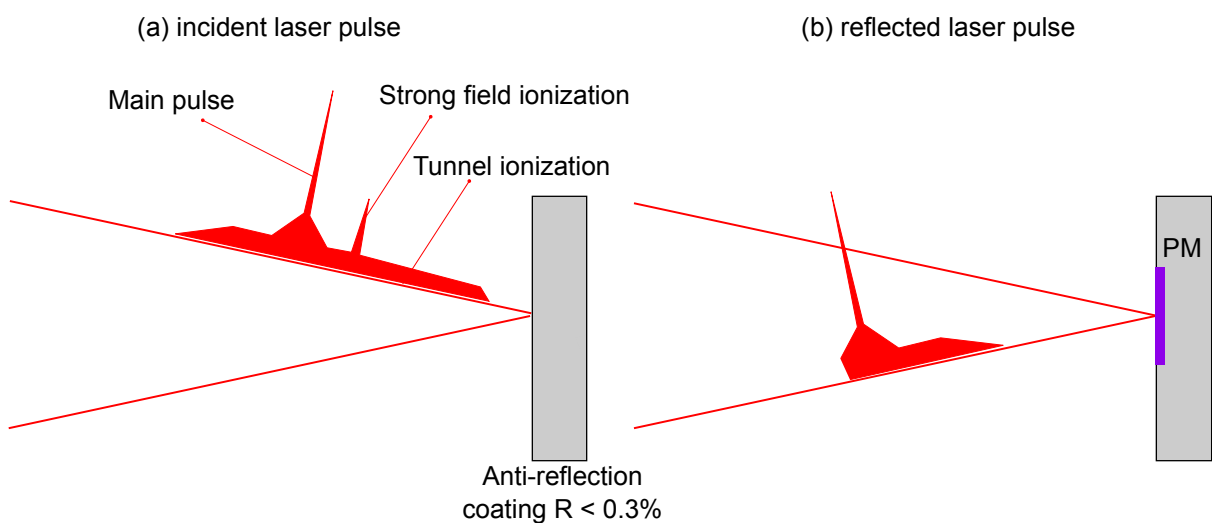


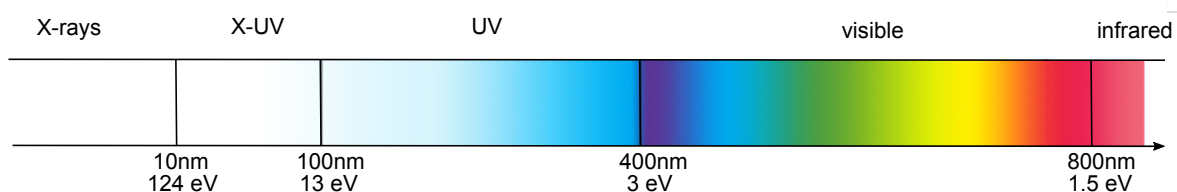
Figure 1.3 – (a) Incident laser pulse with degraded temporal contrast on anti-reflection coated wafer (b) Same laser pulse after reflection on the PM. Energy before the main pulse has been lost in the process of ionization

The energy “before” the main pulse is lost in the ionization process. As a result, the reflected pulse contrast is enhanced [32] from the instant the PM switches on.

In Chapter 3, we present the “Salle Noire’ laser architecture. Here, we will see that another technique, called XPW (fully described in 3.1.2) is used for contrast cleaning of our laser. Therefore, in the work presented in this PhD, we study the other properties of plasma mirrors involving non-linear response to an intense ultrashort laser pulse. In particular, we investigate the generation of X-UV radiation and electron ejection.

### 1.3.4 X-UV emission from plasma mirrors

X-rays can be used to probe the nanostructure of many dense materials (radiography, diffraction), or because of they are an efficient type of ionizing radiation (radiation therapy). It has been known for decades that conventional plasma sources can generate X-rays. When a plasma forms, hot electrons can strip core electrons from colder regions, and as they relax, the ionized atoms emit incoherent X-rays, also called  $K\alpha$  emission [36]. Thermal electrons in motion also emit incoherent X-Bremsstrahlung which depends on the plasma temperature. Moreover, positively charged ions also emit in the X-ray region, which has been extensively studied by spectroscopists over the last 50 years. Scientific curiosity aside, one could wonder why generating X-UV photons or energetic electrons ( $> 100$  keV) from PM is relevant at all, given it has been done for decades using conventional techniques such as X-ray tubes. The answer is in two words: temporal resolution.



Several conventional facilities can provide intense X-ray radiation. In case of synchrotrons, electrons are accelerated in km-long structures and their trajectories are modified with a combination of magnets (undulators) over a few meters. However, the coherence of such a source is limited and the emission does not go below a few picoseconds, mostly because of the electron bunch duration. Using a femtosecond laser to "slice" the electrons into short pulses,  $\sim 100$  fs bursts were produced [37] on a synchrotron, but with a limited number of photons. Free electron lasers (FEL) [38–41] are conventional accelerators which can produce intense X-rays [42] with peak brightness<sup>7</sup> up to one million times greater than

7. The peak brightness of an X-ray pulse is given in  $\text{ph/s}/0.1\% \text{BW}/\text{mm}^2/\text{mrad}^2$  [41]. It is different than the average brightness which accounts for the beam repetition rate

on synchrotrons, with pulse durations as short as  $\sim 5$  fs [43]. Although FELs are by far the most reliable installations to generate intense coherent X-rays, their size ( $\sim$  km installations) and effective cost ( $\sim$  Geuros) limit the number of users. In addition, sub-femtosecond X-rays pulses have so far never been achieved.

With the rapid increase of table-top laser peak powers ( $> 10^{18}$  W/cm<sup>2</sup>), it is possible to accelerate electrons in plasmas and generate X-rays. In 1977, Burnett and al. published the first experiment on the generation of X-UV radiation resulting from the interaction of a CO<sub>2</sub> laser with a plasma mirror [20] called high harmonic generation (HHG). The working principle is as follows: when an intense laser pulse ( $\sim 10^{15}$  W/cm<sup>2</sup>) reflects on a PM, electronic motion at the surface leads to the emission of coherent X-UV radiation with attosecond duration, every laser period. This produces a train of attosecond pulses separated in time by one laser period. Therefore, these pulses interfere constructively in the spectral domain whenever the frequency is a multiple of the driving laser frequency, and for this reason are called high-order harmonics. However, the main limitation of these sources compared to conventional accelerators is the intensity of the source. It is also possible to perform HHG in gas jets with comparable generation efficiencies [44–46], and generate X-UV pulses  $< 100$  as [47, 48]. However, the laser intensity has to remain below the ionization threshold which is an intrinsic limitation of the possible brightness of the sources. On PMs however, the laser intensity can be in principle arbitrarily increased, simultaneously with the brightness of the generated X-ray sub-femtosecond bunches.

Classically, a conversion efficiency is a non-dimensional quantity that measures an energy ratio  $\eta = E_{out}/E_{in}$  associated with a given physical process. For high harmonic generation on PM, the efficiency is defined for a given frequency range so that  $\eta(\omega)$  is an efficiency /s<sup>-1</sup>. We write the energy conservation relation from the temporal to the Fourier domain (Parseval theorem):

$$\int_{\mathbb{R}} |E(\omega)|^2 \frac{d\omega}{2\pi} = \int_{\mathbb{R}} |E(t)|^2 dt$$

where  $|E|^2$  is an energy density. Therefore, the energy contained in one attosecond pulse train is given by the harmonic conversion efficiency corresponding to the pulse spectral content. Based on numerical simulations, an integration of the laser energy before and after the interaction on target yields 75% reflectivity as presented in Fig 1.4. A negligible fraction of the input energy is transferred to the harmonics.

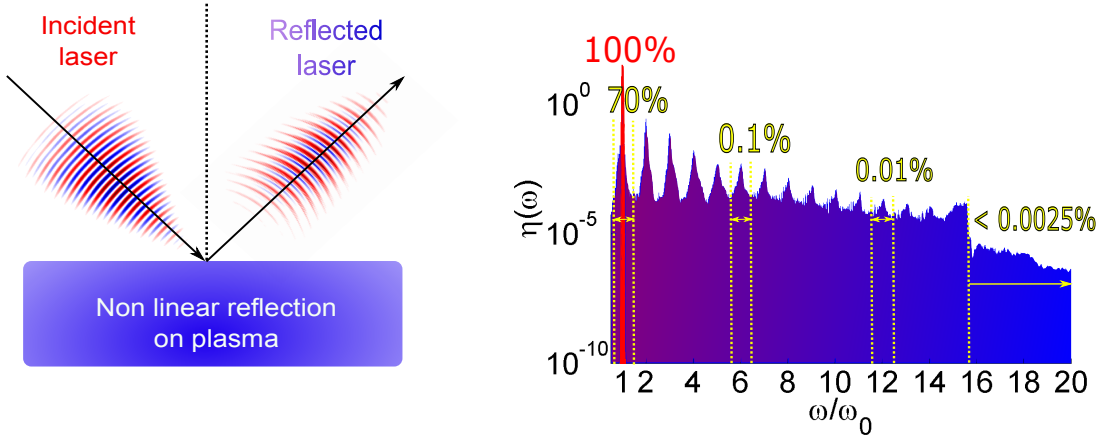


Figure 1.4 – Illustration of HHG for a 30fs laser pulse with intensity  $I = 10^{18} \text{ W/cm}^2$  on a PM with a density of  $200n_c$ . The percentage of energy of the incident laser contained in the harmonics is given in yellow colors

The harmonics shown in Fig 1.4 are generated with an exponentially decreasing conversion efficiency. This is typical of Coherent Wake Emission mechanism [49], which we will describe in section 2.3.1. Here, the energy contained in the harmonics is expected to be linearly increasing with the laser intensity [50, 51]. At much higher intensity however, a new mechanism called Relativistic Oscillating Mirror [52] is now responsible for the emission. For this mechanism, it has been predicted that an increase of the laser intensity would simultaneously enhance the generation efficiency [51]. Numerical simulations performed with a laser intensity of  $\sim 10^{19} \text{ W/cm}^2$  indicate that sub-fs X-UV emission can reach several percent [53] (mostly contained in low HHG orders) and therefore compete with peak-brightnesses obtained using X-FEL lasers.

### 1.3.5 Electron acceleration from plasma mirrors

High energy particle radiation started to become an attractive source for various application after the discovery of artificial nuclear reactions between 1910 and 1930. Physicists had access to alpha and beta particles resulting from nuclear reaction products [54], but were limited in energy and flux. In 1927, Rutherford, publicly announced at the Royal Society of London his “*ambition to have available for study a copious supply of atoms and electrons which have an individual energy far transcending that of the alpha and beta particles*”. In 1929, Walton and Cockcroft built the first proton accelerator to perform fundamental nuclear experiments by means of a high-voltage static electric field  $\sim 10^6 \text{ V}$ , accelerating protons up to 300 keV [55, 56]. This was sufficient to manage the transmutation of lithium nuclei, for which they received a Nobel Prize in 1951. Another type of electrostatic accelerator, developed in parallel by Van de Graff consisted in transporting

charges in a moving belt, lead to particles accelerated up to  $\sim 15$  MeV. During the same period, a new type of accelerator invented by Lawrence in 1932, called cyclotron, was born. The principle is to use a magnetic field to confine electrons into a spiral while a radio-frequency electric field  $\sim 10^3$  V accelerates them (or other charged particles). After World War II, a variant of cyclotrons called “synchrotrons”, still widely used today in medical applications, was born. Because the research had been so far mostly driven by nuclear research, most experiments consisted in the acceleration of charged ions. However, electrons which are also charged and almost two thousand times lighter than protons can also be accelerated, and their trajectories are easy to modulate in time. The first electron accelerator principle was proposed by D. W. Kerst in 1940 and was based on betatron acceleration (synchrotron for “beta” particles) [57] followed by successful table-top proof-of-principle at the University of Illinois. In 1945, 100 MeV electrons were accelerated at General Electric based on this principle. Betatron accelerators were for instance used in the Manhattan project to investigate some basic radioactive components properties. Electrons are accelerated in a circular vacuum chamber through an inductive effect: an alternative magnetic field generates an accelerating radial electric field. Note that a betatron and a linear induction accelerator are quite similar with the difference that the trajectories are circular in case of betatrons. In fact, for acceleration to be significant, electrons need to be circulated millions of times in the toroidal chamber, which explains why an additional magnetic field is added to prevent them from escaping their circular orbits of radius  $R$ .

$$E(\text{MeV}) \leq 300B_s(\text{T})R(\text{m}) \quad (1.1)$$

For example, an energy of 450 MeV could be reached theoretically taking  $R = 1$  m and  $B_s = 1.5$  T. Betatrons are limited in terms of acceleration because of the finite magnet size and radiation losses of the charged particles, but they have the great advantage of being compact devices, which makes them very appealing for industrial and medical applications.

But since the 80's, laser-driven plasma acceleration techniques have emerged: intense laser pulses focused into a gas jet generates compact accelerating structures where the electric field reaches  $\sim \text{TV/m}$ . The concept of plasma acceleration was introduced by Dawson and Tajima in 1979 [58]. The idea is to focus a beam into a gas jet to generate a micrometer accelerating cavity called wakefield. A wakefield cavity resembles that of a RF linear accelerator, but electric fields are orders of magnitude higher. The use of an energetic electron or ion beam was suggested in 1994 to trigger the fusion reaction of laser compressed deuterium pellets [59]. In this so called "fast ignition" scheme,  $\sim 1$  MeV suprathermal electrons are produced in the interaction of an intense laser at the surface of the compressed pellets, which propagate towards the core where they deposit their

energy. This mechanism, fully supported by simulations [59] has not yet been demonstrated experimentally. This initially explained the growing interest of the community in laser-driven solid-density experiments [60–65]. In Chapter 6, we will give a more detailed description of the different mechanisms involved in the interaction of an intense laser beam with a solid density plasma, leading to electron acceleration.

However, as we already mentioned, a solid density plasma is not necessarily a plasma mirror. When the plasma expands into vacuum, its surface quality degrades and the laser interacts with the underdense region of the plasma before it is reflected as described in chapter 2. Few experiments have so far been conducted on the acceleration of electrons from plasma mirrors [66, 67]. The work presented in this PhD focuses on the exploration of this interaction in the sub-relativistic regime. In particular, we will describe the prerequisites for efficiently accelerating electrons from plasma mirrors.

## 1.4 Brief description of the different chapters

- **Chapter 2 :** In this chapter, we describe the basic mechanism behind laser absorption on thin plasma mirrors. We present in detail the so-called "resonant absorption" mechanism, as well as "Brunel Absorption" mechanism, better suited for plasmas with very short scale lengths. In a second time, we will see how a dense plasma responds to an electronic perturbation by generating X-UV light, and discuss the asymptotic case of very long and very short plasma scale length, where this emission can no longer take place.
- **Chapter 3:** In this chapter, we describe the global architecture of our laser. After a brief presentation of the main components, we focus on XPW contrast cleaning and present a source of temporal contrast degradation in our CPA. After discussion on the laser contrast and the possible way of improving it, we describe the solid-target interaction chamber. In particular, we will present the 1kHz rotating target and the main beam characteristics (spatial, temporal) on target.
- **Chapter 4:** In this chapter, we will recall some of the basic properties of Coherent Wake Emission (CWE). The reader is invited to check the provided references for a more detailed description. In a second part, we will see how the divergence and spectral properties of the emitted harmonics are sensitive to spatio-temporal couplings (STC) of the driving laser. In particular, we will show how it is possible to experimentally control an STC of first order called Wave Front Rotation (WFR) and how it can affect harmonic generation. This technique has been already tested successfully to separate attosecond pulses from plasma mirror by changing over time their direction of emission [68]. Here we discuss the possibility of retrieving temporal information on the attosecond train when the pulses are not separated.
- **Chapter 5:** In this chapter we present a technique developed during this PhD called spatial domain interferometry (SDI), which allows us to measure the expansion velocity of the plasma generated on the solid target by a controlled prepulse. We will then discuss the current limitations of this technique such as the pointing stability of the pulses on target, and how it can be easily identified using the intensity profile of the reflected probe. Finally, we will suggest to go one step further with the implementation of a phase-retrieval algorithm allowing the two-dimensional reconstruction of the plasma during its expansion.
- **Chapter 6:** In this chapter, we present experimental results of the simultaneous observation of harmonics and electrons from plasma mirrors. In particular, we show how the emission is anticorrelated with the gradient scale length. We then present the measured electron angular emission profile and energy spectra depending on the plasma scale length.
- **Chapter 7:** This chapter focuses on electron interaction with the laser when it reflects on the plasma surface. We discuss two different regimes namely "pondero-

motive” and “non ponderomotive” laser acceleration in vacuum, and in particular how they depend upon the laser intensity. We also discuss the effect of our strong focusing geometry on the angular emission profile of electrons.

# Chapter 2

## Laser-solid-plasma interaction: overview

### Outline

---

<b>2.1</b>	<b>Laser absorption in plasmas . . . . .</b>	<b>25</b>
2.1.1	Resonant absorption . . . . .	26
2.1.2	Neutral plasma response equations . . . . .	26
2.1.3	Geometrical representation of resonant absorption . . . . .	28
<b>2.2</b>	<b>Brunel absorption mechanism . . . . .</b>	<b>29</b>
2.2.1	Modeling . . . . .	30
2.2.2	Physical interpretation . . . . .	31
<b>2.3</b>	<b>Harmonic response of an overdense plasma . . . . .</b>	<b>33</b>
2.3.1	Plasma perturbative approach . . . . .	33
2.3.2	Coherent Wake Emission . . . . .	35
2.3.3	Influence of spatial spreading of the perturbation . . . . .	38
2.3.4	Landau damping in a homogeneous plasma . . . . .	38
2.3.5	Landau damping in an inhomogeneous plasma . . . . .	40
<b>2.4</b>	<b>Conclusion . . . . .</b>	<b>41</b>

---

### 2.1 Laser absorption in plasmas

In the early 70's efforts to control thermodynamical reactions using pellet targets [69], unusual surface absorption of the intense pulse light was observed experimentally [12, 70, 71], which was a hint that new nonlinear phenomena were taking place. The invoked mechanism to describe these observations was historically called "resonant absorption": the laser propagates in the underdense region of the solid density plasma surface and reaches a regime called "wavebreaking". Here, strong coupling between the laser field and the plasma waves becomes possible. The authors who described this mechanism did not

mention the possibility of high-order harmonic generation in the process, but did state that this could explain hot-electron acceleration from solid plasma targets [72, 73]. This was critical because this hot electron population would preheat the core of the pellet. In the 1993, Tabak [59] proposed a fast ignition scheme where those same hot electrons were chosen to trigger nuclear reactions after an adiabatic compression, which is why their emission properties have to be controlled (low divergence, monoenergetic).

In this chapter, we go over the physical concepts of the “resonant absorption” model, and highlight the different hypotheses made in order for it to be valid, among which that the plasma scale length should be “long”. In his famous article called “not-so-resonant, resonant absorption” [61], Brunel proposed a model, which we trivially call “Brunel model”, more applicable in the case of short plasma scale lengths, as described in 2.2.

### 2.1.1 Resonant absorption

To go over the basic principles of what is generally called "resonant absorption", we will start by writing Maxwell's equations for both the magnetic and electric field in a plasma we assume to be non-magnetic ( $\mathbf{M} = \mathbf{0}$ ) and non polar ( $\mathbf{P} = \mathbf{0}$ ). These equations can be found in Appendix A.

$$\begin{cases} \nabla^2 \mathbf{E}(\mathbf{r}, t) - \nabla(\nabla \cdot \mathbf{E}) - \frac{1}{c^2} \partial_t^2 \mathbf{E}(\mathbf{r}, t) - \mu_0 \partial_t \mathbf{j}(\mathbf{r}, t) = \mathbf{0} & (2.1a) \\ \nabla^2 \mathbf{B}(\mathbf{r}, t) - \frac{1}{c^2} \partial_t^2 \mathbf{B}(\mathbf{r}, t) + \mu_0 \nabla \times \mathbf{j}(\mathbf{r}, t) = \mathbf{0} & (2.1b) \end{cases}$$

To close this system of equations, one needs to make a hypothesis about the response of the current  $\mathbf{j}$  to an electromagnetic field. We therefore suppose that the plasma of initial electronic density  $n_{e0}$  is neutral, and that only the electrons (as opposed to the much heavier ions) are in motion. Moreover, we consider a “cold” plasma, which means we study its dynamics on a time scale where collisions can be neglected in the equation of motion. With those conditions met, we can use the non-relativistic equation of motion known for one electron and retrieve the expression of the current using the relation:

$$\mathbf{j}(\mathbf{r}, t) = -en_e(\mathbf{r}, t)v_e(\mathbf{r}, t)$$

### 2.1.2 Neutral plasma response equations

We suppose that the plasma density is independent of time  $n_e(\mathbf{r}, t) = n_{e0}(\mathbf{r})$ . The function  $n_{e0}(\cdot)$  is often chosen to be exponentially decreasing towards vacuum as explained further in Chap 5. However, we do not need to make such a hypotheses within the scope of the present derivation.

The neutrality of the plasma is imposed at all time, which yields  $\nabla \cdot \mathbf{j}(\mathbf{r}, t) = 0$  because of

the charge conservation. The dynamics of the system are described by the non-relativistic equation of motion ( $\gamma = 1$  and  $\mathbf{B} = \mathbf{0}$ , as described in Appendix A)

$$\frac{d\mathbf{v}_e}{dt} = \partial_t \mathbf{v}_e + (\mathbf{v}_e \nabla) \mathbf{v}_e = -\frac{e}{m_e} \mathbf{E}(r, t) \quad (2.2)$$

To linearize Eq. 2.2, we make the assumption that  $v_e \ll L\omega_0$  where  $L$  is the characteristic scale length of the problem and  $\omega_0$  the driving laser frequency. Note that in a homogeneous plasma,  $L$  is equal to the driving laser wavelength and that condition is automatically verified, but for strongly inhomogeneous plasmas however,  $L$  can be significantly smaller. Assuming the inequality holds true, we have for a monochromatic field:

$$\begin{cases} \mathbf{j}(\mathbf{r}, \omega) = -n_{e0}(\mathbf{r}) \frac{e^2}{i\omega m_e} \mathbf{E}(\mathbf{r}, \omega) & (2.3a) \\ \nabla \times \mathbf{j}(\mathbf{r}, \omega) = \frac{-e^2}{i\omega m_e} [\nabla n_{e0} \times \mathbf{E}(\mathbf{r}, \omega) + n_{e0} i\omega \mathbf{B}(\mathbf{r}, \omega)] & (2.3b) \end{cases}$$

We define:

$$\omega_p(\mathbf{r})^2 = \frac{n_{e0}(\mathbf{r})e^2}{m_e \epsilon_0}$$

By applying the  $\nabla \cdot$  operator to the *Maxwell-Ampere* Equation given in A.9, it is easy to show that  $\nabla j = 0$  implies  $\partial_t(\nabla E) = 0$ . Therefore, supposing the plasma was neutral at time  $t = 0$ , this leads to  $\nabla E = 0$  at all times in Eq. 2.1a. The *Maxwell-Ampere* equation in the Fourier domain also gives the relation:

$$\nabla \times \mathbf{B} = \frac{ic^2\omega}{\omega^2 - \omega_p(\mathbf{r})^2} \mathbf{E}(\mathbf{r}, \omega) \quad (2.4)$$

By injecting Eq. 2.4 in Eq. 2.1 and using the relations in 2.3, we obtain separate equations for  $\mathbf{E}$  and  $\mathbf{B}$ , which are the equations commonly used to propagate the field undergoing “resonant” absorption in a plasma:

$$\begin{cases} \nabla^2 \mathbf{E}(\mathbf{r}, \omega) + \frac{\omega^2 - \omega_p(\mathbf{r})^2}{c^2} \mathbf{E}(\mathbf{r}, \omega) = 0 & (2.5a) \\ \nabla^2 \mathbf{B}(\mathbf{r}, \omega) - \frac{1}{\omega^2 - \omega_p(\mathbf{r})^2} \nabla \omega_p^2 \times \nabla \times \mathbf{B} + \frac{\omega^2 - \omega_p(\mathbf{r})^2}{c^2} \mathbf{B}(\mathbf{r}, \omega) = 0 & (2.5b) \end{cases}$$

Equation 2.5a shows the impossibility for the electric field to propagate for  $\omega < \omega_p(\mathbf{r})$  (this index is negative, as for a metallic mirror) which defines the critical surface equation:

$$n_e(\mathbf{r}) = n_c$$

Above the critical surface, the electric field gets reflected and below, it becomes evanescent.

### 2.1.3 Geometrical representation of resonant absorption

Since resonant absorption applies to long gradient scale lengths, it is quite easy to confuse with the geometrical optics picture of a wave curving its  $k$  vector along propagation as shown in Fig 2.1.

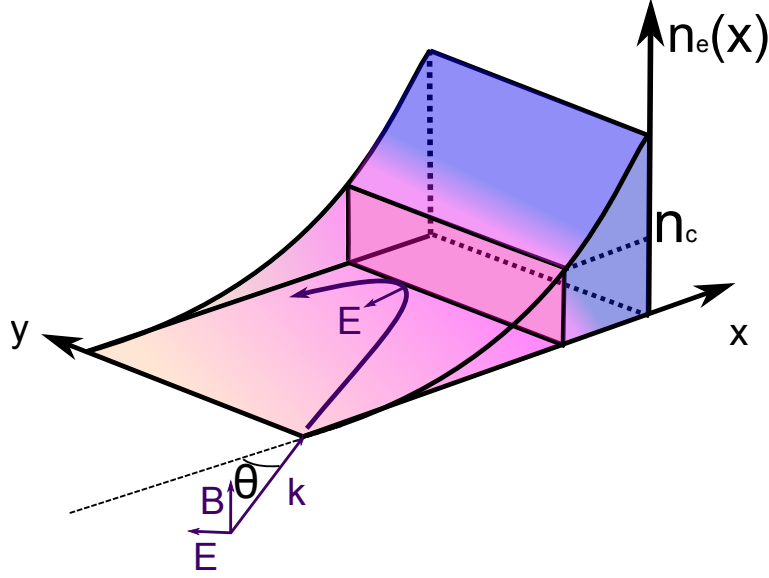


Figure 2.1 – Artistic representation of resonant absorption for a 1-dimensional electron density distribution  $n_e(x)$ .  $\mathbf{k}$  is the incident wave vector and  $\theta$  is the incident angle. The field is reflected at the critical surface  $n_c$ , which coincides with purely normal  $\mathbf{E}$  component. This illustration is largely inspired by Figure 2.5 found in [74].

The geometrical representation of a wave propagating in a density plasma, illustrated by Fig 2.1, becomes wrong for a short scale length  $L$  because the underlying hypotheses behind this representation is that  $L \gg \lambda$  where  $\lambda$  is the driving laser wavelength. Indeed, a representation of an optical wave with  $\vec{k}$  changing direction while propagating along  $x$  is a geometrical optics representation driven by the eikonal equation [75], or in other words the Fermat Principle, and we can write:

$$n(x) \sin \theta(x) = \text{constant} \quad (2.6)$$

That is to say in our case for a propagating wave of frequency  $\omega$ :

$$\left(1 - \frac{\omega_p(x)^2}{\omega^2}\right)^{1/2} \sin \theta(x) = \sin(\theta_0) \quad (2.7)$$

where  $\theta$  is expected to increase with  $x$ , since  $\mathbf{k}$  is directed towards a zone of lower index. In this case, the wave would be refracted by the underdense plasma before it could reach

the critical density  $n_c$ .

This shows that the geometrical approach is incorrect and that propagation in the underdense part of the plasma, when  $L$  is comparable to  $\lambda$ , needs to be treated using wave equations 2.5. However, the mental representation given in Fig 2.1 is still relevant as shown by Freidberg et al. [72] who integrated the system of equations 2.5b for a magnetic field having the form:

$$B = B_z(x)e^{-i(\omega t - k_y y)}$$

where  $k_y = \frac{\omega}{c} \sin \theta$  is independent of  $x$ . The solution in the case of a linear density gradient increasing from 0 to the critical density is evanescent for  $E_y$ . This absorption behavior is optimal for a given angle and gradient length ( $\theta = 23^\circ$  for  $L = 1.6\lambda$ ). The  $E_y$  component of the electric field is rigorously equal to zero at the critical surface while the  $E_x$  component of the electric field significantly increases. Therefore: the geometrical representation given in Fig 2.1 appears correct if instead of picturing the  $\mathbf{k}$  vector turning during the propagation, we impose  $\theta$  to be constant at all time and instead picture the evanescent  $E_y$  component of the electric field. This singular behavior is associated with a strong coupling of  $E_x$  with plasma waves at the critical surface and is responsible for collisionless conversion of the laser energy into electronic kinetic motion [72].

The important remark to make about resonant absorption is that the description of a neutral plasma remains valid as long as the scaling law given in Eq. A.14 holds true. In particular, for a plasma at critical density, this implies:

$$L_0 \gg \frac{V_{osc}}{\omega_0} \approx \lambda_0/6$$

The numerical estimate is done for a typical electric field of  $a_0 = 1$  at  $\lambda_0 = 800$  nm. In the physical mechanism we consider, the plasma length typically scales as a fraction of the laser wavelength, which is why a ‘‘Brunel’’ absorption model, as presented hereafter, is applicable.

## 2.2 Brunel absorption mechanism

Brunel’s absorption mechanism is crucial in order to understand how the laser beam reflecting off the critical surface can transfer its energy to the plasma without penetrating it. Indeed, up until Brunel’s milestone article in 1987 [61], absorption of a short laser pulse (CO<sub>2</sub> lasers with picosecond durations at the time) by overdense plasmas was mainly attributed to resonant absorption [72].

In Brunel’s model, the electrons at the plasma mirror surface respond to the incident laser electric field in such a way that the plasma is no longer considered neutral. At different phase of the driving laser, surface electrons are accelerated towards vacuum following

different trajectories, while the much heavier ions remain static. This creates a charge separation field which tends to pull electrons back towards the plasma. As the laser field changes sign, it adds to the ion static field and electrons accelerated in the direction of plasma bulk gain sufficient energy to cross the critical surface and therefore escape the laser influence. As they cross the critical surface with accumulated kinetic energy and "(...) since the field is null inside, one can see that the kinetic energy given to the particles that reenter the plasma is lost(Brunel,1987 [61])", or in other words the laser transfers its energy to the plasma, justifying the term "absorption".

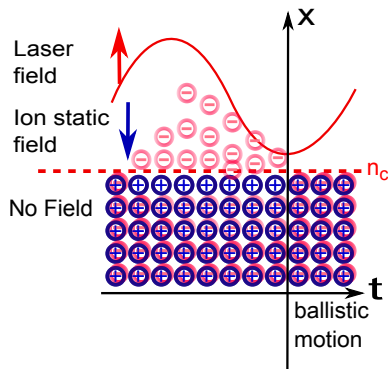
## 2.2.1 Modeling

A 1-dimensional approach allows one to get an analytical expression of the electron trajectories for a given incident laser field  $E_L(t)$  only dependent on time  $t$  and defined at the surface of the plasma. We therefore project the electron equation of motion onto the  $x$  direction of space and impose  $v_y = v_z = 0$  such that:

$$\frac{d(\gamma v_x)}{dt} = -e \underbrace{(\mathbf{E}_I + \mathbf{E}_R) \cdot \mathbf{u}_x}_{\text{reflection}} - e \underbrace{(v_y B_z - v_z B_y)}_{=0} \quad (2.8)$$

where  $E_I$  and  $E_R$  are the incident and reflected fields at the plasma surface. The laser field strength results from their constructive interference such that  $E_L(t) = 2E_I(t) \sin \theta$  with the trivial assumption that  $|E_I| = |E_R|$ .

Electrons are accelerated away from the critical surface into vacuum creating a space charge field due to the static ions. In result, this space charge field will screen the driving laser field. To account for this screening, we impose the electric field to be rigorously equal to zero at the critical density surface and inside the bulk of the plasma.



Relativistic equation of motion without magnetic field for the  $i$ th electron born at time  $t_i$ :

$$\begin{cases} E_i(t) = E_L(t) - E_L(t_i) & (2.9a) \\ \frac{d\gamma_i v_i}{dt} = -e E_i(t) & (2.9b) \end{cases}$$

The system of Eq. 2.9 applies only to vacuum electrons located above the initial critical density surface (represented by the red dotted line). Note that in this case, the critical surface is located at a constant position  $x_c$  in time. This assumption is no longer true for highly relativistic interactions [76] and the motion of the critical surface has to be taken into account. This is done in particular in the work of Gonoskov [77]. The principle of superposition allows one to add the contribution of the laser field, independent of the

position because the electron propagation paths are much shorter than the driving laser wavelength, and the electrostatic field resulting from charge separation. The latter is given by the Poisson equation :

$$\nabla^2 \phi(x, y, z, t) = \frac{\rho(x, y, z, t)}{\epsilon_0} \quad (2.10)$$

In three dimensions, the analytical solution is written:

$$\phi(x, y, z, t) = \frac{1}{\epsilon_0} \int_{\Omega} \rho(x', y', z', t) G(x - x', y - y', z - z') dx' dy' dz'$$

where  $G$  is the Green function derived in Appendix B and  $\Omega$  the charged region of space. In one-dimension, the Green function is defined by  $G(r) = -\frac{1}{2}|r|$  such that we have, with  $\rho$  defined as a linear charge density:

$$E_P(x) = -\partial_x \phi = \frac{1}{2\epsilon_0} \partial_x \left[ \int_{\mathbb{R}} \rho(x') |x - x'| dx' \right] \quad (2.11)$$

$$= \frac{1}{2\epsilon_0} \left[ \int_{-\infty}^x \rho(x') dx' - \int_x^{\infty} \rho(x') dx' \right] \quad (2.12)$$

$$= -\frac{1}{\epsilon_0} \left[ \int_x^{\infty} \rho(x') dx' \right] = -\frac{Q_{x' > x}}{\epsilon_0} \quad (2.13)$$

where  $Q_{x' > x}$  is the total charge integrated over  $x' > x$ . Note that the one-dimension model holds true as long as the electrons are "close" to the critical surface or in other words that the lateral dimension of the charge distribution is much greater than its longitudinal dimension. The equation of motion is the result of two simple hypotheses: (i) The electric field felt by the  $i^{th}$  electron is the superposition of the laser field and the charge separation field as expressed in Eq. 2.14a, (ii) this field is rigorously equal to zero for  $t = t_i^-$  at the beginning of motion.

$$\begin{cases} E_i(t) = E_P(x_i(t)) + E_L(t) \end{cases} \quad (2.14a)$$

$$\begin{cases} 0 = E_P(x_i(t_i)) + E_L(t_i) \end{cases} \quad (2.14b)$$

We subtract 2.14b from 2.14a and note that because of Eq. 2.13, if we impose that the electron trajectories do not cross, we have  $E_P(x_i(t)) = E_P(x_i(t_i))$  at all time such that:

$$E_i(t) = E_L(t) - E_L(t_i) \quad (2.15)$$

## 2.2.2 Physical interpretation

With Eq. 2.9 we can plot the electron trajectories in Fig 2.2: every laser period, a bunch of electrons propagates into the neutral dense plasma with non-negligible kinetic energy. This accounts for Brunel's absorption and, as we describe in the next section, gives rise to electronic plasma waves responsible for the generation of attosecond pulses [51].

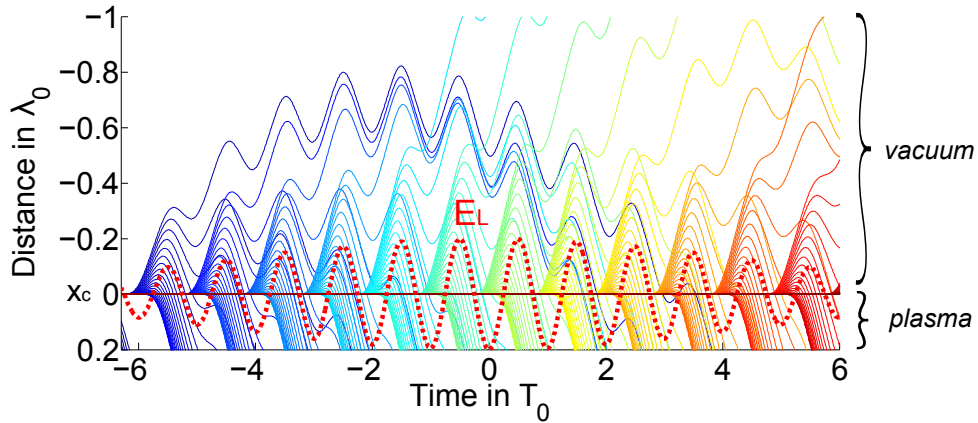


Figure 2.2 – Integration of Brunel’s equation for an electric field of intensity  $a_0 = 1$  ( $a_0$  convention described in AppendixA) and duration  $\tau_{fwhm} = 20\text{fs}$ . Vacuum is located on the side  $x < 0$  and a different color scale is used for electrons emitted from different laser cycles.

The simple integration performed in Fig 2.2 shows that some of the electrons oscillate in vacuum during several laser periods. These electrons are not interesting in the scope of this model because of the 1-dimension hypothesis: in reality, the field should be calculated in three dimensions where it undergoes a  $\propto 1/|r|^2$  decay instead of being constant as it is the case in 1D. What’s more, as the laser pulse is reflected from the critical surface, it generates a time-varying interference pattern which can affect significantly the electron’s dynamic as will be developed in Chapter 7, where we describe the electrons acceleration from the plasma mirrors.

In conclusion, in Brunel’s model, laser absorption is a consequence of surface electrons crossing the critical surface of the plasma as they follow the periodic oscillation of the driving laser pulse. We presented the simple one-dimensional model and observed how bunches of electron periodically escape the field to the overdense plasma region.

Brunel recognized these electrons as "hot electrons", and compared his model with experimental temperature measurement through Bremsstrahlung emission [28,71,78]. Note that several recent articles designate Brunel’s theory as one which can explain acceleration of electrons from solid density target towards vacuum. This shortcoming is an extensive interpretation of the term "hot electrons" where electrons escape the target. In Brunel’s article, the term “hot electron” refers to the suprathermal tail of a Maxwell-Boltzmann distribution. However, using Brunel’s model, we can explain the generation of harmonics occurring in the overdense part of the plasma as we describe hereafter.

## 2.3 Harmonic response of an overdense plasma

One of the great advantages of Brunel's model is to provide a simple equation for the periodic motion of the electrons driven by the laser at the plasma surface. When the returning electrons cross the critical density, their crossing trajectories define an electronic perturbation propagating in the overdense plasma and generating plasma waves in its wake [24, 52, 79]. This gives rise to harmonic generation. We will describe the nature of this perturbation and how it relates to the temporal properties of the harmonic emission in Chapter 4. In this Chapter, we focus solely on the response of a plasma to an arbitrary electronic density perturbation.

### 2.3.1 Plasma perturbative approach

Let's start with the simple case of a static cold plasma of density  $n_e(r, t)$  and study its response to a perturbation. We start with the system of equations:

$$\begin{cases} m_e \frac{d(\gamma v(r, t))}{dt} = -eE(r, t) - ev(r, t) \times B(r, t) \\ \nabla E = \frac{\rho}{\epsilon_0} \\ \partial_t n + \nabla(nv) = 0 \end{cases} \quad (2.16)$$

The density of the fully ionized plasma is defined such that the plasma is neutral at  $t < 0$ . In addition, we make the strong hypothesis that the heavier ions do not move, leading to  $n_i(r, t) = n_{i0}$ . This implies:

$$\begin{cases} \rho(r, t) = Zen_{i0} - en_e(r, t) \\ m = m_e \\ v(r, t) = v_e(r, t) \end{cases} \quad (2.17)$$

We also renormalize the variables in the following way (we define  $Z = 1$  to simplify the notations of the system):

$$\begin{cases} \bar{t} = \omega_0 t \\ \bar{v} = v/c \\ \bar{r} = \frac{2\pi}{\lambda_0} r \\ \bar{n} = \frac{n}{n_{e0}} \quad \bar{\rho} = \frac{\rho}{en_{e0}} = 1 - \bar{n} \end{cases} \quad (2.18)$$

where  $n_{e0}$  is the electron density for  $t < 0$ . In the case of a classical equation of motion ( $\gamma = 1, v \times B = 0$ ) for a charged particle of velocity  $v$ , Eq. 2.16 leads to the system of equations 2.19. The corresponding dimensionless equation is given by Eq. 2.20 and will be used to describe the plasma's dynamical response to a perturbation.

$$\begin{cases} \frac{dn_e}{dt} = -n_e \nabla(v_e) & (2.19a) \\ \frac{d(\nabla v(r, t))}{dt} = \frac{-e\rho(r, t)}{m_e \epsilon_0} & (2.19b) \end{cases}$$

$$\begin{cases} \frac{d\bar{n}}{dt} = -\bar{n} \nabla_{\bar{r}}(\bar{v}) & (2.20a) \end{cases}$$

$$\begin{cases} \frac{d(\nabla_{\bar{r}} \bar{v}(r, t))}{dt} = \bar{n}(r, t) - 1 & (2.20b) \end{cases}$$

Where we pose:

$$\frac{e^2 n_{e0}}{m_e \omega_0^2 \epsilon_0} = 1$$

And by definition:

$$\lambda_0 = \frac{2\pi c}{\omega_0}$$

We obtain a system of differential equations for variables  $\bar{n}$  and  $\nabla \bar{v}$ . One can consider the two-dimensional vector

$$X = \begin{pmatrix} \bar{n}(r, t) \\ \nabla_{\bar{r}} \bar{v} \end{pmatrix}$$

We have according to equations 2.20

$$\begin{cases} \frac{dX}{dt} = f(X) \\ f(x, y) = (-xy, x - 1) \end{cases} \quad (2.21)$$

Looking at Eq. 2.20, the system is obviously stationary for  $(\bar{n} = 1, \nabla_{\bar{r}} \bar{v} = 0)$ , which corresponds to a neutral plasma at rest. This system can be linearized to the first order by calculating the Jacobian matrix of function  $f$  around  $(\bar{n} = 1, \nabla_{\bar{r}} \bar{v} = 0)$ . The resulting system of equations is:

$$\begin{cases} \frac{dX}{dt} = \begin{pmatrix} 0 & -1 \\ 1 & 0 \end{pmatrix} X \end{cases} \quad (2.22)$$

We recognize here the equation of a harmonic oscillator [51, 80] when linearizing the system in Eq. 2.16 around its stationary solution. In Fig 2.3 we compare the phase portrait resulting from the integration of Eq. 2.21 with its linearized system described by Eq. 2.22. In the latter case, we observe a periodic behavior of period  $\bar{T} = 1$  in the response to an initial perturbation which means that the plasma oscillates at frequency:

$$\omega_p = \sqrt{\frac{n_{e0} e^2}{m_e \epsilon_0}}$$

High-harmonic generation is due to this resonant plasma response to an initial perturbation, which locally follows Eq. 2.20. We integrated this equation and show the result on a phase plot in Fig 2.3, where we also see that the linearized integration is a good approximation of the plasma response. In practice, the plasma is perturbed by a peak of density propagating throughout the density gradient at relativistic velocity  $v_p$  and of density several times  $n_c$  [51, 79].

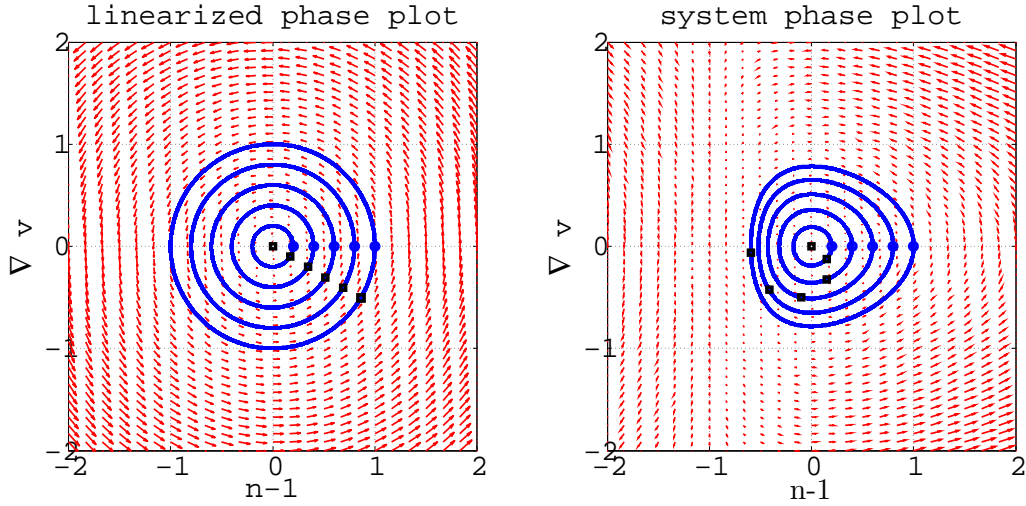


Figure 2.3 – Phase plot comparison between the system of equations 2.16 (right) and its linearized equivalent (left). The trajectories of  $\delta\bar{n} = \bar{n} - 1$  and  $\nabla\bar{v}$  are integrated and represented for initial perturbation represented by solid circles from  $\bar{t} = 0$  to  $\bar{t} = 100$ . Final positions are marked with black solid squares.

So far, the integration has to be done “locally”, which is equivalent to assuming that the plasma is homogeneous. High inhomogeneities make the integration very challenging and can influence drastically the plasma response to a perturbation as discussed in 2.3.4.

### 2.3.2 Coherent Wake Emission

We just described the local electronic response to a perturbation. When the plasma forms at the surface of the solid target, it can not be considered homogeneous as a result of thermodynamical expansion [16]. There, the plasma density is commonly described by a decreasing exponential [34, 81] from homogeneous plasma of density  $n_{max}$  at position  $x_{max}$  to zero density in vacuum as expressed in Eq. 2.23:

$$\begin{cases} \bar{n}_e(x, t) = e^{-(x-x_c)/L} & \text{for } x > x_{max} \\ \bar{n}_e(x, t) = \frac{n_{max}}{n_c} & \text{for } x \leq x_{max} \end{cases} \quad (2.23)$$

where  $n_c$  denotes the critical density at position  $x_c$ . Vacuum is located at  $x > 0$

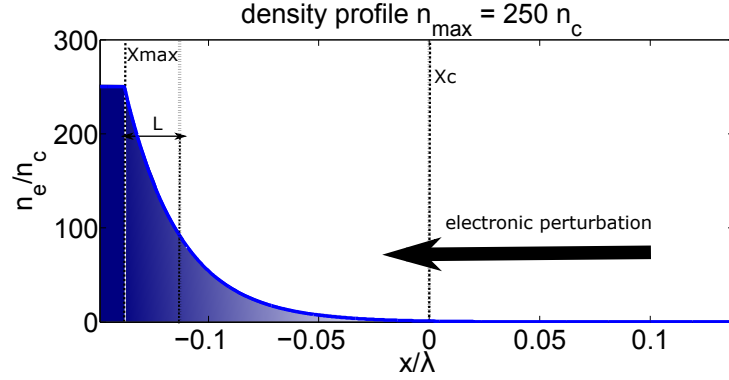


Figure 2.4 – Density gradient representation defined by Eq. 2.23,  $L = \lambda/40$  and  $n_{max} = 250n_c$

Let's now consider a perturbation of the electronic density  $\Delta_n$  propagating at a speed  $v_p$  from  $x = 0$  at  $t = 0$  towards the bulk plasma. The perturbation reaches the coordinate  $x$  at time  $t = \frac{x}{v_p}$ . We can therefore write in the linearized approximation derived in 2.3.1:

$$\begin{cases} \delta\bar{n}_e(x, t) = \Delta_n \cos(\omega_p(x)(t - \frac{x}{v_p})) & \text{for } t \geq \frac{x}{v_p} \\ \delta\bar{n}_e(x, t) = 0 & \text{for } t < \frac{x}{v_p} \end{cases} \quad (2.24)$$

with

$$\omega_p(x) = \sqrt{\frac{n_c e^2}{m_e \epsilon_0}} \sqrt{\bar{n}_e(x)} = \omega_0 \sqrt{\bar{n}_e(x)}$$

where  $\bar{n}_e$  is the normalized electronic density defined in Eq. 2.20.

We illustrate Equations 2.24 in Fig 2.5 where we represent over time the evolution of the plasma perturbation for plasma scale lengths of respectively  $L = \lambda/40$  and  $L = \lambda/15$  for an arbitrary density of  $n_{max} = 250n_c$ . The case  $\lambda/15$  shows that for longer gradients, the perturbation has no time to propagate up to the maximum density before the end of an optical cycle. This explains why plasma waves (and therefore harmonic emission) is only efficient for short plasma scale lengths [24, 51, 74, 79].

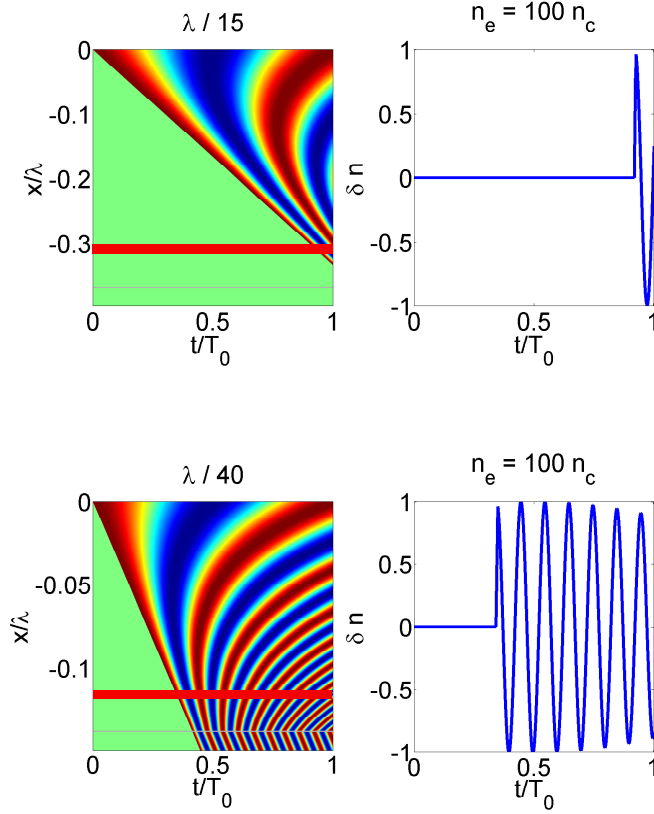


Figure 2.5 – Representation of plasma oscillations over one laser period for gradients with  $L = \lambda/15$  and  $L = \lambda/40$ , where  $n_{max} = 250n_c$ . The position where  $n_e = 100n_c$  is represented by a solid red line on the left-hand-side figures, and the corresponding plasma oscillation is plotted on the right-hand-side figure

The link to the generation of high order harmonics is now quite straightforward. Indeed, since we know that a charge in motion radiates, it follows that plasma waves result in electromagnetic radiation. This emission can be evaluated by integrating the propagation equation applied to the vector potential  $\mathbf{A}$  using a Green function formalism (cf B) [75]. At a position  $\mathbf{r}$  far from the plasma, we calculate the contribution of a volume  $\Omega$  from the plasma to the radiation:

$$\left\{ \begin{array}{l} \mathbf{A}(\mathbf{r}, t) = \frac{\mu_0}{4\pi} \int_{\mathbf{r}' \in \Omega} \frac{\mathbf{j}(\mathbf{r}', t - |\mathbf{r} - \mathbf{r}'|/c)}{|\mathbf{r} - \mathbf{r}'|} d\mathbf{r}' \end{array} \right. \quad (2.25a)$$

$$\left\{ \begin{array}{l} \phi(\mathbf{r}, t) = \frac{-e}{4\pi\epsilon_0} \int_{\mathbf{r}' \in \Omega} \frac{n_e(\mathbf{r}', t - |\mathbf{r} - \mathbf{r}'|/c)}{|\mathbf{r} - \mathbf{r}'|} d\mathbf{r}' \end{array} \right. \quad (2.25b)$$

where  $\mathbf{r}'$  is a position inside the plasma,  $n_e$  the electronic density and  $\mathbf{j} = -en_e\mathbf{v}_e$  the associated current. Knowing that  $\mathbf{E} = -\nabla\phi - \partial_t\mathbf{A}$  and  $\mathbf{B} = \nabla \times \mathbf{A}$ , we see how currents or plasma waves inside the plasma lead to electromagnetic radiation. If we simplify the problem to the 1-dimension case and inject Eq. 2.24 in Eq. 2.25b (where we use the 1-dimension Green function instead), we can write in first approximation for  $t \geq t_p(\cdot)$ , the

time at which perturbations are triggered:

$$E(x, t) = \frac{e\Delta_n}{2\epsilon_0} \int_{x' \in \Omega} \cos(\omega_p(x')(t - |x - x'|/c - x'/v_p)) dx'$$

where we clearly identify the coherent superposition of propagation waves of frequency  $\omega_p(x')$ . This leads to the following conclusion:

- The spectrum of the electromagnetic radiation emitted by the plasma contains all possible values of  $\omega_p(\mathbf{r}')$  such that **Coherent Wake emission** will undergo a spectral cutoff at  $\omega_{p,max}$ . The field here is expressed as the response to one optical cycle plasma response. This process is repeated every laser period which leads to emission of co-propagating pulses separated by  $1/T_0$ . In the spectral domain, these pulses interfere constructively for all multiples of the driving laser: this is designated as "High Harmonic Generation" (HHG).
- The time of emission corresponds to the moment where the integral reaches an optimal value. The harmonic emission properties are extensively described in [51].

### 2.3.3 Influence of spatial spreading of the perturbation

So far, we have considered the perturbation to be a Dirac function in time. Let's see the influence of a temporal spread of the perturbation over an interval  $\tau$ . Given the principle of superposition, we will add the contribution of all resonators born at different time  $t_k$ :

$$\begin{cases} \delta\bar{n}_{e,k}(x, t) = \Delta_k \cos(\omega_p(x)(t - t_k)) & \text{for } t \geq t_k \\ \delta\bar{n}_e(x, t) = \sum_k \delta\bar{n}_{e,k}(x, t) = \sum_k \Delta_k \cos(\omega_p(x)(t - t_k)) \Pi(t - t_k) \end{cases} \quad (2.26)$$

A more accurate way to write this would be to replace the sum by an integral such that:

$$\delta\bar{n}_e(x, t) = \int_{-\infty}^t \Delta(t') \cos(\omega_p(x)(t - t')) dt'. \quad (2.27)$$

Without developing further, it clearly appears that when  $\Delta(t')$  extends over  $1/\omega_p(x)$ , the integral tends to zero which means the perturbation no longer inefficiently stimulates the plasma. We calculate that the perturbation should verify  $\tau \ll 100 - 200$  as for harmonics of order from 10 to 20.

### 2.3.4 Landau damping in a homogeneous plasma

So far, we only use the result derived in 2.3.1 to describe the global plasma response to a perturbation, which means each infinitesimal portion of the plasma is locally homogeneous. In addition, the absence of dissipative term in the system of equations 2.21 ultimately leads the system to oscillate infinitely. However, this representation becomes incorrect for strong inhomogeneities and one should turn to a fluid equation of motion [82]

as described in Appendix A. The dynamics of the system are therefore described by the collisionless, non-magnetic linearized Vlasov equation [83]:

$$\begin{cases} \partial_t f_e + v_e \nabla_{\mathbf{r}} f_e + F(f_e) \cdot \nabla_v f_{e0} = 0 \\ F(v_e) = \frac{e}{m_e} \nabla \phi \end{cases} \quad (2.28)$$

where  $\phi$  is defined by the relation:

$$\nabla^2 \phi = -\frac{e}{\epsilon_0} \int_{\mathbf{v} \in \mathbb{R}} f_e(\mathbf{r}, \mathbf{v}, t) d\mathbf{v} \quad (2.29)$$

This equation describes the dynamical evolution of the electronic distribution  $f_e(r, v, t)$  given an homogeneous initial distribution  $f_{e0}(v)$  at  $t = 0$ . The absence of collisional term in this equation makes it time-reversible. However, Landau derived an exact solution for this equation in 1946 [84], highlighting the non-intuitive behavior of plasma waves as they respond to an initial perturbation: the solution undergoes an irreversible evolution. Over time, plasma oscillations will dissipate  $\propto e^{-\nu t}$  where  $\nu$  is called the damping factor. The solution was derived using plane wave decomposition with  $\mathbf{k}$  as the wave vector, for a perturbation around the non-perturbed distribution  $f_{e0}$  (taken to be equal to a Maxwellian distribution):

$$\begin{cases} f_{e0}(\mathbf{v}) + \int f_{e1}(\mathbf{v}, \mathbf{k}, 0) e^{i\mathbf{k}\mathbf{r}} \\ f_{e0}(\mathbf{v}) + \int f_{e1}(\mathbf{v}, \mathbf{k}, t) e^{i\mathbf{k}\mathbf{r}} \end{cases} \quad \begin{matrix} (2.30a) \\ (2.30b) \end{matrix}$$

Here, 2.30a refers to the initial perturbation imposed on the system, and 2.30b the resulting distribution at an arbitrary time of plasma evolution. With this notation, the Poisson equation is:

$$k^2 \phi = \frac{e}{\epsilon_0} \int_{\mathbf{v} \in \mathbb{R}} f_{e1}(\mathbf{v}, \mathbf{k}, t) d\mathbf{v}. \quad (2.31)$$

In the case  $k\lambda_D \ll 1$ , where  $\lambda_D$  denotes the Debye length defined in Appendix A a solution is given by the relations [83]:

$$\begin{cases} \omega^2 = \omega_p^2 (1 + 3k^2 \lambda_D^2) \\ \nu = \omega \sqrt{\frac{\pi}{8}} \frac{1}{(k\lambda_D)^3} e^{-1/(2k^2 \lambda_D^2)} \end{cases} \quad \begin{matrix} (2.32a) \\ (2.32b) \end{matrix}$$

where one clearly identifies, in Eq. 2.32a, a dispersion relation for plasma perturbations inside the plasma. For increasing  $k$  values, plasma waves are damped over time. In the context of this thesis, only timescales for damping on the order of the driving laser period  $T_0$  are of interest. However, in the worst case scenario ( $k\lambda_D \approx 1$ ) we have:

$$T_0 \nu \approx 2\sqrt{\frac{\pi}{8}} e^{-1/2} \omega_p T_0 \approx 1.5\pi \sqrt{\frac{n_{e0}}{n_c}}$$

This indicates that strong plasma inhomogeneities (relative to the Debye length  $\lambda_D$ ) can be dissipated in a dense plasma on a time scale which compares with the driving laser through Landau damping. In Appendix A, we derive  $\lambda_D$  and evaluate its value for  $\lambda_0 = 800\text{nm}$ ,  $k_B T_e = 100\text{eV}$ , leading to:

$$\lambda_D = \sqrt{\frac{n_c}{n_{e0}}} 1.78 \text{ nm} \quad (2.33)$$

The case  $k\lambda_D \gg 1$  is treated in [84] but is of no interest here. Note that in the present introduction to Landau damping, the plasma is assumed to have a homogeneous density distribution. However, in the context of this thesis, the generated plasma distributions on solid targets (before any perturbation) outline strong inhomogeneities where the typical scale length  $L$  is a fraction of the driving laser wavelength. As a consequence, we have no certainty that the present derivation of plasma response still applies.

### 2.3.5 Landau damping in an inhomogeneous plasma

For very short gradients ( $L < \lambda/300$ ), plasma oscillations undergo strong damping effect as demonstrated by PIC simulations performed in [51]. This ultimately results in a significant drop in CWE emission. Similar to Eq. 2.30, we write the system evolution in the form:

$$\begin{cases} f_{e0}(\mathbf{r}, \mathbf{v}) + f_{e1}(v, r, 0) & (2.34a) \\ f_{e0}(\mathbf{r}, \mathbf{v}) + f_{e1}(v, r, t) & (2.34b) \end{cases}$$

The linearized Vlasov equation given in 2.28 is affected by this and is now:

$$\partial_t f_{e1} = \underbrace{-v_e \nabla_{\mathbf{r}} f_{e0} - v_e \nabla_{\mathbf{r}} f_{e1}}_{\text{inhomogeneity damping}} - \underbrace{F(f_{e1}) \cdot \nabla_v f_{e0} - F(f_{e1}) \cdot \nabla_v f_{e1}}_{\text{thermal damping}} \quad (2.35)$$

The challenging case of an inhomogeneous plasma has been partially treated in [85, 86], where in the case of strong plasma density inhomogeneities, Landau damping becomes important and is quantified by the damping factor:

$$\alpha = -\frac{\omega^2}{2k^2} \frac{1}{L^2}$$

where  $L$  is the characteristic variation length which we identify as our gradient scale length.  $\alpha T_0^2 \gg 1$ , where  $T_0$  is the driving laser period, corresponds to a highly inhomogeneous case.

The rigorous analytical resolution of the inhomogeneous case is quite challenging and remains a current field of research. However, PIC simulations should in principle reproduce this damping effect: we compare the plasma response of a gradient density perturbed by an incoming electron bunch propagating at a velocity close to  $c$  towards the bulk in the

absence of a laser beam. This way, we can only observe a pure plasma wave resulting from the electronic perturbation. In Fig 2.6, the plasma electronic density fluctuation is represented for respectively  $L = \lambda/40$ (left) and  $L = \lambda/300$ (right). One clearly sees that when the plasma scale length is very short, the electronic plasma waves are quickly damped. In this simulation, the plasma temperature is taken equal to zero. In case of Landau damping, we should expect the attenuation to be all the more pronounced as we increase the temperature of the plasma.

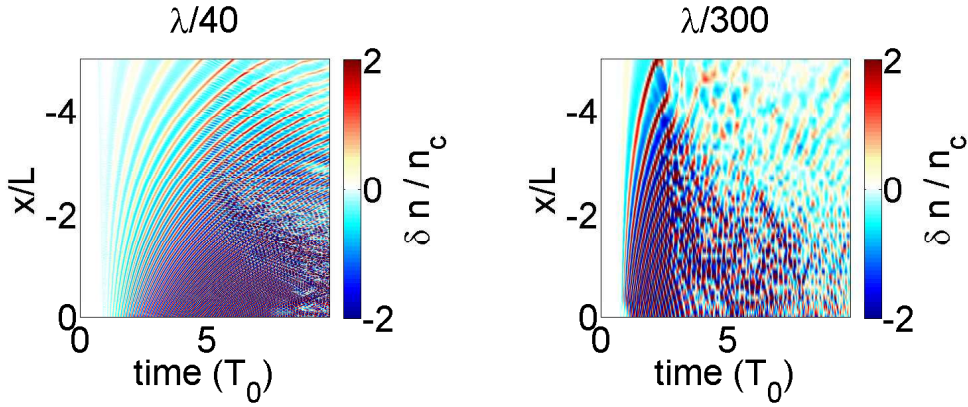


Figure 2.6 – 1D pic simulation of plasma oscillations over time triggered by an electronic perturbation. The maximum density is  $n_e = 100n_c$  the gradients are  $\lambda/40$  (left) and  $\lambda/300$  (right) respectively. The very short gradient shows damping effect due to strong inhomogeneities of the plasma. The electronic perturbation  $\Delta_n = n_c/100$  and propagates at  $v_p \approx c$  towards the plasma. The plasma initial temperature is  $T_e = 0$  eV

## 2.4 Conclusion

In this chapter, we have gone through the detailed presentation of the different mechanisms involved to understand short plasma scale length response to a femtosecond laser pulse. We presented the resonant absorption model only valid for very long plasma scale lengths by placing it in its historical context, that is to say before high-intensity gradient controlled experiments on solid targets were made possible using contrast cleaning techniques.

For short plasma scale lengths, we showed how the Brunel model provides an accurate representation of the electron motion in presence of a laser field. Brunel electrons are responsible for the emergence of electronic perturbations inside the plasma bulk: we explained in details how these perturbations give birth to plasma waves by solving the harmonic equation of the plasma with given density. Plasma waves in return emit X-UV light every laser cycle. This defines the Coherent Wake Emission mechanism [51, 87, 88].

Finally, we have seen how a fluid representation of the plasma is necessary to describe plasma wave damping occurring for very short plasma scale lengths. This is called Landau damping and was confirmed by 1D PIC simulations. We will demonstrate this effect in a gradient-control experiment in Section 4.1.4.

# Chapter 3

## Double-CPA laser architecture

### Outline

---

<b>3.1</b>	<b>Global architecture</b>	<b>44</b>
3.1.1	Overview of the laser chain	44
3.1.2	XPW contrast cleaning	45
3.1.3	Spectral clipping	48
3.1.4	Prepulse generation from post-pulses	48
<b>3.2</b>	<b>Post-compression and beam shaping</b>	<b>54</b>
<b>3.3</b>	<b>Solid-target experimental setup</b>	<b>56</b>
3.3.1	Experimental chamber and beam profile	56
3.3.2	Beam temporal profile	57
3.3.3	kHz solid target	58
<b>3.4</b>	<b>Conclusion</b>	<b>60</b>

---

The laser system in Salle Noire is a sub-TW system delivering a few mJ, 30fs, Carrier Envelope Phase (CEP) controlled, high-contrast beam at 1kHz [89]. TW-class lasers and above often operate at a lower repetition rate, typically in the Hz range [90–92]. However, in laser-plasma interaction schemes, it is very common that users operate in single shot mode regardless of the laser repetition rate (e.g a mechanical shutter) because thermal effects in the laser chain usually degrade the laser performance or simply because other operations, like moving the target to refresh the target surface require more time than available between two successive laser shots [93]. Compared to other installations where high-intensity laser-plasma experiments are conducted, our laser has a relatively low peak-power ( $<TW$ ) so that thermal effects can be efficiently managed for a continuous operation at 1kHz. A high intensity ( $\sim 10^{18} \text{ W/cm}^2$ ) on target is reached by focusing the laser with a parabola of very short focal length ( $f = 52 \text{ mm}$ ) while a stable rotating target developed by Antonin Borot during his PhD [74] enables the surface to be refreshed every millisecond.

## 3.1 Global architecture

### 3.1.1 Overview of the laser chain

Extensive details on the laser system can be found in [94–96], and a schematic representation is given in Fig 3.1. We present here the main constituent blocks of the laser system from the "front-end" towards the solid-target experimental chamber.

**First CPA (Chirped Pulse Amplifier):** The first block of the laser chain, also called front-end, is a commercial Titanium:Sapphire (Ti:Sa) stabilized laser from *Femtolaser GmbH* [97]: the oscillator generates a train of  $\sim$ nJ pulses at a frequency of 80 MHz. The pulse is then stretched to  $\sim$  20 ps with a SF57 bulk stretcher and sent into a 10-pass amplifier (first CPA of the laser chain). After 4 passes, the train frequency is reduced to 1kHz with a Pockels cell. In the end, the front-end delivers 1.8mJ, 30fs CEP stable pulses with a contrast of  $10^8$ .

**XPW:** After this first CPA, the beam is injected into an "XPW contrast filter" (described more in details in 3.1.2) which function is to enhance the temporal contrast of the pulse through a degenerate four-wave mixing process [98].

**Laser stretching before second CPA:** Dispersive propagation in 75cm of SF57 bulk material stretches the laser from roughly 30fs to 45ps.

**Dazzler:** The Dazzler is a commercial acousto-optic modulator (*Fastlite*) [99] used to shape the temporal properties of the incoming laser pulse. Through a user interface, it is possible to linearly shape the spectrum and the phase (decomposed on a polynomial base) of the beam. This module is extremely convenient to finely adjust the compression of the pulse on target.

**Second CPA :** The stretched pulse is then amplified with two consecutive Ti-Sa power amplifiers pumped with a frequency doubled Nd:Yag (*Photonics Industry*).

**Compression:** After amplification, the beam is partially compressed in air with set of gratings (*Fastlite*) chosen because they can compensate the third-order phase introduced by the bulk stretcher. The beam is then focused into a hollow core fiber under vacuum, which filters the beam spatial profile. After the fiber, the beam is recollimated with a spherical mirror and separated into a "main pulse" and a "prepulse" with a beam splitter. The final compression of both pulses is done in the "beam compression" vacuum chamber to avoid non-linear effects in the entrance window, using a set of chirped mirrors.

**Target chamber:** After compression, the beam is expanded by a factor 3 with a telescope to reach the tight focus regime ( $f/1.2$ ) and sent to the experimental solid-target chamber, located at the end of the laser chain. Both main pulse and prepulse are focused on target using the same off-axis parabola. Its full description is given in 3.3.

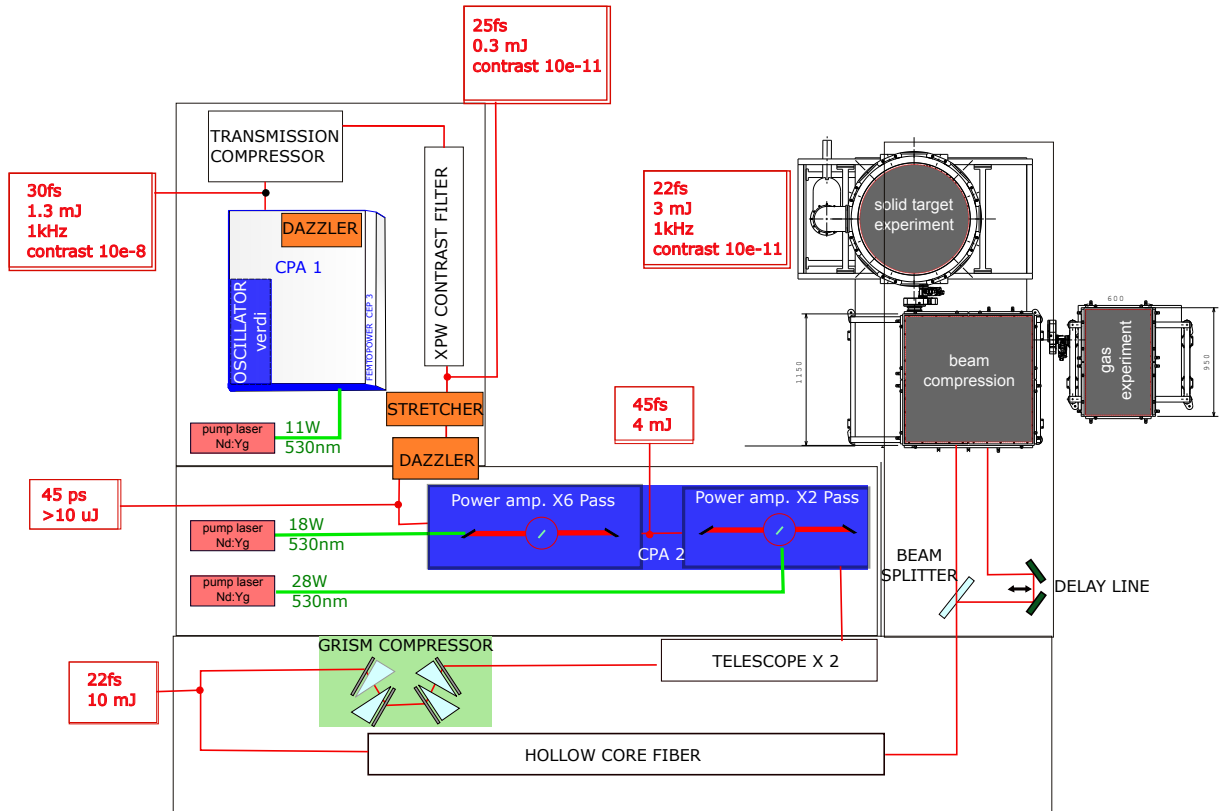


Figure 3.1 – Layout of "Salle Noire" laser

### 3.1.2 XPW contrast cleaning

The temporal contrast of a laser pulse is defined by the ratio of the intensity at time  $t$  and the maximum intensity measured on long time scales with respect to the pulse duration (picosecond to nanosecond). It is a critical parameter in laser-solid plasma interactions since it determines the actual interaction conditions of the laser peak intensity with the plasma. Indeed, as we already discussed in the introduction, a portion of the pulse energy is contained in the temporal pedestal picoseconds to nanoseconds. This pedestal is mainly constituted by a nanosecond-long pulse resulting from ASE<sup>1</sup>, intense enough to preionize a dielectric target for intensities  $\sim 10^{10-11}\text{W}/\text{cm}^2$  [100, 101] and prepulses which sub-picosecond durations where the ionization threshold intensities are typically  $\sim 10^{13-14}\text{W}/\text{cm}^2$  [102]. The plasma therefore has time to expand before the interaction with the pulse peak and dramatically change the non-linearity of the interaction (HHG generation collapses with long plasma scale length as indicated in 2.3.2). To increase the contrast, different techniques have been implemented: saturable absorbers, electro-optic switches up to a few ns before the main pulse [30], non-linear rotation of polarization [103, 104], plasma mirrors [32, 105, 106]. In our laser chain, we use a XPW (Cross-Polarized four Wave mixing process) [98] to increase the contrast after the first

1. Amplified Spontaneous Emission

CPA, as represented in Fig 3.2: the S polarized (with respect to the Glan polarizer) femtosecond output propagates non-linearly ( $\chi^{(3)}$ ) in BaF<sub>2</sub> crystals after going through a hollow core fiber for spatial filtering, and coherently generates a cross polarized beam (called XPW) with an efficiency proportional to  $(I/I_{max})^3$ . The XPW pulse has an improved contrast and is selected with a Glan polarizer. Because the overall efficiency of the process is  $\sim 25\%$ , two additional Ti:Sa amplifiers, represented on Fig 3.1, are necessary to increase the laser energy to more than 10mJ.

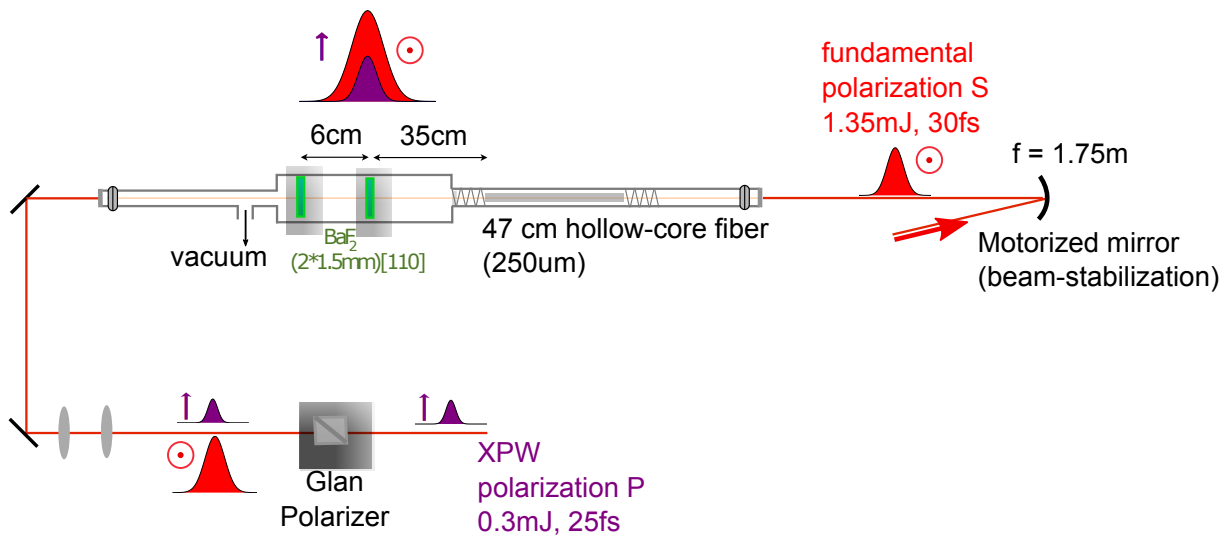


Figure 3.2 – Principle of XPW (Cross Polarization Wave mixing): a S polarized 30fs pulse propagates non-linearly ( $\chi^{(3)}$ ) in BaF<sub>2</sub> crystals and coherently generates a crossed polarized beam (called XPW) with an efficiency proportional to  $(I/I_{max})^3$ . The XPW pulse has an improved contrast and is selected with a Glan polarizer

We performed a contrast measurement using a commercial third-order autocorrelator (Sequoia, from *Amplitude Technologies*). The compressed pulse is split into two replicas. One replica is frequency doubled in a SHG crystal and later combined, at a given delay, with the second initial replica to generate the third harmonic of the initial pulse. The resulting signal is detected with a photomultiplier and reaches its maximum when the pulses overlap, that is to say at  $t = 0$ .

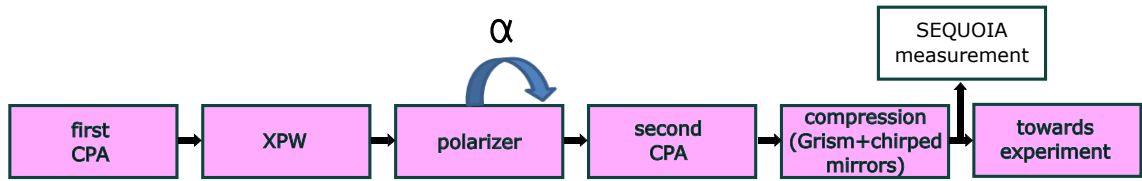


Figure 3.3 – Contrast measurement after XPW contrast cleaning.  $\alpha$  is the polarizer angle.  $\alpha = 0$  corresponds to optimal alignment.

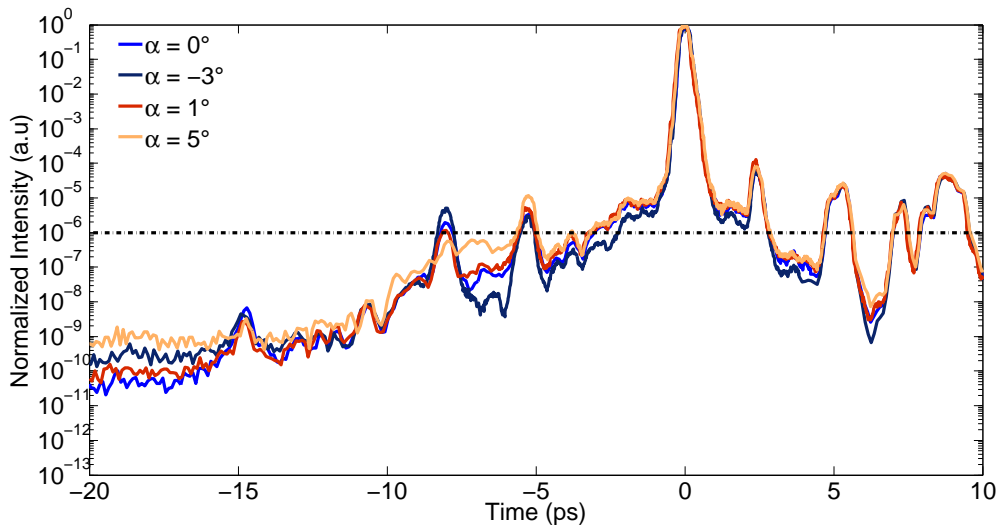


Figure 3.4 – SEQUOIA contrast measurement for different angles of the polarizer after XPW. The dotted horizontal line represents an ionization threshold for fused silica arbitrarily set to  $10^{12} \text{ W/cm}^2$  as an indicator (for  $I_{max} = 10^{18} \text{ W/cm}^2$ )

On the contrast measurement shown in Fig 3.4, we can appreciate the effect of the polarizer angle on the contrast measured after the double CPA followed by compression. The best contrast is obtained for  $\alpha = 0^\circ$  on the long temporal range (up to nanoseconds, not represented here) and reaches  $10^{-11}$  at -20 ps before the arrival of the main pulse. However, around  $-8 \text{ ps}$ , the contrast is on the contrary improved for a polarizer  $\alpha = 5^\circ$ , and around  $-5 \text{ ps}$ , for  $\alpha = -3^\circ$ . This observation has its importance and introduces what we call coherent contrast : when the laser is filtered by the XPW, the higher orders of the spectral phase induce temporal fluctuations which can extend up to  $\sim 20 \text{ ps}$  before and after the main pulse. The laser pulse goes into the  $2^{nd}$  CPA where nonlinearities induce phase modulations, and therefore modulation of the coherent contrast. This is very sensitive to a fine alignment of the XPW, and the optimal angle to filter out the long temporal range contrast is not necessarily the same for the coherent, ie short dynamic range contrast. As a consequence, the coherent contrast ( $t > -20 \text{ ps}$  typically) can be degraded and prepulses with intensities high enough to preionise the target can emerge.

### 3.1.3 Spectral clipping

Any amplitude modulation, such as spectral clipping on the optics, leads to coherent contrast degradation. This spectral clipping can be prevented by narrowing the pulse spectrum (using the Dazzler). The cost associated with this apodization is an increased duration of the compressed pulse. In Fig 3.5(a), we measured the contrast between -100ps and 10ps. The dotted line at -20ps arbitrarily separated the incoherent contrast ( $10^{-11}$  for  $t < -20$ ps) from the coherent contrast ( $t > -20$ ps). In Fig 3.5(b) we simply zoomed on the coherent contrast and we can clearly see the degradation (prepulse at -3ps) due to spectral clipping.

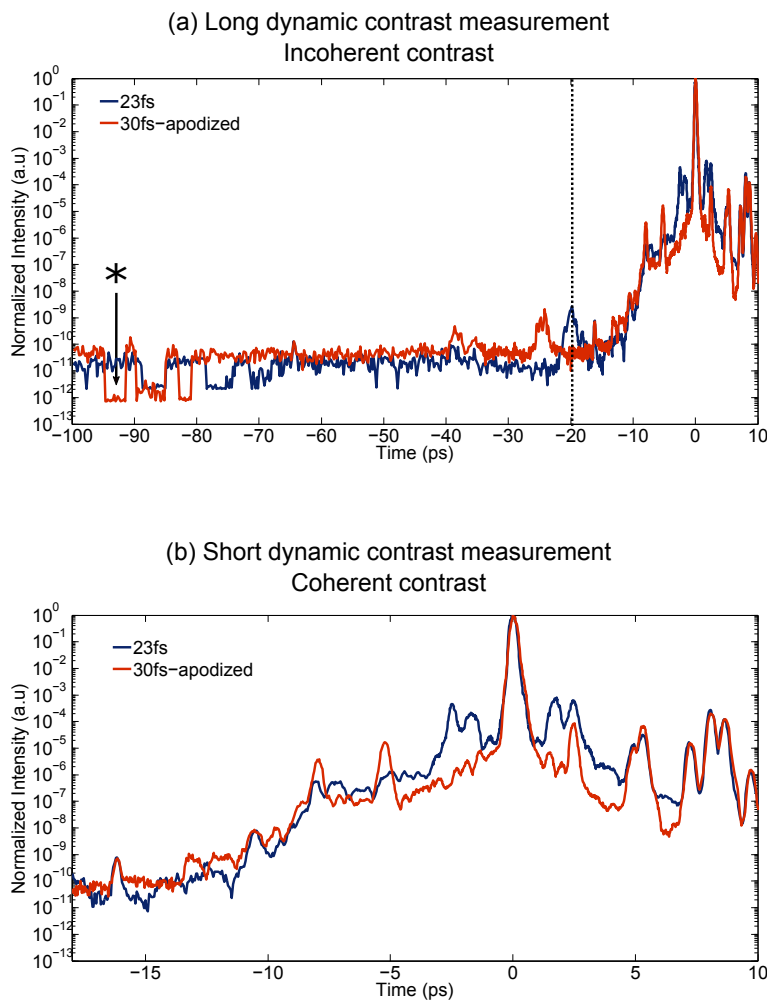


Figure 3.5 – SEQUOIA contrast measurement using sequoia after the double CPA with or without is apodization by the dazzler (respectively 30fs and 23fs FTL). (\*) beam is blocked to show detector noise level

### 3.1.4 Prepulse generation from post-pulses

We have identified an important source of degradation of the laser contrast: post-pulses. In theory, post-pulses arrive by definition after the main pulse, so they cannot

contribute to the target degradation prior to the interaction. However, a non-intuitive phenomenon occurs when a post-pulse propagates nonlinearly in a CPA (high B integral) after the beam has been stretched: a prepulse is generated. This problem has already been described in the context of CPA amplification [107–109] and has been verified experimentally [107, 110]. We show here, as suggested in [111], that nonlinear effects in CPA materials where the B integral is large are responsible for contrast degradation and can generate prepulses.

The experimental demonstration of this effect is summarized in Fig 3.6 where two optical elements (output window of XPW setup, beam splitter for diagnostics prior to amplification) are removed one after the other. We clearly see on the contrast measurement the successive suppression of the prepulses at respectively  $-8\text{ps}$  and  $-6\text{ps}$ .

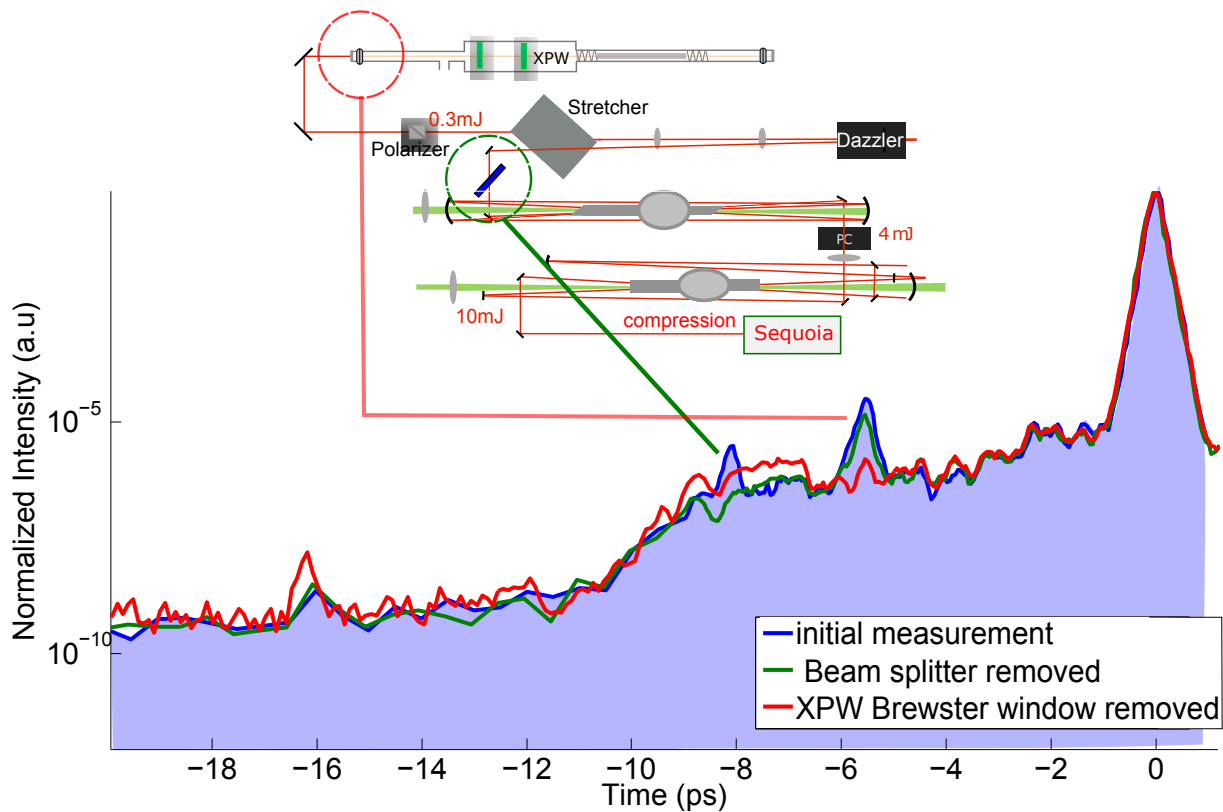


Figure 3.6 – Comparative temporal contrast measurement: removal of optics prior to the second CPA which induce post-pulses, and hence prepulses after the second CPA

We now show how self-phase modulation (SPM) can account for this behavior. We do not take into account the spatial profile of the pulse as it does not help to highlight the physical origin of nonlinear prepulse generation. We consider a laser pulse of duration  $\sigma_t$  in Fourier limit, defined by its temporal variable only. We model the effect of an arbitrary

stretcher using analytical relations found in [79], and we add an identical postpulse of relative amplitude  $\eta$  at a delay  $\tau$ :

$$E(t) = A_0(t) \exp(-i\omega_0 t) + \eta A_0(t - \tau) \exp(-i\omega_0(t - \tau)) \quad (3.1)$$

where the temporal envelop  $A_0$  is defined by [79]:

$$A_0(t) = \exp\left(-\frac{t^2}{2(1 + \xi^2)\sigma_t^2}\right) \exp(-i\phi(t)) \quad (3.2)$$

where  $\xi = \frac{\phi^{(2)}}{\tau^2}$  is the normalized spectral chirp induced by the stretcher and:

$$\phi(t) = \frac{1}{2\sigma_t^2} \frac{\xi t^2}{1 + \xi^2} + \frac{1}{2} \arctan(\xi)$$

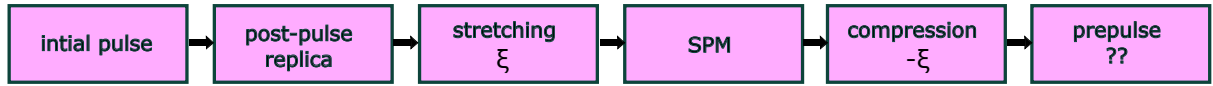


Figure 3.7 – Block diagram describing the operations performed on the initial pulse leading to prepulse generation. The first three blocks are contained in Eq 3.1 and Eq 3.2. The pulse is compressed by imposing a negative chirp opposite to that induced by the stretcher.

Since the effect we want to illustrate is due to the nonlinear index of the material, the simplest approach is to consider **Self-Phase-Modulation**, which is the "first order" temporal nonlinearity to consider in a material. If we neglect dispersion and spatio-temporal couplings, and in the slowly varying envelope approximation, the accumulated nonlinear temporal phase is given by:

$$\phi_{NL}(t) = \gamma |E(t)|^2 \quad (3.3)$$

Where  $\gamma = \frac{n_2 \pi}{\lambda}$  which gives, after development using 3.1:

$$\phi_{NL}(t) = \gamma |A_0(t)|^2 + \gamma \eta^2 |A_0(t - \tau)|^2 + 2 |A_0(t) A_0(t - \tau)| \cos(\phi(t) - \phi(t - \tau) + \omega_0 \tau) \quad (3.4)$$

In addition, **the B integral** is a measure of the amount of non-linear phase accumulated induced by propagation of a pulse of intensity  $I$  over a distance  $L$  inside a material defined by its non-linear index  $n_2$ , and is expressed by the relation:

$$B[\text{Rad}] = \frac{2\pi}{\lambda} L \int_0^L n_2 I(0, z) dz \quad (3.5)$$

When the two stretched pulses do not overlap, we have by definition  $A_0(t) A_0(t - \tau) = 0$  which cancels the interference term in Eq 3.4. When they overlap, the temporal phase

oscillates in the overlapping region. When the pulse is positively chirped, the blue frequencies are delayed relative to the red ones, therefore the blue will be modulated in case  $\xi > 0$ . When the pulse is negatively chirped ( $\xi < 0$ ), it is the opposite and the red component will overlap with the postpulse, and therefore be modulated. This is illustrated in Fig 3.8 where we show the spectrum of the pulse when we add SPM on the stretched pulse for  $\xi = 5$  and  $\xi = -5$ , after recompression.

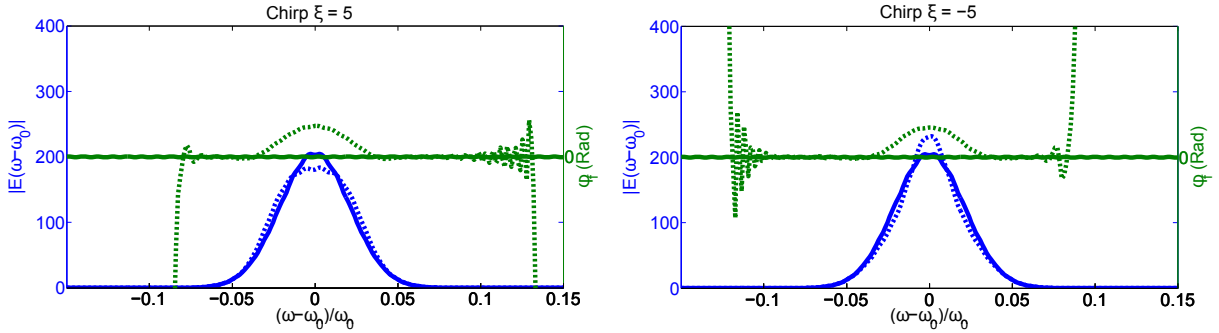


Figure 3.8 – Spectrum and phase prior to pulse stretching (continuous lines) and after compression (dotted lines) with a postpulse of  $\eta = 1\%$  relative intensity added prior to stretching. The chirp factor introduced by the stretching is  $\xi = \pm 5$ . When  $\xi > +5$  (left), higher phase modulations appear in the blue part of the spectrum. When  $\xi < -5$  (right) higher phase modulations appear in the red part of the spectrum.

The high-order phase modulations described above can of course only occur when the main pulse overlaps with its delayed replica. In Fig 3.9, we vary the stretching factor from  $\xi = 0$  (no stretching) to  $\xi = 5$ . The initial temporal profile of the pulse is represented on a linear scale on the left column for each  $\xi$ , and the corresponding temporal profiles after stretching+SPM+compression in logarithmic scale on the right column: for  $\xi = 5$ , a prepulse with relative intensity  $> 10^{-4}$  is clearly visible.

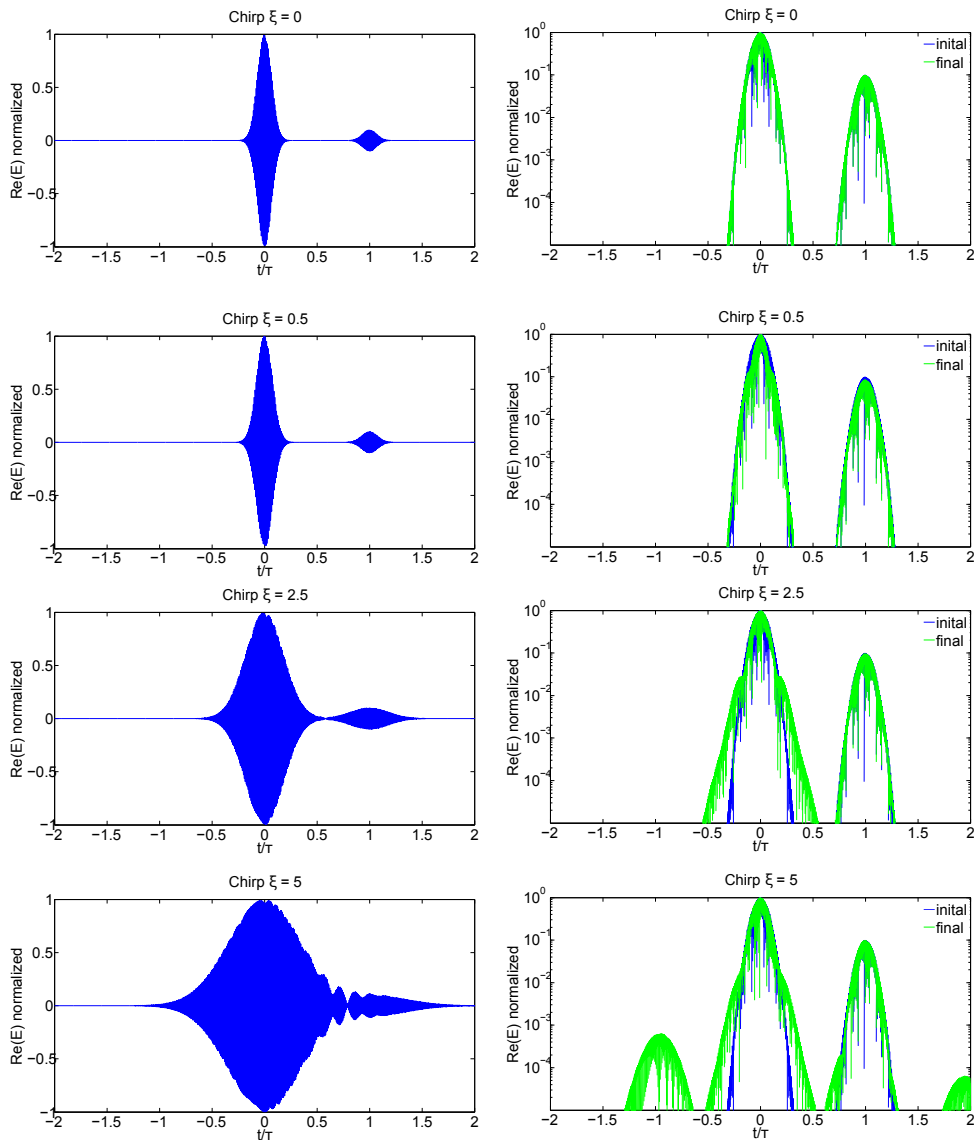


Figure 3.9 – Influence of SPM on prepulse generation. The left column represents the chirped pulses temporal profile for  $\xi = 0, 0.5, 2.5$  and  $5$  before SPM takes place. The right column shows the temporal profile of the pulses after SPM, and after compression (performed by adding  $-\xi$  in spectral domain) on a logarithmic scale. For  $\xi = 5$  a prepulse is generated at  $t = -\tau$

Now that we have shown with a simple example the underlying physics behind the post-pulse generation, we check we can reproduce this effect using the propagation code *Miró* developed at CEA. Here the size of temporal windows was increased to a few ps to accommodate the experimental duration of the chirped pulse. The input parameters are summarized in the following table:

<i>Miró</i> input	value
Temporal window	$-67.5/ + 67.5$ ps
Spatial	$N = 1$
Duration	23fs
Stretched pulse duration	45ps
Calculation Mode	Phase modulation
Peak intensity	$8.9 \times 10^{11}$ W/cm <sup>2</sup>
Postpulse delay	5.3ps
Postpulse relative intensity	$10^{-4}$

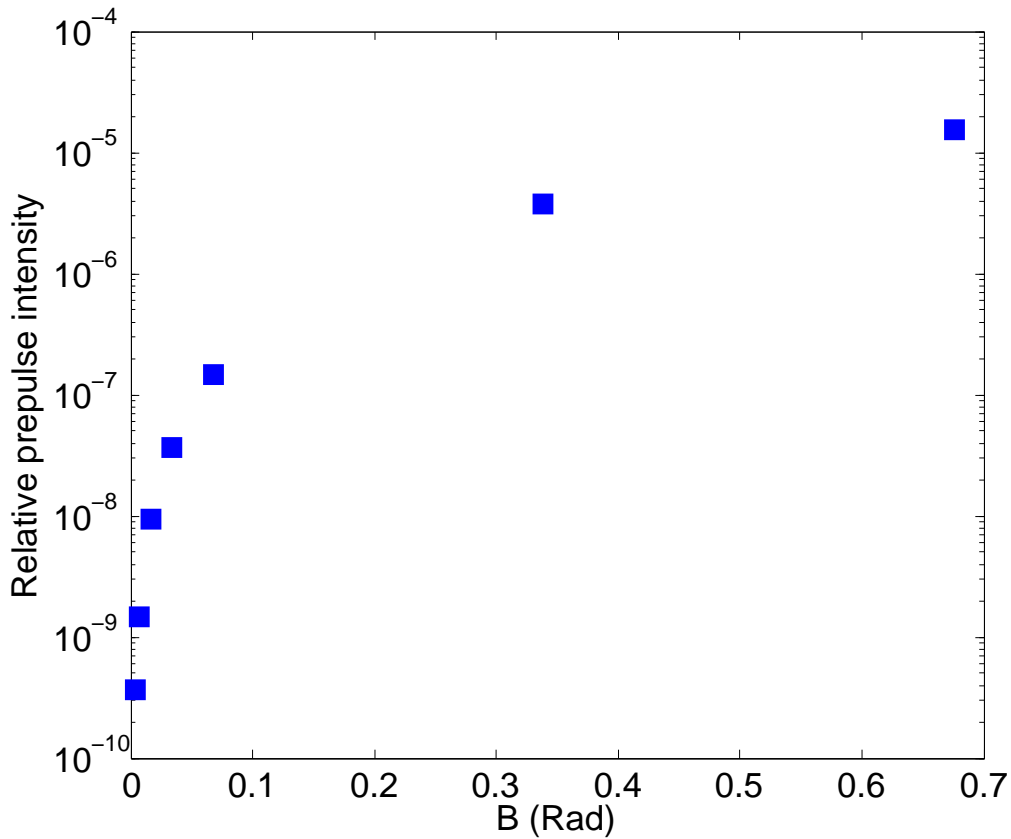


Figure 3.10 – Result using simulation code *Miró*

We first ran the simulation by propagating the stretched pulse in an amplifier with a B integral of 0.3rad and observed the prepulse formation when both stretched pulses overlapped before amplification. The result was similar (neglecting linear dispersive contribution effects) by replacing the amplifier with a glass plate with identical B integral. This is a further confirmation that prepulse generation from postpulses is due to non-linear phase distortions, independently of the medium considered. To study the relative conversion efficiency of the process, it was convenient to propagate the pulse into a simple

glass plate. The prepulse relative intensity was retrieved as a function of the B integral and is plotted in Fig 3.10.

### 3.2 Post-compression and beam shaping

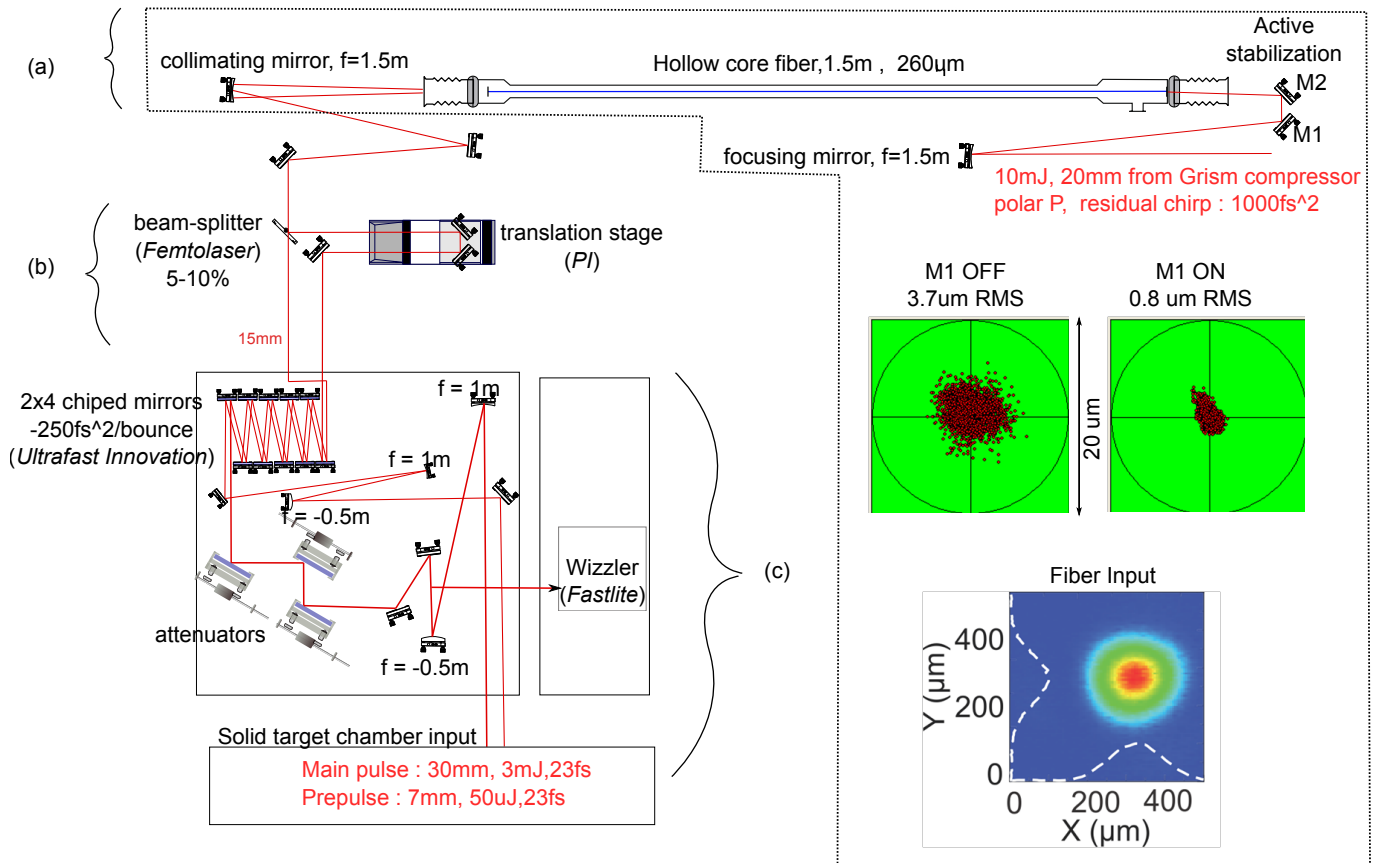


Figure 3.11 – (a) Hollow core fiber setup with active stabilization (b) Prepulse generation using a zero-order broadband beamsplitter reflecting 5 to 10% of the main pulse. The pump/probe delay is adjusted by translation of a motorized delay stage with sub- $\mu\text{m}$  resolution. (c) Final compression chamber under vacuum ( $\sim 10^{-5}\text{mBar}$ ). We compress both main pulse and prepulse on a set of 2 times 4 chirped mirrors introducing  $\phi^{(2)} = -250\text{fs}^2/\text{bounce}$  (Ultrafast Innovation). The main pulse can then be attenuated by translating a home-made optical block from a mirror coated to an uncoated surface with  $< 1\%$  transmission. The main pulse is sent to a 2x telescope and the prepulse 0.5x telescope and both collimated pulses are sent to the experimental chamber to be focused on target

As represented in Fig 3.1, after the two amplifiers, the beam is compressed in a set of transmission gratings (Fastlite) which have been chosen because they compensate well the third-order phase induced by the stretcher. The beam is then spatially filtered with

a 1.5m long hollow core fiber with  $260\ \mu\text{m}$  inner diameter. The beam focused into the fiber is projected onto the Bessel propagation modes.

We used the fiber without any gas inside for spatial filtering and pointing stability: any pointing fluctuation at the fiber input becomes an energy fluctuation at the fiber output. We add an active stabilization of the fiber entrance focus (*Femtolaser*) in closed retraction loop by measuring the far field leaking through the last mirror (M2) with a 4 quadrant photodiode and controlling it with a piezo actuator (M1). The fiber setup is represented in Fig 3.11(a).

The beam is divergent at the fiber output so it is recollimated using a  $f = 1.5\text{m}$  spherical mirror near normal incidence. Then, the beam is split with an ultrathin broadband beam splitter (*Femtolaser*) to generate a low intensity prepulse, as represented in Fig 3.11(b). The relative delay of the prepulse is adjusted with a translation stage having a 10-cm travel range (minimal increment of 100nm, specified pitch and yaw  $\pm 30\ \mu\text{rad}$ ).

Both beams are then sent into the so called "compression chamber", a vacuum chamber where they are shaped temporally then spatially. A set of 2" ultrafast chirped mirrors (*Ultrafast Innovation*) is used to compress both beams in copropagating geometry. The main pulse (much more energetic) can be attenuated by reflecting attenuators mounted on motorized translation stages. This type of optics is represented in Fig 3.12 and was carefully designed to limit the amount of second order phase (GDD) introduced through attenuation. This way, we could perform trustworthy temporal characterization of the attenuated beam by picking up the beam using a motorized flipper mirror.

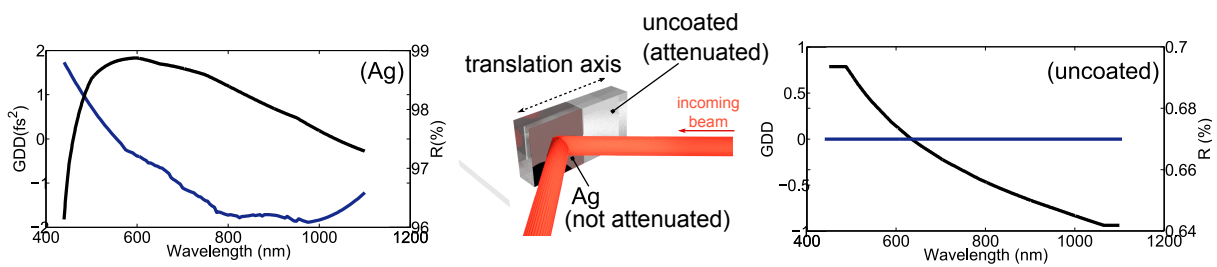


Figure 3.12 – Attenuator optic: one surface-enhanced Ag-coated (*Femtolaser*), one uncoated bare fused silica surface. Corresponding reflection and GDD are represented

After the attenuator blocks, the main pulse is sent to a 2x telescope and the prepulse to a 0.5x telescope and both collimated pulses are sent to the experimental chamber to be focused on target as represented in Fig 3.11(c). We measured the overall transmission of the hollow-core fiber, the beamsplitter and the propagation inside the compression

chamber. Considering this, we enter the experimental chamber with a 30mm, 23fs, 3mJ compressed pulse, and a prepulse of 7mm,  $\sim 50 \mu\text{J}$  also compressed to 23fs. The spatial profile at the focus of the off axis parabola is measured and the beam is attenuated by inserting a motorized microscope objective sending the magnified image of the focus on a CCD camera place outside the vacuum chamber.

### 3.3 Solid-target experimental setup

#### 3.3.1 Experimental chamber and beam profile

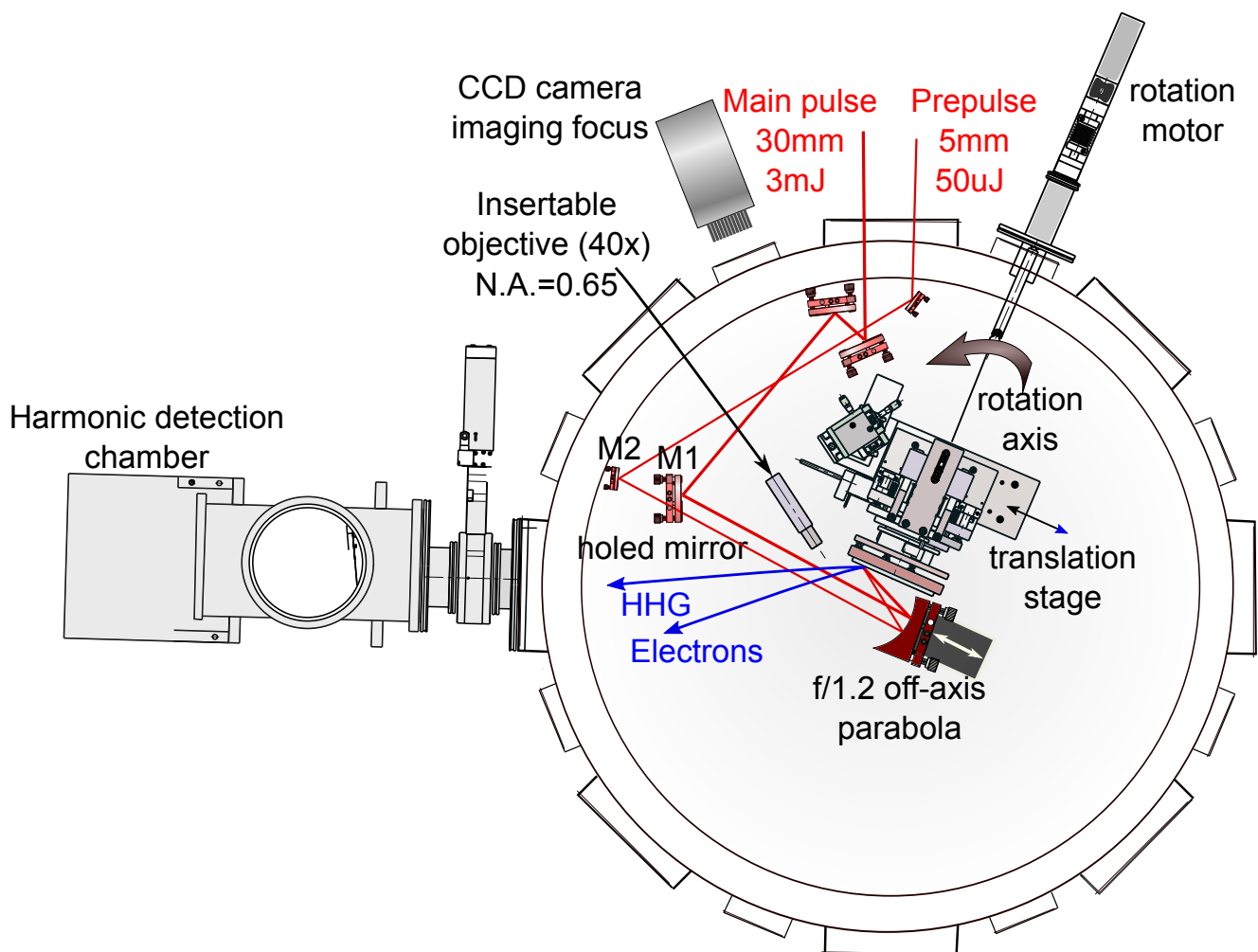


Figure 3.13 – Experimental setup of pump/probe experiment on solid target at a 1kHz laser repetition rate

The experimental setup is represented in Fig 3.13. Details of the different diagnostics installed for electrons and harmonic detection will be given in the following chapters. Here, the 30fs, 3mJ 800nm main pulse exiting the compression chamber enters the inter-

action chamber and is focused with a  $f/1.2$  off axis parabola mounted on a translation stage used for controlled defocusing. The focusing plane of the parabola is carefully aligned with the solid-target plane. The prepulse is focused using the same parabola to facilitate alignment and minimize pump/probe temporal jitter. To do so, a 8mm hole was made in the last mirror M1 to make both beams collinear prior to the focusing parabola. Using the attenuators installed in the compression chamber (previously described in Fig 3.11), the profile of the beam at focus is recorded with a CCD camera placed outside vacuum: to image the focus, we simply need to translate the target holder to align the microscope objective with the optical axis defined after the parabola with no need to break the vacuum in the chamber. In Fig 3.14 we represent the spatial profile of the main pulse (a) and the prepulse (c) at the focus of the parabola. We could also bypass the telescope to decrease the beam aperture, which ultimately increases the focus spot size by a factor  $\sim 2$ .

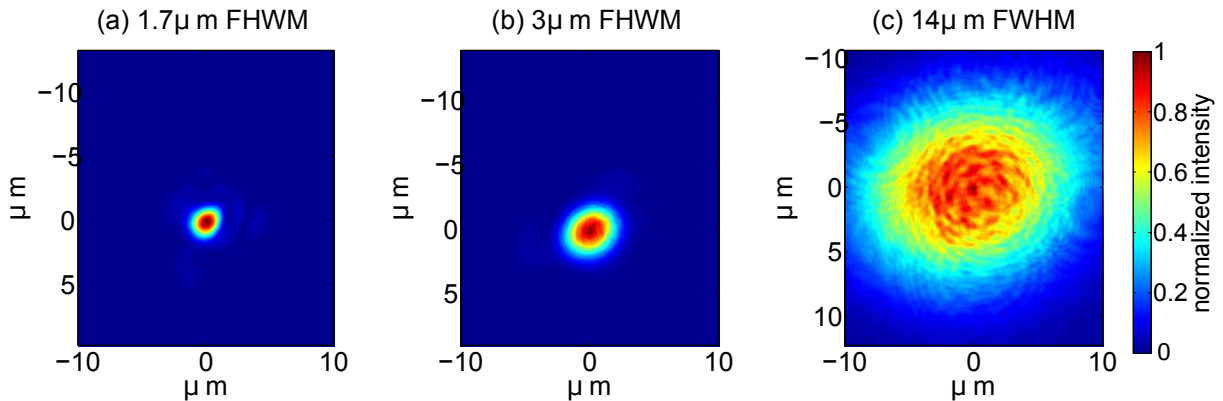


Figure 3.14 – Profile recorded at the focus of the parabola (a) Beam expander in the compression chamber (b) Bypassing the beam expander (c) Prepulse profile

### 3.3.2 Beam temporal profile

The temporal profile of the main pulse is measured after the attenuator with a Wizzler (*Fastlite*). Two crossed polarized and delayed replicas of the pulse are generated using a Calcite plate and sent to a  $BaF_2$  crystal where the most intense pulse creates a crossed polarized replica through XPW. This XPW reference beam interferes with the first replica which creates spectral fringes. Using a well-suited retrieval algorithm, it is possible to reconstruct both the spectrum and phase of the initial beam. This is illustrated in Fig 3.15 where we performed a Wizzler measurement for the compressed pulse with or without apodization of the spectrum using the Dazzler (cf section 3.1.3).

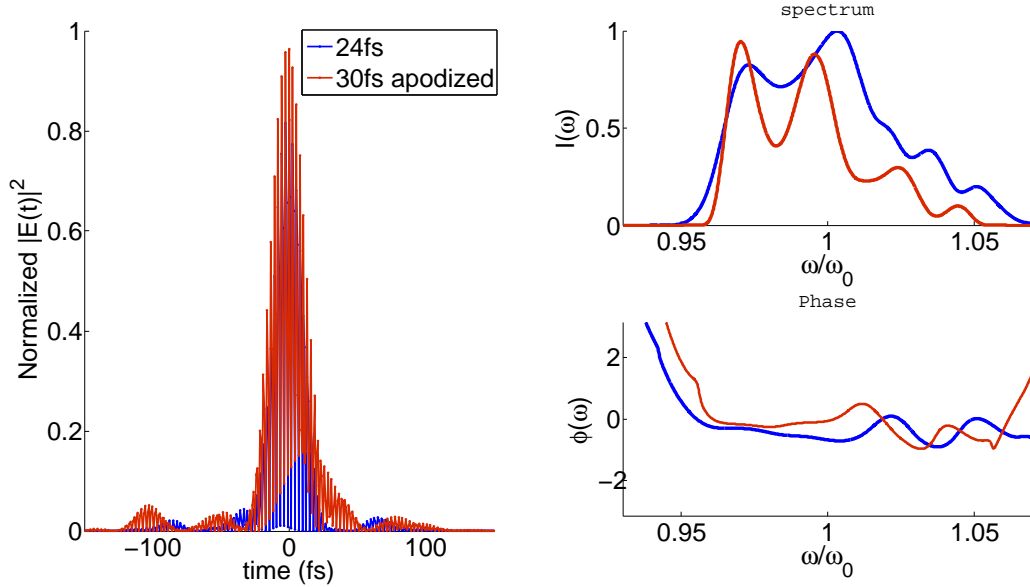


Figure 3.15 – Wizzler measurement before the interaction for compressed 24fs pulse (blue curve) and when apodizing the spectrum to improve the laser contrast (red curve), resulting in an increase to 30fs. On left caption, we represent the square of the real part modulus of the field in both cases.

On the femtosecond scale, no net difference can be observed between the non-apodized and the apodized pulse except that the latter has a longer pulse duration (30fs as opposed to 24fs). The clear advantage of spectral apodization has been described in 3.1.3 and relates to the ps coherent contrast. However, the measurement from Fig 3.15 shows that the spectral modulations combined with the residual spectral phase of the beam will result in the generation of satellite pulses on the femtosecond time scale, and with intensities  $\sim 5\%$  that of the main pulse. This is enough to initiate High Harmonic Generation and therefore, generate a complex structure of harmonics with spectral modulations  $\Delta\omega$ , which we can evaluate to be of the order of:

$$\Delta\omega/\omega_0 \sim 0.05 - 0.3$$

This is typical of what we can observe experimentally on our harmonics spectra, especially for increased intensities.

### 3.3.3 kHz solid target

In order to perform solid-target experiments at 1kHz, the surface of the target has to be refreshed every millisecond. In many low-repetition-rate laser facilities, the standard

method to refresh the target consists in translating a solid bulk material after every shot [112]. In our case, the target is a 4 inch cylindrical fused silica wafer optically polished to  $\lambda/20$  surface flatness and mounted on a rotation axis with adjustable rotation speed [25]. Typically, we set the rotation speed to  $\sim 9$  rad/s in order to separate each successive shot by at least  $\sim 100 \mu\text{m}$  to account for the damage extent (the focus is only a few microns large) as illustrated by Fig 3.16.

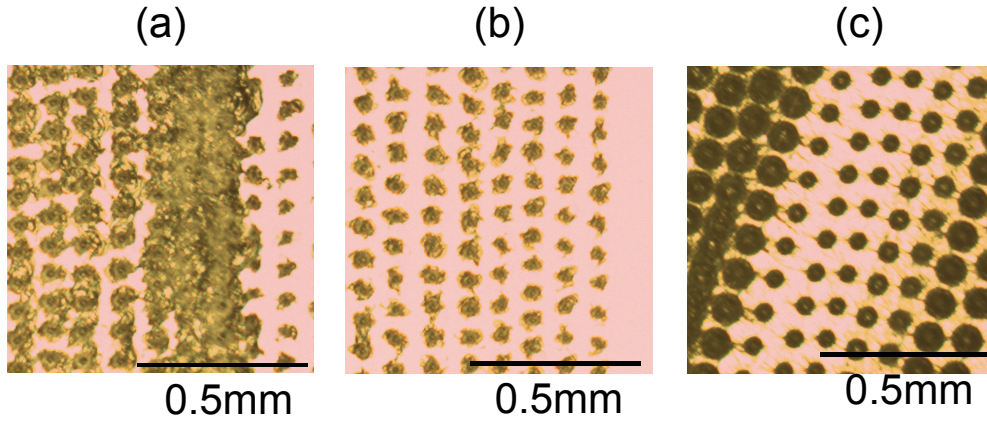


Figure 3.16 – Solid-target surface after an experiment visualized with an optical microscope (a) Shots on fused silica where shot overlap is due to the low target rotation velocity (b) Shots on fused silica with correct spacing (c) Shots on plastic with correct spacing where different impact sizes correspond to different laser energies

Before running the experiment, we align very precisely the target plane normal to the rotating axis using 3 piezo actuators and minimize the horizontal and vertical angular fluctuations  $\alpha_x$  and  $\alpha_y$  down to  $50 \mu\text{rad}$  (mechanical limit). The measurement of these angular fluctuations as well as the depth variation is done interferometrically using a stabilized He-Ne sent inside a Mach Zehnder interferometer in that horizontal plane, and following the interference pattern as the target is rotating. This alignment procedure, represented in Fig 3.17, is essential to ensure the good reproducibility of our experiment: the depth fluctuations of the target surface should be inferior to the Rayleigh length of the focused beam, which is  $\sim 2 \mu\text{m}$ . On Fig 3.17(e),  $d$  is retrieved as a function of target revolution with peak-to-valley values  $\sim 1 \mu\text{m}$  which is good enough to run an experiment.

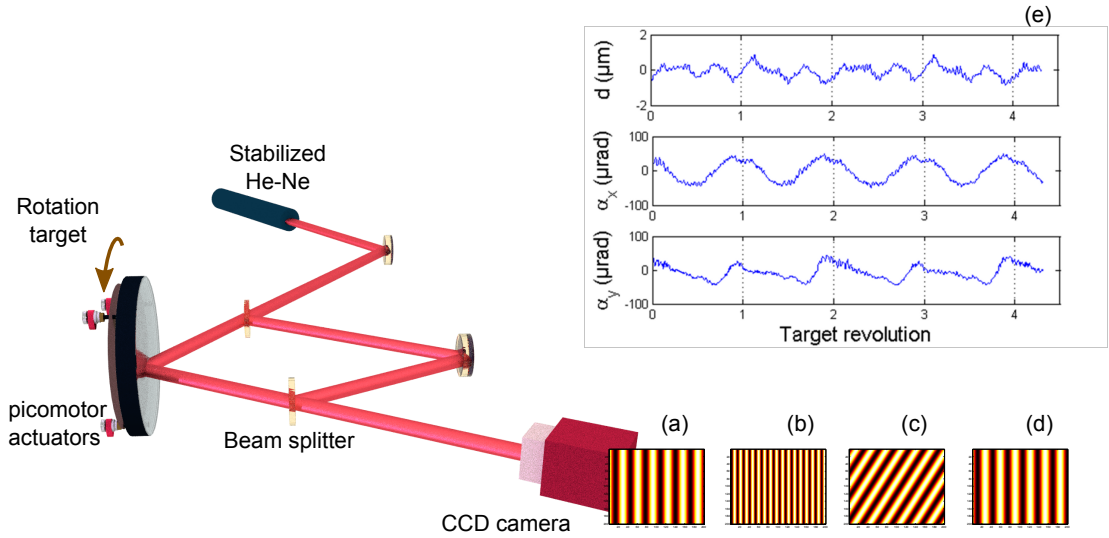


Figure 3.17 – Target stabilization setup (a) Reference fringes when the target is not rotating (b) Effect of horizontal phase corresponding to angle  $\alpha_x$  variation resulting in fringes spacing (c) Effect of vertical phase corresponding to angle  $\alpha_y$  variations resulting in a tilt of the fringes (d) Effect of constant phase shift corresponding to depth fluctuations: translation of the fringes (e) Retrieved  $\alpha_x$ ,  $\alpha_y$  and depth  $d$  when target is rotating

### 3.4 Conclusion

In this section, we have presented the overall architecture of our double CPA system, which delivers a few mJ, sub-30fs pulses at a 1 kHz repetition rate to our experimental chamber. In our solid-target experiment, controlling the laser temporal contrast is crucial to prevent destruction of the target by a pedestal, which is why there is an XPW contrast filter between the two CPA units. However, filtering the contrast alone is not enough to ensure the absence of prepulses. One must also prevent postpulses from forming before stretching the pulse to picosecond durations to avoid nonlinear prepulse creation. Finally, the experiments which will be presented in this manuscript are possible thanks to the solid-target stability and the possibility to refresh the target surface every millisecond. This way, we accumulate hundred of shots on our detectors, enabling good interaction statistics.

# Chapter 4

## Attosecond pulses from plasma mirrors

### Outline

---

<b>4.1</b>	<b>HHG on plasma mirrors</b>	<b>62</b>
4.1.1	Experimental setup for HHG measurement	62
4.1.2	From harmonic emission time to CWE basic properties	63
4.1.3	Harmonic coherence properties	67
4.1.4	Influence of gradient scale length on HHG	70
4.1.5	Reconstruction of harmonics in the far field	72
<b>4.2</b>	<b>Attosecond chirp experiment</b>	<b>73</b>
4.2.1	Definition of Wavefront rotation (WFR)	73
4.2.2	Analytical model to evaluate WFR at focus	75
4.2.3	WFR measurement	77
<b>4.3</b>	<b>Basic principle of attosecond FROG retrieval</b>	<b>82</b>
<b>4.4</b>	<b>Conclusion</b>	<b>86</b>

---

The high-order harmonic generation (HHG) from plasma mirrors has been extensively studied both theoretically [24, 51, 53, 77, 79, 113] and experimentally [20, 21, 25, 51, 96, 114, 115] over the last decades. Depending on the intensity, two emission mechanisms have been identified: (i) Coherent Wake Emission (CWE) dominant at low intensity ( $a_0 < 1$ ) and (ii) Relativistic Oscillating Mirror (ROM) at high intensity ( $a_0 > 1$ ). In the first mechanism, already presented in Section 2.2, an attosecond pulse is emitted every laser period in the specular direction of the driving laser pulse. In the second mechanism, electrons emit X-UV during the phase of acceleration from the plasma bulk. This also occurs for every laser period and is a coherent process. However, this process is very sensitive to the laser intensity and difficult to observe when it is not fully relativistic. In this chapter, we will recall some of the basic properties of CWE harmonics. The reader is invited to check the provided references for a more detailed description. In a second

part, we will see how the divergence and spectral properties of the emitted harmonics are sensitive to spatio-temporal couplings (STC) of the driving laser. In particular, we will show how it is possible to experimentally control first-order STCs called Wave Front Rotation (WFR) and how it can affect HHG. This technique has been already tested successfully to separate attosecond pulses by changing their direction of emission over time [68]. Here we discuss the possibility to retrieve temporal information on the attosecond train when the pulses are not separated.

## 4.1 HHG on plasma mirrors

### 4.1.1 Experimental setup for HHG measurement

The laser system and its spatial and temporal properties at focus have been presented in Chapter 3 ( $\sim 30$  fs, few mJ pulse centered at 800 nm). Here, X-UV emitted by the plasma are analyzed by means of a home-made spectrometer located in the specular direction as represented in Fig 4.1(a).

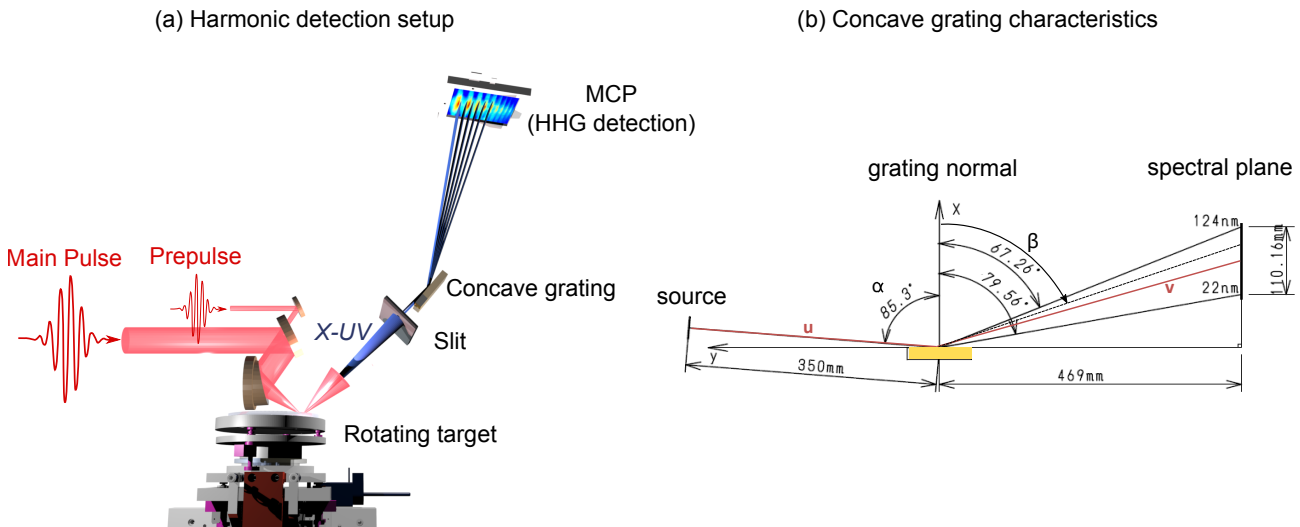


Figure 4.1 – (a) Experimental setup for HHG detection (b) spherical grating (*Hitachi* 001-0639) for home-made spectrometer. The MCP is placed in the spectral plane and imaged using a triggered CCD.

The spherical grating was installed with respect to the focal spot in the configuration represented in Fig 4.1(b), that is to say 469mm from the focal spot in the specular direction. In the direction orthogonal to propagation, the beam is diverging. The resulting X-UV spectrograph is recorded using a single-stack MCP<sup>1</sup> (*Photonis*) continuously biased at 1kV (amplification gain of  $\sim 10^5$ ). The MCP has an effective detection area of  $H \times W$

1. Micro-channel Plate: high-voltage photomultiplier micro-array for the detection of single photons with a wavelength below 120nm

= 75 × 93mm. A P46 phosphor screen also biased at 1kV is stacked to the MCP. Its decay time is on the order of 100 ns, which enables recording the MCP signal at 1kHz refresh rate.

We define  $x$  and  $y$  as the local spatial coordinates respectively in the horizontal and vertical MCP image plane. After the optical imaging system has been properly calibrated, we transform  $y$  from mm to rad dividing its value by the quantity  $u+v$  [mm] corresponding to the averaged propagation distance of the beam from the source to the detection plane. In doing this, we assume that  $v$  is independent of  $\lambda$ , which yields a calibration error of 2%. To transform  $x$  from mm to wavelength, we used the diffraction relation:

$$\sin \alpha + \sin \beta = \lambda \sigma_0$$

where  $\alpha = 85.3^\circ$ ,  $67.3^\circ \leq \beta \leq 80^\circ$  are defined in Fig 4.1(b),  $\lambda$  is the wavelength and  $\sigma_0 = 1/600$  mm the groove density.

Also represented in Fig 4.1(a), is the possibility of adding a prepulse, aligned collinear to the main pulse through a holed mirror, in order to generate a controlled preplasma with intensity  $\sim 10^{14}$  W/cm<sup>2</sup>. Full details on the experimental chamber and beam characteristics have already been discussed in Chapter 3.

### 4.1.2 From harmonic emission time to CWE basic properties

The 1D Brunel model used to calculate the electron trajectories at the surface of the plasma is described in details in Section 2.2. Here, we use this model to highlight some basic properties of CWE. A more detailed description of this model can also be found in [24,79]. We recall the equation of motion for an electron  $i$  starting its motion at  $t > t_i$ :

$$\frac{d(\gamma_e v_e)}{dt} = -a_0[\bar{E}(t) - \bar{E}(t_i)] \quad (4.1)$$

where  $\gamma_e$  is the relativistic gamma factor of the electron,  $v_e$  its velocity, and  $a_0$  the normalized electric field amplitude. We solve this equation for every laser cycle, and every electron returning to the plasma bulk is considered ballistic past the critical density. The electron crossing trajectories overall describe a caustic in time, which for a given optical cycle, is defined by the relation:

$$x_c(t) = \min_i [v_i(t_{ri})(t - t_{ri})] \quad (4.2)$$

where  $t_{ri}$  defines the time at which the  $i^{th}$  electron crosses the critical density, and  $v_{ri}$  its corresponding velocity.

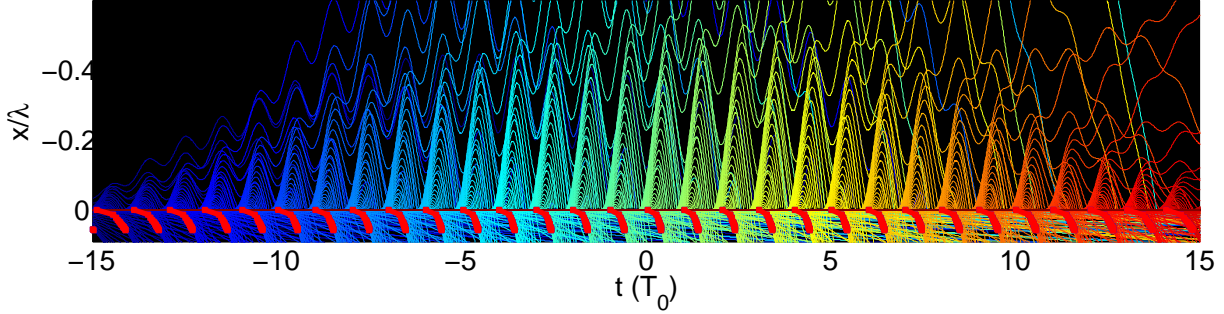


Figure 4.2 – Trajectories of Brunel electrons in vacuum for a 30 fs Gaussian pulse,  $a_0 = 1$  and a gradient length  $L = \lambda/100$ . Each laser period, electrons are pulled out of and back into the plasma where trajectories cross. The "crossing" time is represented by the red caustics in the  $x < 0$  region ( $x = 0$  defines the critical surface).

This is well described in [51] where it is shown that  $x_c(t)$  can be approximated by a quadratic function of time. The retrieved  $x_c$  values in the case  $a_0 = 1$  are plotted in red in Fig 4.2 as an illustration. Once  $x_c$  is retrieved, we can calculate the so-called emission times of the harmonics. In other words, this is equivalent to provide information on the spectral phase of each emitted frequency. Indeed, we saw in section 2.2 how an overdense plasma submitted to an electronic perturbation emits coherent light at a frequency  $\omega_p(x) = \sqrt{e^2 n_e(x)/(m_e \epsilon_0)}$ , where  $x$  is the position where the plasma density equals  $n_e(x)$ . Therefore, the emission time  $t_e$  of the  $n^{\text{th}}$  harmonic, for a given optical cycle, is defined by the relation:

$$\omega_p[x_c(t_e)] = n\omega_0$$

In Fig 4.3 we calculate the emission times for a laser intensity of respectively  $a_0 = 0.2$  and  $a_0 = 1$ . One can clearly see that the relative emission delay from one optical cycle to the next decreases with increasing  $a_0$ . We can also show that this delay, also called **femtosecond chirp**, increases with the gradient scale length [79]. This **femtosecond chirp** is a signature of CWE emission and will have a direct influence over the spectral width of the generated harmonics. This was very well described in previous PhD work [24, 74, 79, 116].

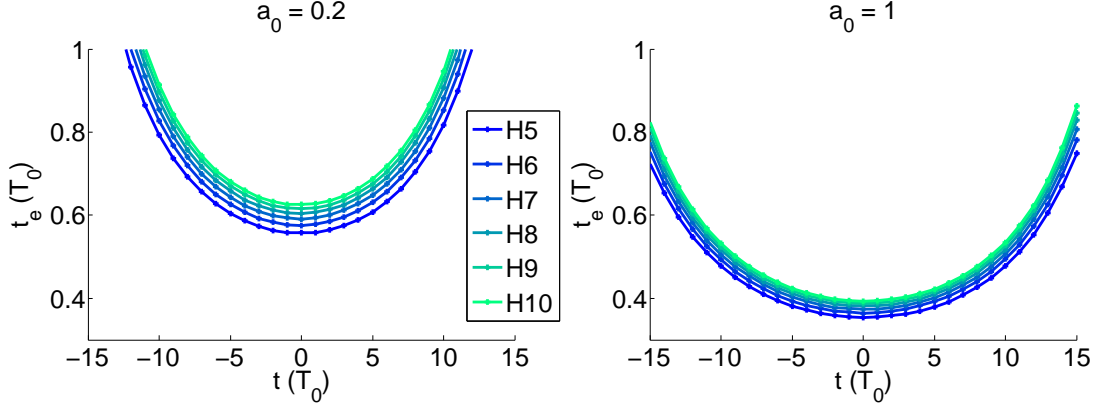


Figure 4.3 – CWE emission time calculated using 1D Brunel model for harmonics 5 to 10, a Gaussian pulse of 30 fs duration, a gradient length  $L = \lambda/100$  and laser intensities of  $a_0 = 0.2$  and  $a_0 = 1$  respectively.

Using the calculated emission times  $t_e(n, \cdot)$  for every optical cycle  $n$  of the driving laser pulse, one can define the HHG spectrum as the coherent sum of each component  $\omega \in [\omega(n_c) \ \omega(n_{max})]$  such that [79]:

$$E_{\text{HHG}}(\omega) = \sum_n A_n(\omega) \exp[i\omega(nT_0 + t_e(n, \omega))] \quad (4.3)$$

where  $n$  denotes the optical cycle,  $T_0$  the driving laser period and  $A_n(\omega)$  the spectrum of the attosecond pulse generated during the  $n^{\text{th}}$  optical cycle. This expression is quite explicit and it appears straightforward that in the ideal case where  $t_e(\cdot, \omega)$  would be independent of  $n$  (i.e. perfect periodicity of the attosecond pulses emission), the corresponding spectral phase can be factorized in front of the sum and the harmonic spectra would be convolved by a purely Dirac comb. This corresponds to the minimum harmonic spectral width.

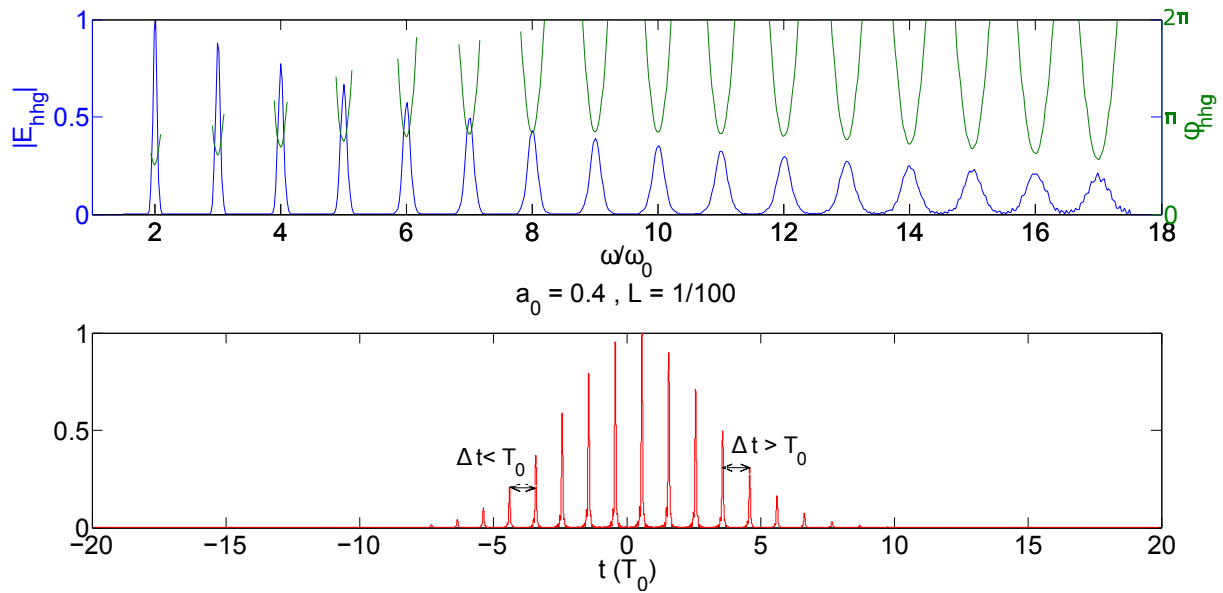


Figure 4.4 – CWE emission spectral and temporal profile for a 30 fs Gaussian pulse, a gradient length  $L = \lambda/100$  and an intensity of  $a_0 = 0.4$

On the other hand, when  $t_e(n, \cdot)$  varies with  $\omega$ , each harmonic line broadens spectrally. When the driving laser pulse is compressed, the emission time varies from cycle to cycle, as represented in Fig 4.4 for  $a_0 = 0.4$ . We represent the intensity of the corresponding attosecond pulse train in the temporal domain, where we can see a variation in the train periodicity. This can be observed experimentally by chirping the driving laser pulse. Indeed, a positive chirp will shift the lower frequencies to the beginning of the pulse, and the higher frequencies to the end. As a consequence, the change of instantaneous period as the pulse generates harmonics can compensate the intrinsic femtosecond chirp. This will lead to spectrally narrow harmonics, as clearly demonstrated in Fig 4.5 where we used the Dazzler to introduce a second order chirp of  $\phi^{(2)} = 400 \text{ fs}^2$  ( $\xi = 0.6$ )<sup>2</sup> in the driving laser.

2. The normalized chirp is define by  $\xi = \phi^{(2)}/\sigma^2$ , defined for a Gaussian pulse of intensity  $\propto e^{-t^2/(2\sigma^2)}$

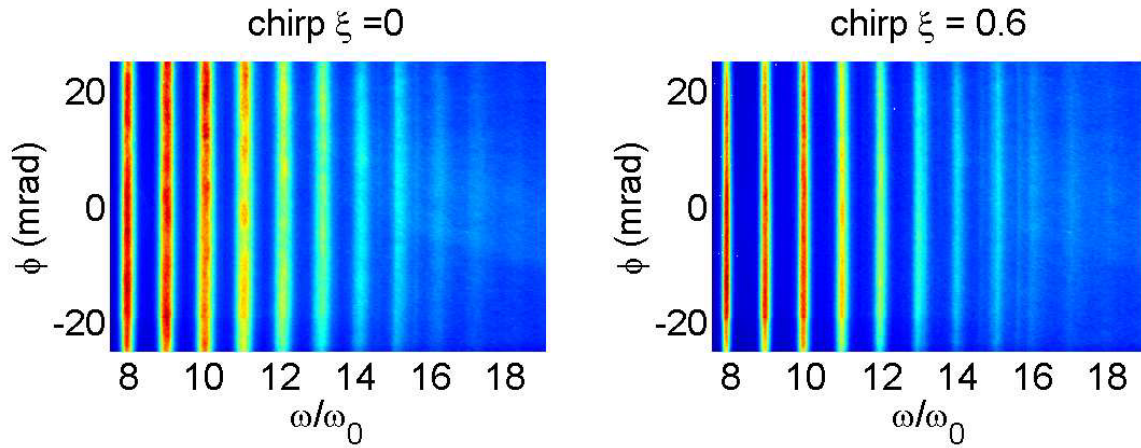


Figure 4.5 – CWE experimental spectra for a compressed 26 fs pulse with  $a_0 = 0.4$  (left caption) and with a normalized order chirp of  $\xi = 0.6$  (right panel)

### 4.1.3 Harmonic coherence properties

The generated X-UV source conserves the coherence properties of the initial laser pulse. In other words, the X-UV generation plane defined by the target surface can be pictured as the coherent superposition of infinitesimal sources with a well-defined phase relation between them. The wavefront is convex with respect to the direction of propagation, which is to be expected: considering that the intensity at the center of the driving laser is higher than on the edges, the emission therefore occurs “sooner”. This spatially dependent delay of harmonic emission corresponds to a CWE wavefront curvature [79]. In other words, if the harmonic beam were to be approximated by a Gaussian beam as represented on Fig 4.6, its waist (position where the spatial phase is flat) would be located before the focusing plane of the driving IR laser. Any modification of the emission time at focus (linked to a change of gradient length, compression, laser intensity) therefore translates into variations of the beam divergence and can be compensated by adjusting the driving laser defocus [24, 79].

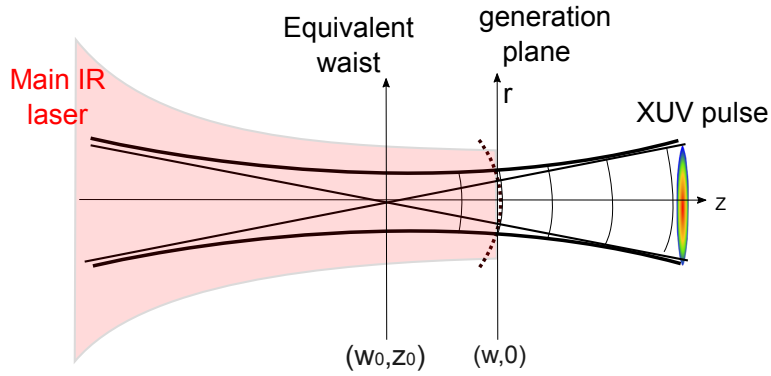


Figure 4.6 – Gaussian beam representation for X-UV pulse generated at the focus of a driving IR femtosecond pulse. The "generation plane" refers to the solid-target surface.

The divergence for harmonic  $n$ , of frequency  $\lambda_0/n$  and waist  $w_{0,n}$  is therefore:

$$\Delta_n = \frac{\lambda_0}{n\pi w_{0,n}} = \frac{\lambda_0}{n\pi w_n} \sqrt{1 + \frac{z_{0,n}^2}{Z_{R,n}^2}} \quad (4.4)$$

where  $w_n$  is the waist in the plane of generation,  $z_{0,n}$  the distance from the waist position as represented in Fig 4.6 and  $Z_{R,n}$  the Rayleigh length.

We reproduce a simple original experiment which was the first to highlight the coherence properties of the X-UV emission [117]. It consists in adding a transmission mask in the form of a comb, as drawn in Fig 4.7(a) in the collimated incident laser beam. As a result of diffraction, the beam splits into several sources separated by  $4\mu\text{m}$  as determined by the image of the focus shown on Fig 4.7(b-c), where only the 3 central diffraction orders intense enough to be detected on the camera are represented.

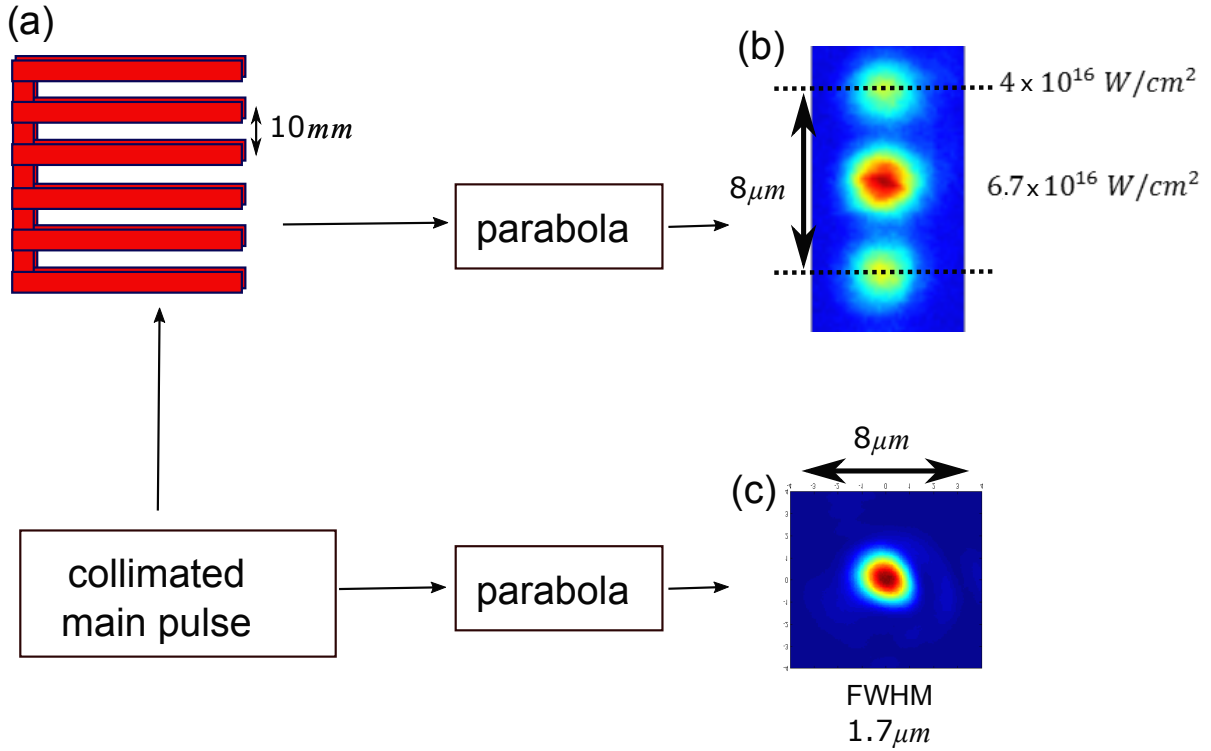


Figure 4.7 – A transmission mask (a) is inserted into the collimated IR driving laser prior to the parabola. At focus, the main focal spot (c) splits into 3 replicas (b) relatively separated out by  $4 \mu\text{m}$  as a result of diffraction.

The central spot intensity is evaluated to be  $\sim 6.7 \times 10^{16} \text{ W/cm}^2$ , and a little over half for the satellites. This will lead the harmonics to interfere constructively in the far field. In the result presented in Fig 4.8, we performed a vertical Fourier transform of the HHG image detected on the MCP, and defined the vertical axis by  $r_1 = \lambda f_\theta$ . This way, the vertical axis is homogeneous to a distance and the first-order diffraction should be located at  $r_1 = 4 \mu\text{m}$  which corresponds to the focal spot spacing measured in Fig 4.7(b) (cf Appendix D). The result of this operation is represented in Fig 4.8 for harmonics 10 to 12. The side band located at  $4 \mu\text{m}$  is a clear indication the three sources are individually generating X-UV radiation even when the laser is out of focus. The lines are slightly larger for H10 than they are for H12. This is to be expected and corresponds to a waist  $w_n$  (using the same notation as in Eq 4.4) that decreases with the emission wavelength. The frequencies are more effectively generated in the zone of higher intensity as described in Appendix D.

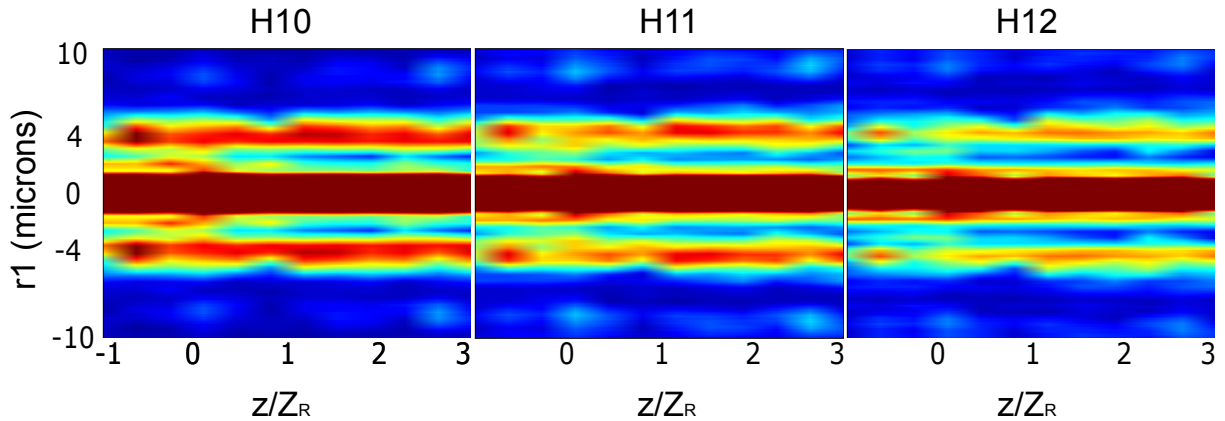


Figure 4.8 – Retrieved spatial separation  $r_1$  between individual HHG sources generated on target as a function of laser defocusing. The result is given for three different harmonic orders (H10, H11 and H12). The  $0^{th}$  order was intentionally saturated to highlight the side bands.

#### 4.1.4 Influence of gradient scale length on HHG

As already explained in section 2.3, the plasma scale length has a dramatic influence on the harmonic generation. In particular, the generation becomes inefficient for very long ( $L \gg \lambda/5$ ) or very short ( $L \ll \lambda/100$ ) plasma scale length. Observing the drop in harmonic generation efficiency with the gradient scale length is a rather simple experiment to conduct as it simply requires to degrade the laser contrast. On the other hand, observing the optimum in generation efficiency is rather challenging because it requires a very good control of the laser contrast. We saw in Section 3 how prepulses could very well emerge in a laser chain even in the presence of an XPW contrast filter because of non-linear effects. In Fig 4.9(a) we show how upgrading the laser chain contrast enabled us to observe an optimum CWE generation efficiency for  $L/\lambda \sim 1/100$ . Nevertheless, the laser intensity had to be kept at  $a_0 \leq 0.35$  for this optimum to be visible. Since we observed this optimum in PIC simulations for  $a_0 > 0.35$ , we conclude that unless the intensity of the main pulse is kept low, the target surface quality is sensitive to the coherent contrast of the laser. In Fig 4.9(b), the gradient length in units of  $\lambda$  was retrieved using SDI (described in section 5). For the sake of comparison with what should be expected for the optimal gradient length, we performed a 2D PIC simulations using Epoch code [118] with  $a_0 = 0.4$  and Fig 4.10 shows the results of CWE efficiency for gradient scale lengths of respectively  $L = \lambda/5, \lambda/10, \lambda/20, \lambda/40$  and  $\lambda/80$ .

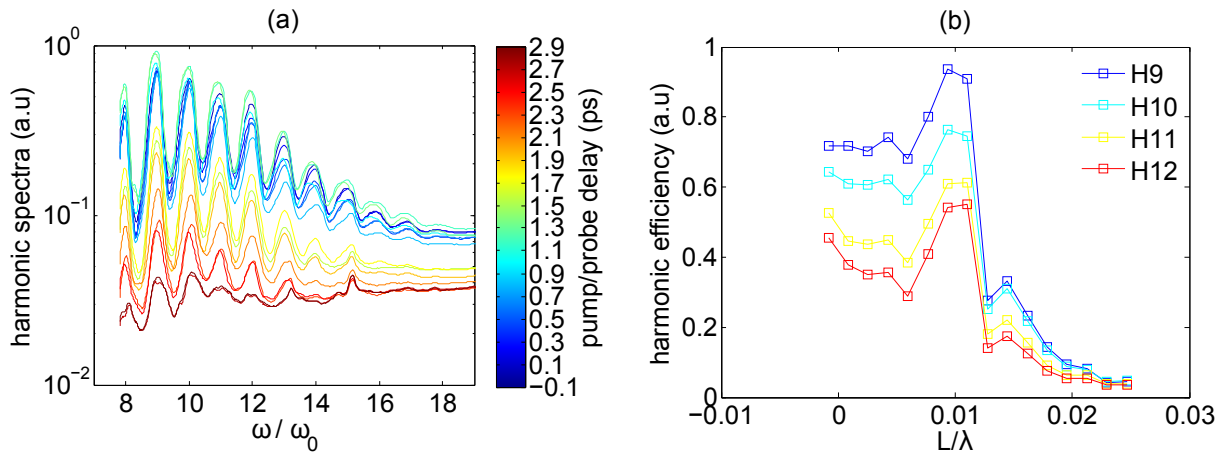


Figure 4.9 – (a) Experimental harmonic spectra integrated along the vertical direction at different prepulse delays indicated in the colorscale. (b) Corresponding relative intensity of harmonics 9 to 12. Experimental conditions: 30 fs laser pulse with  $a_0 = 0.35$ . The prepulse intensity is  $1.3 \times 10^{14}$  W/cm<sup>2</sup>.

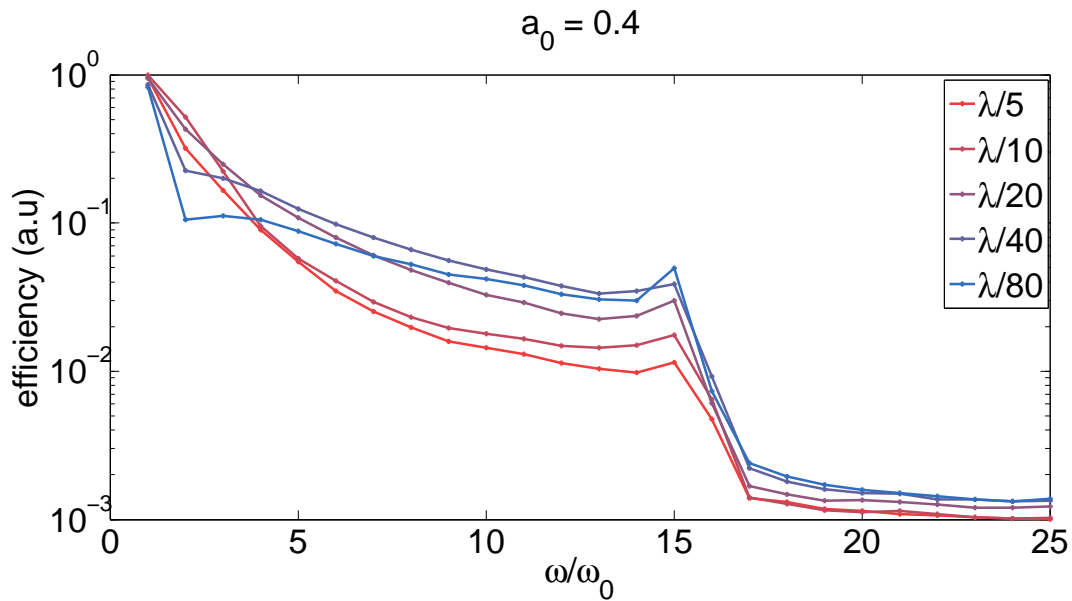


Figure 4.10 – 2D PIC simulation using Epoch: Influence of gradient length on CWE efficiency for  $a_0 = 0.4$  and gradient scale lengths of respectively  $L = \lambda/5, \lambda/10, \lambda/20, \lambda/40$  and  $\lambda/80$ . The peak at  $\omega/\omega_0 = 15$  corresponds to a numerical resonance and is non-physical; the efficiency is plotted on a log scale.

In the simulation, the optimum appears for  $L = \lambda/40$ , that is to say for a gradient length

nearly twice that observed in the experiment. This result is not surprising because we estimated the expansion velocity to be  $c_s \approx 6.8 \text{ nm/ps}$  to convert the pump-probe delay to gradient length (the measuring technique is fully described in Chapter 5), but also made the hypothesis that the gradient length is rigorously equal to zero at time  $t = 0$ . It is important to note that when measuring the plasma expansion velocity over one laser wavelength, this assumption introduces a negligible error on the retrieved velocity provided the actual initial plasma scale length is negligible with respect to the laser wavelength. Here we see the initial plasma scale length should be on the order  $\sim \lambda/100$  for the experiment to fit the simulation.

### 4.1.5 Reconstruction of harmonics in the far field

We now consider the transverse dimension  $y$  of the laser focus and calculate numerically the emission time over each point for a laser waist of  $w_0 = 2.5 \mu\text{m}$  using the model presented in 4.1.2. This enables us to reconstruct a harmonic spectrogram with one coordinate being  $y$  and the other the spectral frequency. Using a Fourier transform along  $y$ , the far field harmonic spectrum is shown in Fig 4.11, where  $\phi$  refers to the angular direction normal to the optical plane.

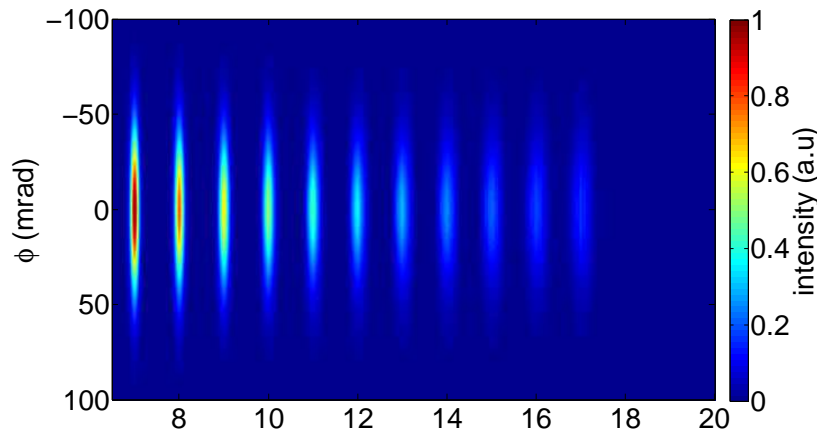


Figure 4.11 – Modelling of CWE emission spectra between H7 and H20 for a pulse of 30 fs, a gradient length  $L = \lambda/100$  for laser intensity of  $a_0 = 0.4$  and a waist  $w_0 = 2.5 \mu\text{m}$

A representation of the temporal profile of the attosecond train is represented in Fig 4.12(a). In Fig 4.12(b), we zoom on one attosecond pulse taken between the two dotted white lines. This is a time-domain visualization of the spatial phase in the generation plane discussed in 4.1.3.

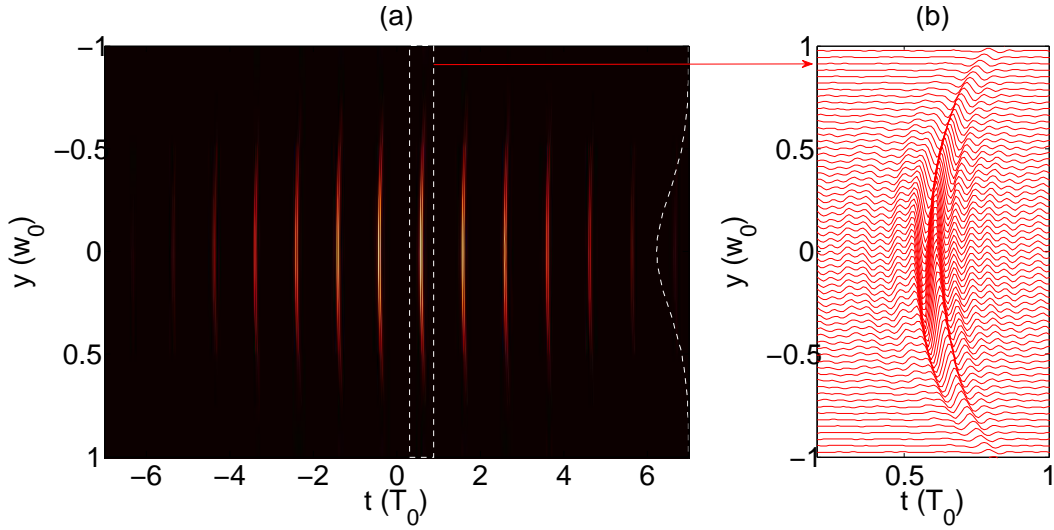


Figure 4.12 – (a) CWE temporal emission along  $y$  direction for a 30 fs Gaussian pulse, a gradient length  $L = \lambda/100$ . The laser intensity of  $a_0 = 0.4$  and its waist  $w_0 = 2.5$ . (b) Zoom on one attosecond pulse over one laser period.

The angular emission spectrum of an attosecond train, as we just explained, is intrinsically related to the spatially dependent emission time of each attosecond bunch. As a consequence, the laser spatio-temporal coupling (STC) will directly transfer to the harmonics [76]. This simple statement naturally leads us to investigate the relative variation of spectrum and divergence with respect to a particular laser STC called Wavefront rotation, which we describe in the following section.

## 4.2 Attosecond chirp experiment

### 4.2.1 Definition of Wavefront rotation (WFR)

Wavefront rotation (WFR) is a particular case of STCs [119,120]. In the presence of a spatial chirp at focus, the field can no longer be written as the product of a spatial profile times a temporal envelope, and the wavefronts can be viewed as "rotating" over time at velocity  $v_{rot}[\text{mrad/fs}]$ . The attosecond bunches resulting from the interaction are emitted in different directions of space. This so-called "attosecond lighthouse" was experimentally implemented in our group to generate isolated attosecond pulses [68,74], after it had been exposed by Henri Vincenti during his PhD [76,121].

When we misalign a dispersive element in the laser beam path, like a compressor grating or a pair of wedges, the  $\vec{k}(\omega)$  vector of all spectral components  $\omega$  are no longer collinear: the beam has an angular chirp, as represented in Fig 4.13. One can therefore directly derive the consequence for the beam at focus: each frequency will be focused at different

position along the chirp direction such that the beam is said to be spatially chirped at focus.

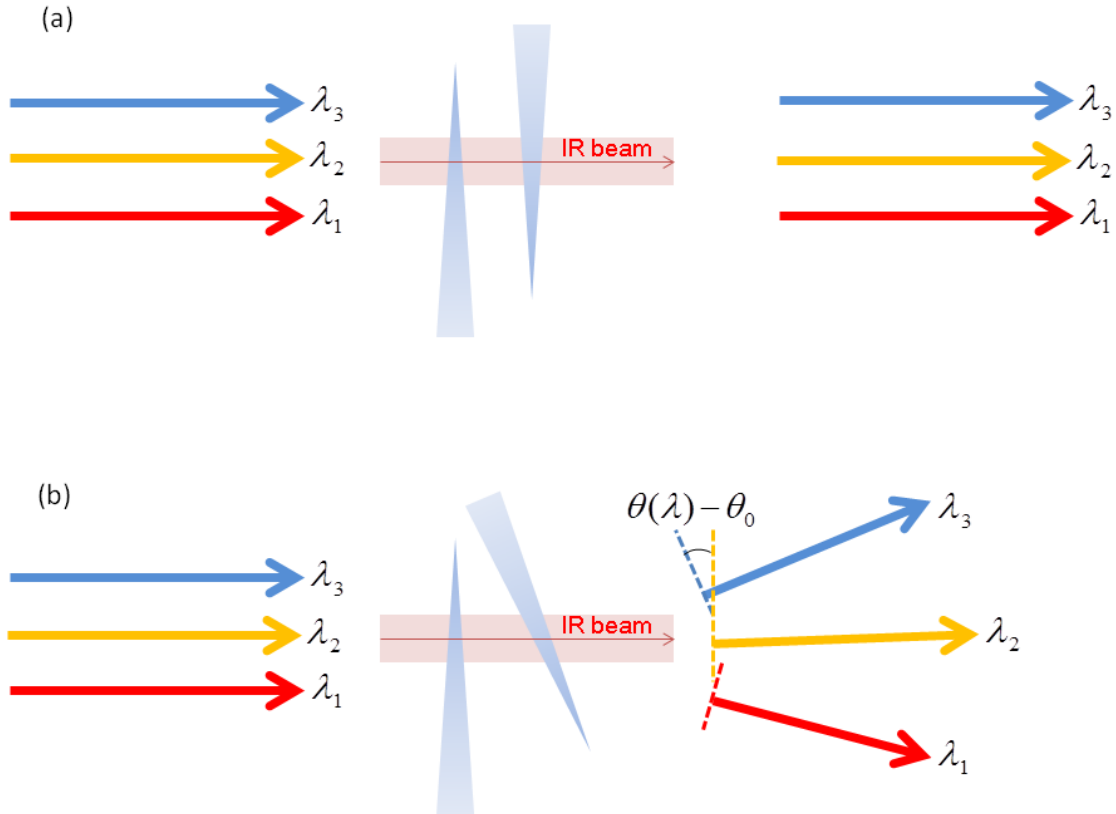


Figure 4.13 – (a) Effect of propagation direction for different laser wavelengths when two wedges are parallel (b) One of the wedges is tilted: the propagation direction for each wavelength is tilted by  $\theta(\lambda)$  with respect to the initial case.

The influence of a spatial chirp at focus on the temporal profile of the pulse is illustrated in Fig 4.14. Looking only at the central line of the focal spot represented by a black dotted line, we illustrate how the temporal profile is distorted in presence of spatial chirp. In the  $y > 0$  region, the average frequency is blue shifted, which means the electric field period increases. On the contrary, towards the  $y < 0$  region, the average frequency is red shifted, which means the electric field period decreases. The result is that the beam wavefront appears to be rotating from cycle to cycle.

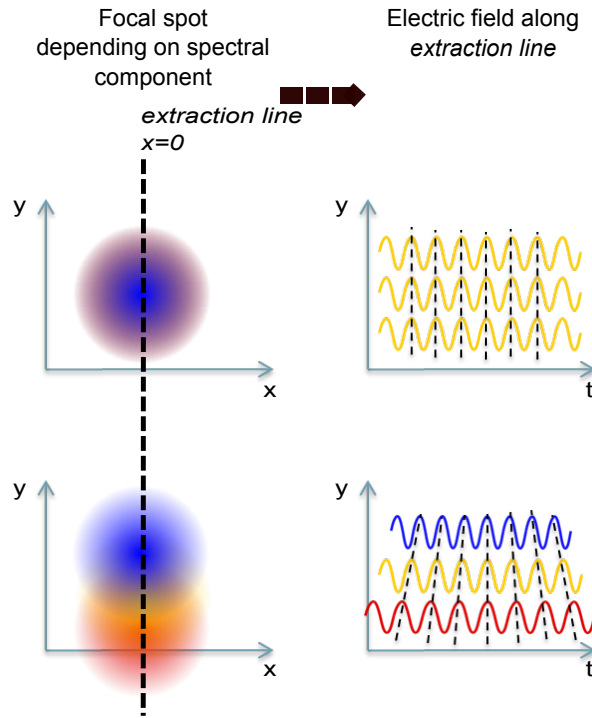


Figure 4.14 – Influence of spatial chirp at focus in artistic view. Top: no WFR when all wavelengths are spatially overlapped. Bottom: WFR because low frequencies are shifted towards the  $y > 0$  region and high frequencies towards the  $y < 0$  region.

The consequence of this effect is quite intuitive: from cycle to cycle, attosecond pulses are generated in a direction which "rotates" as a function of time.

## 4.2.2 Analytical model to evaluate WFR at focus

We show here how we calculate the amount of WFR by only measuring the angular dispersion induced by the wedges (Fig 4.13). This simple model is compared to a measurement and is useful to calculate the emission time of the harmonics when the laser is spatially chirped at focus.

We call  $\beta$  [ $\mu\text{rad}/\text{nm}$ ] the angular dispersion. The phase shift of each frequency along the vertical direction  $y$  of the beam (the absolute reference  $\phi = 0$  is imposed for  $\omega = \omega_0$  with no loss of generality) is given by:

$$\phi(y, \omega)[\text{rad}] = k(\omega)y[\theta(\omega_0) + \int_{\omega} \beta(\lambda)d\lambda] = -k(\omega)y \int_{\omega} \beta(\omega) \frac{2\pi c d\omega}{\omega^2} \quad (4.5)$$

We now only consider the first-order WFR such that  $\beta(\omega) = \beta$  is independent of  $\omega$ . An integration of Eq 4.5 leads to the expression:

$$\phi(y, \omega)[\text{rad}] = \alpha y \quad (4.6)$$

where we define:

$$\alpha[\text{rad/mm}] = 2\pi\beta\left(1 - \frac{\omega}{\omega_0}\right)$$

The expression of the collimated field  $E_{\alpha,0}$  in the spectral domain with WFR is simply related to the field before the wedges (which we write  $E_{\alpha=0,0}$ ) by the product:

$$E_{\alpha,0}(x, y, \omega) = E_{\alpha=0,0}(x, y, \omega)e^{i\alpha(\omega)y} \quad (4.7)$$

We make the paraxial approximation such that the field with ( $E_\beta$ ) or without ( $E_{\beta=0}$ ) WFR at the focus of the parabola of focal length  $f$  is written:

$$\begin{cases} E_{\beta=0}(x, y, \omega) = i\frac{\omega}{2\pi fc}e^{-i\frac{\omega}{c}f}\mathcal{F}[E_{\alpha,0}](k_x = \frac{\omega x}{cf}, k_y = \frac{\omega y}{cf}) & (4.8a) \\ E_\beta(x, y, \omega) = i\frac{\omega}{2\pi fc}e^{-i\frac{\omega}{c}f}\mathcal{F}[E_{\alpha=0,0}](k_x = \frac{\omega x}{cf}, k_y = \frac{\omega y}{cf}) & (4.8b) \end{cases}$$

where  $\mathcal{F}$  denotes the spatial 2D Fourier transform. Eq 4.7 implies the simple relation [122]:

$$\mathcal{F}[E_\alpha](k_x, k_y, \omega) = \mathcal{F}[E_{\alpha=0}](k_x, k_y - \alpha(\omega), \omega) \quad (4.9)$$

Combining Eq 4.8 and Eq 4.9, we verify that adding WFR to a pulse is equivalent to shifting the focal spot center of wavelength  $\lambda$  by a distance  $\Delta y(\lambda)$ :

$$E_\beta(x, y, \omega) = E_{\beta=0}(x, y - \Delta y(\omega), \omega) \quad (4.10)$$

where:

$$\Delta y(\lambda)[mm] = 2\pi\beta f\left(\frac{1}{\omega} - \frac{1}{\omega_0}\right)$$

which gives after normalization by  $\omega_0$ :

$$\overline{\Delta y} = 2\pi\beta f\left(\frac{1}{\bar{\omega}} - 1\right)$$

Note that we have imposed the WFR to be equal to zero for  $\bar{\omega} = 1$ , meaning WFR is symmetric with respect to the carrier frequency  $\omega_0$ . In that case, we necessarily have  $\overline{\Delta y} = 0$  for  $\bar{\omega} = 1$ . The different wavelengths therefore overlay at the center. By making a vertical transverse cut of the field at the position  $x = 0$  (just as done experimentally closing the entrance slit of our imaging spectrometer, described in 4.2.3), we find the expression for the field intensity with ( $\beta > 0$ ) and without ( $\beta = 0$ ) WFR:

$$S_{\beta=0}(\omega, y) = \omega^2|E_{\beta=0}(0, \frac{\omega y}{cf}, \omega)|^2 \quad (4.11)$$

$$S_\beta(\omega, y) = \omega^2|E_{\beta=0}(0, \frac{\omega(y - \Delta y(\omega))}{cf}, \omega)|^2 = S_{\beta=0}(\omega, y - \Delta y(\omega)) \quad (4.12)$$

We can write that last relation using normalized variables for better clarity:

$$S_{\beta=0}(\bar{\omega}, \bar{y}) = S_{\beta=0} \left( \bar{\omega}, \bar{y} - 2\pi\beta f \left( \frac{1}{\bar{\omega}} - 1 \right) \right) \quad (4.13)$$

Based on Eq 4.13, we can construct a simple geometrical transformation to emulate the intensity shaping resulting from WFR at focus. In particular, posing  $X = \frac{1}{\bar{\omega}}$  et  $Y = \bar{y}$ . We define the function  $\hat{S}$  of natural variables  $X, Y$  by the relation:

$$\begin{cases} \hat{S}_{\beta=0}(X, Y) = S_{\beta=0}\left(\frac{1}{X}, Y\right) \\ \hat{S}_{\beta}(X, Y) = S_{\beta}\left(\frac{1}{X}, Y\right) = S_{\beta=0}\left(\frac{1}{X}, Y - 2\pi\beta f(X - 1)\right) = \hat{S}_{\beta=0}(X, Y - 2\pi\beta f(X - 1)) \end{cases} \quad (4.14)$$

We now see that  $\hat{S}_{\beta}$  et  $\hat{S}_{\beta=0}$  are simply related by linear transformation of the system of coordinates:

$$\begin{pmatrix} X' \\ Y' \end{pmatrix} = \begin{pmatrix} 1 & 0 \\ -2\pi f\beta & 1 \end{pmatrix} \begin{pmatrix} X \\ Y \end{pmatrix} + \begin{pmatrix} 0 \\ 2\pi f\beta \end{pmatrix}$$

where we clearly identify a shearing of the coordinates  $X, Y$ .

### 4.2.3 WFR measurement

The experimental setup allowing us to control the angular chirp of the main laser pulse is represented in Fig 4.15. Wedges are introduced in the main beam path at Brewster angle in a parallel configuration. WFR in the plane of polarization is obtained by turning one of the wedges with respect to the other. For the WFR to be in the vertical plane, we introduce a periscope after the wedges, which rotate the WFR direction, but unfortunately also the beam polarization as indicated in Fig 4.15. Therefore, we add a half-wave plane after the periscope. This way, the polarization is turned back to P with respect to the target while the WFR remains vertical.

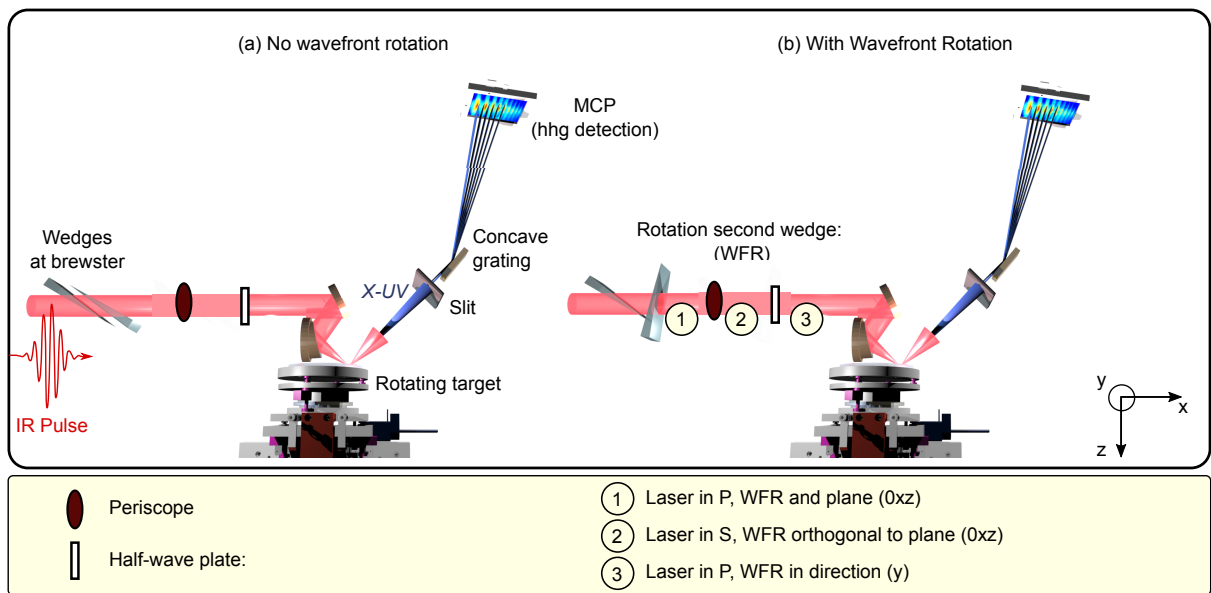


Figure 4.15 – Experimental setup: Wedges are introduced in the main beam path in a parallel configuration (a). WFR is obtained by turning one of the wedges with respect to the other (b)

WFR can be measured by imaging the focal spot of the laser on the entrance slit of an imaging spectrometer.

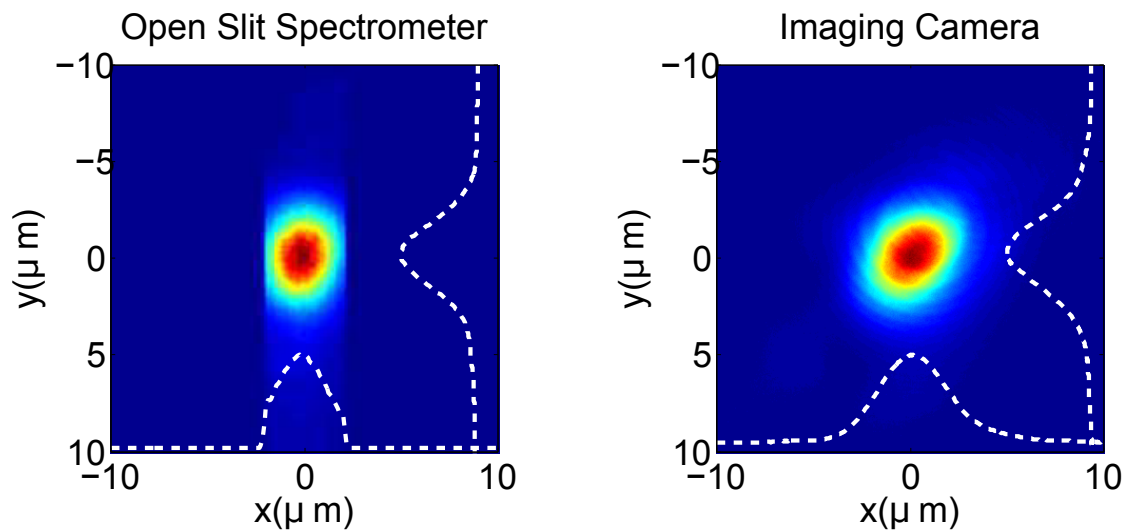


Figure 4.16 – Imaging spectrometer at  $0^{\text{th}}$  order with an open slit (left) after setting the calibration  $0.09 \mu\text{m}/\text{px}$ . The measured focal spot is  $4 \mu\text{m}$  (FWHM). Comparison to an image given by our standard imaging camera (right)

By closing this slit to let through the light in the central vertical line of the spot and adjusting the diffraction grating to the central wavelength (800 nm), we can retrieve the

spectrum at each position  $y$  of the focus. Fig 4.16 shows the profile of the focal spot imaged on the open slit (right) when the grating is positioned to reflect the  $0^{th}$  order (i.e. specular reflection), where we find the focus to be  $4\mu\text{m}$  at FWHM. We now apply this transformation described in 4.2.2 to a temporal and spatial Gaussian beam with  $\tau_{fwhm} = 30\text{fs}$ . The angular dispersion  $\beta$  is calculated theoretically from the relative angle of the two prisms, and reported in the following table:

angle(deg)	70	60	50	40	30	15	0
$\beta(\mu\text{ rad/nm})$	2.012	0.9049	0.4799	0.2545	0.1232	0.02369	0

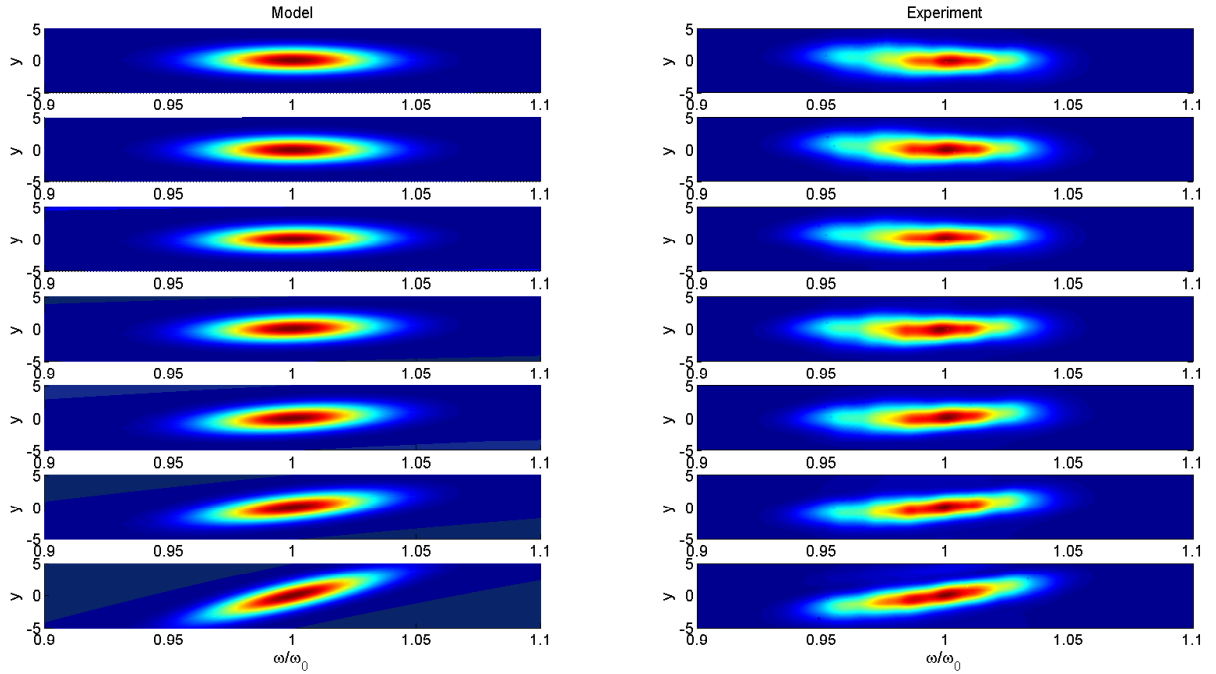


Figure 4.17 – Comparison of model to experimental measurement of vertically resolved pulse spectra with WFR at focus, where  $y$  is given in  $\mu\text{m}$ . In the model (left) we considered a 30 fs pulse with the spatial dimension as measured experimentally. The spectra  $S(\omega, y)$  is obtained by shearing the coordinate as described in 4.2.2. The experimental measured spectra are obtained by rotating the wedges of  $\theta = 0^\circ$  (top),  $15^\circ$ ,  $30^\circ$ ,  $40^\circ$ ,  $50^\circ$ ,  $60^\circ$  and  $70^\circ$  (bottom) in order.

One can then calculate the WFR velocity by calculating the variation of the mean frequency along  $y$ , which leads to Fig 4.18. For a given spectrum, the wavefront rotation does not always increase with the angular dispersion (or the angle of the wedge). There exists an optimal value. This is understandable because as the spatial chirp increases at

focus, the beam “elongates” which has the effect of decreasing the WFR. The optimal angle for the wedges is a trade-off between the spectral spread of the different frequencies along  $y$  with which  $V_{rot}$  increases and the beam spatial elongation with which  $V_{rot}$  decreases. The existence of such an optimum has been studied in great detail in [76] and is clearly visible in Fig 4.18.

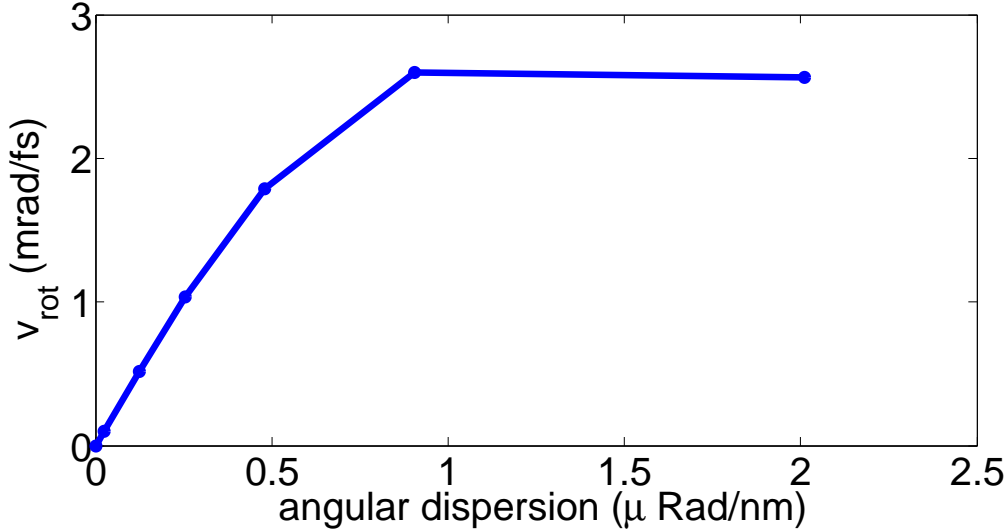


Figure 4.18 – Evaluation of  $V_{rot}$  with respect to angular dispersion  $\beta$  calculated for each angular position of the wedges using the analytical model described in 4.2.2

### Effect of WFR on harmonic generation:

Fig 4.19 presents a comparison between the simulation using the 1D model and the experimental measurement of the angularly-resolved spectrum harmonics (H7 to H17) when WFR is added at the focus by rotating the second wedge by  $70^\circ$ . The first observation is that both in the model and the experiment, the harmonics are tilted when WFR is added to the driving laser at focus. This effect was predicted, because as we described in 4.1.2, the periodicity of the attosecond train increases during the generation process. But since in the presence of WFR, the beginning of the pulse is emitted in the direction of high angles, and the end in the direction of low angles, the recorded image on the MCP is the result of a time-to-space mapping of the attosecond pulses. Because of this, the upper region of the spectrum will be blue shifted while the lower one will be red shifted, i.e. the harmonics become “tilted”. In the experiment, we note that in the absence of WFR, the harmonics are spectrally wider than in the model, which indicates an undervaluation of the femtosecond chirp in the model. A second observation is that the tilt in presence of WFR is more pronounced in the experiment, which again is symptomatic of strong femtosecond chirp and therefore consistent with the broad harmonic line profile observed

in the absence of WFR.

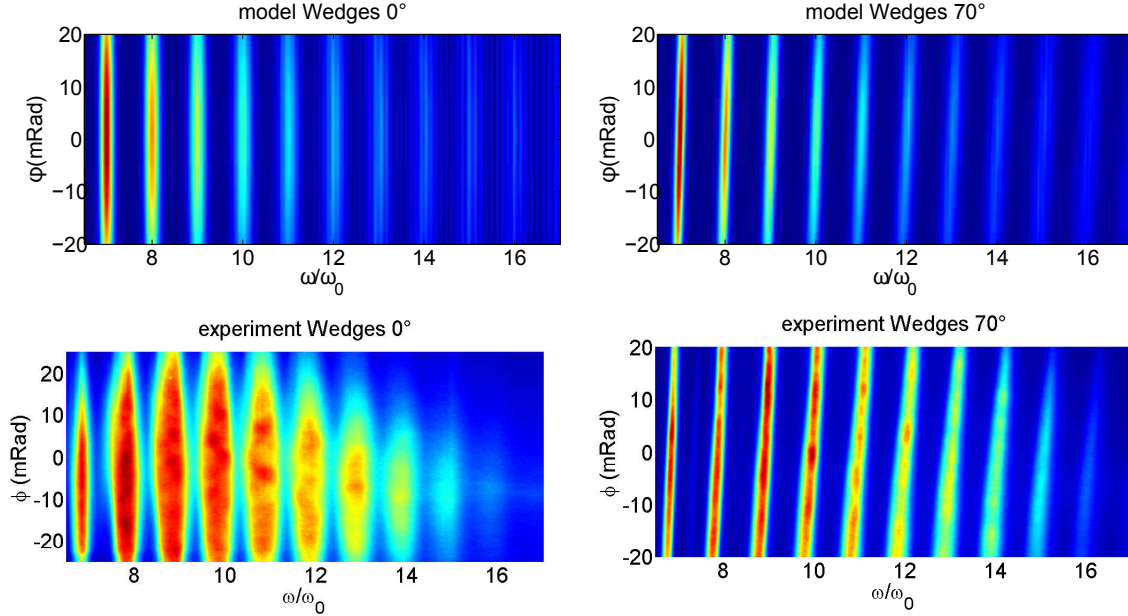


Figure 4.19 – Simulated (top) and experimental (bottom) influence of WFR on harmonic spectra for  $a_0 = 0.1$  .

### Influence of gradient expansion:

As the plasma expands, the intrinsic harmonic femtosecond chirp is expected to increase. Consequently in the experiment, the harmonics are expected to "bend" with pump-probe delay. This is what we observe as can be seen in the screen shot of angular X-UV emission spectra measured for pump-probe delays between -0.1ps and 0.7ps represented in Fig 4.20, for a prepulse intensity is  $\sim 10^{14}$  W/cm<sup>2</sup>. Note that this observation is not so straightforward after 0.5 ps. Indeed, this experiment was very challenging because of the pump/probe spatial overlap fluctuations. For this reason, this result is only preliminary and no quantitative information have been computer from it. We plan to actively stabilize the pump/probe overlap in our future experiment.

To conclude, we have demonstrated that controlled WFR of the driving laser pulse at focus allows one to perform a time-to-space mapping of the attosecond train by means of wavefront rotation of the driving laser pulse. This idea was implemented in the "attosecond lighthouse" [68] with the difference that here, the attosecond pulses are not fully separated in the vertical direction. This principle is called "gating" and has already been investigated both theoretically and experimentally [76, 123]. Temporal gating is used in FROG measurement techniques [124] in order to fully characterize the temporal profile of optical laser pulses. By varying the relative delay between the gate and the pulse under study and measuring its spectrum, one builds a spectrogram that allows us to fully reconstruct the temporal pulse profile. We will discuss hereafter the possibility of applying

such a technique to attosecond streaking in order to perform an “attosecond FROG”.

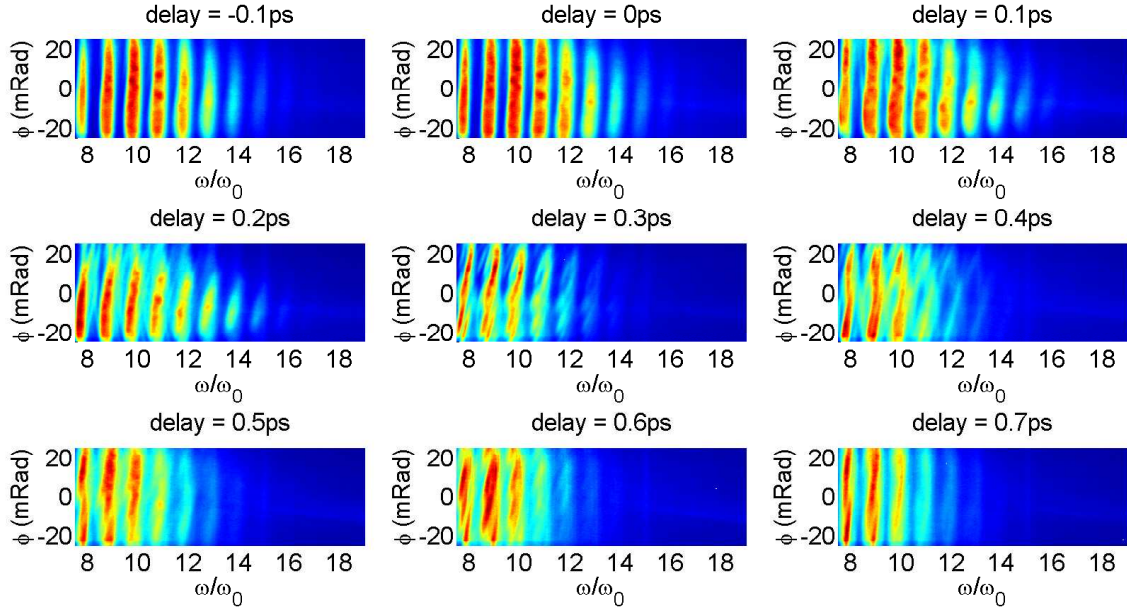


Figure 4.20 – Angularly-resolved harmonic spectra recorded on the MCP with WFR. The prepulse intensity is  $\sim 10^{14}$  W/cm<sup>2</sup>.

### 4.3 Basic principle of attosecond FROG retrieval

Following Trebino’s notation [124], a FROG trace is defined by the following expression:

$$I_{FROG}(\omega, \tau) = \left| \int_{t \in \mathbb{R}} E(t)g(t - \tau)e^{-i\omega t} dt \right|^2 \quad (4.15)$$

where  $E$  is the electric field to be measured,  $g$  the gate function. Inverting the FROG trace, that is to say reconstructing  $E$  knowing  $I_{FROG}$ , is a type of inversion problem that has been extensively studied in various fields of science such as holography, astrophysics and biology. We describe in more details the required conditions for this inversion to be possible in Section 5. Inversion of Eq 4.15 is possible using a FROG retrieval algorithm converging to a (very often) unique solution. Let us adapt the algorithm to the attosecond streaking case.

**Spectrogram in the case of attosecond streaking:**

Unlike Trebino's definition of a FROG trace, the field  $E_{hhg}(\theta_y, t)$  to reconstruct is two-dimensional. When turning a wedge, angular dispersion  $\beta$  is no longer 0 such that we can assess the following relation for the harmonic field:

$$E_{hhg,\beta}(\theta_y, t) = E_{hhg,\beta=0}(\theta_y - v_{rot}t, t)$$

where  $E_{hhg,\beta=0}$  denotes the harmonic field in absence of WFR, and  $E_{hhg,\beta}$  after we introduce WFR with velocity  $v_{rot}$ . Using this empirical relation, this leads to the definition of the following spectrogram:

$$I_{FROG}(\omega, \theta_y) = \left| \int_{t \in \mathbb{R}} E_{hhg,\beta=0}(\theta_y - v_{rot}t, t) e^{-i\omega t} dt \right|^2 \quad (4.16)$$

One clearly sees the problem we are faced with so far: in order to write  $I_{FROG}$  in the form of a FROG trace, as defined by Trebino, and therefore reconstruct the field using a singular value decomposition (SVD) inversion algorithm [125], one needs to write  $E_{hhg,\beta=0}$  as the product of a temporal function with a spatial envelop, that is to say neglect all spatio-temporal couplings:

$$E_{hhg,\beta=0}(\theta_y, t) = g(\theta_y) E_{hhg,\beta=0}(0, t) \quad (4.17)$$

Which means the spectrogram writes:

$$I_{FROG}(\omega, \theta_y) = \left| \int_{t \in \mathbb{R}} E_{hhg,\beta=0}(0, t) g(\theta_y - v_{rot}t) e^{-i\omega t} dt \right|^2 \quad (4.18)$$

In Fig 4.21, we implemented the SVD algorithm on a numerically generated attosecond pulse train, where the condition 4.17 was met, and show the successful reconstruction with a error  $< 0.5\%$  in Fig 4.21.

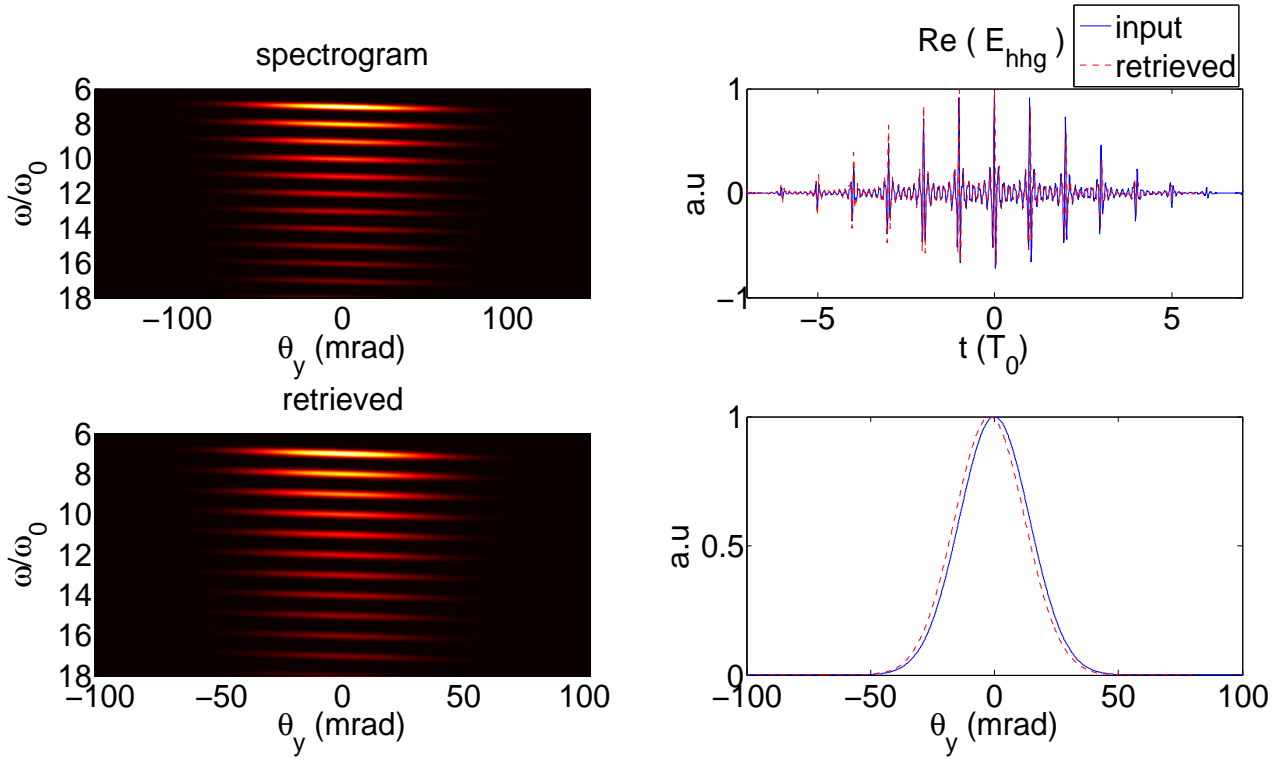


Figure 4.21 – Result of iterative SVD FROG algorithm for input trace generated using  $V_{rot} = -2 \text{ mrad}/[T_0]$ , where the residual error is  $< 0.5\%$ . The initial harmonic field is represented in blue (top right), where we superimposed in red the retrieved field after 500 iterations. The corresponding gate is represented in the bottom right plot.

Unfortunately, running the reconstruction on the experimental data was not possible for the reasons described in the following paragraph.

### Experimental limitations of the method:

We ran the SVD algorithm on our experimental traces shown on Fig 4.22, and found retrieved errors of the order of several percent, which were too high to consider this measurement as an actual characterization of the attosecond pulse train. Several reasons can account for the bad reconstruction:

- The signal recorded on the MCP did not show the whole distribution of the harmonic spectrum. The signal was cut at the edges because of the limited angular range of detection. This can be addressed by relaxing the focusing condition to get a larger waist, and therefore decrease the divergence of the harmonics. It will be implemented in future experiments.
- The reconstruction is intrinsically dependent on the exact measurement of  $v_{rot}$  which would require us to characterize the phase of the IR pulse in addition to the spectrum in the focusing plane. We plan to perform full spatio-temporal characterization of our focused laser using the "Thermite" [126,127] technique to

address this problem.

- The signal/noise ratio –visible on some images in Fig 4.22– is always a limitation when the reconstruction is based on phase retrieval. This problem is partially solved by adding filters to our imaging system and pulsing the MCP detection, but all ambient radiation sources degrading the harmonic signal remain under investigation.

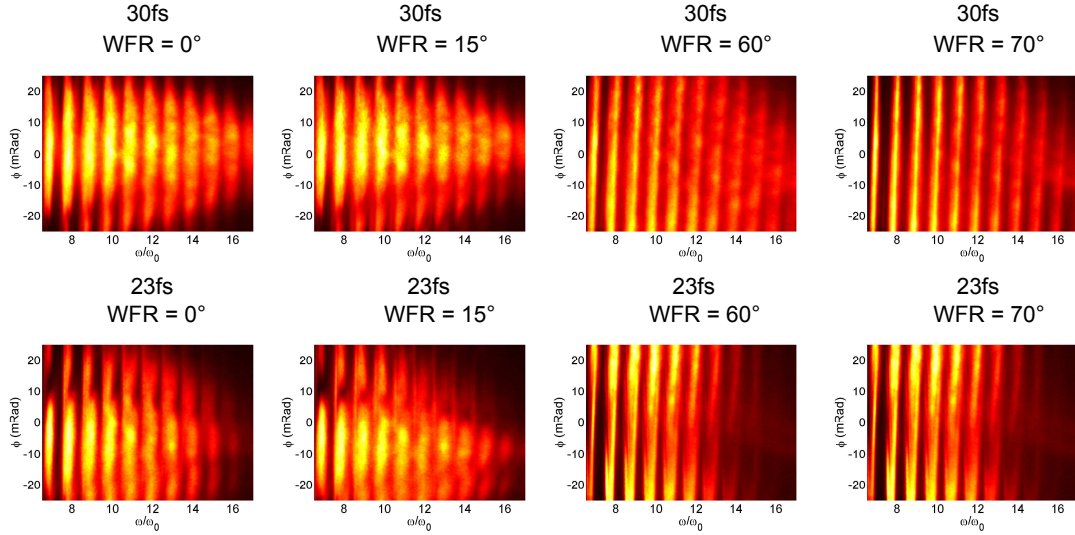


Figure 4.22 – Experimental attosecond FROG traces for  $a_0 = 0.15$ . Top: Laser spectrum is apodized which yields to a compressed pulse of 30 fs, Bottom: compressed laser to 23 fs (see Chapter 3 for description of apodisation method)

One should now consider a more fundamental limitation to this measurement technique, which is intrinsically related to the implementation of the algorithm. Indeed, we made the hypothesis that the harmonic field could be written as the product of a spatial profile with a temporal profile. In practice, there is no rigorous justification allowing for this separation-of-variables. In particular, spatio-temporal coupling of the laser beam due to inhomogeneous compression, inhomogeneous spatial distribution of a prepulse (and therefore inhomogeneous gradient expansion) will directly affect the phase front of the harmonic profile.

In a final observation on these limitations, it would be necessary to implement a retrieval where (i)  $v_{rot}$  does not need to be accurately calibrated and (ii) the full two-dimensional profile  $E_{hhg,\beta=0}(\theta_y, t)$  is reconstructed, as opposed to its value in  $\theta_y = 0$ . This goes beyond the scope of the work presented here but constitutes an interesting theoretical challenge.

## 4.4 Conclusion

We have performed a series of experiments validating the harmonic emission properties from plasma mirrors already demonstrated in the literature [51,74,76,79,117,123], namely how each attosecond pulse emission time depends on the temporal structure of the driving laser pulse [51, 74, 79]. The HHG emission is coherent and phase-locked to the driving laser intensity and phase profile. We have shown how the spectral components of the X-UV light depends on the spatial intensity distribution of the driving laser. This then led us to study the feasibility of an "attosecond FROG" type measurement by controlling the angular chirp of the main laser pulse, and observing the subsequent tilt of the harmonic lines in the angularly resolved emission spectra. This effect can be fully predicted by a simple one-dimensional model used to calculate the emission time at each position of the laser across the laser focus with WFR. We have implemented an SVD retrieval algorithm similar to that used for standard FROG retrieval of IR laser pulses. However, our approach is limited: the quality of the images has to be improved, the driving laser has to be fully characterized at focus, and most of all, the retrieval algorithm should be made independent of the laser WFR.

# Chapter 5

## Measuring the plasma expansion

### Outline

---

<b>5.1</b>	<b>Spatial Domain Interferometry (SDI)</b>	<b>87</b>
5.1.1	Introduction	87
5.1.2	Basic principle	88
5.1.3	Illustration with a step-like density profile	90
5.1.4	Plasma expansion model	90
5.1.5	Experimental setup	93
5.1.6	Experimental results	94
<b>5.2</b>	<b>Sensitivity to beam alignment</b>	<b>95</b>
5.2.1	Single-order phase shift and experimental limitations	95
5.2.2	Break of symmetry	99
<b>5.3</b>	<b>Perspectives for phase retrieval</b>	<b>101</b>
5.3.1	Inversion problem	101
5.3.2	One-dimension retrieval	102
5.3.3	Modifying the reference probes to break the symmetry	107
5.3.4	Two-dimensional retrieval ambiguities	109
<b>5.4</b>	<b>Conclusion and perspectives</b>	<b>110</b>

---

## 5.1 Spatial Domain Interferometry (SDI)

### 5.1.1 Introduction

When the intensity of a pulse interacting with matter exceeds  $\sim 10^{11}$  W/cm<sup>2</sup>, ionization takes place and any solid material turns into a plasma. The zero pressure inside the experimental chamber does not balance the plasma thermal pressure (typically  $T \sim 100$  eV) which consequently expands towards vacuum at approximately the speed of sound ( $c_s \sim 10$  nm/ps). The characteristic spatial and temporal expansion scale lengths

(< 10 nm, < 1 ps respectively) make femtosecond (fs) laser pulses the best candidates to perform accurate measurements using phase-sensitive detection schemes such as Frequency Domain Interferometry (FDI) [128–132]. The principle of FDI is as follows:

A probe beam of short duration (several fs) is split into two copropagating replicas separated by an adjustable delay. The first replica is reflected by the target in the absence of plasma, and the second is reflected after the plasma expansion has been triggered by a pump pulse. Both replicas are sent into an imaging spectrometer to visualize the spectral modulations resulting from their interference. In the region of space where the second replica was phase shifted because of plasma expansion, the changes in the spectral pattern enable the reconstruction of the plasma spatial profile for a given pump-probe delay.

Although FDI can reach  $\lambda/2000$  resolution [128], it is rather complex to implement on a running plasma mirror experiment. In this chapter, we present a technique we developed called Spatial Domain Interferometry (SDI). It is easier to implement experimentally, based on time-resolved spatial phase-shift imaging interferometry. We present the basic principle of the technique and show experimental results applied to the characterization of the gradient generated by our controlled prepulse.

### 5.1.2 Basic principle

We showed in the previous section that the main pulse was used to generate high-order harmonics on a solid target after it is ionized by prepulse with adjustable delay. For a SDI measurement of the plasma expansion, we transform the "main pulse" into a "plasma expansion probe pulse" by adding a periodic transmission mask in the main beam path prior to the focusing parabola. The mask is a simple blocker with periodic holes represented in Fig 5.1(a), which causes a diffraction pattern in the focusing plane where we can identify several diffraction orders as represented in Fig 5.1(b). The spacing between the  $0^{th}$  order and the first-order ring is chosen such that only the  $0^{th}$  order is reflected by the expanded plasma, represented with orange color in Fig 5.1(b). In this configuration, only one order is phase shifted as the probe is reflected by the plasma, the other orders impinge on a non-irradiated target surface. This ultimately leads to intensity modulations of the far-field after propagation as illustrated in Fig 5.1(c) for a phase shift of respectively  $\Delta\phi = 0$  and  $\pi$ . The principle of SDI is therefore to retrieve the shape of the plasma and its expansion velocity from these spatial intensity modulations.

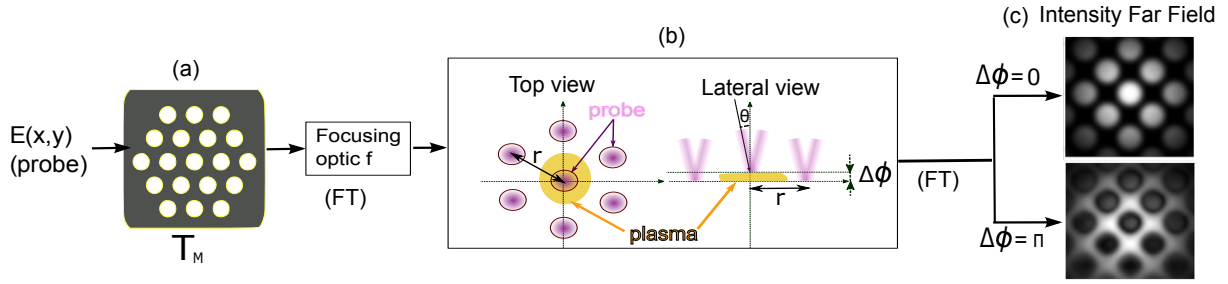


Figure 5.1 – SDI principle applied to ultrafast plasma mirror imaging: the probe field  $E(x, y)$  is diffracted by a transmission mask  $T_M$  (a) onto a plasma mirror in the focusing plane (b). The phase shift,  $\Delta\phi$ , of the central diffraction spot induced by the plasma expansion leads to a modulation of the far-field spatial intensity profile (c) of the reflected probe with respect to  $\Delta\phi$ .

We designate by  $T_M$  the transmission mask introduced in the collimated probe beam prior to the focusing optic of focal length  $f$ . As a consequence, the probe pulse focus spot splits into several spots spaced by  $\Delta x = \frac{\lambda f}{a}$ , where  $a$  is the period of the mask and  $\lambda$  the central wavelength. The probe field after the mask is defined by:

$$E_M(x, y, \omega) = E(x, y, \omega)T_M(x, y). \quad (5.1)$$

Within the paraxial approximation, the field  $E_{ref}$  in the focusing is given by:

$$E_{ref}(x, y) = \mathcal{F}[E_M](\nu_x = \frac{x}{\lambda f}, \nu_y = \frac{y}{\lambda f}) \quad (5.2)$$

where  $\mathcal{F}$  denotes the spatial Fourier transform, and  $(\nu_x, \nu_y)$  the spatial frequencies. As shown in Fig 5.1, the expanding reflective plasma introduces a phase shift where it spatially overlaps with  $E_{ref}$ . We designate its effect on the reference field by the complex transfer function  $T$  which allows us to define a new field:

$$E_2(x, y) = E_{ref}(x, y)T(x, y) \quad (5.3)$$

where  $T = |T|e^{i\phi}$  is the transfer function of the plasma.  $|T| \neq 1$  is therefore equivalent to a variation of the reflectivity.

We finally call  $E_F$  the field after propagation and far from the plasma surface ( $z \gg Z_R$ ) which can be calculated by Fourier transform of Eq 5.3:

$$E_F(x, y) = \mathcal{F}[E_2](\nu_x = \frac{x}{\lambda f}, \nu_y = \frac{y}{\lambda f}). \quad (5.4)$$

We recall the property of the Fourier transform of a function  $f$ :

$$(\mathcal{F}^{-1}f)(x) = (\mathcal{F}.f)(-x)$$

This ultimately implies the identity  $\mathcal{F}[\mathcal{F}.f](x) = f(-x)$  and we can write:

$$\begin{cases} E_F(x, y) = \mathcal{F}\left(\mathcal{F}[E_M]T\right)\left(\nu_x = \frac{x}{\lambda f}, \nu_y = \frac{y}{\lambda f}\right) \end{cases} \quad (5.5a)$$

$$\begin{cases} E_F(x, y) = E_M(-x, -y) + \mathcal{F}\left(\mathcal{F}[E_M](T - 1)\right) \end{cases} \quad (5.5b)$$

Using the relation  $\mathcal{F}(fg) = \mathcal{F}(f) * \mathcal{F}(g)$ , we can verify that the reflected intensity  $I = |E_F|^2$  is equal to (we replace  $(-x, -y)$  by  $(x, y)$  in Eq 5.5b for better clarity):

$$I(x, y) = |ET_M + \iint ET_M(x - x', y - y')h(x', y')dx'dy'|^2, \quad (5.6)$$

where

$$h(x, y) = FT(T - 1)\left(\frac{x}{\lambda f}, \frac{y}{\lambda f}\right). \quad (5.7)$$

The information about the plasma response is therefore contained in the function  $h$ . When  $T = 1$ , we find the trivial result that  $I = |ET_M|$ , which means that the plasma behaves as a perfect mirror.

### 5.1.3 Illustration with a step-like density profile

To estimate the effect of the plasma mirror-induced phase shift on the reflected image, we can make the simple assumption that all diffracted spots are reflected equally by the plasma and that only the 0<sup>th</sup>-order is phase shifted by a spatially uniform  $\phi_0$ . Mathematically, this translates into  $|T| = 1$  and  $\phi(x, y) = \phi_0$  for  $|x|, |y| < \frac{\lambda f}{2a}$ . This allows us to express  $h$  by limiting the Fourier integration domain to  $[-\frac{\lambda f}{2a}, \frac{\lambda f}{2a}]$ , such that:

$$h(x, y) = (e^{i\phi_0} - 1) \left(\frac{\lambda f}{a}\right)^2 \text{sinc}\left(\frac{x}{2a}\right)\text{sinc}\left(\frac{y}{2a}\right). \quad (5.8)$$

This particular solution shows that the convolution function,  $h$ , is periodic with  $\phi_0$  since the interference term in Eq 5.6 leads to an inversion of the far-field pattern every time  $\phi_0 = \pi[\pi]$ . It is this periodicity that confers SDI the ability to directly visualize the monotonic expansion of the plasma mirror surface.

Our experiment is however different from this ideal case because the plasma mirror spatial shape is inherited from the prepulse spatial profile which differs from the step like case, and is closer to a Gaussian profile. This, however, does not prevent the inversions from being visible in the far-field intensity pattern, as we will see in the following section.

### 5.1.4 Plasma expansion model

The description of the plasma along the target normal has already been done in subsection 3.1.2 and we saw it was described by a decreasing exponential of gradient scale

length  $L$ . The plasma expansion in vacuum is a standard problem solved by Krueer [34] using the isothermal equation of state for the electrons and its solution is given by the self-similar solution:

$$n_e(x, t) = n_c \exp\left(-\frac{x - x_c(t)}{c_s t}\right). \quad (5.9)$$

where  $c_s = (Zk_b T_e / m_i)^{1/2}$  is the ion sound velocity and  $n_c = (\omega_0^2 m_e \epsilon_0) / e^2$  the critical density. In these expressions,  $Z$  is the ion charge state,  $e$  is the electron elementary charge,  $k_b$  the Helmholtz constant,  $T_e$  the electron temperature,  $m_e$  and  $m_i$  respectively the electron and ion mass.

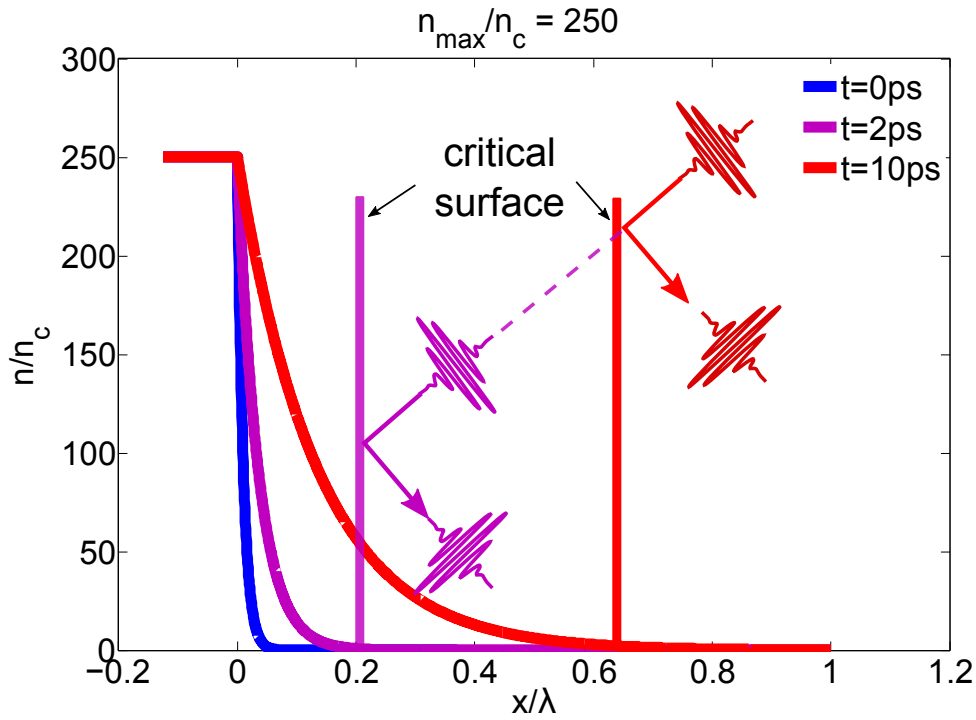


Figure 5.2 – Illustration of gradient expansion with  $c_s = 10$  nm/ps for a prepulse delay of respectively  $t = 0, 2$  and  $10$ ps. The initial gradient scale length is taken  $\delta L = \lambda/100$ . The IR probe pulse is shown to reflect on the critical density at respectively  $2$  and  $10$ ps.

In 5.9 we clearly identify  $L(t) = c_s t$  as the gradient length which is proportional to  $x_c(t)$ , the coordinate of the critical density where the probe is reflected, as represented in Fig 5.2. For a fully ionized silica target the overdense maximum density is about  $250n_c$  such that  $x_c(t) = \ln(250)L(t) \approx 5.5L(t)$ .

Assuming the electron temperature  $T_e$  depends linearly on the energy deposited on target when the plasma is created, that is to say on the prepulse intensity  $I_p$ , we can write, according to its definition, that for a fixed pulse duration:

$$c_s \propto \sqrt{I_p}$$

The prepulse intensity is taken homogeneous on each isolated diffracted spot of the main pulse in order to define a corresponding expansion velocity.  $I_{p,1}$  is the prepulse intensity at the center,  $I_{p,2}$  on the first order diffracted spots.

$$\begin{cases} c_{s,1} \propto \sqrt{I_{p,1}} \\ c_{s,2} \propto \sqrt{I_{p,2}} \end{cases} \quad (5.10)$$

This means that the center of the plasma expands faster than its edges for a Gaussian shaped prepulse.

### Phase shift due to the expansion:

Taking into account the angle of incidence of  $\theta$  with respect to the target normal, we express the phase difference  $\Delta\phi$  between the zero and first-order probe spots as a function of the relative critical surface position difference  $\Delta x_c(t) = x_{c,1}(t) - x_{c,2}(t)$ :

$$\Delta\phi(t) = \frac{4\pi}{\lambda} \Delta x_c(t) / \cos(\theta). \quad (5.11)$$

where the expansion velocity at the center of the prepulse ( $I_p = I_{p,1}$ ) verifies:

$$\Delta x_c(t) = \ln(n_{max}/n_c) c_{s,1} \left(1 - \frac{c_{s,2}}{c_{s,1}}\right) t \quad (5.12)$$

Using Eq 5.11 and Eq 5.12, we evaluate the expansion velocity over the 0<sup>th</sup> order of the probe  $c_s = c_{s,1}$ :

$$[c_s t] = [\ln(n_{max}/n_c) \left(1 - \sqrt{\frac{I_{p,2}}{I_{p,1}}}\right) \frac{4\pi}{\lambda} / \cos(\theta)]^{-1} \Delta\phi(t) \quad (5.13)$$

Note that in the above derivation, we have neglected the phase shift induced by the propagation in the underdense portion of the plasma. Indeed, its contribution for a given value of  $L$  can be calculated for the carrier frequency  $\omega_0$ :

$$\phi_u = \frac{2\pi}{\lambda} \int_{-\infty}^{n_c} \frac{\omega_P^2(x)}{\omega_0^2} dx = 4\pi \frac{L}{\lambda} \quad (5.14)$$

Which would give rise to an additional phase difference at any time  $t$ :

$$\Delta\phi_u(t) = 4\pi \frac{\Delta x_c}{5.5\lambda} \quad (5.15)$$

Calculating the exact phase difference for a short femtosecond pulse becomes more complex since shearing and group delays all have to be accounted for. Therefore, we neglect this term in the following ( $\Delta\phi_u/\Delta\phi \sim 0.1$ ) and focus on the basic principles of the exposed method.

### 5.1.5 Experimental setup

The experimental pump-probe setup has already been described in Section 3.3. The main pulse is sent through a periodically holed hexagonal mask of period  $a = 4$  mm. The resulting diffraction pattern is shown in Fig 5.3 where we superimposed the measured pump (gray scale) used for plasma generation and the diffracted probe (color scale) beam profiles. The central diffracted probe spot intensity is  $\sim 10^{16}$  W/cm<sup>2</sup>. The peak intensity of the prepulse is  $I_{p,1} = 3.5 \times 10^{14}$  W/cm<sup>2</sup> in the center and  $I_{p,2} = 8.7 \times 10^{13}$  W/cm<sup>2</sup> where it overlaps with the first order diffraction spots.

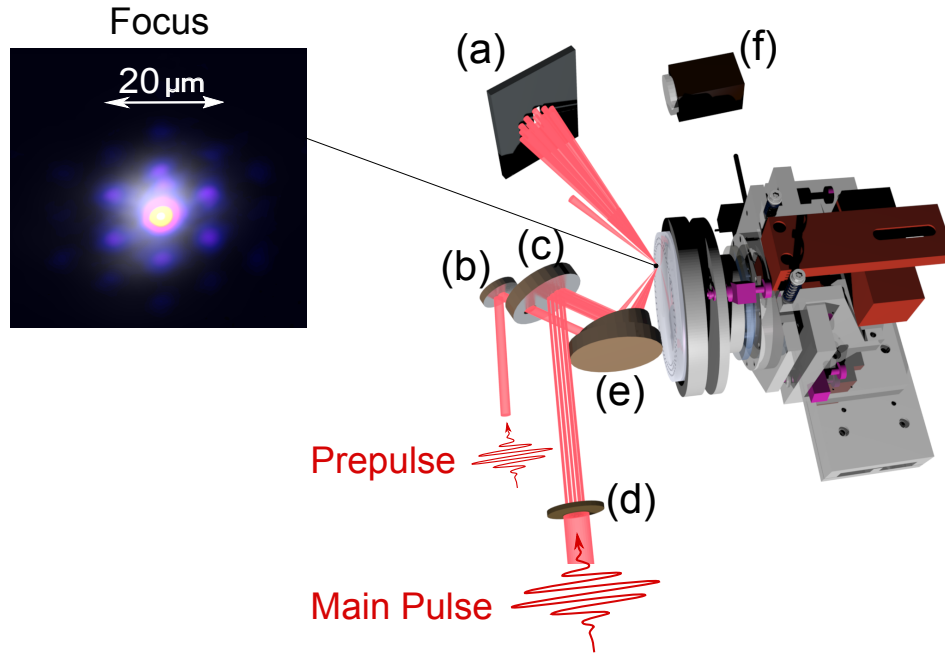


Figure 5.3 – (a) Entrance slit for XUV generation (b) Silver mirror for prepulse (c) Holed mirror for main pulse (probe) (d) Transmission mask (e) Off-axis f/1.2 focusing parabola (f) Camera placed under vacuum imaging the entrance slit.

Our experiment consists in recording the intensity pattern of the main pulse reflected in the specular direction as a function of pump-probe delay. No particular plane of the reflected beam is imaged, but a camera records the reflected probe beam integrated over 100 shots by imaging the anodized vertical slit usually used to block the laser before the XUV spectrometer. The results for four different pump-probe delays are displayed in the top row of Fig 5.4. We take the intensity profile recorded at zero pump-probe delay as our reference. The first inversion of the intensity profile appears at  $\simeq 12$  ps and the second inversion occurs at  $\simeq 20$  ps. The profile inversion patterns are well reproduced by the simulations shown on the bottom row of Fig 5.4, where we used the actual experimental pump pulse profile to simulate the phase shift due to the plasma expansion, using the model presented in subsection 5.1.4.

### 5.1.6 Experimental results

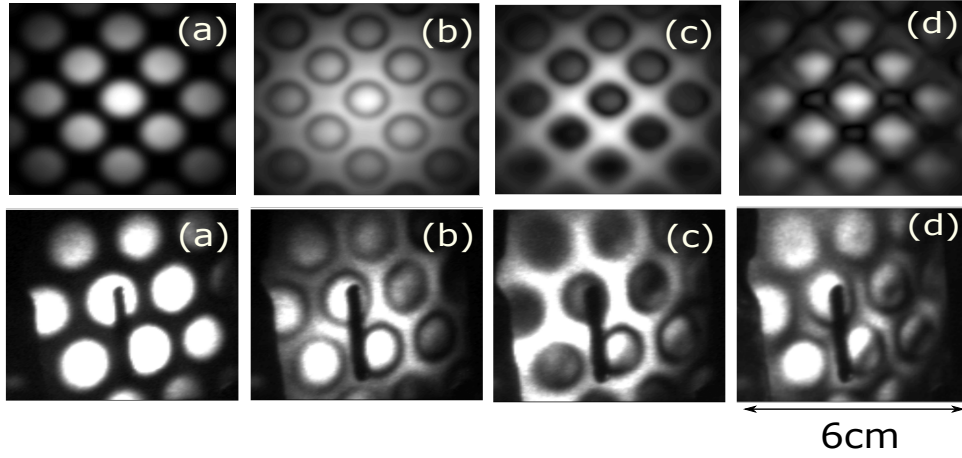


Figure 5.4 – Simulated and experimental far-field probe beam intensity profile inversions at respectively 0 ps(a) 6 ps(b), 12 ps(c) and 20 ps(d) pump-probe delay. The simulations are performed using the measured pump beam profile and assuming the plasma expansion velocity  $c_s \propto \sqrt{I_p}$ .

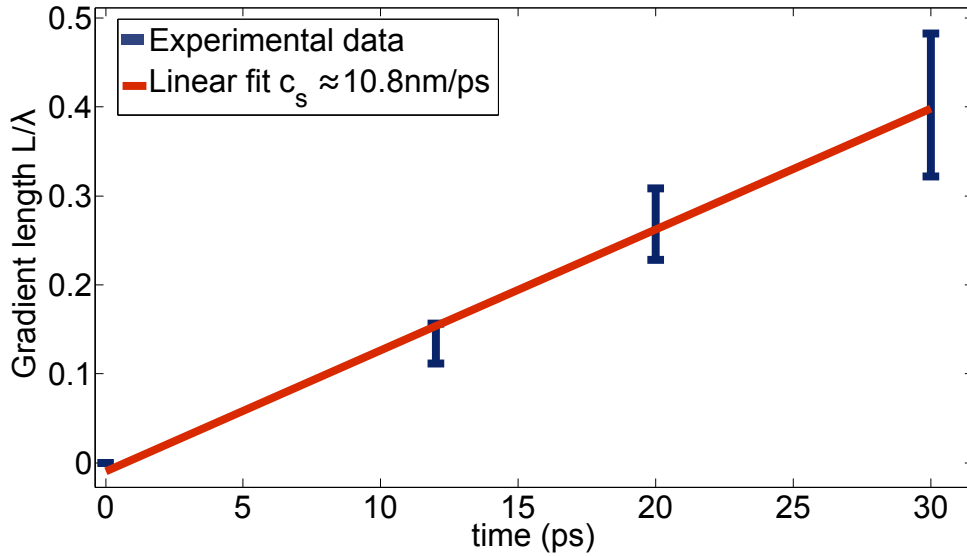


Figure 5.5 – Measurement of plasma relative expansion for a prepulse intensity of  $I_{p,1} = 3.5 \times 10^{14} \text{ W/cm}^2$  as a function of pump-probe delay. Each experimental point corresponds to a  $\pi$  inversion in the intensity profile of the reflected probe. The corresponding linear fit allows one to retrieve a plasma expansion velocity of  $c_s \approx 10.8 \text{ nm/ps}$

The phase inversion corresponding to the experimental data points reported in Fig 5.5 are identifiable by eye, and the corresponding error bar increases with pump-probe delay (inversion become less and less clear because energy fluctuations of the pump pulse impact the expansion velocity of the plasma).

A few important remarks need to be made about that measurement technique so far:

- The retrieved  $c_s$  is intrinsically contingent on the hypothesis that the expansion velocity in vacuum is proportional to the square root of the pump laser intensity. An absolute measurement of the expansion would require phase retrieval for any pump-probe delay rather than looking for inversions supposedly corresponding to  $\Delta\phi = n\pi$  where  $n$  is integer. This point will be developed in Section 5.3. In addition, note that we measure the expansion of the critical surface. The proportionality factor between this surface and the gradient length  $L$  is based on the hypotheses that the plasma has an exponential profile and that the electron temperature does not vary during the expansion. Any violation of these hypotheses leads to an error on the retrieved gradient length  $L$ .
- The error bars in Fig 5.5 do not take into account the fact that the relative position between the pump and probe beam (and consequently the relative intensity  $I_{p,1}$  and  $I_{p,2}$ ) changes during an experiment. The pointing stability can degrade over several hours, or thermal lens effects in the chain can lead to both beam going out of alignment when they are attenuated as we describe in 5.2.2. This could ultimately lead to an error bar of the order the  $c_s$  which is why the previous measurement should only be considered as a proof-of-principle at this time.
- Similar to the fs pump-probe spatial imaging technique employed in [133], our time resolution is simply limited by the duration of the pulse used to probe the plasma expansion induced by the pump pulse.

As a conclusion, we have demonstrated the basic proof-of-principle of SDI but a lot of effort needs to be made to improve the beam stability at full power to properly evaluate the error bar relative to the measurement as illustrated in the following section.

## 5.2 Sensitivity to beam alignment

### 5.2.1 Single-order phase shift and experimental limitations

In the previous experiment, we were in a configuration where the first diffracted orders were also affected by the plasma expansion because the diffraction spacing  $r$  was not large enough.

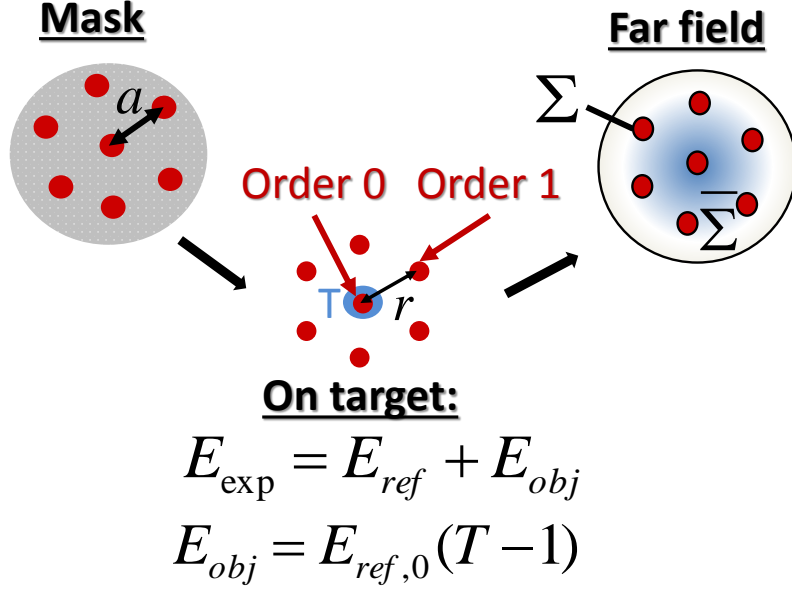


Figure 5.6 – Definition of the variables  $a$ : mask spacing,  $T$ : plasma transfer function on target,  $E_{\text{ref}}$ : field on target when  $T = 1$ ,  $E_{\text{ref},0}$ :  $0^{\text{th}}$  order diffracted spot on target,  $E_{\text{exp}}$ : field on target for arbitrary  $T$ ,  $r$ : distance from center to first diffraction order,  $\Sigma$ : reflected far-field conjugate to mask holes,  $\bar{\Sigma}$ : reflected far-field conjugate to mask

If we suppose that for a laser intensity  $I_p < I_{\text{lim}} = 10^{10} \text{ W/cm}^2$ , neither ionization nor small phase distortions of the surface affect the reference field  $E_{\text{ref}}$ , we find a **separation spacing criterion** for the diffracted spot for a prepulse intensity  $I_p$ :

$$r > (d_{1/2}/2) \sqrt{\ln(I_p/I_{\text{lim}})/\ln(2)} \quad (5.16)$$

Where  $r$  is the distance from the center to the first diffracted spot represented in Fig 5.6, and  $d_{1/2}$  the prepulse spatial FWHM. Using this constraint, we can retrieve a maximum period for the transmission mask:

$$a = \frac{\lambda f}{r} < \frac{\lambda f}{d_{1/2}/2 \sqrt{\ln(I_p/I_{\text{lim}})/\ln(2)}} \quad (5.17)$$

In our experimental conditions where  $5 \times 10^{14} \text{ W/cm}^2$ ,  $d_{1/2} \approx 22 \mu\text{m}$ , this implies that  $r \gtrsim 2d_{1/2}$  which for  $\lambda = 800 \text{ nm}$  gives:

$$a \lesssim 960 \mu\text{m}$$

We designed masks with spacing matching this separation condition by drilling holes in metal banks using the smallest available drill diameter ( $\sim 0.8\text{mm}$ ).

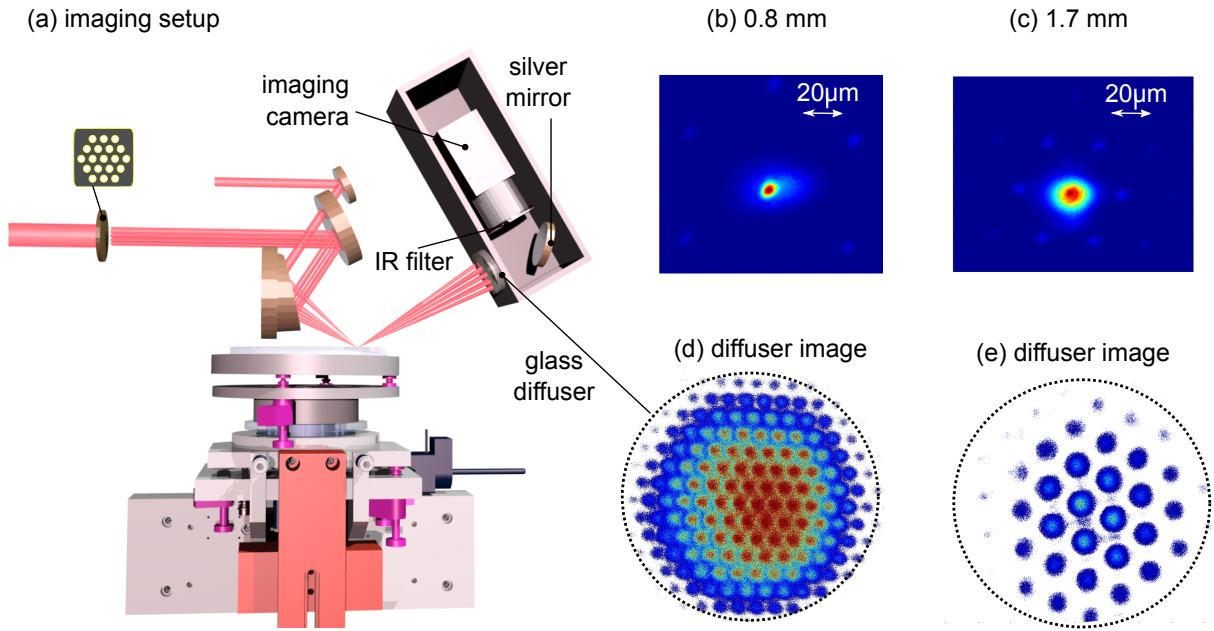


Figure 5.7 – Image recorded on the glass diffuser positioned in the specular direction of the probe beam as represented in (a). Superimposed pump and probe spatial profiles for a mask spacing of  $a = 0.8\text{mm}$  (b) and  $a = 1.7\text{mm}$  mask (c). Profile on diffuser integrated over 50 consecutive shots with no prepulse for  $a = 0.8\text{mm}$  (d) and  $a = 1.7\text{mm}$  (e). The probe intensity is high enough to induce ionization on several diffracted orders.

We recorded the reflected fluence of the probe on a glass diffuser (*Thorlabs*) with  $2\ \mu\text{m}$  grain size placed in the specular direction and imaged onto a CCD camera as shown in Fig 5.7. The diffuser was used to prevent direct imaging of the reflected probe in addition to a  $800\text{nm}$  filter placed before the imaging camera. Unfortunately, the grain size appeared to be limiting the spatial resolution of the recorded images ( Fig5.7(d)). Because of that degradation, the intensity contrast drops for the  $a = 0.8\text{mm}$  mask while remaining acceptable when increasing the mask periodicity to  $a = 1.7\text{mm}$  ( Fig5.7(e)). For this reason, we could not exploit the experimental data taken with the  $a = 0.8\ \text{mm}$  mask, but it is still worth insisting on some of the basic properties to expect for a successful experiment where **the separation spacing criterion** is met:

We define the far-field contrast on  $\Sigma$  and  $\bar{\Sigma}$ , defined in Fig 5.6 by the relation:

$$c_{\Sigma} = \frac{\sum I(r \in \Sigma)}{\sum I(r \in \bar{\Sigma}) + I(r \in \Sigma)}$$

and

$$c_{\bar{\Sigma}} = \frac{\sum I(r \in \bar{\Sigma})}{\sum I(r \in \bar{\Sigma}) + I(r \in \Sigma)}$$

where  $I$  denotes the intensity of the reflected probe field in an arbitrary plane and  $r$  the pixel coordinate in that plane (experimentally, it corresponds to the imaged diffuser

plane). For negative pump-probe delays, that is to say in the case where  $T = 1$ ,  $I$  equals zero on  $\bar{\Sigma}$  because it is conjugated to the mask by two Fourier transform operations as seen in 5.1.2. As soon as  $T$  differs from 1, since it only modifies the central order  $E_{ref,0}$ , we can write for the field  $E_{obj}$  also defined in 5.1.2 on target:

$$E_{obj} = TE_{ref} = TE_{ref,0} + (E_{ref} - E_{ref,0}) = (T - 1)E_{ref,0} + E_{ref} \quad (5.18)$$

The reflected far field is obtained by performing a Fourier transform of Eq 5.18, which is a linear operation. As a consequence,

$$I_{\Sigma} = |\mathcal{F}\left((T - 1)E_{ref,0}\right) + \mathcal{F}\left(E_{ref}\right)|_{\Sigma}^2 \quad (5.19)$$

and

$$I_{\bar{\Sigma}} = |\mathcal{F}\left((T - 1)E_{ref,0}\right)|_{\bar{\Sigma}}^2 \quad (5.20)$$

Eq 5.20 shows that the contrast on  $\bar{\Sigma}$  will follow the same periodicity as  $T$  in time. As an illustration, we show the experimental result were the  $a = 1.7\text{mm}$  mask (not satisfying the separation spacing criteria but for which the same underlying ideas still apply) in Fig 5.8. We clearly see a decrease in the oscillating period of  $c_{\bar{\Sigma}}$  and  $c_{\Sigma}$  corresponding to a faster expansion as we increase the prepulse energy. The variations in contrast agree well with the scaling law  $c_s \propto \sqrt{I_p}$  already used in the previous section.

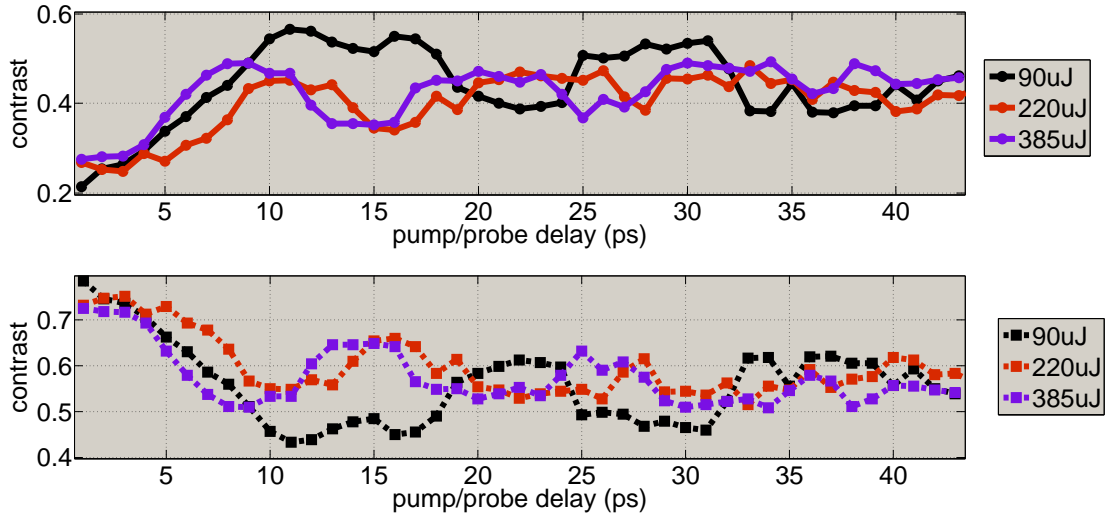


Figure 5.8 – Contrast evolution of the far-field for 3 different prepulse energies  $E = 90, 220$  and  $385 \mu\text{J}$ , respectively (corresponding to prepulse intensity  $I_p = 4, 10$  and  $18 \times 10^{14}$ ,  $\text{W}/\text{cm}^2$ , respectively).  $\bar{\Sigma}$ (top),  $\Sigma$ (bottom).

Note that the initial contrast  $c_{\bar{\Sigma}}$  is not rigorously equal to zero because of background in the experimental chamber and also because after the probe has ionized the target, we

can no longer assess that the measurement plane is conjugated with the mask plane. As a consequence, the initial contrast will always be slightly degraded.

### 5.2.2 Break of symmetry

If we make the hypothesis that both prepulse and probe pulse are perfect Gaussian beams, it is quite straightforward that the generated plasma will expand symmetrically with respect to the origin and that the far-field intensity modulations also show a central symmetry. However, experimental data indicate that this assessed symmetry is broken during the expansion as illustrated by the screen shot in Fig 5.9 where tilted fringes appear at 30ps pump-probe delay. This pattern is actually the consequence of an uncontrolled shift of the prepulse position relative to the probe pulse from the initial alignment and can in turn drastically affect the interpretation of the data. We simulated this effect in Fig 5.10 and observed a similar pattern with the appearance of fringes in sub-figures (c) and (d) where the prepulse was voluntarily misaligned with respect to the probe.

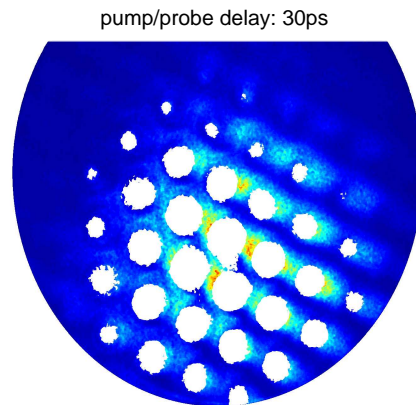


Figure 5.9 – Image over  $\bar{\Sigma}$  for a prepulse energy on target of  $385 \mu\text{J}$  and a pump-probe delay of 30ps. In the case where prepulse and probe are misaligned on target: tilted fringes indicating a break in symmetry

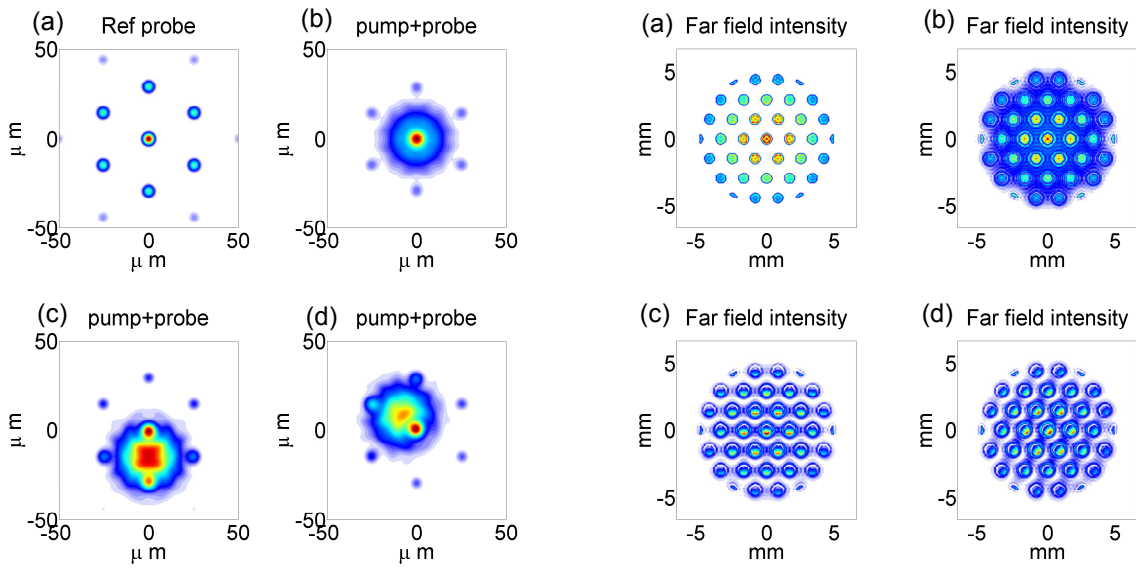


Figure 5.10 – Simulated effect of beam misalignment on reflected far-field intensity of pump-probe for a maximum phase shift  $\pi$  induced by the prepulse. (b)(c)(d) where both beams are superimposed at focus (left captions). Corresponding far fields are obtained by Fourier transform (right captions). (a): reference in case of no prepulse

However, higher-order symmetry breaks have also been observed during plasma expansion as confirmed by our colleagues from CEA Saclay for a configuration matching the separation spacing criterion and where high-order asymmetric patterns are observed on  $\bar{\Sigma}$ , as illustrated with Fig 5.11. Possible causes for this include (i) break of symmetry in the intensity profile of the prepulse from attenuated to full energy (ii) Break in symmetry in the spatio-temporal profile because of uncontrolled spatio-temporal couplings.

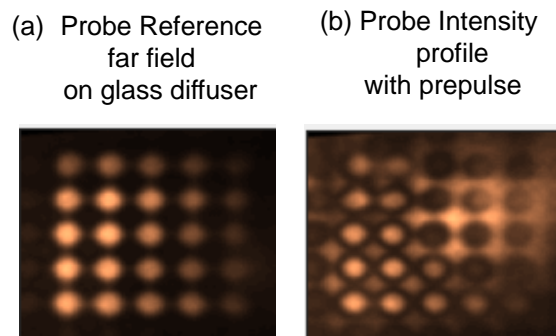


Figure 5.11 – Experimental screen shot obtained by Adrien Denoëud during SDI measurements performed with UHI100 laser at CEA Saclay.

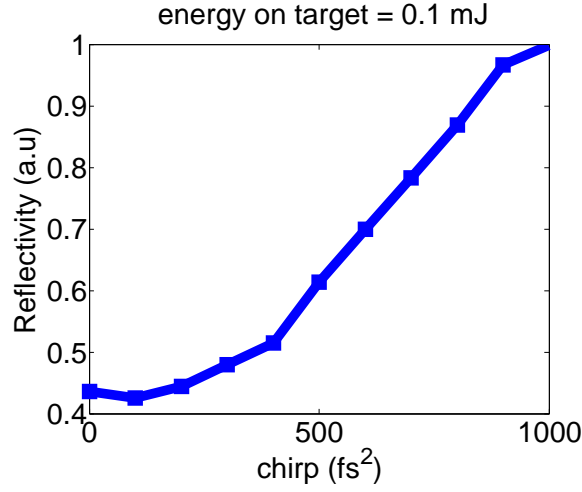


Figure 5.12 – Evolution of the reflectivity as a function of chirp for an energy on target of 0.1mJ. Each data point corresponds to the integration of 50 consecutive shots.

In order to investigate (ii), we measured the change in pulse reflectivity on target in absence of prepulse. The pulse intensity on target is on the order of  $\sim 10^{14}$  W/cm<sup>2</sup>, and its temporal duration is 30 fs. Fig 5.12(b) shows that a chirped pulse exhibits enhanced reflectivity. One possible explanation is that the plasma mirror is triggered sooner when the pulse is chirped. In conclusion, when a compressed prepulse is used to ionize a target prior to an interaction, spatio-temporal couplings (such as inhomogeneous compression) can lead to energy deposition not only dependent on the fluence . As a result, the plasma expansion can lead to high-order asymmetric plasma profiles.

## 5.3 Perspectives for phase retrieval

### 5.3.1 Inversion problem

Let's define what we call an "inversion problem". Suppose that we know the relation:

$$y = f(x) \tag{5.21}$$

where  $x$  is any unknown variable, and  $y$  an "observable". An inversion problem simply consists in retrieving  $x$  when  $y$  is known. For example,  $y$  could be the fluence measured in 2 different planes along the propagation axis of a monochromatic laser beam. In this case,  $f$  refers to Maxwell's equations and  $x$ , the fluence and phase in an arbitrary plane along the same axis of propagation. By measuring  $y$ , one could in principle retrieve  $x$  using an available inversion algorithm like the Gerchberg-Saxton algorithm commonly

employed for this particular problem [134, 135]. One question naturally arises when one is faced with an inversion problem: is it really possible to invert the system. Or, to put in more mathematical terms: is  $f$  injective ?

In our experiment, we measure the far-field intensity  $I$  of the probe pulse, which according to Eq 5.5a takes the form:

$$I = |\mathcal{F}(f)|^2 \quad (5.22)$$

where  $f = \mathcal{F}[E_M]T$ .

**We want to answer the following question:** is it possible to retrieve the complex transfer function  $T$  from  $I$  ?

### 5.3.2 One-dimension retrieval

Without any further constraints, it is quite straightforward that a solution of Eq 5.22 is never unique because  $f = \mathcal{F}^{-1}(Ie^{i\phi})$  is always a solution, for any  $\phi$  we consider. Therefore, the uniqueness can only arise from a constraint imposed on the function  $f$ . For example, a constraint used in optical retrieval [125, 136, 137], where  $f$  is a two-dimensional matrix, is that its rank is equal to one (ie the matrix is the product of a column times a line vector). If enough information is known about the object to be reconstructed from its Fourier modulus to ensure the uniqueness of the solution, a Fienup [138] inversion algorithm, which is described schematically in Fig 5.13, can be used. Every iteration, the reconstruction error  $f$ , calculated using  $f'$  estimate, decreases.

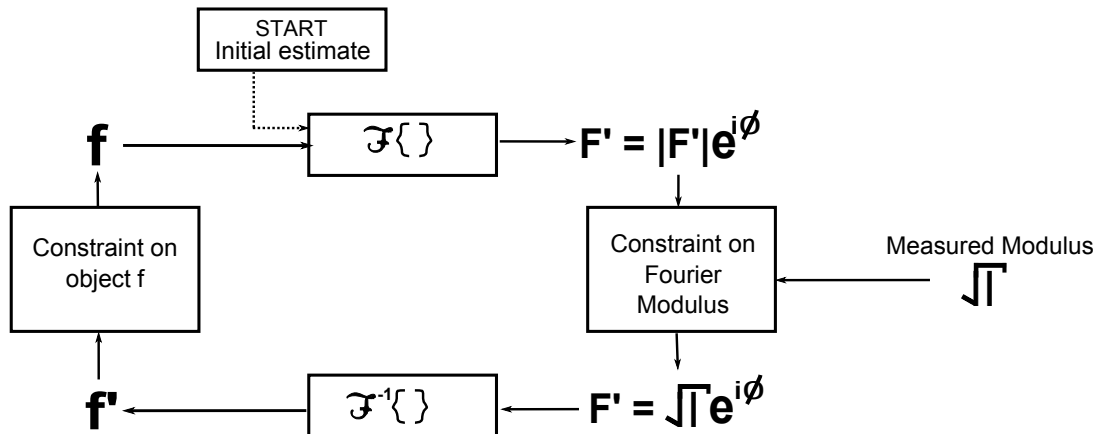


Figure 5.13 – Fienup phase retrieval principle

In case of SDI, supposing the laser beam has a perfectly flat phase prior to focusing, the reference field  $E_{ref}$  is obtained by a Fourier transform of the measured near-field

square root intensity, or by an inverse Fourier transform of the square root intensity of the reflected field when  $T = 1$ . When the plasma starts expanding or modifying the reflectivity over the  $0^{th}$  order  $E_{ref,\sigma} \equiv E_{ref,0}$ , other diffracted orders which we generically label  $E_{ref,\bar{\sigma}}$  remain unchanged as illustrated by Fig 5.14, which represents three spatially separated Gaussian sources, where only the central one is multiplied by an arbitrary transfer function  $T$ , represented in small insert at the top.

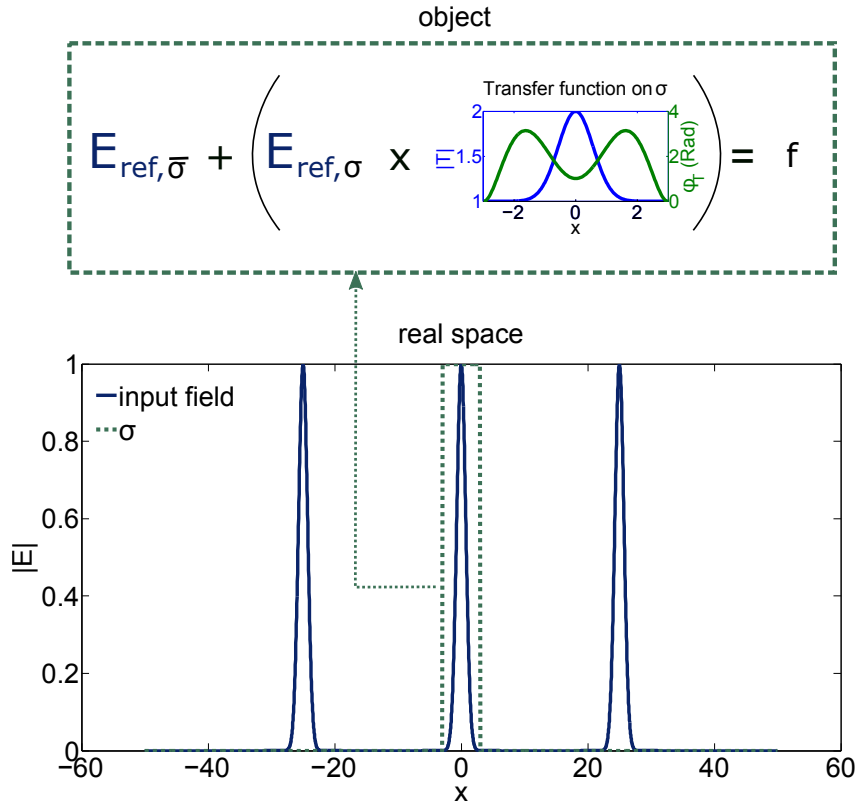


Figure 5.14 – Construction of object  $f$ : The central Gaussian source  $E_{ref,\sigma}$  is multiplied by the plasma complex transfer function  $T$  without affecting the other sources positioned symmetrically around  $x = 0$ , which we define as  $E_{ref,\bar{\sigma}}$

$E_{ref,\bar{\sigma}}$  will be the value of the field we impose in the Fienup-like retrieval algorithm represented in Fig 5.13. In Fig 5.15, we give an example of the results of the retrieval algorithm with three sources after 200 iterations for a complex function  $T$ , where  $|T| = 1$  and  $\phi_T$  polynomial. The object  $f$  is known on  $\bar{\sigma}$ , and we want to retrieve it on  $\sigma$  only. In Fig 5.15(a), we represent both its phase and superimpose the retrieved values after running the Fienup algorithm. In Fig 5.15(b), we represent the Fourier transform modulus of the object and superimpose its retrieved modulus.

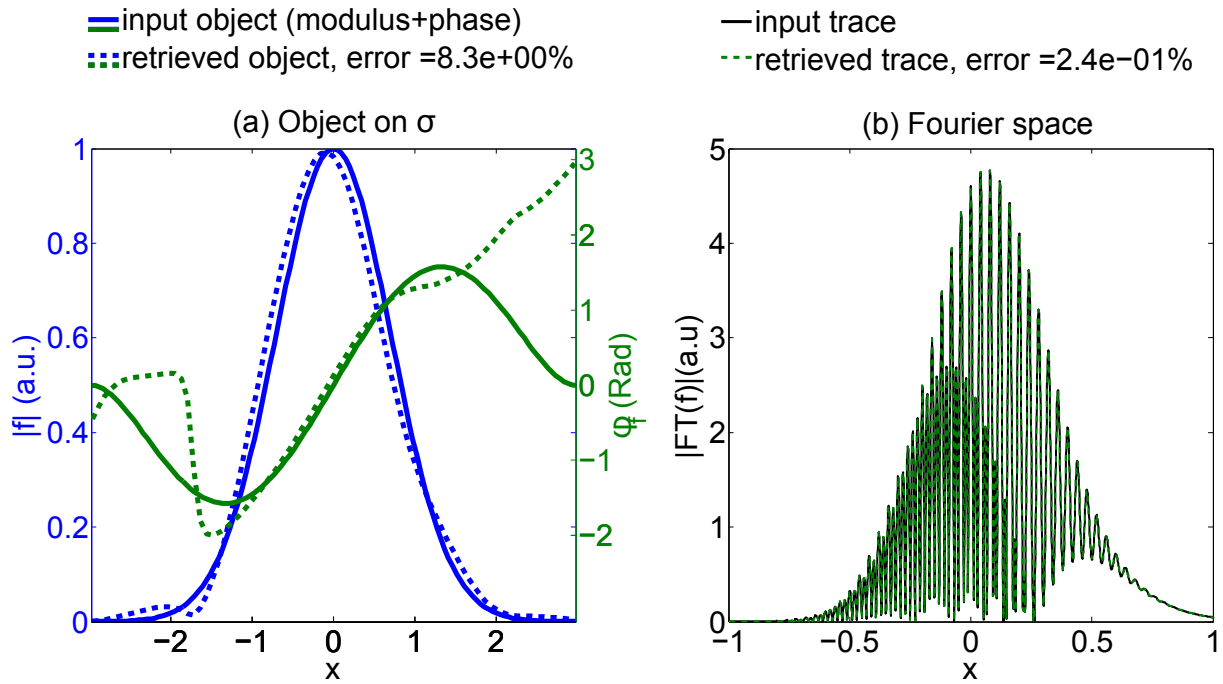


Figure 5.15 – Phase reconstruction (a): initial modulus and phase of object on  $\sigma$  (plain) and reconstructed object using Fienup algorithm (dotted). (b): constraint modulus in Fourier space (black plain) and reconstructed modulus (green dotted) after 200 iterations.

The retrieval error in Fourier domain is defined by the root mean square relation [138]:

$$e = \left( \frac{\sum_x ||F'(x)| - \sqrt{I(x)}|^2}{\sum_x I(x)} \right)^{1/2} \quad (5.23)$$

where  $F'$  is the retrieved Fourier transform and  $\sqrt{I}$  its constraint (measured) modulus. The retrieval error in the object domain on  $\sigma$ :

$$e = \left( \frac{\sum_{x \in \sigma} |f'(x) - f(x)|^2}{\sum_x |f'(x)|^2} \right)^{1/2} \quad (5.24)$$

The employed algorithm is quite robust and always converges (final error in Fourier domain  $e \ll 1$ ) for all the transfer functions  $T$  we imposed. However, the algorithm can converge in the Fourier domain without converging in the object domain. Indeed, two very distinct objects can have the same Fourier transform modulus. In other words, the uniqueness of the inversion problem is not always ensured. This explains why the object error in Fig 5.15(a) is much greater than the Fourier modulus error in Fig 5.15(b).

Phase retrieval has been an active and challenging field of research for over a century. So far, demonstrating the uniqueness of the solution for an arbitrary object support<sup>1</sup> constraint is an open problem. Uniqueness has been demonstrated in restricted cases however:

1. Domain of definition of a function  $f$  where  $f \neq 0$

- For the one-dimensional inversion problem where both the support of  $f$  and  $\mathcal{F}(f)$  are discrete, the uniqueness of the solution (supposing it exists, which is of course always the case experimentally) is ensured [139] with the underlying hypothesis that two solutions  $f_1$  and  $f_2$  verify the relation  $f_1 = af_2(x + b)$  where  $a, b \in \mathbb{R}$  are equivalent.
- The uniqueness of phase for one and two-dimensional inversion problems for a real positive object has been demonstrated [140, 141].
- Holography principle: the object includes a delta function, also called reference point, sufficiently separated from the object to reconstruct [142, 143]. In this case phase reconstruction is possible.

In our case, to address the problem of uniqueness, we run our retrieval algorithm on test functions where  $|T| = 1$  and the phase of  $T$  is taken of polynomial form:

$$P(x) = a_0 + a_1x + a_2x^2 + ..a_6x^6 \quad (5.25)$$

in the seven following cases:

$$\begin{aligned}
(a_0, a_1, a_2, a_3, a_4, a_5, a_6) &= (1, 0, 0, 0, 0, 0, 0) \text{ (case1)} \\
&= (0, 1, 0, 0, 0, 0, 0) \text{ (case2)} \\
&= (0, 0, 1, 0, 0, 0, 0) \text{ (case3)} \\
&= (0, 0, 0, 1, 0, 0, 0) \text{ (case4)} \\
&= (0, 0, 0, 0, 1, 0, 0) \text{ (case5)} \\
&= (0, 0, 0, 0, 0, 1, 0) \text{ (case6)} \\
&= (1, 1, 1, 1, 1, 1, 1) \text{ (case7)}
\end{aligned} \quad (5.26)$$

with a maximum value of  $\pi$ . The corresponding result is given in Fig 5.16. It appears that for cases 3 and 5, uniqueness is not ensured since the retrieved objects are different from the input object. We empirically found it was possible to drastically reduce these discrepancies by breaking the symmetry of the reference field on  $\bar{\sigma}$  with respect to the origin as shown in 5.3.3.

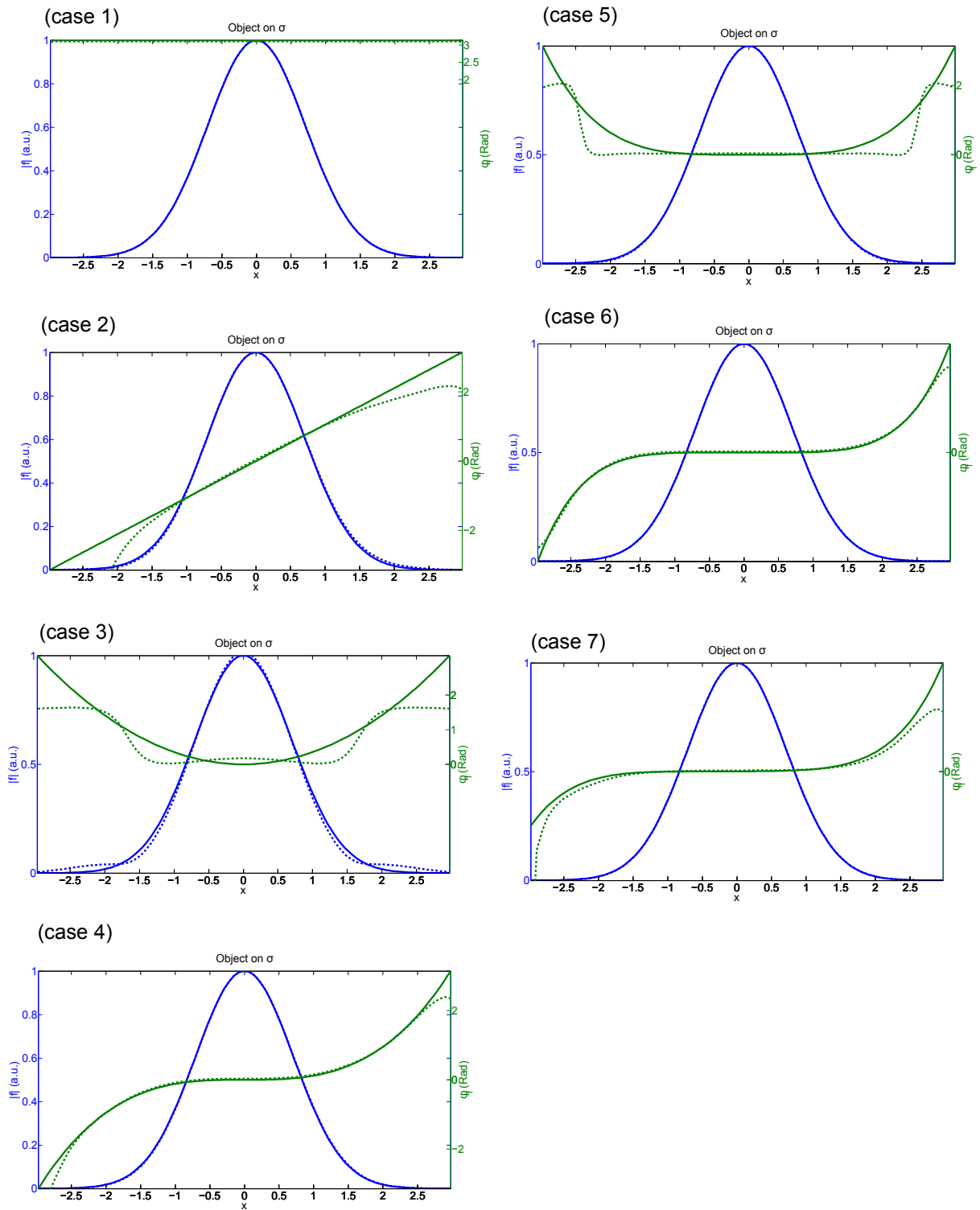


Figure 5.16 – Amplitude and phase reconstructions

### 5.3.3 Modifying the reference probes to break the symmetry

So far, the reference field was constructed using 3 spatial Gaussian functions: one to which we apply the transfer function  $T$  defined on  $\sigma$ , and 2 others, defined on  $\bar{\sigma}$ , symmetrically positioned with respect to the origin as already described in Fig 5.14. Here, we break this symmetry by positioning them at respectively  $x = -30$  and  $x = 25$ , instead of  $x = \pm 25$ . We then run the same retrieval algorithm on the previously defined 7 cases and find the results shown in Fig 5.18 after 200 iterations. The difference is striking: all cases converge to the right solutions in object domain as if uniqueness resulted from this break of symmetry. The residual errors in object domain is plotted in Fig 5.17, where the symmetric and non symmetric case are compared: when the probes are not positioned symmetrically with respect to the object on  $\sigma$ , the final error is reduced by two orders of magnitude.

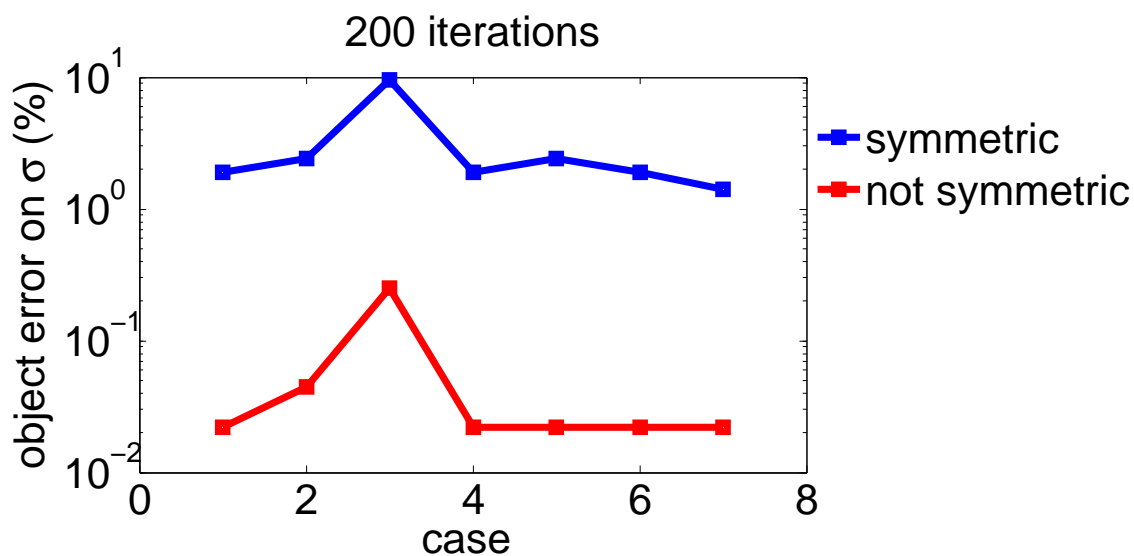


Figure 5.17 – Phase reconstruction error for a symmetric reference field on  $\bar{\sigma}$  (blue) and when this symmetry is broken (red)

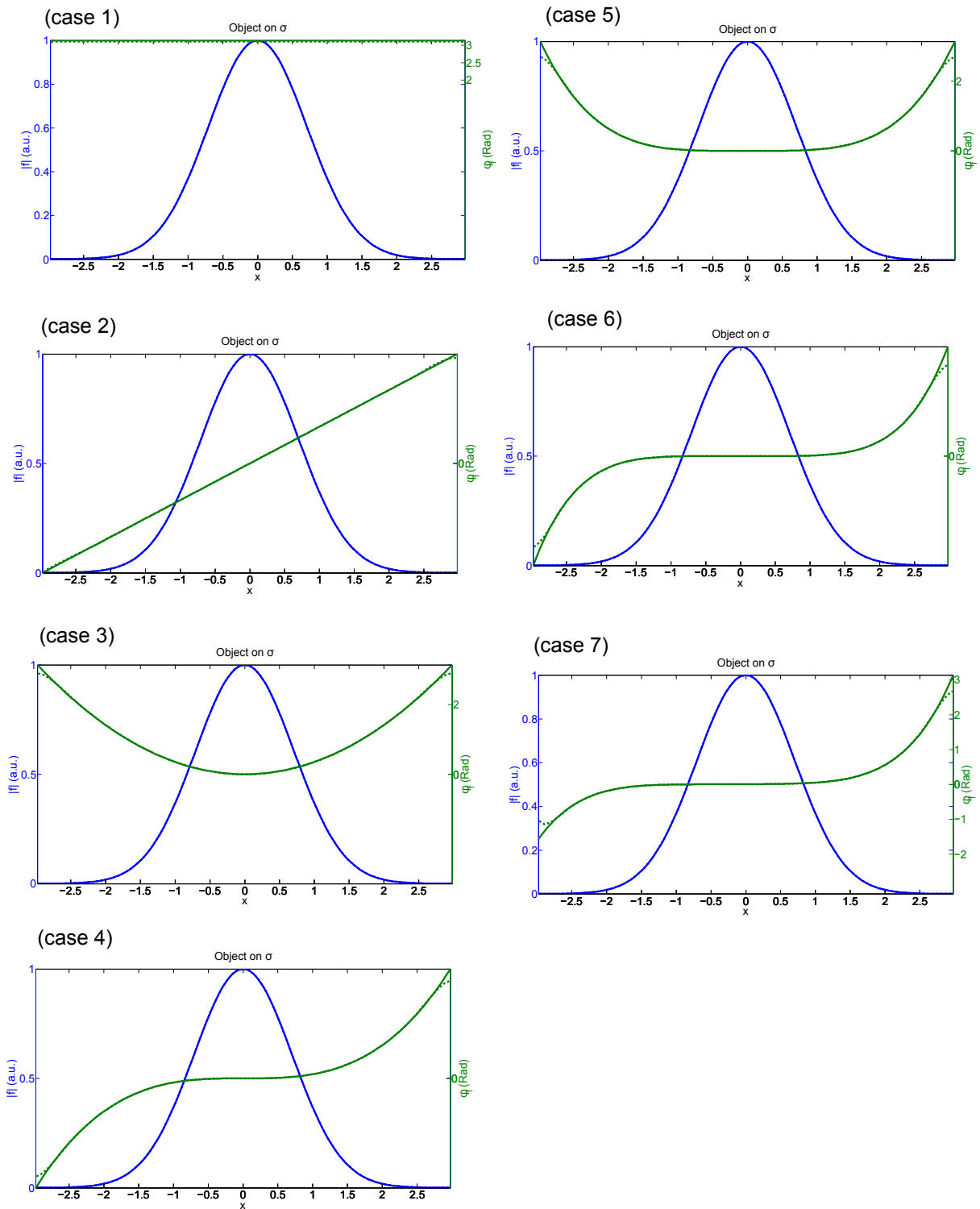


Figure 5.18 – Amplitude and phase reconstructions for non symmetric reference field on  $\bar{\sigma}$

### 5.3.4 Two-dimensional retrieval ambiguities

It is commonly stated that many phase retrieval problems can be solved in two dimensions when often they can't in one dimension. Such statement is the result of several successful empirical reconstructions in 2 dimensions [144–146]. Since the late 70's, algebraic approaches to the problem of phase inversion [147, 148] lead to the understanding of this singular two-dimensional behavior. The principle is simple: let's consider Eq 5.27, where  $S$  is the expression of the discrete Fourier transform modulus of the function  $f$  defined on a rectangle of size  $N \times M$ . One can define the polynomial in Eq 5.28, also known as the corresponding z-transform [149], where  $z$  and  $\eta$  are complex variables:

$$S(k_x, k_y) = \frac{1}{NM} \left| \sum_n \sum_m f(x_n, y_m) \underbrace{e^{-ik_x n dx}}_{z=e^{-ik_x dx}} \underbrace{e^{-ik_y m dy}}_{\eta=e^{-ik_y dy}} \right|^2 \quad (5.27)$$

$$P(z, \eta) = \frac{1}{NM} \sum_n \sum_m f(x_n, y_m) z^n \eta^m \quad (5.28)$$

where  $n$  and  $m$  are integers corresponding to the index in the  $x$  and  $y$  directions respectively. Here, the inversion problem defined in Eq 5.27 is simply equivalent to the factorization of Eq 5.28. In other words, if by measuring  $|P(z, \eta)|$  we can enumerate all its zeros<sup>2</sup>, then  $P$  and therefore  $f$  is known. Many mathematical tools exist to deal with algebraic problems, and they allow to understand the singular difference between one and two-dimensional problems. Indeed, it has been shown [140] that uniqueness emerges from the sufficient (but not necessary) condition that the factorization of Eq 5.28 is not possible. On the one hand, it is always possible in 1D to factorize a polynomial. One understands that in that case, the uniqueness of the inversion problem requires a strong support constraint. On the other hand, the probability of finding non-factorisable solutions increases in 2D [150, 151] which explains why, in general, 2D retrieval algorithms are more robust.

This being said, we ran the SDI reconstruction algorithm presented in section 5.3.1 using simulated 2D traces and found that the reconstruction performance was slightly, but not significantly, increased for the pathological cases presented in 5.3.1 (where the probe is symmetric with respect to the object to reconstruct). However, the counterpart is a quadratic increase in computing time. When the probe is asymmetric, the reconstruction is very good and converges in less iterations, as illustrated with the example given in Fig 5.19. Here, we present the phase object (left) and its 2D reconstruction after 20 iterations (right).

---

2. Roots of the polynomial. For polynomial  $P$  of degree  $N$ , if  $z_i$  for  $i \leq N$  are the roots of  $P$ , then  $P = \alpha \prod_i (z - z_i)$  where  $\alpha \in \mathbb{C}$

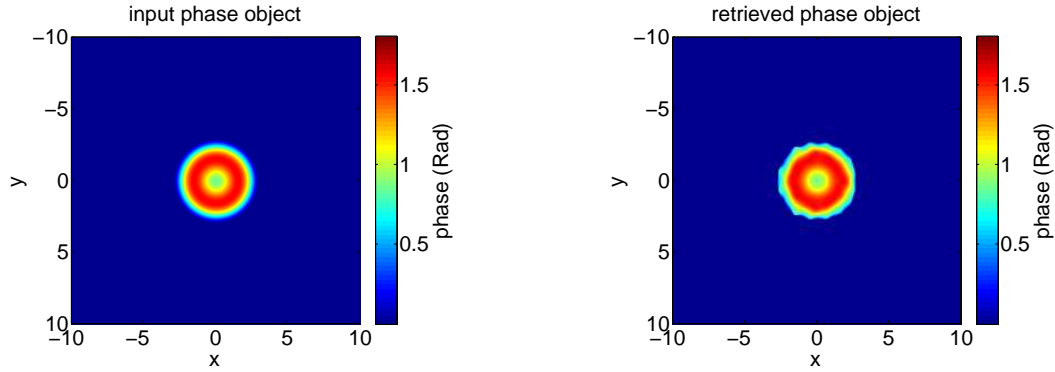


Figure 5.19 – Result of central object phase reconstruction after 20 iterations using non symmetrically distributed sources. The residual reconstruction error measured in the Fourier modulus is  $e = 5 \times 10^{-4}$

## 5.4 Conclusion and perspectives

We have seen how inserting a simple periodic transmission mask in the path of the intense IR probe, we can use the higher order diffraction spot at the focus on target as a reference for a SDI measurement. When plasma expansion is induced by the delayed prepulse, the change in reflectivity and phase of the probe can in principle be fully retrieved using an inversion algorithm. In our experiment, the image quality was not sufficient (limited dynamic range of CCD, diffuser grain size, low signal to noise ratio due to background radiation) to implement such an algorithm. Moreover, we realized after the experiment that breaking the central symmetry in the focusing plane would be an excellent way to increase the retrieval accuracy. One easy solution to do this is to reflect one of the first-order diffraction spots on the plasma rather than on the  $0^{th}$  order. This will be tested in future experiments in order to fully reconstruct the 2D plasma expansion profile from its instant of creation.

# Chapter 6

## Harmonics and electrons from plasma mirrors

### Outline

---

<b>6.1</b>	<b>Review of electron acceleration mechanisms . . . . .</b>	<b>112</b>
6.1.1	Resonant absorption . . . . .	112
6.1.2	Vacuum heating . . . . .	112
6.1.3	$J \times B$ heating . . . . .	113
6.1.4	Laser channel . . . . .	113
6.1.5	Surface plasmon resonance . . . . .	114
6.1.6	Stochastic heating . . . . .	114
6.1.7	Conclusion . . . . .	115
<b>6.2</b>	<b>Simultaneous HHG and electron detection . . . . .</b>	<b>116</b>
6.2.1	Description of the experiment . . . . .	116
6.2.2	CWE/electron anticorrelation vs plasma scale length . . . . .	118
6.2.3	PIC simulations . . . . .	121
<b>6.3</b>	<b>Electron angular emission . . . . .</b>	<b>125</b>
6.3.1	LANEX detection plane: stereographic losses . . . . .	125
6.3.2	LANEX imaging: non isotropic emission losses . . . . .	127
6.3.3	Spatial distribution of ejected electrons . . . . .	131
6.3.4	Gyromagnetic confinement for short gradient scale length . . . . .	136
<b>6.4</b>	<b>Electron spectra . . . . .</b>	<b>139</b>
6.4.1	Electron spectrometer . . . . .	139
6.4.2	Experimental results . . . . .	140
<b>6.5</b>	<b>Conclusion . . . . .</b>	<b>141</b>

---

## 6.1 Review of electron acceleration mechanisms

Electron acceleration mechanisms from solid-density plasma are highly dependent on the plasma scale length, intensity regime and pulse duration. Moreover, the notion of acceleration, or "heating", can designate electrons that remain inside the plasma or manage to "escape" from it. With nanosecond lasers for example, electron heating through inverse Bremsstrahlung due to collisions [152, 153] has to be taken into account to describe the formation of a hot-electrons population inside the plasma. When the plasma expands, the interaction with underdense regions is considerably increased. As a consequence, self modulation of the laser and filamentation appear, making the acceleration mechanism very complex [28]. It would be too ambitious to present an exhaustive list of the electron acceleration schemes based on solid-density targets. We will focus on acceleration schemes involving sub-picosecond to femtosecond laser interactions at relativistic intensities, essentially based on collisionless absorption mechanisms.

Interest for electron acceleration emerged with the need of collimated relativistic electron beams ( $\sim$ MeV) for fast ignition applications [60]. Different acceleration mechanisms have been proposed to account for the production of fast electrons. We will give an overview of the different mechanisms found in the literature, which apply to planar solid targets (rather than cones, specific to fast ignition schemes) and highlight the specific experimental conditions in which they unfold.

### 6.1.1 Resonant absorption

We already described in section 2.1 the principles of resonant absorption. Electron acceleration, or creation of a "hot-electron" population, is due a non-linear process called "plasma wave-breaking" occurring near the critical density [72, 73]. In this model, the local plasma response around the critical density can be viewed, at a given time, as a phase wave which traps electrons and sweep them outwards, just like a surfer would catch a wave. However, this scheme is only valid for relatively long plasma scale length ( $> \lambda$ ).

### 6.1.2 Vacuum heating

The so-called "vacuum heating" mechanism occurs for short plasma scale length ( $L \ll \lambda$ ) as opposed to resonant absorption. As exposed in [154], the term "vacuum heating" is not properly defined in the literature, and therefore two definitions emerge: (i) Vacuum heating is equivalent to the "Brunel mechanism" (detailed description in section 2.2) and designates electrons return to the plasma bulk [61, 62, 155]; (ii) Vacuum heating is here again in reference to the "Brunel mechanism", but this time refers to electrons escaping into vacuum [156, 157].

### 6.1.3 $J \times B$ heating

We talk about  $J \times B$  heating when the magnetic force is comparable to or even dominates the electric force  $\sim e\mathbf{E}$ . This heating mechanism is counter-intuitive at first sight, because of the well known assessment that the magnetic force does not work, since  $\delta W_{j \times B} = (J \times B) \cdot \mathbf{v} dt = 0$ . However, non averaged ponderomotive force (addressed in detail in section 7.1) is equivalent to the creation of  $2\omega_0$  oscillating electric field [158]. As a consequence, electrons undergo oscillations inside the plasma at twice the driving laser frequency [159]. In this mechanism, electrons do not escape the plasma. It is mostly efficient for low sub-critical densities ( $\sim 10n_c$ ) and its efficiency decreases exponentially with electron density [160], which means that it is suitable for very long gradient scale lengths. The experimental evidence of  $j \times B$  electron heating was performed on very long plasmas ( $\sim 40 \mu\text{m}$ ) by collecting the  $2\omega_0$  radiation at the rear of a thin solid target [161].

### 6.1.4 Laser channel

PIC simulations show that self-focusing or filamentation in near-critical plasmas is systematically associated with electron acceleration, up to 10 – 100 MeV for relativistic intensities [63, 64]. A model developed by Pukhov et al [162] confirmed by 3D PIC simulations states that when electrons are confined to a laser channel by quasi-static electromagnetic self-induced fields, they undergo betatron oscillations in the direction of the laser polarization. When the betatron frequency equals that of the driving laser, a resonance occurs, generating electron bunches every laser period. Note that the plasma scale length involved in this mechanism is  $L \sim 30\lambda$  in the direction of propagation  $x$ , at near-critical densities. The betatron frequency is given by the relation [162]:

$$\omega_\beta^2 = (\kappa_E + v_x \kappa_B) / \gamma \quad (6.1)$$

resulting from the equation of motion being integrated for an electron moving in a electric field  $E_y = \kappa_E y$  and a static magnetic field  $B_z = -\kappa_B y$ .

Chen and al. [156] adapted this laser channel scheme to solid-density plasmas of scale length  $L \sim 3\lambda$  and a laser intensity  $a_0 \sim 2$  at grazing incidence  $\theta_L = 70^\circ$  with respect to normal. The formation of quasistatic electromagnetic fields was attributed to the hot current due to  $J \times B$  and vacuum heating. The analytical approach is similar to that of Pukhov et al a resonance occurs between the laser frequency and the betatron oscillations for:

$$\omega_\beta = \omega_0(1 - \sin(\theta_L)) \quad (6.2)$$

where  $\omega_0$  is the laser frequency. This acceleration scheme shows similarities with plasmonic resonance, described hereafter.

### 6.1.5 Surface plasmon resonance

We already saw in section 2.3.1 that a perturbed plasma resonates at the plasma frequency  $\omega_p$  in response to a perturbation of its electron density. A semi-infinite plasma with a step like density profile is a resonator, which means that an emission line at frequency  $\omega_p$  will be observed experimentally in the direction satisfying momentum conservation with the perturbation (photons, electrons for example). Ritchie et al. demonstrated in 1957 [163] that in addition to the bulk response of the vacuum / semi infinite plasma (or metals such as Aluminum or Gold), there exist proper surface modes that can also be excited, and therefore be detected experimentally in the emission spectrum either directly or through couplings with the driving laser, like Fano resonances for instance. These oscillation modes, called plasmons, are a consequence of Maxwell's continuity-equations at an interface between two media of respective permittivity  $\epsilon_m$  and  $\epsilon_d$ . The plasmon wave vector in the plane defined by the interface is given by the relation:

$$k_{SP} = \frac{\omega}{c} \sqrt{\frac{\epsilon_m \epsilon_d}{\epsilon_m + \epsilon_d}} \quad (6.3)$$

Note that the tangential component of the field in both media is implicitly supposed not equal to zero. This means that a laser undergoing perfect reflection on a plane surface does not generate plasmons because  $E_{\parallel}(0^+) = 0$  by symmetry, but a surface with local defects, partially absorbing the light, breaks this symmetry and can give rise to plasmonic effects. In particular, plasmon-photon coupling on metallic coated gratings (where absorption is also possible) have been extensively investigated [164]. Some research groups have demonstrated that it is possible to enhance the magnitude of surface plasmons at an interface by choosing the right incident angle for the driving laser [165].

$$\frac{\omega}{c} \sin(\theta_L) + \frac{n\pi}{d} = k_{SP}(\omega) \quad (6.4)$$

where  $d$  is the grating period,  $\omega$  the laser frequency and  $n \in \mathbb{Z}$  the enhancement order. Experimental evidence of plasmonic enhancement has been achieved with relativistic-intensity fs laser pulses on structured plasma targets to accelerate protons [166] and electrons [165]: particles confined by the plasmonic magnetic field near the surface are accelerated "for a longer time" than in the case a planar surface by the purely electrostatic plasmonic potential. As a result, they gain more energy in the direction defined by vector  $k_{SP}$  (i.e. parallel to the target surface).

### 6.1.6 Stochastic heating

Rigorously, a stochastic system is a system that cannot be described other than through a probability density function on a large number of particles. In the case of electron acceleration, electrons undergo stochastic (or chaotic) motion when they can no

longer be described by well defined orbitals, or in other words, for an arbitrarily small perturbation of their initial position or canonical momentum, their trajectories in time can be radically different.

The observation of stochastic electronic motion in interference fields is a well-known topic. For instance, in the case of two counterpropagating laser pulses (plane waves) [65] the final temperature of the electrons can exceed that predicted by the laser ponderomotive potential in a near critical density plasma medium by a factor close to 5. Other authors have shown multiwave systems could easily lead to suprathermal electrons because of stochastic heating [167]. The mechanism they described is an extension of wakefield acceleration schemes and consists in plotting the orbital solutions of the Hamiltonian corresponding to two counter-propagating lasers. For relativistic intensities, the motion is dominated by stochastic motion and the stable orbits are shifted to higher energy zones.

However, when one drastically reduces the spatial dimensions of the laser focus (strong focusing geometry) and temporal duration (fs laser pulses), the establishment of stochastic heating is no longer possible when (i) the mean propagation length of an electron compares with the laser Rayleigh length and (ii) the establishment of chaos is long relative to the pulse duration. In our solid-target experiment, the interference field is located at the target surface over a distance comparable to the Rayleigh length such that chaotic heating will be negligible.

### 6.1.7 Conclusion

This review of different heating mechanisms shows the high sensitivity of electron acceleration to the plasma scale length and electron density of the plasma. Therefore, in order to study each of these mechanisms in experiments, it is necessary to ensure that there is no uncontrolled preionisation of the target prior to the interaction. At the same time, reaching  $\sim 1$  MeV electron energies and above requires relativistic intensities. This means that the laser contrast should be  $\geq 10^{9-10}$  up to a few picoseconds before the pulse peak to prevent the thermal expansion of the plasma [34], which increases the complexity of the laser system because of the need for efficient contrast cleaning. This explains why most experiments have been conducted at high-intensity and long plasma scale lengths [156, 161, 168–170] or low intensity ( $a_0 < 0.1$ ) and short plasma scale lengths [171, 172]. Very few high-intensity experiments ( $a_0 \sim 1$ ) with gradient control ( $L < \lambda$ ) have been reported [66, 67].

In the following section, we present our experimental results on electron acceleration for very short plasma scale length at near-relativistic intensities. We simultaneously detected high-order harmonic emission in the specular direction of the driving laser to increase our comprehension of the plasma mirror dynamics on sub-femtosecond time scales. We will consider further the important role played by (i) the space-charge field created at the

surface of the plasma during the interaction and (ii) address the interaction of electrons with the reflecting laser in vacuum in Chapter 7.

## 6.2 Simultaneous HHG and electron detection

### 6.2.1 Description of the experiment

In our experiment, we simultaneously detect high-order harmonics and the electrons generated on our plasma mirror as a function of the gradient scale length. Our laser pulse is focused on the fused silica rotating target by means of a f/1.2 off axis parabola. The focal spot is  $1.7\ \mu\text{m}$  at FWHM and the intensity  $\sim 10^{17-18}\ \text{W}/\text{cm}^2$  ( $0.2 \leq a_0 \leq 1$ ). A few percents of the main pulse energy is picked off using a beam splitter and focused on target using the same parabola, with an intensity of  $\sim 10^{14}\ \text{W}/\text{cm}^2$  and a focal spot 5 times greater, to ensure homogeneous plasma conditions. The laser characteristics on target are detailed in Chapter 3.

**HHG detection:** Already described in 4.1.1. The harmonics of the laser are detected in the specular direction with a concave grating positioned behind a vertical slit. The beam is diffracted in the optical plane only and keeps diverging in the other direction. The resulting signal is detected on an MCP.

**Electron detection:** Ballistic electrons are detected using a fluorescent screen called "LANEX" emitting at 546 nm, corresponding to phosphor emission. The detection efficiency is shown in Fig 6.2: only electron of energy  $> 150\ \text{keV}$  are detected. The  $6 \times 17\ \text{cm}$  LANEX screen is positioned 10 cm parallel to the target without blocking the HHG entrance slit. The angular electron emission profile in this geometry is recorded as a function of  $\theta \in [-20^\circ ; 35^\circ]$ , the angle to normal in the azimuthal plane of incidence and  $\phi \in [-20^\circ ; 20^\circ]$ , the angle being defined in the tangential plane.

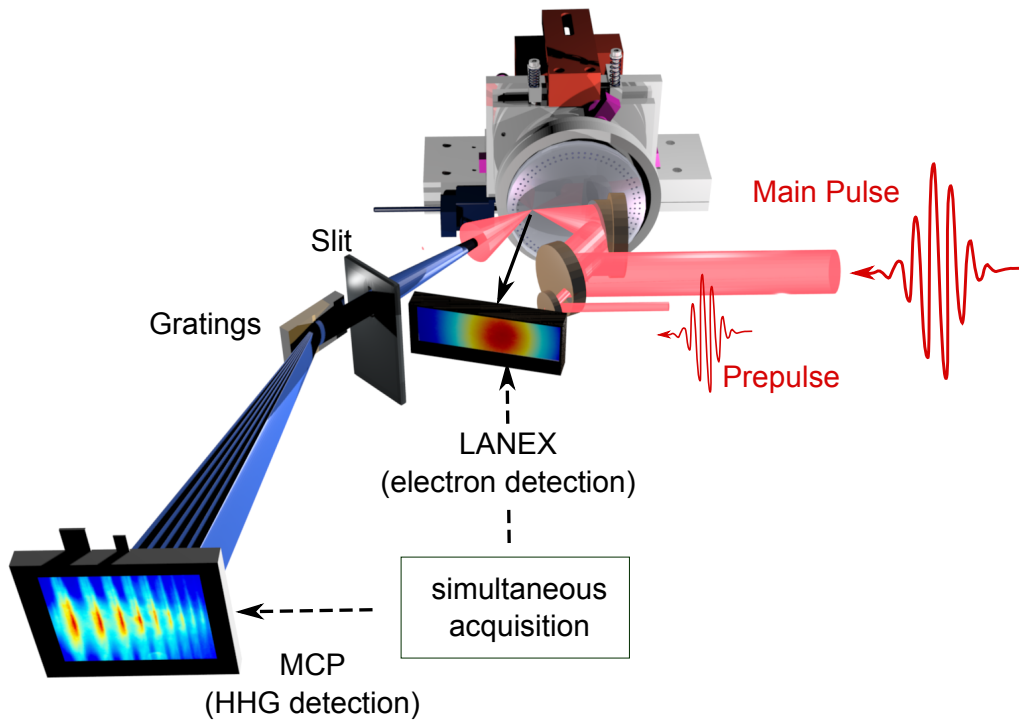


Figure 6.1 – Experimental setup: Main pulse and prepulse are focused on a rotating fused silica target with an off-axis parabola. The HHG signal is detected in the specular direction and the electronic emission with a LANEX screen placed normal to the target. Both signals are recorded simultaneously for each firing sequence (integration over  $\sim 100$  laser shots). Prepulse intensity on target:  $\sim 10^{14}$  W/cm<sup>2</sup>, Main laser intensity on target  $\sim 10^{18}$  W/cm<sup>2</sup>.

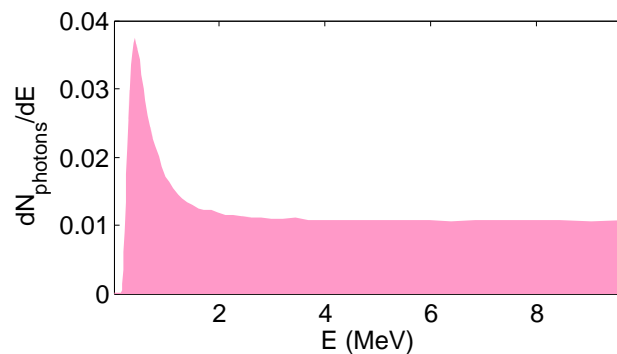


Figure 6.2 – LANEX response based on Monte Carlo simulations [173]

## 6.2.2 CWE/electron anticorrelation vs plasma scale length

By varying the plasma scale length from arbitrarily small values  $L \sim \lambda/100$  to  $L \sim \lambda$  using the pump-probe delay, we observe that the emission of harmonics and electrons is anticorrelated: CWE emission is efficient at short plasma scale length  $L < 0.05\lambda$ , while electron ejection from the target is optimal for longer gradients  $L \sim 0.1\lambda$ .

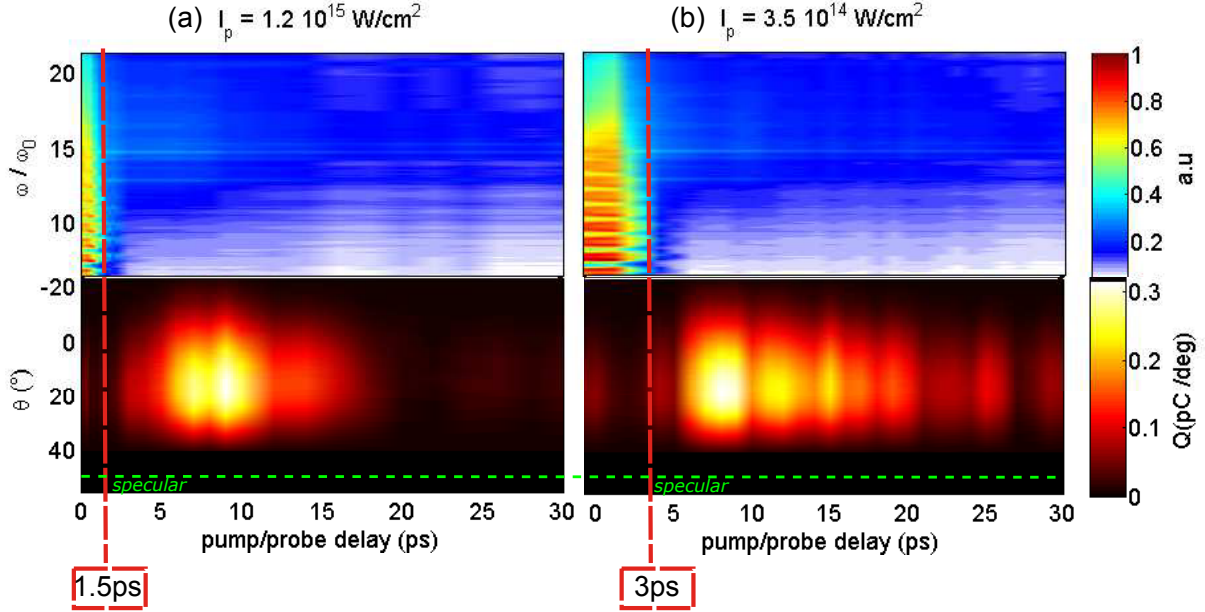


Figure 6.3 – Experimental results comparing simultaneous harmonic and electron emission for a prepulse (pump) intensity of (a)  $I_p = 1.2 \times 10^{15} \text{ W/cm}^2$  and (b)  $I_p = 3.5 \times 10^{14} \text{ W/cm}^2$ . In both cases, the main (probe) laser intensity is  $a_0 = 0.85$ . The LANEX detection range in the horizontal plane is  $\theta \in [-20^\circ \ 35^\circ]$ . The azimuthal spread was artificially extended to show the specular angle of  $49.3^\circ$  indicated by the green dotted line

Experimental results are gathered in Fig 6.3. The harmonic spectra are integrated along the divergence angle and the LANEX signal along its tangential coordinate  $\phi$ . As a result, we present the evolution of the harmonic intensity and the angular electron distribution as a function of the pump-probe delay, for two different prepulse intensities namely (a)  $I_p = 1.2 \times 10^{15} \text{ W/cm}^2$  and (b)  $I_p = 3.5 \times 10^{14} \text{ W/cm}^2$ . In both cases, the anticorrelation pattern is the same: as we increase the pump-probe delay, the harmonic signal drops and we observe a rise of the electron emission signal on the LANEX. The sharp drop in harmonic generation is marked on Fig 6.3 by a vertical red dotted line. Harmonics disappear for (a)  $t \approx 1.5 \text{ ps}$  or (b)  $t \approx 3 \text{ ps}$  depending on the prepulse intensity, for the same main pulse intensity  $a_0 = 0.85$ . This is consistent with an increased expansion velocity of the plasma  $\propto \sqrt{I_p}$ , which predicts that the plasma expands  $\sim 1.8$  times faster in (a) than in (b). The optimal delay for electron generation is not very well defined in 6.3, but rather spans over several gradient lengths. The optimal value in (b)

is reached for  $t \approx 8$  ps, which corresponds to  $L \sim 0.1\lambda$ . However, for long pump-probe delays, the electron emission drops after a delay again consistent from (a) to (b), if we account for a variation of the expansion velocity  $\propto \sqrt{I_p}$ .

### Why this anticorrelation?

We already answered half of this question in Section 2.3 when we explained that CWE mechanism is only efficient at short gradient scale length. For electrons to escape the plasma into vacuum, they need to gain sufficient energy in the space-charge field created at the surface to escape Brunel's confined orbitals [174,175], which is why  $L$  needs to be increased.

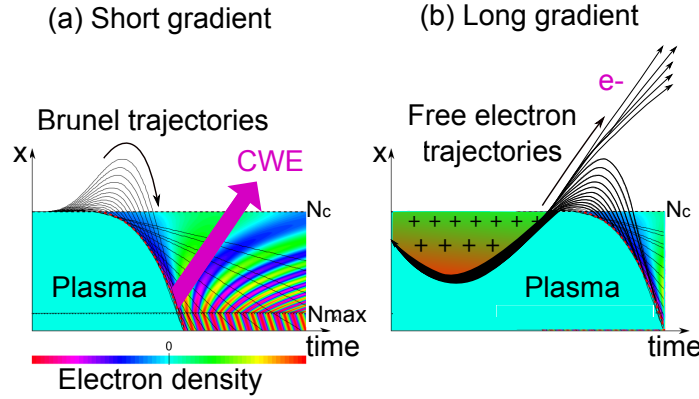


Figure 6.4 – Artistic representation of HHG/electron anticorrelated behavior of plasma mirrors. (a) Efficient CWE generation for  $L/\lambda < 0.05$   
(b) Efficient electron ejection for  $L/\lambda \sim 0.1$

As we already described in Section 2.2, the plasma field  $E_P(x)$  due to charge separation at the surface is simply evaluated using an exponential profile:

$$E_P(x) = \frac{1}{\epsilon_0} \int_x^\infty e n_c e^{-(x'-x_c)/L} dx' = \frac{m_e}{e} \omega_0^2 L \exp\left(-\frac{x-x_c}{L}\right) \quad (6.5)$$

where  $x_c$  denotes the critical surface coordinate with density  $n_c$ , and  $L$  the gradient scale length. If in addition we impose that the plasma field completely screens the laser when all electrons are pushed below  $x < x_s$ , then we have:

$$a_0 c = \omega_0 L \exp\left(-\frac{x_s - x_c}{L}\right) \quad (6.6)$$

We calculate, for this fixed value of  $x_s$  the work provided by the plasma using Eq 6.5:

$$\begin{aligned} W(E_P) &= \int_{x_s}^\infty -e E_P(x) dx = m_e \omega_0^2 L^2 \exp\left(-\frac{x_s - x_c}{L}\right) \\ &= 2\pi (m_e c^2) a_0 \frac{L}{\lambda_0} \end{aligned}$$

This gives us a scaling for the electron final energy when the plasma contribution only is considered:

$$W(E_P)(\text{keV}) = 3.2 \times 10^3 a_0 \frac{L}{\lambda_0} \quad (6.7)$$

This simple scaling will of course only be accurate for very short plasma scale length. For  $L > \lambda$ , the laser propagates in the underdense region and the hypotheses made to derive the scaling are no longer valid. For  $L/\lambda < 1$  and  $a_0 \sim 0.8$  we have  $W(E_P) < 500$  keV, which is consistent with the experimental data later presented in 6.4.

Finally, comparing the two scaling laws obtained respectively for the laser and the plasma, we can write that the plasma becomes "more efficient" in accelerating the electrons when:

$$L/\lambda > a_0/6.4$$

In Fig 6.5, we show how the anticorrelated behavior can be used to track the position of the focus at high-energy. Indeed, thermal effects in the laser chain can lead to few-micron defocusing of the laser on target, even when only reflective optics are used. A high-intensity diagnostic of the focus position therefore becomes very useful. Removing the prepulse, we degraded the laser contrast by misaligning the Glan polarizer after the XPW(cf Chapter 3), which leads to consequent preionisation of the target. We observe the signal obtained for both HHG and electrons when scanning the focal spot. Indeed, if we compare two scans at low ( $a_0 = 0.25$ ) and high ( $a_0 = 0.4$ ) intensity, we find that again, in both cases HHG and electron emission are anticorrelated but in the high-energy case, the electron emission decreases at focus because the contrast is so poor. Defocusing the laser in both directions allows to recover the signal. Note that this scan constitutes a good test to probe the quality of the laser contrast at full energy.

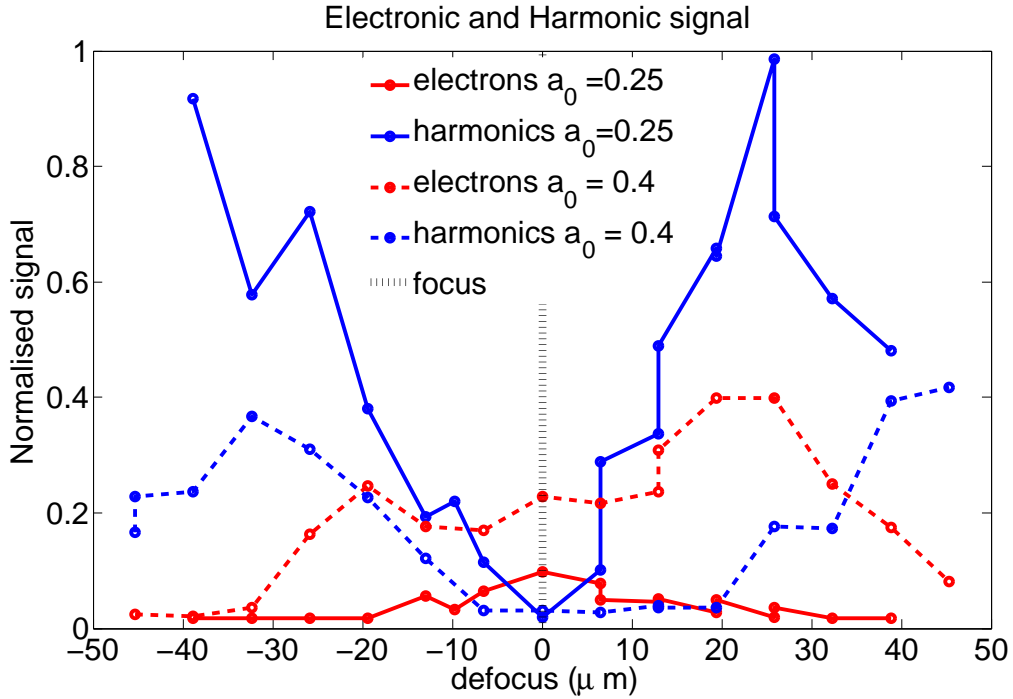


Figure 6.5 – Integrated counts on MCP and LANEX measuring respectively the harmonic and electron generation efficiencies with respect to focus position in  $\mu\text{m}$ . The focal spot size is  $3.5 \mu\text{m}$  FWHM.

### 6.2.3 PIC simulations

We performed 2D simulations using the particle-in-cell simulation code EPOCH [176] in order to demonstrate the anticorrelated behavior of electron ejection and harmonic generation. We first performed simulations close to our experimental conditions and listed the inputs in table 6.1 for the **Scan-a0-0.8** simulation run.

Table 6.1 – EPOCH input

name	$\theta_i$	$\lambda$	$a_0$	$\tau_{fwhm}$	$n/n_c$	$L_g$	$w_0$
<b>Scan-a0-0.8</b>	$45^\circ$	$0.8 \mu\text{m}$	0.8	30 fs	250	$\lambda/80 \rightarrow \lambda/2.5$	$1.8\lambda$
<b>Scan-a0-0.4</b>	$45^\circ$	$0.8 \mu\text{m}$	0.4	30 fs	250	$\lambda/80 \rightarrow \lambda/2.5$	$3.6\lambda$

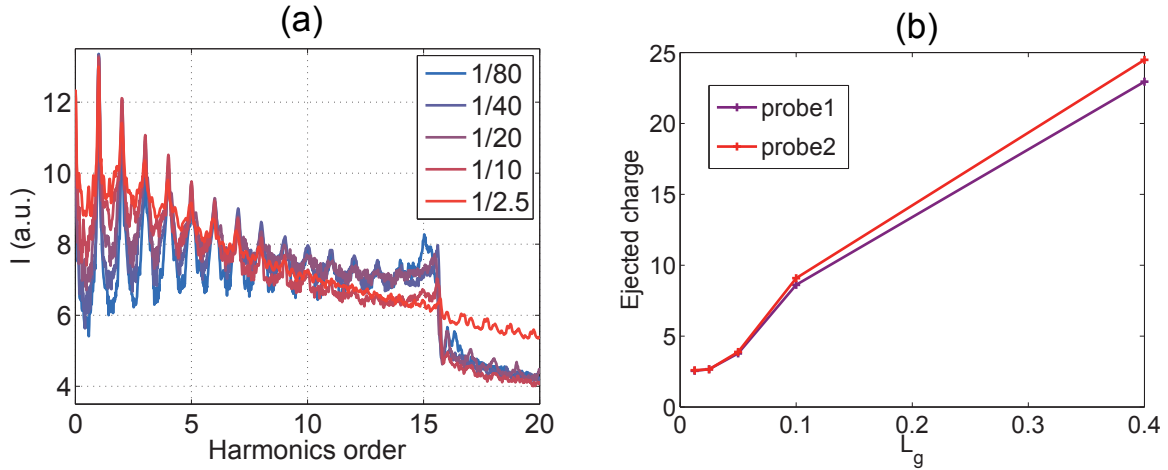


Figure 6.6 – **Scan-a0-0.8** simulations. (a) HHG emission spectrum in log scale for initial plasma scale length  $L_g/\lambda \in [1/80 \ 1/2.5]$  (b) Ejected charge in  $\text{pC}/\mu\text{m}$  for respectively  $8\lambda$  (probe 2) and  $9\lambda$ (probe1) from plasma edge ( $n_c/5$ )

The harmonic emission spectra for different gradient scale lengths is represented in Fig 6.6. The clear cut-off at  $\omega/\omega_0 = \sqrt{250} \approx 15$  is the signature of CWE emission [76,79]. For  $L = \lambda/2.5$ , this cut-off disappears as a signature of ROM emission [51,79]. Simultaneously, the ejected charge is detected with two probes placed at respectively  $8\lambda$  and  $9\lambda$  from the plasma edge (defined at  $n_c/5$ ) and plotted in Fig 6.6(b). We observe that long plasma scale lengths favour electron ejection. This simulation confirms the anticorrelation behavior between HHG generation and electron acceleration observed in our experiment. However, to make sure that this conclusion still holds true when harmonics are generated in a purely CWE regime, we performed a second run of simulations **Scan-a0-0.4** decreasing the laser intensity to  $a_0 = 0.4$ .

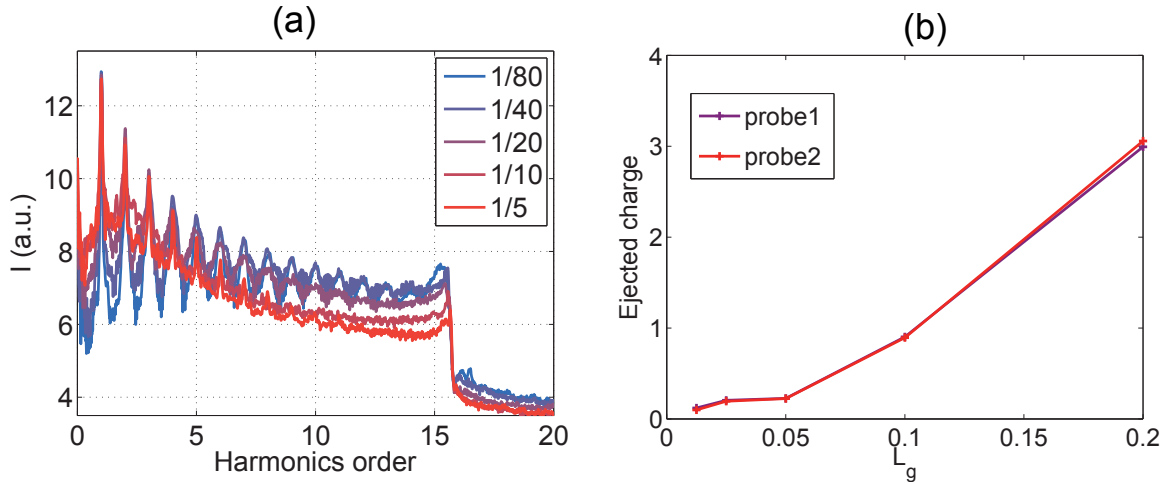


Figure 6.7 – **Scan-a0-0.4** simulations. (a) HHG emission spectrum in log scale for initial plasma scale length  $L_g/\lambda \in [1/80 \ 1/5]$  (b) Ejected charge in pC/ $\mu\text{m}$  for respectively  $8\lambda$  (probe 1) and  $9\lambda$ (probe2) from plasma edge ( $n_c/5$ )

The results are given in Fig 6.7. The CWE cut-off is visible for all gradient scale lengths, which confirms that we are in a purely CWE-emission regime, similar to the experiment. The two simulation runs are compared in Fig 6.8 in order to highlight the anticorrelated CWE/electron emission seen in Fig 6.5.

To observe an "optimal" gradient length for electron ejection, we would need to make simulations for much larger  $L_g$  values than what is presented in Fig 6.8(a). The total number of macro-particles in the simulation increases dramatically with  $L_g$  (565 million for  $L_g = 0.1\lambda$  and 928 million for  $L_g = 0.2\lambda$ ), essentially because modeling HHG requires a very small spatial mesh. For this reason, we only performed two extra simulations for  $L_g = 0.6\lambda$  and  $L_g = \lambda$ , as shown in Fig 6.9. One can clearly see that the ejected charge finally decreases for very long gradients. This optimum can be located anywhere between  $0.2\lambda$  to  $\lambda$ , but a detailed investigation of its location is extremely time consuming and would anyway be more accurate with 3D simulations to account for the  $1/r^2$  decrease of the space charge field from the plasma surface.

Electrons are mostly ejected between  $0^\circ$  (target normal) and  $45^\circ$ (specular). In the experimental data presented in Fig 6.5, the average angle of emission for the optimal gradient scale length is  $\sim 16^\circ$ , whereas its value is closer to  $30^\circ$  in our simulations. This apparent discrepancy is actually due to a loss of signal when positioning the LANEX normal to the target. We see in the following that not only, when the LANEX is placed orthogonal to the specular direction, the measurement matches the simulation, but we also observe a hole in the electron angular emission profile typical of ponderomotive interaction of the electron with the reflected laser.

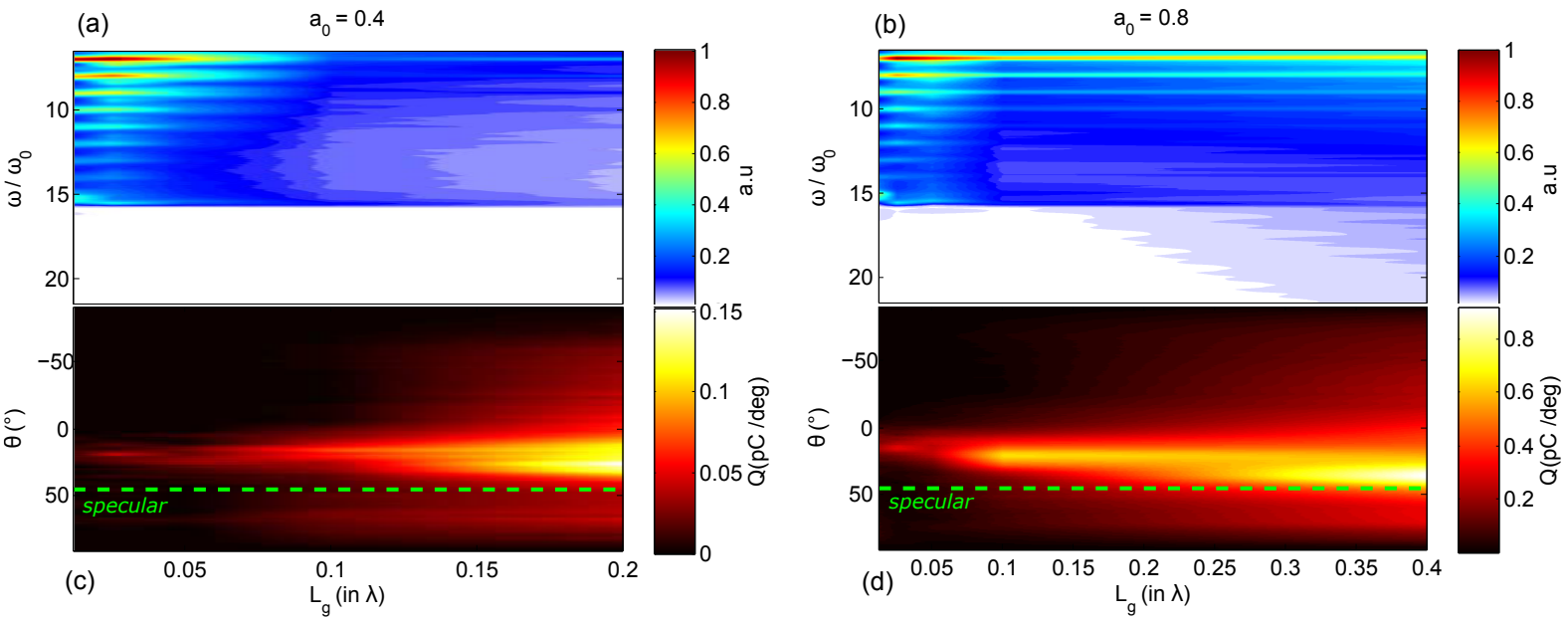


Figure 6.8 – 2D PIC simulation using the simulation code EPOCH comparing the  $a_0 = 0.4$  and  $a_0 = 0.8$  simulation cases. (a) and (b) HHG spectral emission integrated along its divergence as a function of initial plasma scale length. (c) and (d): electron angular emission as a function of plasma scale length. The laser specular direction at  $45^\circ$  is indicated by the dotted green line.

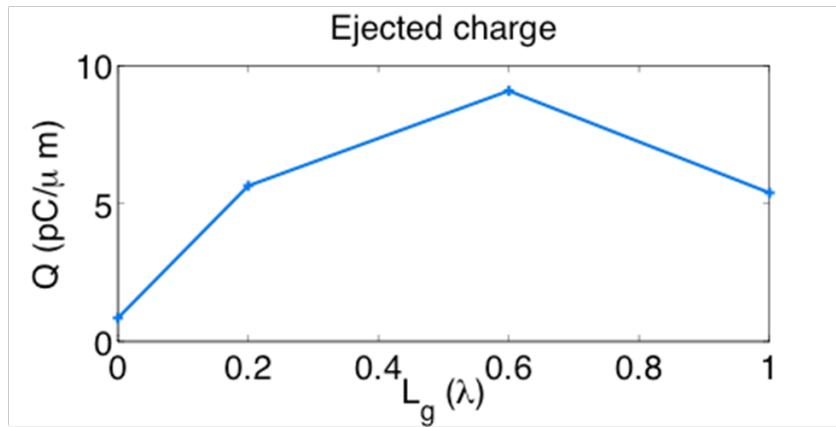


Figure 6.9 – Ejected charge retrieved from 2D PIC simulations for density of  $250n_c$  and  $a_0 = 0.4$  as function of gradient scale length  $L_g$

## 6.3 Electron angular emission

### 6.3.1 LANEX detection plane: stereographic losses

The LANEX geometry is an important factor to consider for the deconvolution of the measured electron beam profile. We detect electrons coming from the focal spot we defined by the point  $(x, y, z) = (0, 0, 0)$ , after ballistic propagation. We define by  $(x, y, z)$  a point of the LANEX detection plane  $\mathcal{L}$  and express it in spherical coordinates:

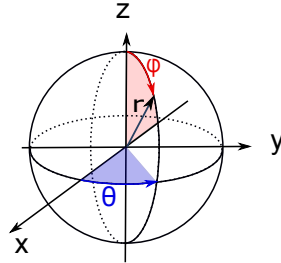
$$\begin{cases} x = r \cos(\theta) \sin(\phi) \\ y = r \sin(\theta) \sin(\phi) \\ z = r \cos(\phi) \end{cases} \quad (6.8)$$

For the hemisphere  $\theta \in [0, \pi]$ ,  $\phi \in [0, \pi]$  as represented in Fig 6.10

The LANEX plane ( $\mathcal{L}$ ) equation is:

$$y = ax + b \quad (6.9)$$

(a) Spherical parametrization



(b) Top view

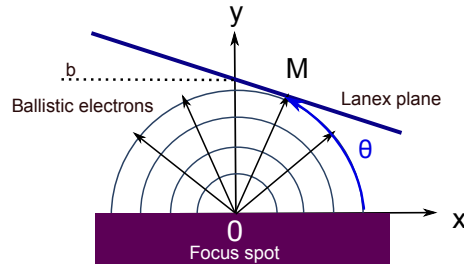


Figure 6.10 – (a) Spherical parametrization of the coordinates (b) Top view

If we consider a point  $M \in \mathcal{L}$ , it will verify Eq 6.9 such that only two parameters are necessary, namely  $(x, z)$  or  $(\theta, \phi)$ , to define its position. One can easily verify by eliminating  $r$  from Eq 6.8, that they are related by the equation:

$$\begin{cases} x = \frac{b}{\tan(\theta) - a} \\ z = \frac{b}{\tan(\phi)(\sin(\theta) - a \cos(\theta))} \end{cases} \quad (6.10)$$

Being careful that  $\theta \in [0, \arctan(a)[$  if  $a > 0$  or  $\theta \in [0, \pi + \arctan(a)[$  if  $a < 0$  (our conditions) and  $\phi \in ]0, \pi[$ . The signal is detected experimentally on the LANEX, however, it is the angular distribution information we are interested in. In order to derive its expression, we can write the conservation of the number  $N$  of ejected electrons when switching from Cartesian to spherical coordinates:

$$N = \underbrace{\iint_{\mathcal{L}} n_{xz}(x, z) dx dz}_{n_{xy}[\text{cm}^{-2}]} = \underbrace{\iint_{\theta, \phi} n_{\theta\phi}(\theta, \phi) \sin(\phi) d\theta d\phi}_{n_{\theta\phi}[\text{sRad}]} \quad (6.11)$$

Using 6.10, we calculate the Jacobian matrix relative to the change of coordinates:

$$J = \begin{pmatrix} \frac{-b}{(\sin \theta - a \cos \theta)^2} & 0 \\ \partial_{\theta}[z(\theta, \phi)] & \frac{-b}{(\sin(\theta) - a \cos(\theta)) \sin(\phi)^2} \end{pmatrix} \quad (6.12)$$

With the relation  $n_{xz} |\det J| = \sin(\phi) n_{\theta\phi}$  where "det" is the determinant of  $J$ . We finally have:

$$n_{\theta\phi} = n_{xz} \frac{b^2}{\sin(\phi)^3 |\sin(\theta) - a \cos(\theta)|^3} \quad (6.13)$$

Fig 6.11 illustrates the geometrical projection effect on the signal recorded using the example of an isotropic emission from the target detected on a plane screen. The projected distribution is not uniform because its density increases at closer distances to the point source. Therefore, the angle of the LANEX relative to the target normal can artificially shift the measured distribution, as shown in the two image projections for a LANEX plane positioned at respectively  $0^\circ$  (left) and  $45^\circ$  (right) to target normal:

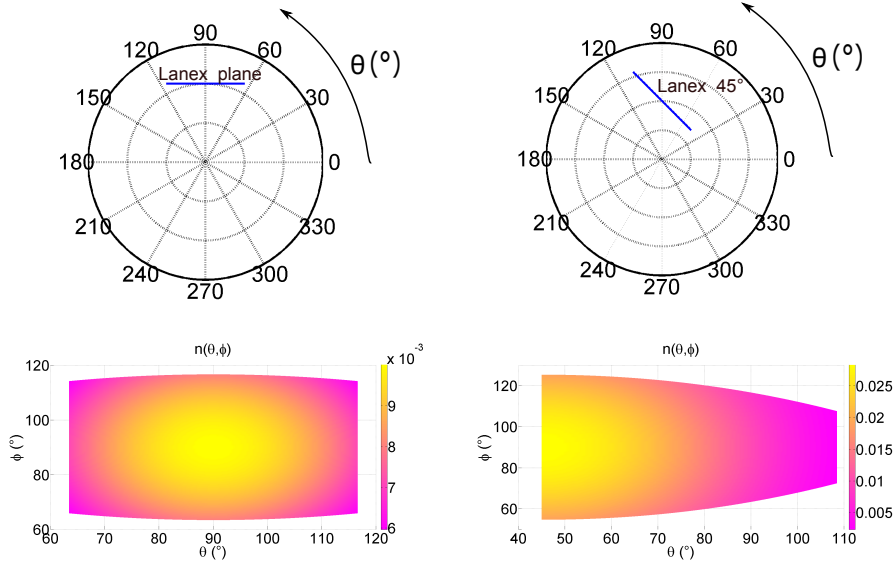


Figure 6.11 – Projection on the LANEX plane  $\mathcal{L}$  of an isotropic ballistic emission for respectively  $\mathcal{L} : y = -10$  (bottom left) and  $\mathcal{L} : y = -x - 10$  (bottom right)

It is therefore important to accurately measure the LANEX position  $\mathcal{L}$  for proper signal deconvolution. However, this effect is of second order relative to the non-isotropic emission of the LANEX presented in the following paragraph.

### 6.3.2 LANEX imaging: non isotropic emission losses

An other element to take into account in the electron signal deconvolution is the anisotropic emission of the LANEX which is known to be Lambertian, that is to say  $\propto \cos(\alpha)$  [173], where  $\alpha$  is the angle to the normal direction. This means that the LANEX fluorescence reaching the camera objective at high incident angles is hardly detected. To calibrate this response  $R$ , we translated the camera along the plane  $\mathcal{L}$  defined by the LANEX and recorded the signal intensity distribution, shown in Fig 6.12(c). For each position, the integrated signal on camera is given by Eq 6.14:

$$S_{\text{CCD}}(x) = R(x)S(x - \Delta x) \quad (6.14)$$

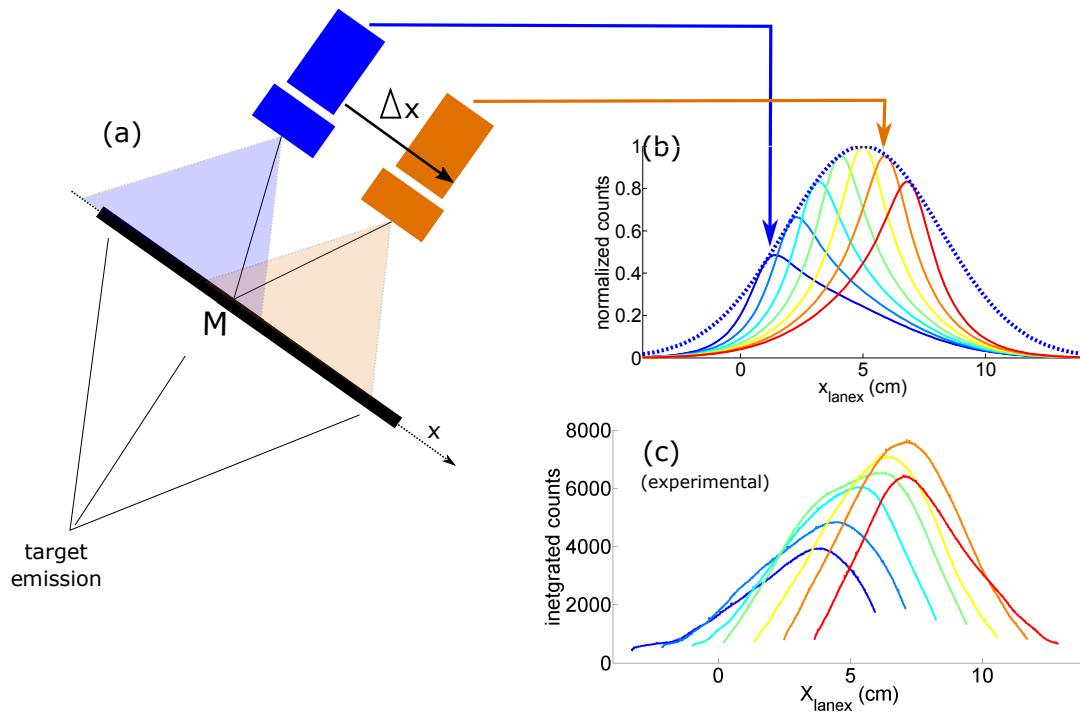


Figure 6.12 – (a) Layout of the experiment: the electron signal is recorded along a given plane for different positions of the CCD (illustrated by blue and orange colors). (b) Simulation of the effect due to LANEX Lambertian emission. A Gaussian distribution is represented by the dotted line. Each successive color lines correspond to this signal intensity for a displacement of  $\Delta x$ . Each color corresponds to a displacement of 1cm. (c) Experimental results obtained by translating the LANEX along  $\mathcal{L} : y = -0.46x + 10(\text{cm})$  as a comparison. CCD counts are integrated in the vertical direction.

where  $S$  is the electron signal on the LANEX,  $R$  the response due to anisotropic emission and  $\Delta x$  is the value to which the camera has been translated. For a given displacement  $\Delta x$ , the maximum signal  $S_{\text{CCD}}$  is obtained when two conditions are met: (i)  $S(x - \Delta x)$  is maximal and (ii) the LANEX response is maximal  $R(x) = 1$ . This can be visualized in Fig 6.12. As a consequence, the curve represented by  $S$  will always be tangent to the measurement  $S_{\text{CCD}}$  every time  $R = 1$ . We use this property to sample the signal at 7 different positions. Moreover, we consider that the measured signal gives us no information when it is just within the background noise. The result of the LANEX response reconstruction is given in Fig 6.13. We find that the LANEX response can be fitted with a polynomial function of fourth order centered around the optical axis of the imaging system. The deviation from a Lambertian emission profile is certainly due to the convolution with the imaging objective of the camera.

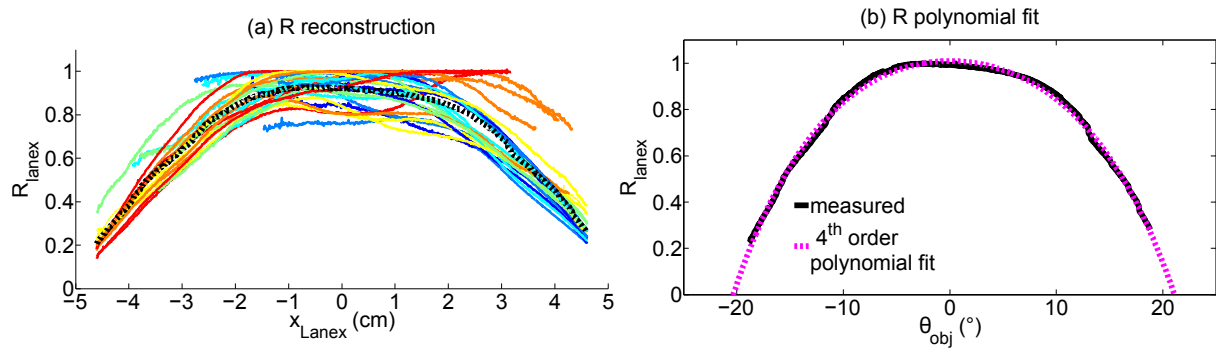


Figure 6.13 – (a) R reconstruction: average over 20 sequences of 100 shots each (b) Corresponding polynomial fit of LANEX response as a function of incident angle on camera objective

### Consequences:

We already mentioned the discrepancies between the electron average angle of emission in experiment and simulations when the LANEX is normal to the target. We just described how geometrical projections and non-isotropic emission are responsible for signal losses. Deconvolution of a signal within the camera noise limit does not make sense, which is why we say the signal is "lost". We illustrate this effect by recording the electron profile when the LANEX is placed normal to the specular direction in Fig 6.14.

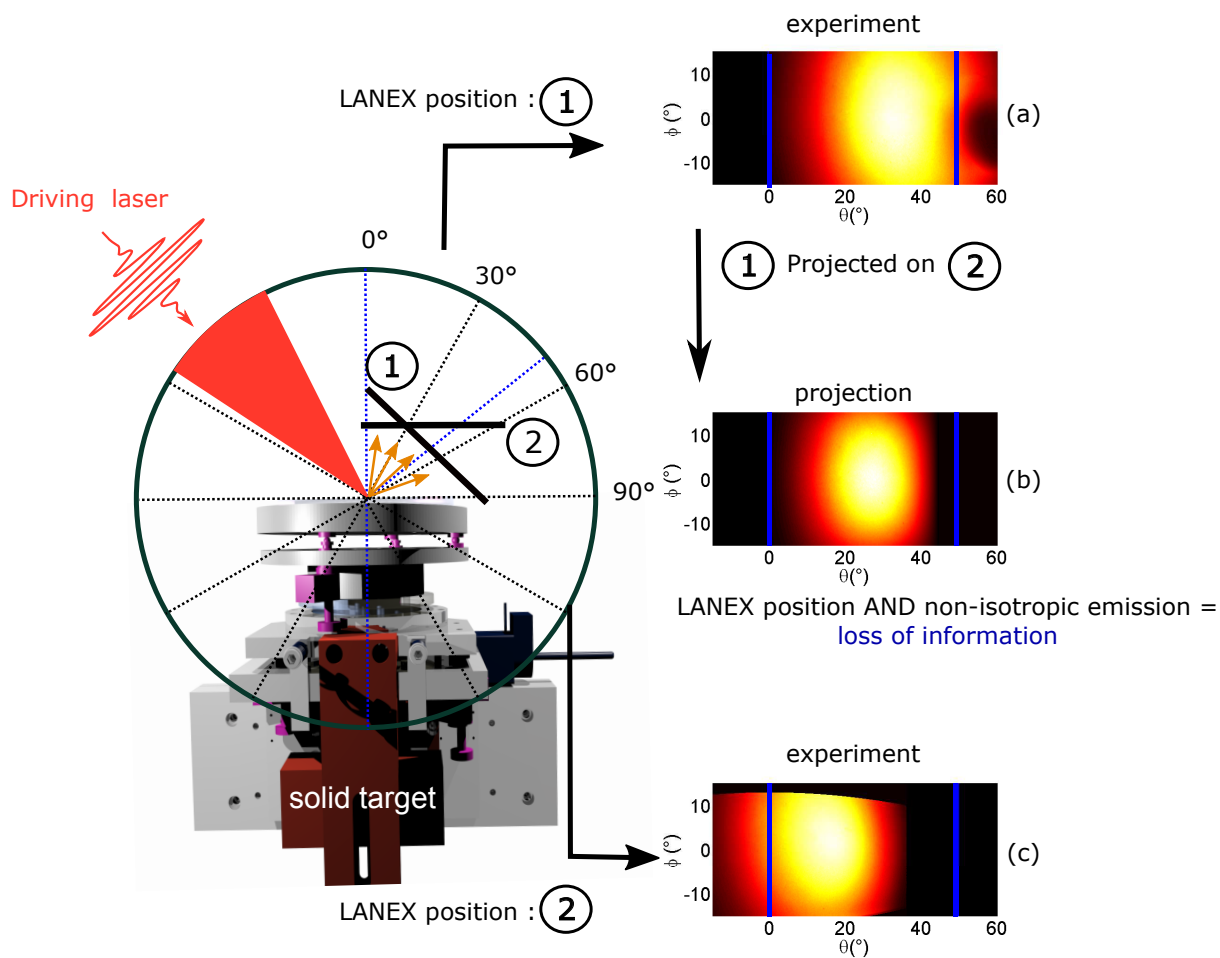


Figure 6.14 – Projection on the LANEX (indicated with black solid line) of the electron angular distribution. One can clearly see the loss of information due to the geometrical position of the LANEX and its non-isotropic emission response

### 6.3.3 Spatial distribution of ejected electrons

The angle at which electrons are ejected from a solid target is subject to debate. Experimental results for a laser intensity of  $a_0 \sim 1$  [66] suggest electrons are ejected around  $34^\circ$  from the target normal with an angular divergence on the order of  $10^\circ$ . Another experiment where  $a_0 \sim 0.13$  [177] hints towards highly collimated beams ( $\sim 3^\circ$  divergence) in the specular direction, while other experiment for long gradient demonstrate normal [178] or grazing acceleration [156, 179]. The diversity of these results highlights the importance of the interaction parameters, namely the intensity on target and the gradient scale length. If providing a highly collimated and monoenergetic electron is the long-term objective, the priority so far is to understand the close correlations between the emission profile and spectral distribution of electrons with respect to the gradient scale length and laser intensity.

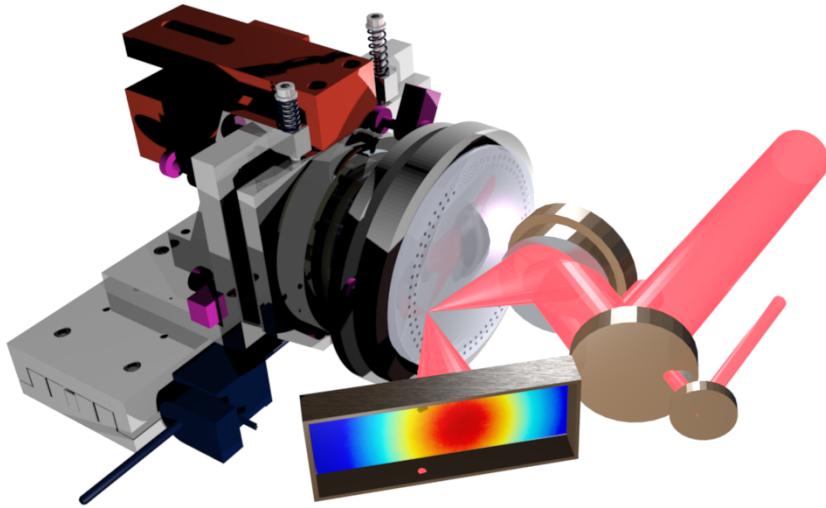


Figure 6.15 – Experimental setup for electron detection in the specular direction. Prepulse:  $I \sim 10^{14} \text{ W/cm}^2$  and main pulse:  $I \sim 10^{18} \text{ W/cm}^2$ . The laser incidence angle is  $50^\circ$ .

In the previous results, we detected electrons ejected  $\sim 16^\circ$ , but mostly because the LANEX used for detection was positioned normal to the target. In the following experiment, we position the LANEX normal to the specular direction to recover the full angular emission profile of ejected electrons as represented in Fig 6.14, thereby obstructing HHG detection. We now discuss the underlying mechanisms of electron acceleration and ejection from an overdense plasma target, at subrelativistic intensities and for  $L < \lambda$ .

### **Importance of laser contrast:**

We have already discussed the importance of the plasma scale length during the interaction, and illustrated this statement with the experimental results presented in 6.2. In Fig 6.17, we can clearly see the influence of the laser contrast on the electron emission profile by changing the output angle  $\alpha$  of the XPW polarizer (description in section 3.1.2). When the angle is large enough, that is to say  $\alpha > 2^\circ$ , the contrast is degraded on the nanosecond time scale, which means that we are in presence of a very long gradient scale length. As a result, electrons are ejected closer to target normal and their profile is more chaotic. On the other hand, as we saw in Section 3- 3.1.2, there exists a range of XPW polarizer angles between  $-3^\circ \leq \alpha \leq 1^\circ$  where only the coherent contrast is altered. In this case, the plasma scale length does not vary significantly and neither does the electron emission profile.

### **Hole in angular emission profile:**

Within this range, we can clearly identify in Fig 6.17, the edges of a ponderomotive "hole" formed by the laser on the right side of the specular direction (indicated by a solid black line). Its size is nearly half that of the laser divergence ( $\sim 25^\circ$  based on geometrical considerations). The presence of such a ponderomotive hole has already been reported in literature [66,67,170,180]. It is attributed to the ponderomotive force [66] and systematically measured in the specular direction [66,67], except in [170] where the hole is formed to the side of the specular direction, however no comment is made on the matter by the authors. However, we notice that in [66], the result of a 2D PIC simulation (showing the angular energy distribution of ejected electrons for  $L = \lambda/5$  and  $a_0 = 1$ ), the "hole" is also located on the side of the specular direction (towards grazing incidence). Again, no comment is made by the authors on the matter. In Fig 6.17, our experimental data clearly indicate that the hole is not formed in the specular direction, but at larger angles (toward grazing incidence). This peculiar effect will be investigated in future experiments. One possible explanation is that we are not exactly at focus on the target plane. In Fig 6.17, the hole is located on the right side of the specular direction as already mentioned. By translating the focusing parabola, we will see (Fig 6.19) that it is possible to shift the position of the hole closer to the specular direction. However, the specular direction is never reached, and a "depletion" line appears when we are in focus. This will be discussed further in 7.2.5

### **Hole disappearance with plasma expansion:**

In Fig 6.18, we represent the electron angular emission profile when varying the pump-

probe delay from 0 ps to 20 ps, which corresponds to plasma gradients between  $L \sim \lambda/100$  and  $\sim \lambda/2$ . As expected, there is an increase of the ejected charge with increasing pump-probe delay, reaching an optimal of  $\sim 17$  pC for 6 ps delay, which is consistent with our previous results. In addition, three remarks can be made on the profile evolution:

- For short delays, the electron angular distribution shows a symmetry with respect to the plane of polarization. In addition, there is a small collimated electron spot near the ponderomotive hole formed by the reflected laser. This pattern is highly reproducible as shown by the 4 consecutive first images, and vanishes after 2ps. We attribute this spot to non-ponderomotive laser acceleration in vacuum, as described in 7.1.3. This effect is much clearer at relativistic intensities [67], and might explain why some authors have observed "highly collimated electron beams" in laser plasma acceleration experiments performed at subrelativistic intensities [177].
- As the gradient expands, the hole formation is purely ponderomotive and gets smaller in size. This is consistent with a strong contribution of the plasma to electron acceleration.
- Finally, for long gradient scale lengths, the ponderomotive hole vanishes, and simultaneously the ejected charge drops.

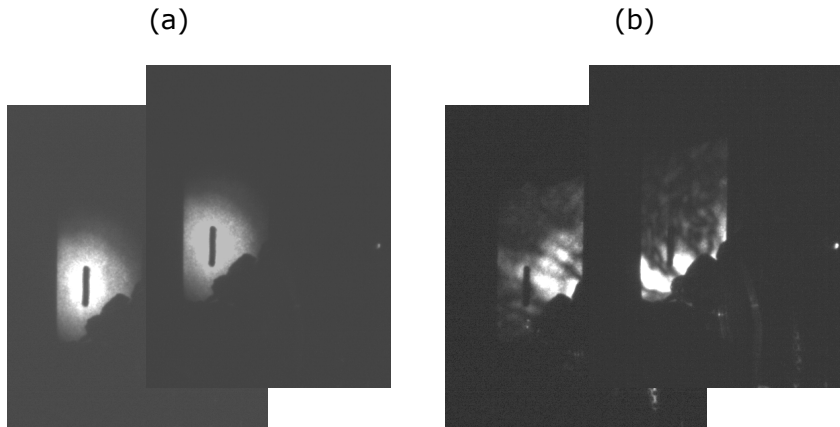


Figure 6.16 – Image of HHG entrance slit with (a) or without (b) prepulse

Still invoking [66], the disappearance of the ponderomotive hole from  $\lambda/5$  to  $\lambda/2$  can be reproduced with PIC simulations. If the hole disappears for long gradients, then either (i) the reflected laser does not overlap with the electrons or (ii) the electrons no longer see ponderomotive effects because of their high propagation velocity. If (ii) were true, we would expect to see a significant increase of electron energy with gradient scale length. This is not the case as shown in 6.4, where no significant variation of the spectra is observed at long gradient lengths. Moreover, for a pump-probe delay where the maximum ejected charge is reached, the ponderomotive hole is still clearly visible on the LANEX. Therefore, the disappearance of the hole should be due to (i). As shown in Fig 6.16, the intensity profile of the laser gets distorted as the plasma expands and therefore, it becomes difficult

to identify a "beam". This is consistent with the highly perturbed emission profile of the electrons for long gradients.

XPW polarizer 1° angle shifts

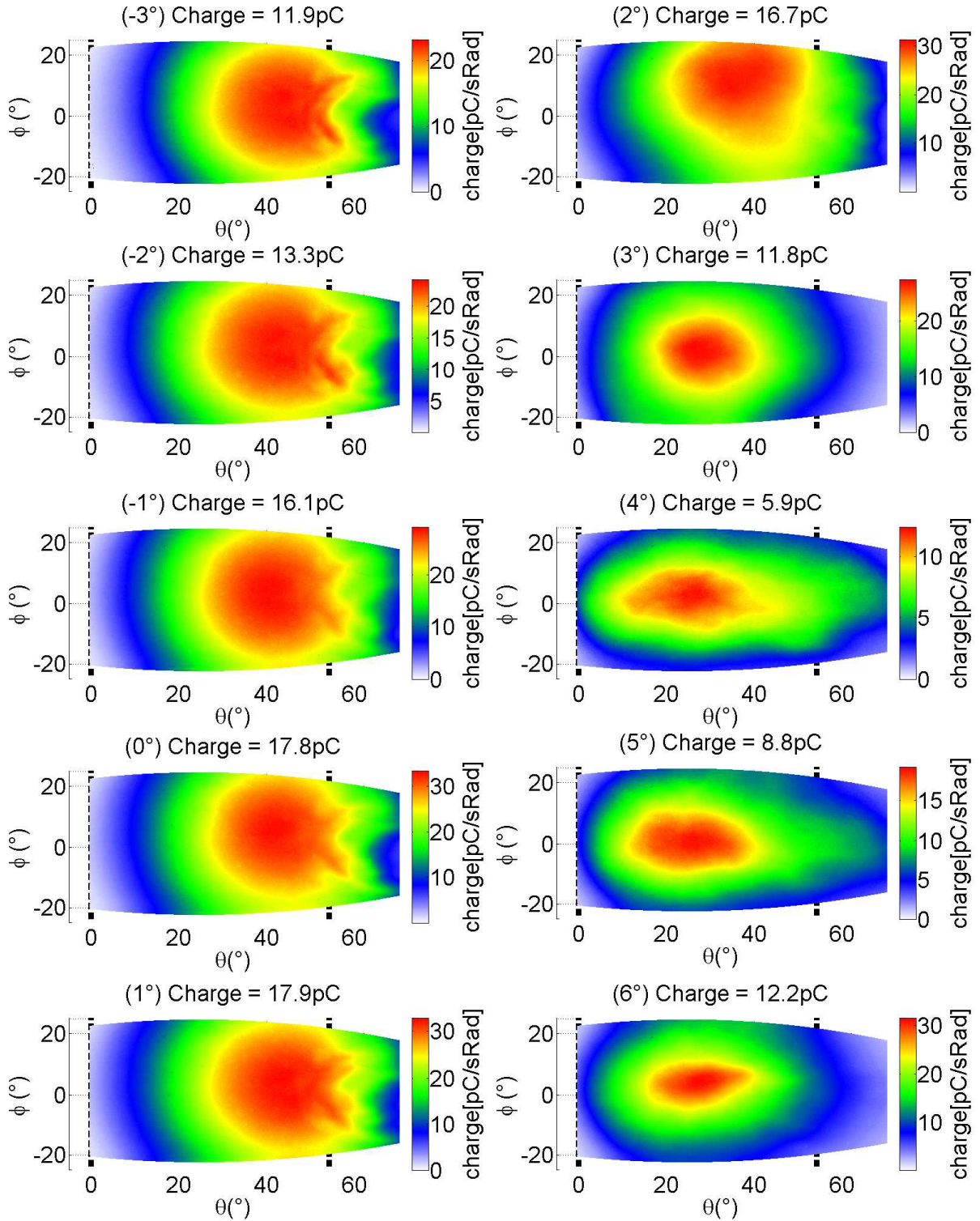


Figure 6.17 – Influence of laser contrast on electron angular distribution. LANEX plane  $\mathcal{L} : y = -0.51x + 7.7(\text{cm})$ . Both normal and specular directions are indicated by back dotted lines at respectively  $0^\circ$  and  $54^\circ$ . Laser intensity is  $a_0 = 0.6$ , focal spot size  $2.5 \mu\text{m}$  FWHM.

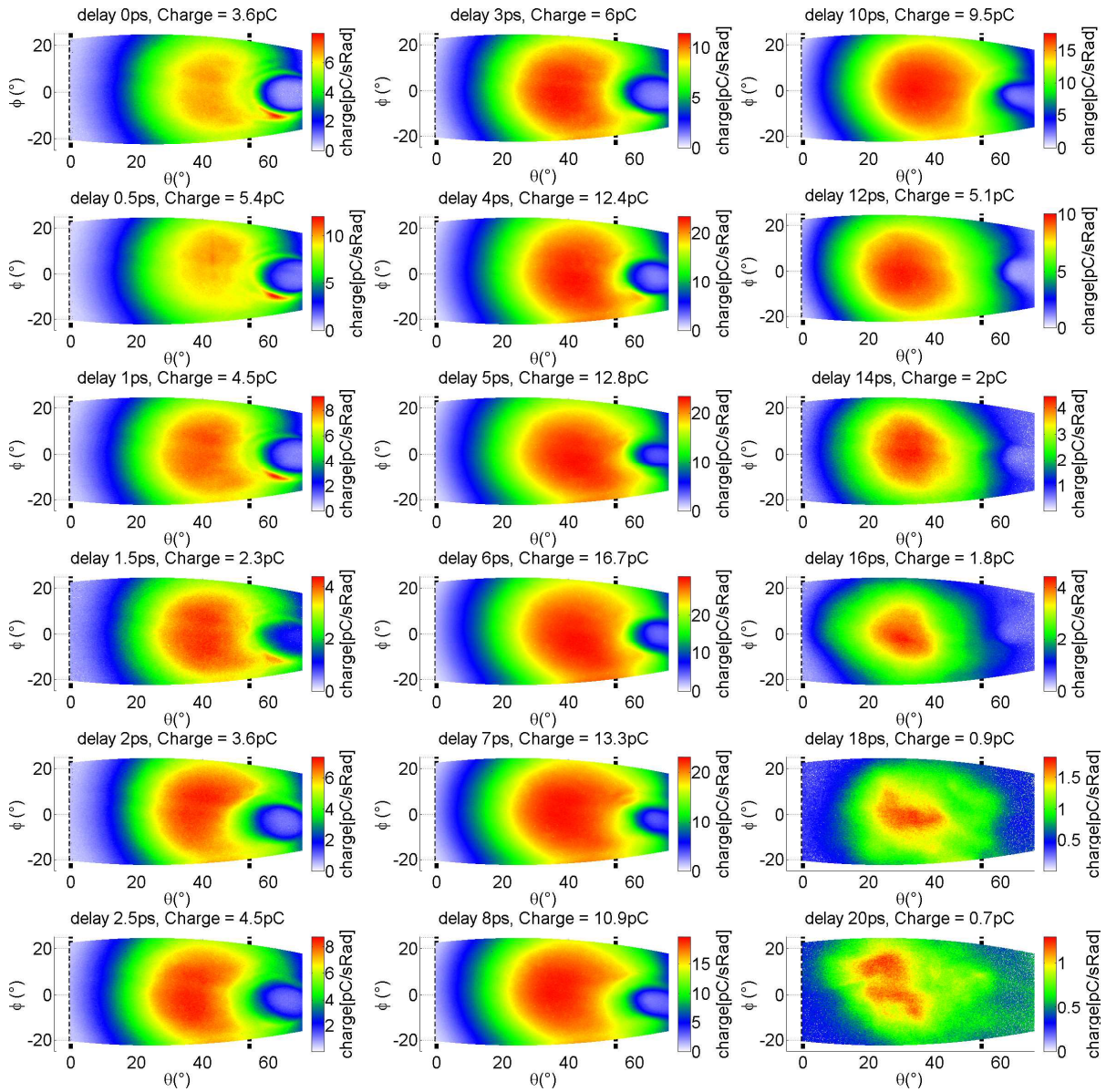


Figure 6.18 – Experimental electron angular distribution in the plane of laser polarization for an intensity on target  $a_0 = 0.77$  for a waist of  $2.5\mu\text{m}$  FWHM. Prepulse intensity is  $I_p = 2 \times 10^{14} \text{ W/cm}^2$

### 6.3.4 Gyromagnetic confinement for short gradient scale length

The present discussion is based only on the following experimental observation: for short plasma scale length, the optimal ejected charge does not correspond to a laser in focus, where the peak intensity is maximal.

The gyromagnetic effect, described in 2006 [181], could very well account for this experimental observation. The principle is that for relativistic intensities and very steep gradient density profiles, an imbalance between the  $E$  and  $B$  fields – a ratio not like in

an EM wave propagating in vacuum – leads the magnetic force to confine electrons at the surface of the plasma, and these can no longer escape. This explains the drop in the amount of charge detected when the laser is in focus. Note that this observation requires a good laser contrast, and is different from the result presented in Fig 6.5, where the contrast was voluntarily degraded. On the contrary there, the increase in plasma scale length limits electron ejection when the laser is in focus.

To evaluate the importance of this effect one should compare the cyclotron frequency  $\omega_{ce}$  (Appendix A) to  $\omega_0$ , the laser frequency. For a p-polarized pulse reflecting on an ideal mirror as described in 7.2.4:

$$\frac{\omega_{ce}}{\omega_0} = a_0 \frac{cB_{\parallel}}{E_{\perp}} = \frac{a_0}{\sin(\theta)}$$

where  $\theta$  is the angle of incidence. This means that increasing  $a_0$ , or decreasing the incident angle, will also increase the cyclotron frequency. In our experimental conditions, this ratio is close to 1, since  $a_0 \sim 0.8$  and  $\theta \sim 50^\circ$ . The result of the laser focus z-scan is shown in Fig 6.19 for a laser pulse of duration 30fs (left column) and 23fs (right column). We begin the scan at  $\Delta z = 0$ , which corresponds to the position of optimal charge ejected. The laser focuses after being reflected by the plasma mirror. When we progressively move the focus position closer to the target surface, that is to say for  $\Delta z < 0$ , we observe a significant decrease in the total ejected charge, and note that a depletion line at  $\phi = 0^\circ$  becomes visible in the spatial profile of the ejected electrons. We will explain the appearance of this depletion in section 7.2.5.

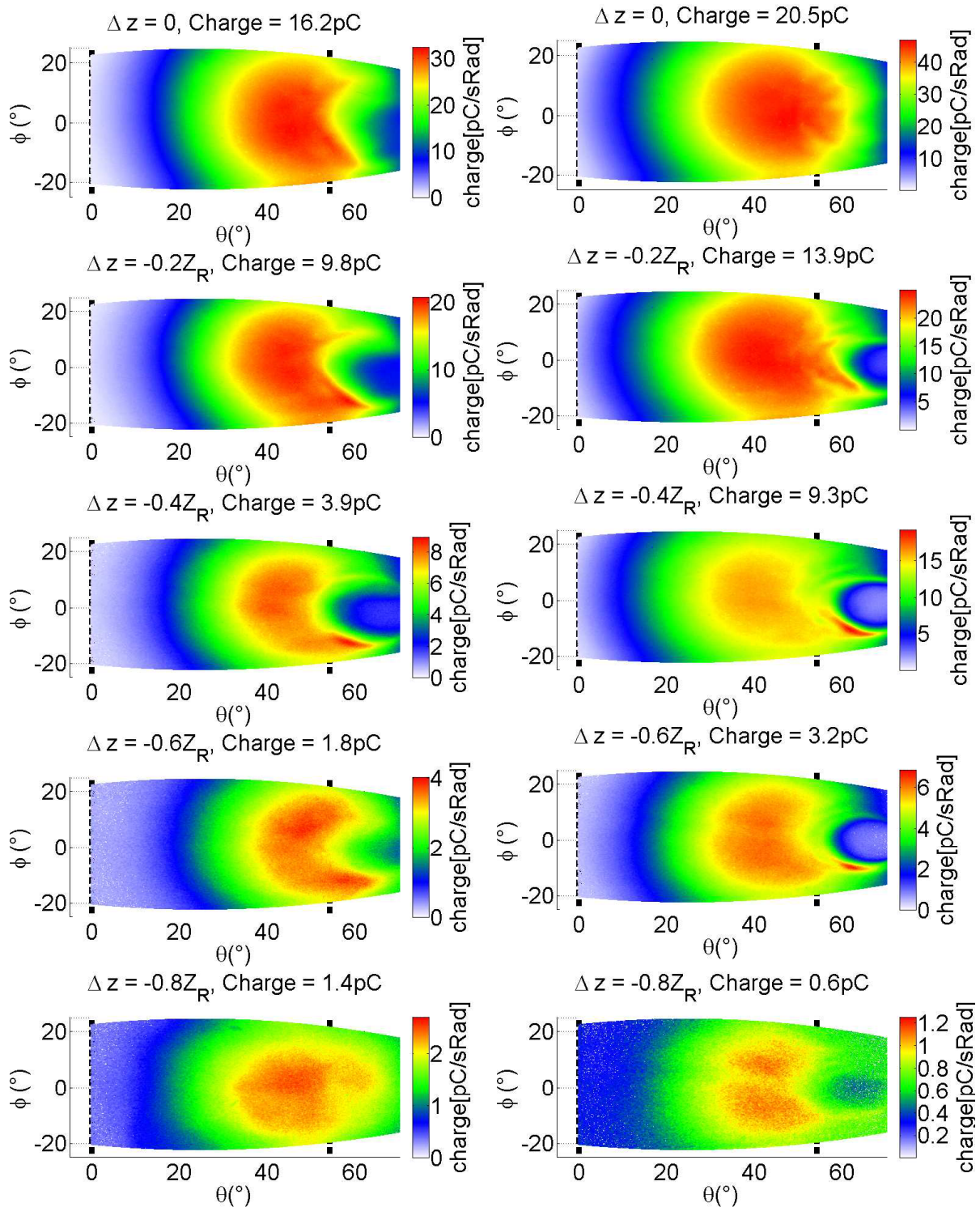


Figure 6.19 – Laser focus z-scan  $\Delta z$  while measuring the electron angular emission profile. The pulse duration is 30 fs with  $a_0 = 0.6$  (the left column) and 23 fs with  $a_0 \sim 0.7$  (right column). Laser focal spot size is  $2.2 \mu\text{m}$  FWHM

## 6.4 Electron spectra

In order to measure the energy spectra of the electron ejected in our experiment, we removed the LANEX screen and replaced it with a purpose-built spectrometer. Here, we give details on the construction of this spectrometer and present experimental data.

### 6.4.1 Electron spectrometer

The basic design is presented in Fig 6.20(a) for the spectrometer normal to the target. It was mounted on a rotation stage centered on the focal spot such that we could rotate the angle of detection of the electrons. The entrance of the spectrometer is a 0.5 mm pinhole placed 100 mm from the focal spot. Neodymium magnets are inserted in the electron path and mounted on a vertical translation stage for proper calibration of the 0 deviation position. The magnetic field along direction  $y$  has been properly calibrated with a Hall probe along the line  $(x, z) = (0, 0)$  and the results is given in Fig 6.20(b). Electrons are deviated in direction  $z > 0$  by the magnetic field and the trace is detected with a phosphor screen imaged with a CCD camera under vacuum.

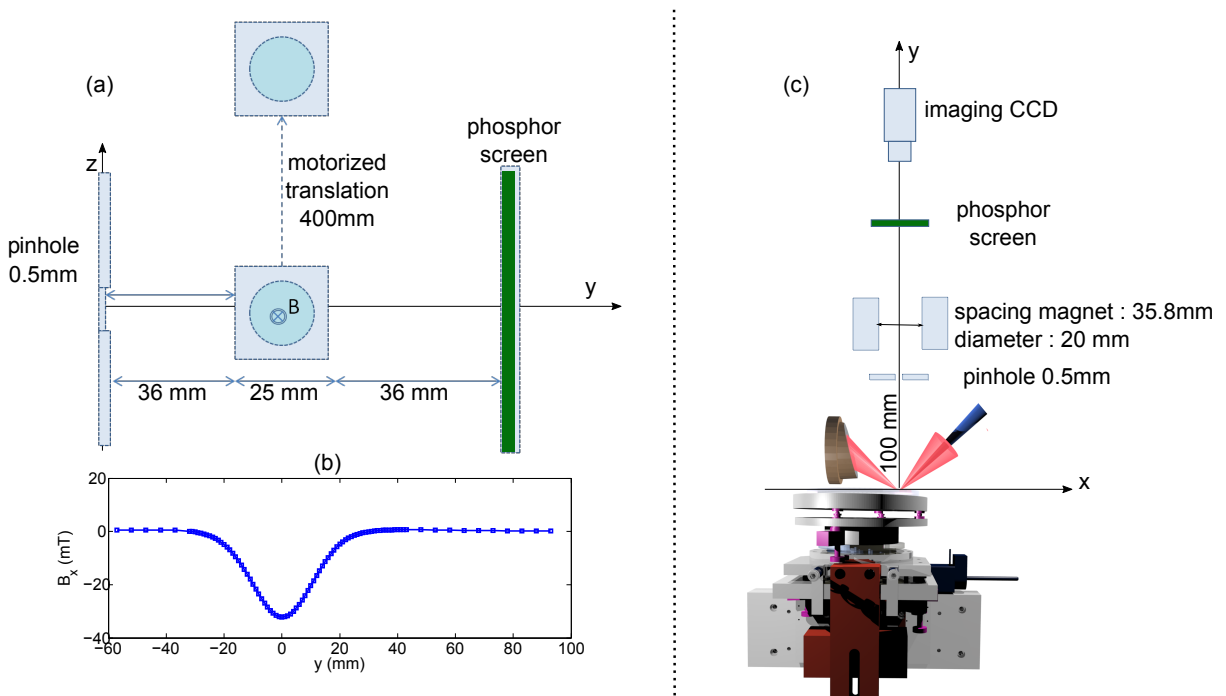


Figure 6.20 – Electron spectrometer setup

To calibrate the detectable energy range in this configuration, we calculated the electron trajectories using the measured magnetic field map. Each final  $z$  position of the electrons on the plane delimited by the phosphor therefore corresponds to a given kinetic energy.

## 6.4.2 Experimental results

Deconvolved electron spectra are consistent with the scaling law provided by Eq 6.7, since for  $a_0 \sim 0.8$  and  $L/\lambda \sim 0.1$ , we expect electrons with energies of  $\sim 300$  keV .

### Influence of plasma gradient:

Electrons are indeed accelerated to several hundreds of keV. In Fig 6.21, we show the influence of the gradient scale length on the ejected electrons final energies. We observe that when the gradient is optimal (maximum signal on LANEX), the spectra extends up to 600keV. For short gradient scale length, that is to say in the absence of a prepulse, the spectrum peaks around 200keV. This indicates selective conditions for electrons to be efficiently accelerated, or in other words "trapped" in the reflected laser pulse. This is consistent with the previous observation that short gradient scale length can lead to highly collimated peaks in the global angular emission profile of electrons. We will discuss this further in Chapter 7.

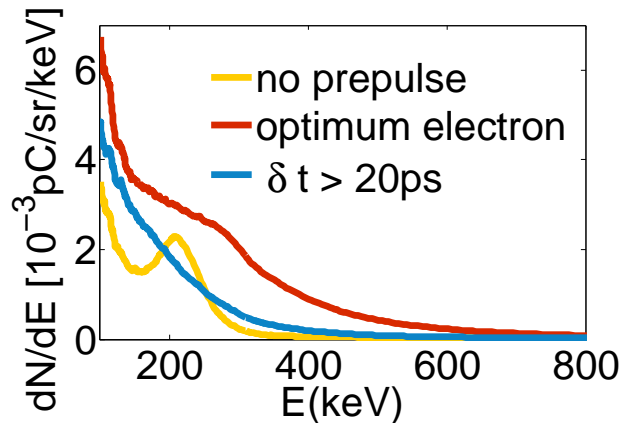


Figure 6.21 – Electron spectra normal to target. Signal is recorded when no prepulse is added, for a pump-probe delay  $\delta t$  corresponding to an optimum on the LANEX, and for long pump/probe delays

### Influence of angle to normal:

We do not observe significant differences in the electron energy spectra depending on the emission angle to the target from 0 to 40°. In Fig 6.22, a prepulse of  $3 \times 10^{14}$  W/cm<sup>2</sup> preionizes the target at a pump-probe delay of 6 ps before the interaction. We find that electrons are accelerated up to several hundreds of keV.

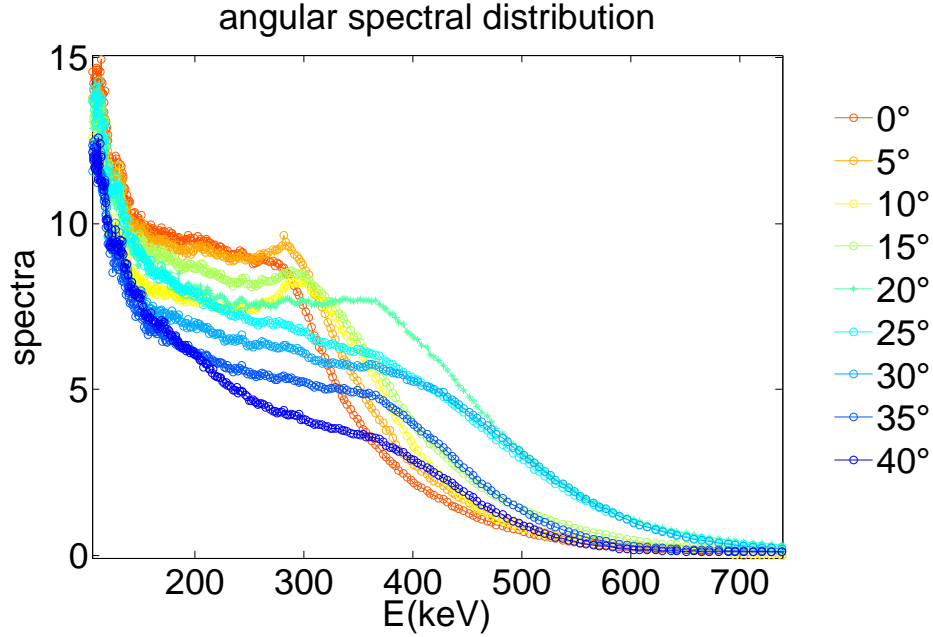


Figure 6.22 – Electron spectra for various angles  $\theta \in [0^\circ \text{ } 40^\circ]$ .  $a_0 = 0.7$ ,  $L/\lambda \sim 0.1$ . Pump/probe delay is 6 ps with a prepulse intensity of  $3 \times 10^{14} \text{ W/cm}^2$

## 6.5 Conclusion

We have demonstrated that in the sub-relativistic regime, the electron and harmonic emission from plasma mirrors have opposite dependence on the plasma scale length. Harmonic emission requires very short plasma scale length  $< 0.06\lambda$  for  $a_0 \sim 0.8$  while electron emission becomes efficient once the plasma has expanded. This behavior was successfully reproduced by 2D PIC simulations, and the increase of ejected charge attributed to the effect of space charge field creating on the surface of the plasma. When this emission is optimal, electron acceleration is the most efficient and reaches several hundreds of keV as expected by simple scaling laws. In addition, the presence of a ponderomotive hole in the electron emission angular profile, where no peaks of emission can be seen, shows that electrons are not "trapped" inside the laser but rather gain most of their energy in the plasma before being ejected.

# Chapter 7

## Laser-electron interaction in vacuum

### Outline

---

<b>7.1</b>	<b>Ponderomotive force and electron motion in vacuum . . . .</b>	<b>142</b>
7.1.1	Classical ponderomotive force derivation . . . . .	143
7.1.2	Relativistic ponderomotive force derivation . . . . .	144
7.1.3	Non-ponderomotive laser acceleration . . . . .	147
7.1.4	Strong focusing field decomposition . . . . .	149
<b>7.2</b>	<b>Hole formation and spectral shaping in vacuum . . . . .</b>	<b>151</b>
7.2.1	Two regimes of acceleration . . . . .	151
7.2.2	Application to the relativistic case . . . . .	152
7.2.3	Application to the sub-relativistic case . . . . .	154
7.2.4	Effect of interference field . . . . .	156
7.2.5	Non-axis-symmetrical components of the interference field . . .	159
<b>7.3</b>	<b>Conclusion . . . . .</b>	<b>161</b>

---

### 7.1 Ponderomotive force and electron motion in vacuum

When electrons are accelerated away from the plasma, they do not propagate ballistically in vacuum immediately since they keep interacting with the driving laser reflecting at the plasma surface. In this section, we will describe the nature of this interaction, and in particular distinguish between the so-called "ponderomotive" regime, where electrons are expelled from high-intensity regions of the laser and the "non-ponderomotive" regime which we will describe hereafter. The Lawson-Woodward theorem states that a free charged particle cannot acquire energy from a plane wave. However, the hypotheses for this theorem to be valid are [182]:

1. The laser propagates in vacuum without boundaries

2. The electron is relativistic in the direction of propagation  $v_z \approx c$
3. No static E or B are present
4. non linear forces (such as the ponderomotive force) are neglected

In the present context of strongly focused ultra-short laser pulses, all these hypotheses are violated such that electron acceleration is not forbidden by theory.

### 7.1.1 Classical ponderomotive force derivation

The ponderomotive force is a local force proportional to the average acceleration of one electron during one laser period. The existence of this force is the consequence of an inhomogeneous spatial profile of the field envelope as opposed to non-physical plane waves. If we picture an electron oscillating at the center of a Gaussian beam: (i) During one half period, the electron will accelerate in one direction of space. (ii) The electron is now located in the region of lower field strength so it will be less decelerated when regaining its original position. (ii) On average over one optical cycle, the electron will have moved from the high-intensity to low intensity region of the beam.

The starting point, as usual, is the equation of motion of an electron given in a electromagnetic given field which we linearized at position  $\mathbf{r}_e^{(0)}$ .

$$\underbrace{\frac{d\mathbf{v}_e^{(1)}}{dt}}_{\text{fast motion}} + \underbrace{\frac{d\mathbf{v}_e^{(2)}}{dt}}_{\text{drift}} = -\frac{e}{m_e} \mathbf{E}(\mathbf{r}_e^{(0)} + \mathbf{r}_e^{(1)}(t), t) - \frac{e}{m_e} (\mathbf{0} + \mathbf{v}_e^{(1)} + \dots) \times \mathbf{B}(\mathbf{r}_e^{(0)} + \mathbf{r}_e^{(1)}(t), t) \quad (7.1)$$

In the hypothesis of a purely monochromatic beam  $\mathbf{E}(\mathbf{r}) \cos(\omega_0 t)$  combined with Maxwell-Gauss equation, we have:

$$\begin{cases} \mathbf{E}(\mathbf{r}_e^{(0)}, t) = \mathbf{E}(\mathbf{r}_e^{(0)}) \cos(\omega_0 t) & (7.2a) \\ \mathbf{B}(\mathbf{r}_e^{(0)}, t) = \frac{1}{\omega_0} \nabla \times \mathbf{E}(\mathbf{r}_e^{(0)}) \sin(\omega_0 t) & (7.2b) \end{cases}$$

Developing Eq 7.1 and identifying the terms corresponding to slow drift and fast motion:

$$\begin{cases} \frac{d\mathbf{v}_e^{(1)}(t)}{dt} = \frac{d^2 \mathbf{r}_e^{(1)}(t)}{dt^2} = -\frac{e}{m_e} \mathbf{E}(\mathbf{r}_e^{(0)}) \cos(\omega_0 t) & (7.3a) \\ \frac{d\mathbf{v}_e^{(2)}(t)}{dt} = -\frac{e}{m_e} (\mathbf{r}_e^{(1)} \nabla) \mathbf{E}(\mathbf{r}_e^{(0)}) \cos(\omega_0 t) - \frac{e}{m_e} \mathbf{v}_e^{(1)}(t) \times \mathbf{B}(\mathbf{r}_e^{(0)}, t) & (7.3b) \end{cases}$$

Eq 7.3a describes the motion of an electron in a homogeneous electric field. This implicitly means that the fluctuations  $\mathbf{r}_e^{(1)}(t)$  are far less than the field spatial variations.

Eq 7.3b can be simplified by replacing  $\mathbf{r}_e^{(1)}$  and  $\mathbf{v}_e^{(1)}$  using the result of first and second temporal integration of Eq7.3a. By then calculating the average of Eq 7.3b over one laser period, the terms in  $\cos(\omega_0 t)^2$  and  $\sin(\omega_0 t)^2$  both equal to  $1/2$  will appear such that we finally have:

$$\left\langle \frac{d\mathbf{v}_e^{(2)}(t)}{dt} \right\rangle = -\frac{1}{2} \frac{e^2}{\omega_0^2 m_e^2} \left( (\mathbf{E}(\mathbf{r}_e^{(0)}) \nabla) \mathbf{E}(\mathbf{r}_e^{(0)}) + \mathbf{E}(\mathbf{r}_e^{(0)}) \times (\nabla \times \mathbf{E}(\mathbf{r}_e^{(0)})) \right) \quad (7.4)$$

using the relation  $\frac{1}{2} \nabla |F|^2 = F \times (\nabla \times F) + (F \nabla) F$  :

$$\left\langle \frac{d\mathbf{v}_e^{(2)}(t)}{dt} \right\rangle = -\frac{1}{2} \frac{e^2}{2\omega_0^2 m_e^2} \nabla |\mathbf{E}(\mathbf{r}_e^{(0)})|^2 \quad (7.5)$$

The expression of the ponderomotive force, independent of the laser polarization, is therefore:

$$\mathbf{F} = -\frac{1}{2} \frac{e^2}{2\omega_0^2 m_e} \nabla |\mathbf{E}(\mathbf{r}_e^{(0)})|^2 \quad (7.6)$$

### 7.1.2 Relativistic ponderomotive force derivation

The derivation of the relativistic ponderomotive force has been performed by several authors and in particular in a low density plasma by Mora and Antonsen [183]. We are here interested in the derivation of that force in vacuum, which simplifies the approach because plasma wave contributions are neglected. Another advantage of the derivation in vacuum is that the potential vector  $\mathbf{A}$  (defined by  $\mathbf{E}(t) = -\partial_t \mathbf{A}(t)$ ) verifies Maxwell's equation of propagation (or in other words the Helmholtz equation) such that in the limit of the paraxial approximation we have an analytical solution for the field if we suppose it is polarized along  $x$ , orthogonal to the direction of propagation  $z$ :

$$A_x(r, z, t) = \frac{w_0 A_0}{w(z)} e^{-\frac{r^2}{w(z)^2}} e^{-\frac{(t-z/c)^2}{t_0^2}} \cos(\xi(z) + \omega_0(t - \frac{z}{c}) - k \frac{r^2}{2R(z)} + \phi_0) \quad (7.7)$$

We would rather write the more general form:

$$A_x(r, z, t) = A_0(r, z) f(t - \frac{z}{c}) \quad (7.8)$$

where  $A_0$  is the field envelope and  $f$  the temporal profile.

The starting point is the relativistic equation of motion applied to one electron. Instead of using Einstein notations, which does not speak to a broad audience, we write the equivalent equations in a standard way (cf Appendix C for details on the derivation), which we develop into 4 equations:

$$\left\{ \begin{array}{l} \frac{d}{dt}[\gamma v_x - \frac{e}{m_e} A_x] = -\frac{e}{m_e} \mathbf{v} \partial_x \mathbf{A} \\ \frac{d}{dt}[\gamma v_y - \frac{e}{m_e} A_y] = -\frac{e}{m_e} \mathbf{v} \partial_y \mathbf{A} \\ \frac{d}{dt}[\gamma v_z - \frac{e}{m_e} A_z] = -\frac{e}{m_e} \mathbf{v} \partial_z \mathbf{A} \\ \frac{d}{dt}(\gamma c^2) = \frac{e}{m_e} \mathbf{v} \partial_t \mathbf{A} \end{array} \right. \quad \begin{array}{l} (7.9a) \\ (7.9b) \\ (7.9c) \\ (7.9d) \end{array}$$

where Eq 7.9c and Eq 7.9d can be combined into one equation:

$$\frac{d}{dt}[\gamma v_z - \frac{e}{m_e} A_z - \gamma c] = -\frac{e}{m_e} \mathbf{v} (\partial_z + \frac{1}{c} \partial_t) \cdot \mathbf{A} \quad (7.10)$$

This very convenient way of writing the electron equation of motion using the vector potential  $\mathbf{A}$  for a field propagating in vacuum highlights the underlying physics of the interaction. In particular, considering the problem of injecting an electron inside the field at time  $t = 0$ , it appears that the initial electron momentum  $\mathbf{p}_0/m_e$  ( $= \gamma_0 \mathbf{v}_0$ ) and the initial vector potential  $\frac{e}{m_e} \mathbf{A}_0$  have the same dimension and play symmetric roles. In one dimension,  $\partial_x = \partial_y = 0$  such that a variation of the initial condition ( $\mathbf{p}_{0\perp}$ ) is equivalent to a variation of the initial phase of the transverse field  $\mathbf{A}_\perp$ .

Equation 7.10 is useful to understand the mechanism behind particle acceleration in the longitudinal direction. The vector potential is a function of  $t - z/c$ , corresponding to propagation. Therefore, applying the operator  $(\partial_z + \frac{1}{c} \partial_t)$  will only affect the pulse envelope  $A_0$ :

$$\frac{d}{dt}[\gamma v_z - \frac{e}{m_e} A_z - \gamma c] = f(t - \frac{z}{c}) \mathbf{v} (\partial_z + \frac{1}{c} \partial_t) \mathbf{A}_0$$

The first-order development of system 7.9 corresponds to the plane-wave approximation, which is equivalent to  $\partial_x = \partial_y = 0$  and  $(\partial_z + \frac{1}{c} \partial_t) = 0$ :

$$\left\{ \begin{array}{l} \frac{d}{dt}[\gamma v_x^{(0)} - \frac{e}{m_e} A_x] = 0 \\ \frac{d}{dt}[\gamma v_y^{(0)} - \frac{e}{m_e} A_y] = 0 \\ \frac{d}{dt}[\gamma v_z^{(0)} - \frac{e}{m_e} A_z - \gamma c] = 0 \end{array} \right. \quad \begin{array}{l} (7.11a) \\ (7.11b) \\ (7.11c) \end{array}$$

The first-order development of 7.9, where  $p = p^{(0)} + p^{(1)}$ , gives:

$$\left\{ \begin{array}{l} \frac{d}{dt}[p_x^{(1)}] = -e \frac{1}{\gamma^{(0)}} \mathbf{A} \partial_x \mathbf{A} \\ \frac{d}{dt}[p_y^{(1)}] = -e \frac{1}{\gamma^{(0)}} \mathbf{A} \partial_y \mathbf{A} \\ \frac{d}{dt}[p_z^{(1)} - \gamma^{(1)} m_e c] = -e f(t - \frac{z}{c})^2 \frac{1}{\gamma^{(0)}} \mathbf{A}_0 (\partial_z + \frac{1}{c} \partial_t) \mathbf{A}_0 \end{array} \right. \quad \begin{array}{l} (7.12a) \\ (7.12b) \\ (7.12c) \end{array}$$

Combining Eq 7.12a and 7.12b we find the expression for the ponderomotive force:

$$\frac{d(\gamma v_{\perp}^{(0)})}{dt} = -\frac{e}{2\gamma m_e} \nabla_{\perp} \mathbf{A}^2 \quad (7.13)$$

Note that the  $\gamma^{(0)}$  used in this equation corresponds to that of the non-perturbed (zero<sup>th</sup> order) equation, in other words, that it can be expressed by the relation:

$$(\gamma^{(0)})^2 \left(1 - \frac{1}{c^2} ((v_x^{(0)})^2 + (v_y^{(0)})^2 + (v_z^{(0)})^2)\right) = 1$$

From Eq 7.12c, we conclude that the temporal envelope of the pulse will also drive electron acceleration in the direction of propagation.

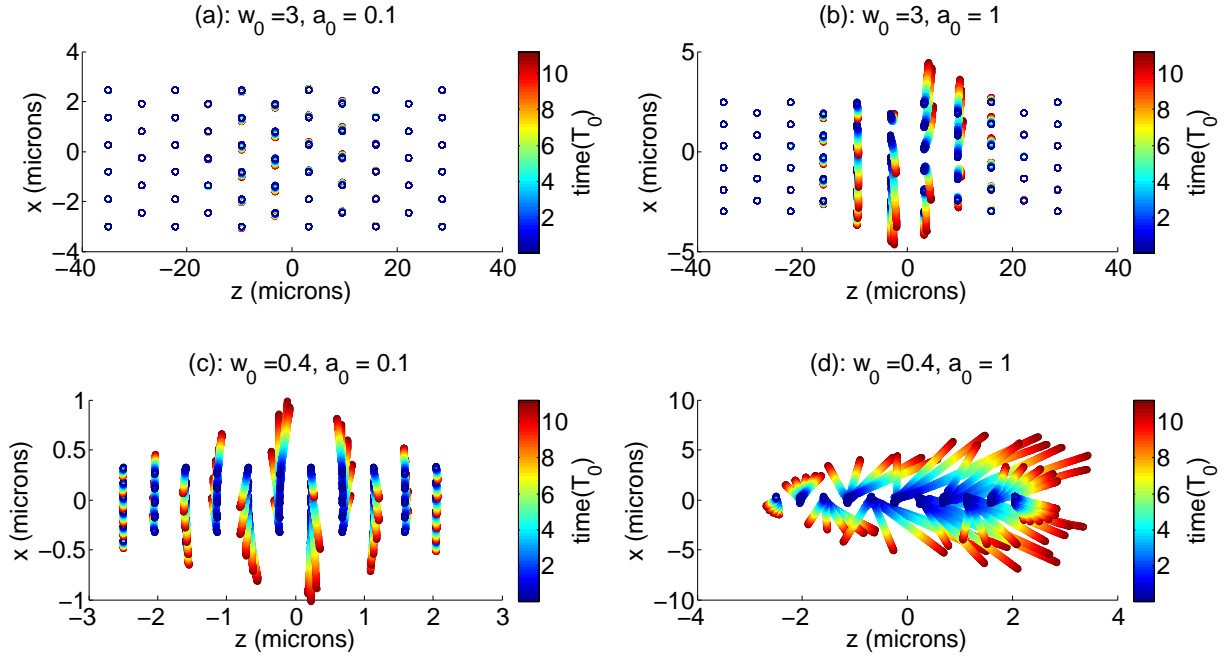


Figure 7.1 – 63 test electron trajectories in a Gaussian beam. All particles are injected at time  $t = 0$  when the laser is at focus. Particles are initially at rest and located in the domain  $x_{i0} \in [-w_0 \ w_0]$ ,  $z_{i0} \in [-Z_r \ Z_r]$ . The laser is 30 fs FWHM and the simulation performed from  $t = 0$  to  $t = 30$  fs. Laser parameters: (a)  $w_0 = 3 \mu\text{m}$ ,  $a_0 = 0.1$ , (b)  $w_0 = 3 \mu\text{m}$ ,  $a_0 = 1$ , (c)  $w_0 = 0.4 \mu\text{m}$ ,  $a_0 = 0.1$ , (d)  $w_0 = 0.4 \mu\text{m}$ ,  $a_0 = 1$ ,

We now take test particles initially at rest in the plane  $[x, z]$ , where  $x$  spreads along the laser waist, and  $z$  along the Rayleigh length as described in Fig 7.1. At  $t = 0$ , the test electron trajectories are calculated using a 3 dimensional code based on the field calculation presented in the following section 7.1.4. The final gained electron energies are given in Fig 7.2 and increase in a strong focusing geometry.

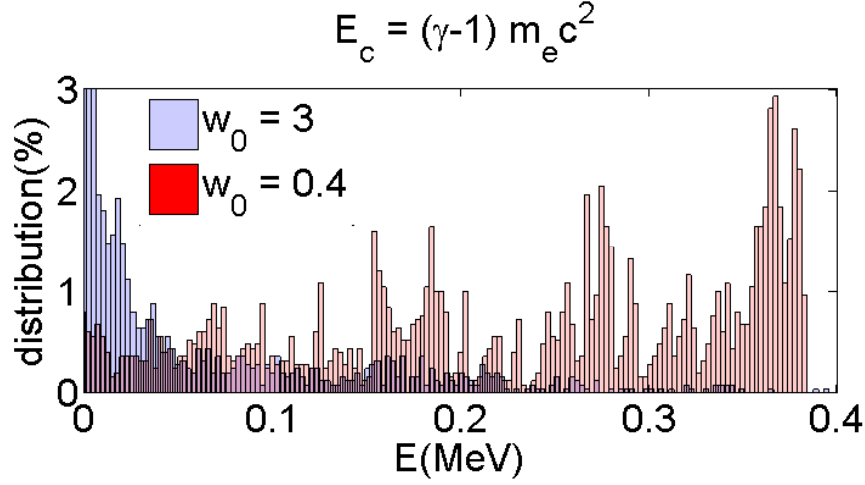


Figure 7.2 – Final energy distribution after  $t = 30$  fs at  $a_0 = 1$  for  $w_0 = 0.4$  (red) and  $w_0 = 3$  (blue) for 2500 test particles

The results show enhanced acceleration in the case of strong focusing geometry, a direct consequence of the increasing ponderomotive potential in all directions (radial and longitudinal).

### 7.1.3 Non-ponderomotive laser acceleration

Here we wish to examine the other asymptotic case of an electron interacting with an electromagnetic field with no consideration for ponderomotive effects. This consists in integrating Eq 7.11, corresponding to the plane-wave approximation, and leads to the trivial result:

$$\left\{ \begin{array}{l} \gamma v_x - \frac{e}{m_e} A_x = \gamma_0 v_{x0} - \frac{e}{m_e} A_{x0} \end{array} \right. \quad (7.14a)$$

$$\left\{ \begin{array}{l} \gamma v_y - \frac{e}{m_e} A_y = \gamma_0 v_{y0} - \frac{e}{m_e} A_{y0} \end{array} \right. \quad (7.14b)$$

$$\left\{ \begin{array}{l} \gamma v_z - \frac{e}{m_e} A_z - \gamma c = \gamma_0 v_{z0} - \frac{e}{m_e} A_{z0} - \gamma_0 c \end{array} \right. \quad (7.14c)$$

to which we add the relation:

$$\gamma^2 = 1 + \gamma^2 \frac{v_x^2}{c^2} + \gamma^2 \frac{v_z^2}{c^2} \quad (7.15)$$

To simplify the resolution, the laser is polarized along  $x$ , such that  $A_y = A_z = 0$  at all time. We define  $a_0 = \frac{e}{m_e c} (A_{x0} - A_x)$  for better clarity.

$$\left\{ \begin{array}{l} \gamma v_x / c - \gamma_0 v_{x0} / c = a_0 \end{array} \right. \quad (7.16a)$$

$$\left\{ \begin{array}{l} \gamma (1 - v_z / c) = \gamma_0 (1 - v_{z0} / c) \end{array} \right. \quad (7.16b)$$

The combination of Eq 7.16 and relation 7.15 gives:

$$(1 - v_z/c) = 2\left(1 + \frac{1 + (\gamma_0 v_{x0}/c + a_0)^2}{\gamma_0^2(1 - v_{z0}/c)^2}\right)^{-1} \quad (7.17)$$

and

$$\gamma = \frac{\gamma_0}{2}(1 - v_{z0}/c)\left(1 + \frac{1 + (\gamma_0 v_{x0}/c + a_0(t))^2}{\gamma_0^2(1 - v_{z0}/c)^2}\right) \quad (7.18)$$

In this formulation, we see that an electron initially at rest can gain energy from the laser according to the scaling law:

$$(\gamma - 1)mc^2[\text{MeV}] \approx \frac{a_0^2}{2}$$

Note that the laser will contribute to the electron acceleration when, by definition,  $\gamma - \gamma_0 > 0$ . The previous derivation shows that for some initial value of the vector potential  $A_{x0}$ , we can have  $\gamma - \gamma_0 < 0$ , which corresponds to a deceleration of the electron by the laser.

We define the **dephasing length** as the distance the electron has to propagate in order to accumulate a phase difference of  $\pi/2$  with the driving laser when propagating in the direction  $z$ , for a vector potential of the form  $a(t) = a_0 \cos(\omega_0 t - k_0 z)$ . For this scaling relation, we impose  $u_{x0} = 0$  and  $\beta_0 = v_{z0}/c$ . Indeed, the phase difference is:

$$\phi(t) = \omega_0 t - k_0 z(t)$$

which implies

$$\phi(t)' = \omega_0\left(1 - \frac{v_z}{c}\right) = \omega_0 \frac{\gamma_0}{\gamma}\left(1 - \frac{v_{z0}}{c}\right)$$

Using the relation  $\phi'(t)z'(\phi) = z'(t)$  we find this dephasing length equals:

$$Z_{deph} = \frac{\lambda_0}{4}\gamma_0^2(1 + \beta_0)\left(\frac{a_0^2}{4}(1 + \beta_0) + \beta_0\right) \quad (7.19)$$

For an efficient acceleration effect of the laser, this value has to be greater than the Rayleigh length of the laser used to accelerate electrons. Of course, since what matters is the energy gain from the laser, when  $\beta_0$  is close to one, the electron has a ballistic trajectory and hardly interacts with the laser such that when  $Z_{deph}$  tends to infinity,  $\gamma - \gamma_0$  tends to zero. In other words, for an efficient acceleration of the electron by the laser, there is an optimal  $Z_{eff} > Z_R$  value allowing the electron to stay phase-locked to the laser and gain energy from the field.

### 7.1.4 Strong focusing field decomposition

A monochromatic electromagnetic field propagating in vacuum can easily be propagated from one plane to another in the Fourier space (Fourier transformed relative to  $(x, y)$  coordinates, then multiplication by a propagation transfer function). This is convenient for a polarized field since it can be considered "scalar". In real life however, an electromagnetic field has 6 degrees of freedom ( $E_x, E_y, E_z, B_x, B_y, B_z$ ). Naively, retrieving the full field from a plane requires using the scalar approach 6 times, one per degree of freedom. In reality, the real degree of freedom is reduced to 2 because of Maxwell's equations [184], which means for example that if both  $E_x$  and  $E_y$  are known, all other components (namely  $E_z, B_x, B_y, B_z$ ) can be calculated without ambiguity.

If we consider a linearly polarized Gaussian beam  $E_x$  propagating along  $z$ , its field does not satisfy the electromagnetic wave equation but instead the so-called Paraxial Equation. As a consequence, when one gets to the strong focused regime, that is to say when the paraxial approximation is no longer valid, only one component of the field  $E_x$  is not enough to quantify the field in focus. In particular, suppose  $E_x$  is a linearly polarized Gaussian beam along the direction  $x$ , and  $E_y = 0$  everywhere. Since  $\nabla \cdot E = \partial_x E_x + \partial_z E_z = 0$ :

$$\begin{aligned} \partial_z E_z(x, y, z) &= -\partial_x \left[ \iint_{\mathbb{R}^2} E_x(k_x, k_y, z) e^{-ik_x x - ik_y y} dk_x dk_y \right] \\ &= -\partial_x \left[ \iint_{\mathbb{R}^2} E_x(k_x, k_y, 0) e^{-iz\sqrt{k^2 - k_x^2 - k_y^2}} e^{-ik_x x - ik_y y} dk_x dk_y \right] \end{aligned} \quad (7.20)$$

Where the square root function is defined on complex number ( $\sqrt{-1} = -i$  according to Eq 7.20 convention). The integration of Eq 7.20 in focus, which we define by  $z = 0$ , shows that the  $E_z$  component can not be equal to zero and is given by:

$$E_z(x, y, z) = \iint_{\mathbb{R}^2} \frac{k_x e^{-iz\sqrt{k^2 - k_x^2 - k_y^2}}}{\sqrt{k^2 - k_x^2 - k_y^2}} E_x(k_x, k_y, 0) e^{-ik_x x - ik_y y} dk_x dk_y \quad (7.21)$$

where  $E_x(k_x, k_y, 0)$  is the Fourier transform of  $E_x$  at focus.

The formula shows, as illustrated by Fig 7.3 that for very small focal spot sizes relative to the laser wavelength,  $E_z$  is no longer negligible relative to  $E_x$ , such that the polarization of the field has a component along  $z$ . Therefore, the force exerted by charged particles when the focal spot compares with the laser wavelength has to be calculated using these components of the field. We will see this can have drastic consequences on the predicted result.

Since we want an analytical expression of the laser beam in order to calculate the trajectories of test electrons, we will rely on strong field decomposition. Indeed, it has been shown [185] that the field can be developed relative to a small parameter  $\epsilon = \frac{\lambda}{2\pi w_0}$

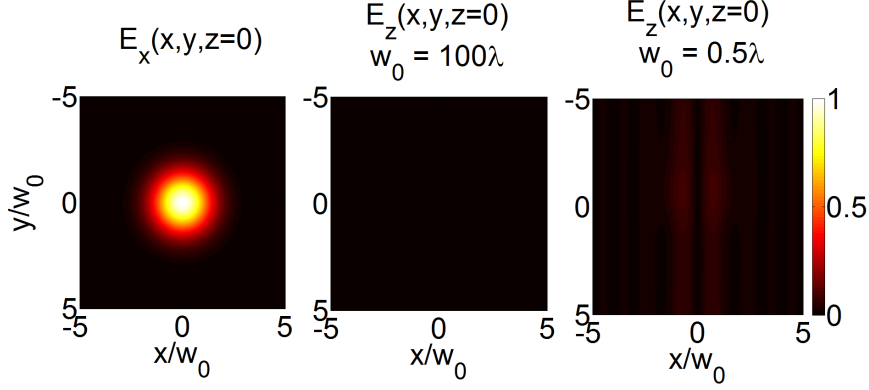


Figure 7.3 –  $E_x(x, y, z = 0)$  is a Gaussian beam of waist  $w_0$ .  $E_z(x, y)$  calculated with Eq 7.21 for  $w_0 = 100\lambda$  and  $w_0 = 0.5\lambda$ . All images are normalized by the maximum value of  $|E_x|$ .

$$\begin{cases} E_x = E_x^{(0)} + \epsilon^2 E_x^{(2)} + \dots & (7.22a) \\ E_y = \epsilon^2 E_y^{(2)} + \dots & (7.22b) \\ E_z = \epsilon E_z^{(1)} + \epsilon^3 E_z^{(3)} + \dots & (7.22c) \\ B_x = \epsilon^2 B_x^{(2)} & (7.22d) \\ B_y = B_y^{(0)} + \epsilon^2 B_y^{(2)} & (7.22e) \\ B_z = \epsilon B_z^{(1)} + \epsilon^3 B_z^{(3)} & (7.22f) \end{cases}$$

where **the zeroth order** is the well-known Gaussian beam:

$$E_x^{(0)} = cB_y^{(0)} = \frac{E_0}{w(z)} e^{-ikz} e^{-ik\frac{r^2}{2q(z)}} e^{i\xi(z)} \quad (7.23)$$

The higher order terms are calculated by identifying the terms of a polynomial series (we will not get into the details of the demonstration as it is very well described in [185]). Now artificially imposing a Gaussian envelope for the temporal profile (the field is no longer monochromatic) for  $(x, y, z, t)$ :

$$E_x^{(0)} = \frac{w_0 E_0}{w(z)} \exp\left(-\frac{(t - z/c)^2}{t_0^2}\right) \exp\left(-\frac{r^2}{w(z)^2}\right) \cos(\xi(z) + \omega t - kz - k\frac{r^2}{2R(z)} + \phi_0) \quad (7.24)$$

The series is expanded using 7.22 and gives us an accurate decomposition of the field at focus. We use this decomposition to calculate the trajectories of test electrons. This will be referred to later as our "3D particle code". We give in Fig 7.4 a schematic view of the system coordinates defined inside the particle code and used in hereafter.

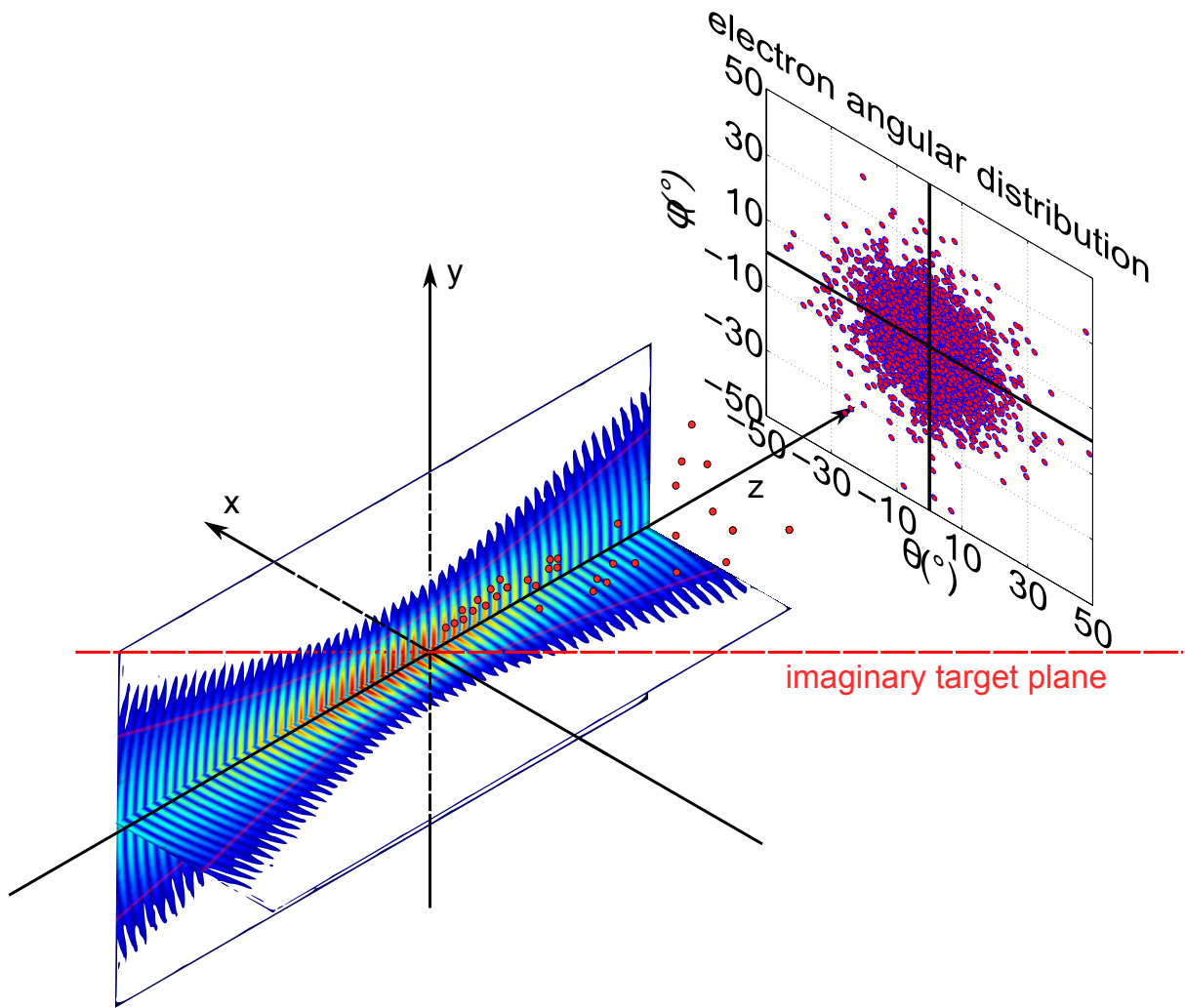


Figure 7.4 – Schematic view of the 3D particle code:  $z$  is the direction of propagation and  $x$  the direction of the zero order Gaussian beam  $E_x^{(0)}$ .  $\theta$ : angle in the  $(x,z)$  plane with the conventions  $\theta < 0$  toward the target normal, and  $\phi$  the angle in vertical plane

## 7.2 Hole formation and spectral shaping in vacuum

### 7.2.1 Two regimes of acceleration

We saw in Section 7.1.2 the role played by the ponderomotive force: a focused laser will expel electrons from the zone of highest intensity toward zones of lower intensity. The expression of the ponderomotive force indicates a radial force  $\propto \nabla I$  independent of laser polarization. However, we also discussed the possibility for non-ponderomotive acceleration to occur when an electron escapes the laser field before we can consider an averaged, i.e. purely ponderomotive, acceleration. Taking again the example given in Section 7.1.2 of a 30 fs,  $a_0 = 1$  laser field, for the two cases  $w_0 = 3 \mu\text{m}$  and  $w_0 = 0.4$ , we

inject test particles initially at rest at time  $t_{in} = 0$  (at that time, the laser is exactly at focus) and retrieve the angular emission profile of electrons with positive final momentum with respect to the direction of propagation. The result is given in Fig 7.5: on the left panel representing the final angular profile of the accelerated electrons, 2 populations are clearly visible namely (i) electrons radially spread by the purely ponderomotive effect, also corresponding to the lowest part of the spectrum ( $\leq 0.15$  MeV) and (ii) electrons accelerated in the direction of polarization of the laser forming two zones of higher energy ( $> 0.15$  MeV). Depending on their initial position (i.e. phase) in the driving laser, electrons could be trapped in phase with the propagating laser such that they do not average over the whole acceleration path. This leads to the two distribution bulbs located on the polarization plane  $\phi = 0^\circ$ .

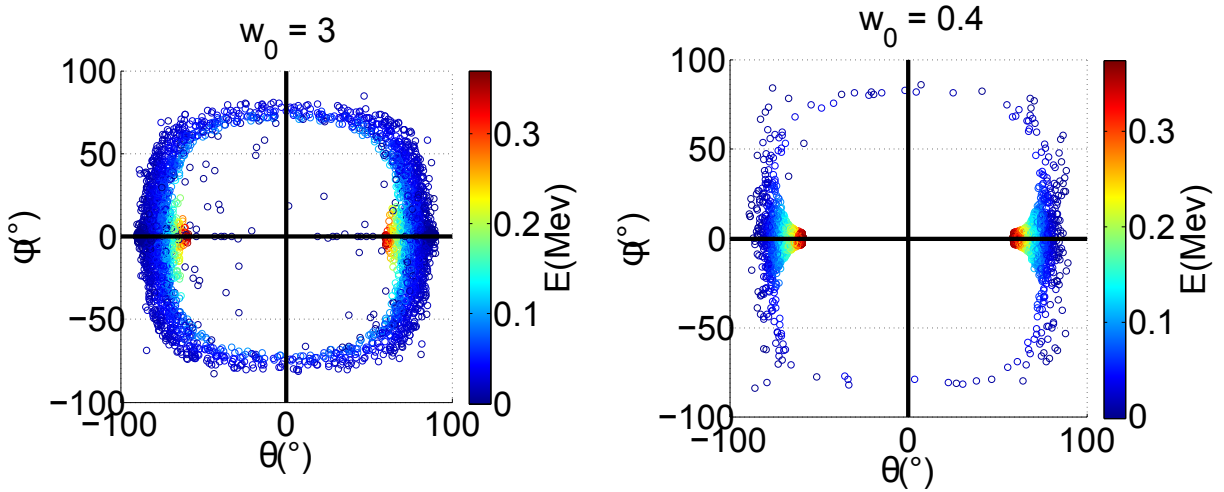


Figure 7.5 – Result of 3D particle code showing final electron angular distribution with final kinetic energy  $E_c = (\gamma - 1)m_e c^2$  in color scale. 5041 test particles initially at rest are randomly injected in the cylinder defined by  $z_0 \in [-Z_R, Z_R]$ ,  $r_0 \in [0, w_0]$  in a  $\tau_{fwhm} = 30$  fs,  $a_0 = 1$  focused laser beam polarized in the plane  $\phi = 0$  with a waist of respectively  $w_0 = 3$  (left) and  $w_0 = 0.4$  (right).

This non-ponderomotive electron acceleration by the laser was demonstrated experimentally in the relativistic case ( $a_0 > 1$ ) [67] as described in the following. Since the acceleration efficiency depends on the phase of injection, this mechanism is designated as "vacuum injection".

## 7.2.2 Application to the relativistic case

In a solid target experiment conducted on UHI100 at CEA [67], for a laser intensity  $a_0 = 2.5$  and  $w_0 = 5 \mu\text{m}$ , non-ponderomotive acceleration (or vacuum injection) of

electrons has been demonstrated. The electrons energies reached  $\sim 10$  MeV and were emitted in a collimated beam near the ponderomotive hole formed by the laser in the angular emission profile.

In 7.1.3, we defined a scaling length  $Z_{eff}$  which, if greater than the laser waist, indicates that non-ponderomotive acceleration is dominant. Using the laser characteristics from CEA, we plotted  $Z_{eff}$  in Fig 7.6.

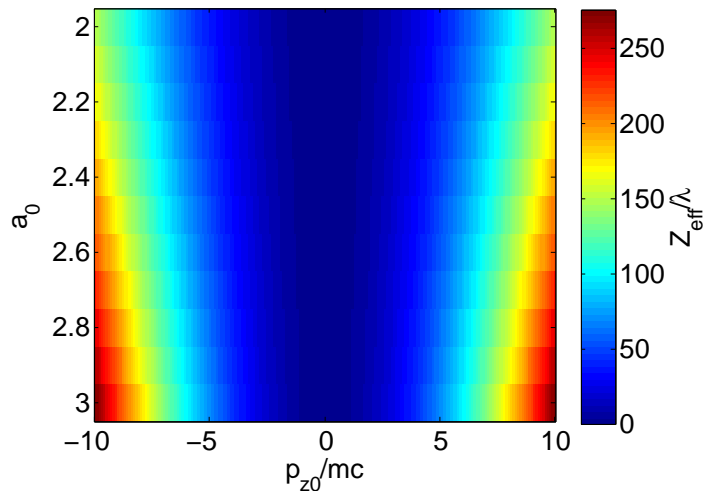


Figure 7.6 –  $Z_{eff}$  as a function of  $a_0$  and initial momentum  $p_{z0}/mc$  from Fig 7.7 for relativistic case  $a_0 \sim 2.5$ . Here,  $\lambda = 0.8 \mu\text{m}$

As described in [67], the experimental angular profile and emission spectra were reproducible combining 1D PIC simulations with a 3D particle code. The 3D particle code allowed one to calculate the electron trajectories once they have escaped the influence of the plasma. The PIC simulations are necessary to extract the "initial conditions", that is to say their initial momentum distribution and phase inside the laser. As a result of PIC simulations, the initial phase of electrons corresponds to a switch of the magnetic field from negative to positive values. In addition, the initial momentum distribution represented in Fig 7.7 was retrieved from 1D PIC simulations by probing the current of ejected particles at the position  $n(x) = n_c/5$  (beginning of the plasma, the density in the simulation cell is imposed rigorously equal to zero above this limit). Using the 3D code presented previously, we reproduced the final angular emission of the electrons shown in Fig 7.7 using 5041 test electrons as already performed in [67]. The final angular distribution showing a peak of energetic electrons located near the hole, and visible on Fig 7.7, is exactly the profile measured in the experiment [67], which proves the consistency of the scaling parameter  $Z_{eff}$  plotted in 7.6.

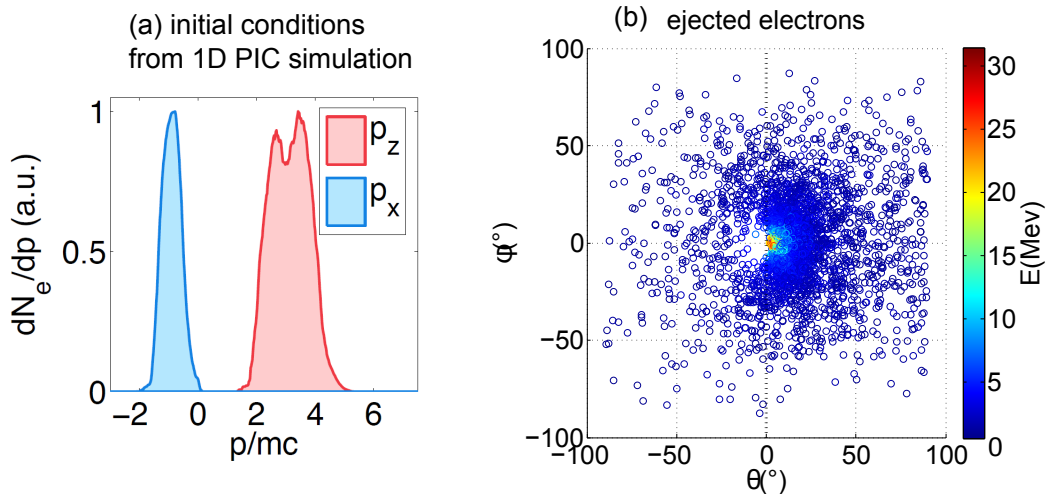


Figure 7.7 – (a) Initial conditions of injected electrons (screen shot from Reference [67]) extracted from 1D PIC simulation. Particles are injected when the magnetic field  $B_y$  switches to positive values with random distribution  $t_0 \in [-0.33 \text{ fs} ; 0.33 \text{ fs}]$  Laser conditions:  $a_0 = 2.5$ ,  $\tau_{FWHM} = 15 \text{ fs}$ ,  $w_0 = 5 \mu\text{m}$  and  $\lambda = 0.8 \mu\text{m}$ . (b) Angular distribution of ejected electrons were (each point corresponds to an electron). The colorbar indicates the final energy in MeV.

### 7.2.3 Application to the sub-relativistic case

Based on the previous discussion, we can legitimately wonder whether vacuum injection is still efficient at sub-relativistic intensities. We reproduce the previous analysis for  $a_0 \sim 0.4$ . At first sight, the problem looks similar and we expect to reproduce the experimental profile of ejected electrons shown in section 6.3.3. However, using our laser parameters, we find that the coherent length  $Z_{eff}$  is smaller than the laser waist  $w_0 \sim 1.2 - 1.6\lambda$ . This means that the initial injection phase inside the laser will quickly depend on the probing plane using the PIC simulation, which makes it more difficult to clearly define. In Fig 7.9 we give an example of what we can extract for 1D PIC simulation for  $L = \lambda/10$ ,  $a_0 = 0.4$  when placing a probe at position  $0.1\lambda$  from the end of the plasma in vacuum.

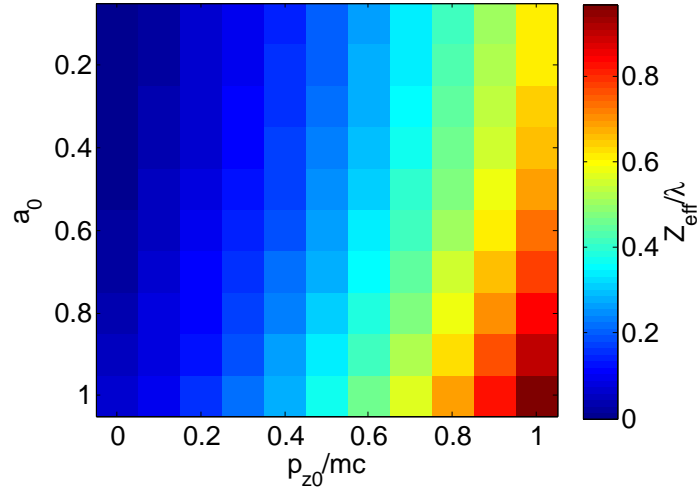


Figure 7.8 –  $Z_{eff}$  as a function of  $a_0$  and initial momentum  $p_{z0}/mc$

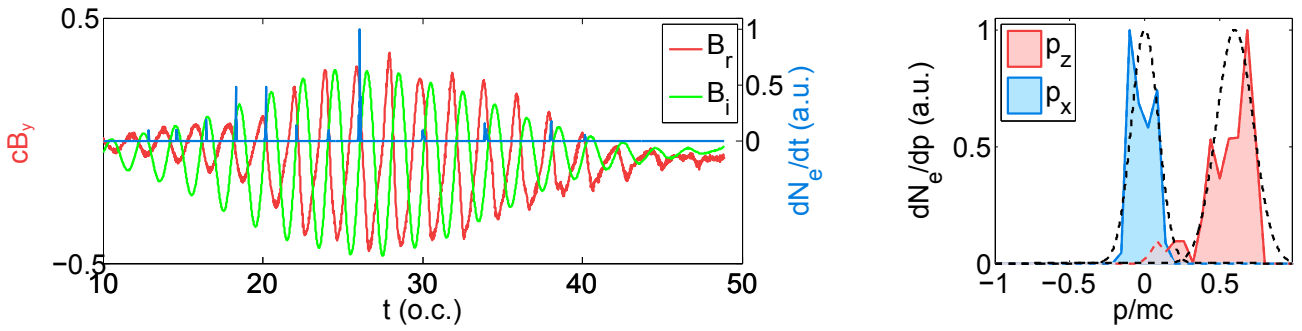


Figure 7.9 – Injecting conditions retrieved from 1D PIC simulations with parameters  $a_0 = 0.4$ ,  $L = \lambda/10$ . The dotted line of the right-hand-side figure corresponds to the initial Gaussian fit used for the 3D particle simulation code.

Using injection conditions from Fig 7.9, we use our 3D particle code to derive the final electron angular profile and get the angular profile corresponding to  $\phi = 0$ , that is to say precisely when the magnetic field  $B_y$  switches from positive to negative. The electrons are all located on the left of the ponderomotive hole. In Fig 7.10(b) we plot the electric field felt by the electrons from the moment they are injected into the laser. The initial electric field is  $< 0$ , which corresponds to an electric force positive towards  $\theta < 0$ , and is consistent with the final electron angular distribution obtained in Fig 7.10(a).

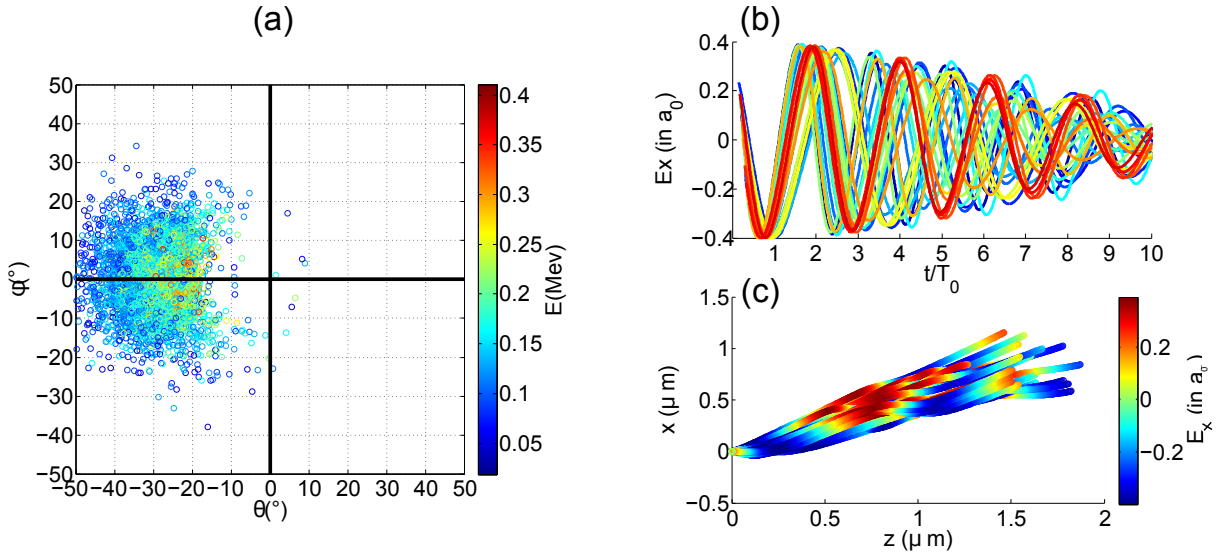


Figure 7.10 – (a) Final electron angular profile. The final energy is indicated by the colorbar. The solid cross indicates the direction of propagation (b) Field  $E_x$  felt by 25 test electrons from the moment they are injected into the propagating laser at position  $(0, 0)$ . (c) Trajectories of these 25 test electrons. The laser characteristics are  $a_0 = 0.4$ ,  $w_0 = 2$ .

In the sub-relativistic regime, electrons are quickly dephased from the laser as illustrated in Fig 7.10(b), where we plotted the field actually felt by 25 test electrons inside the laser field during 10 optical cycles. In other words, they will "see" several oscillations of the laser, which means they experience ponderomotive acceleration. However, it is interesting to see from Fig 7.10(c) how the trajectories, and therefore the final angular distribution, is affected by the initial electron injection phase.

## 7.2.4 Effect of interference field

In a solid-target experiment, accelerated electrons that escape the plasma interact with a beam reflecting off the critical surface. This means that the incident and reflected pulse interfere. We wish to estimate the effect of this interference field on the electron acceleration and spatial shaping. We already saw in the description of standard electron acceleration schemes that interference fields can alter the acceleration mechanism (two wave beating, stochastic heating). However, in these schemes the interference field is constructed with long laser pulses in the plane-wave approximation. For short ( $\sim$  fs) tightly focused ( $\sim \lambda$ ) pulses, it is no longer possible to derive the effect of an interference field using standing plane waves because the electrons can very easily "escape" the field in a time comparable to the laser period. We use our 3D particle code to construct the interference field by building a reflection on the target plane now defined by  $z = 0$  as follows:

- Two laser beams are added with intensities  $a_{01}$  and  $a_{02}$ , respectively. For construction, we impose  $a_{01} = a_{02} = a_0$ . The respective  $\mathbf{k}$  vector directions are obtained by rotating the vector  $(0, 0, 1)$  by respectively  $\theta_1 = -3\pi/4$  and  $\theta_2 = -\pi/4$  in the  $(x, z)$  plane. This leads to  $\mathbf{k}_i \propto (-1, 0, -1)$  and  $\mathbf{k}_r \propto (-1, 0, 1)$  as represented in Fig 7.11.

$$\left\{ \begin{array}{l} E_x \\ E_z \end{array} \right\}_r = \begin{pmatrix} \cos(\theta_1) & \sin(\theta_1) \\ -\sin(\theta_1) & \cos(\theta_1) \end{pmatrix} \begin{pmatrix} E_0 \\ 0 \end{pmatrix} \quad (7.25)$$

$$\left\{ \begin{array}{l} E_x \\ E_z \end{array} \right\}_i = \begin{pmatrix} \cos(\theta_2) & \sin(\theta_2) \\ -\sin(\theta_2) & \cos(\theta_2) \end{pmatrix} \begin{pmatrix} E_0 \\ 0 \end{pmatrix} \quad (7.26)$$

- The field is taken equal to zero in the region  $z < 0$ .
- Electrons are injected at a given phase of the reflected laser from plane  $z = 0$ . Because of the angle of incidence, this implies the relation

$$t_{in} + \frac{x \sin(\pi/4)}{c} = constant$$

Of course, this way of constructing the reflection ultimately leads the field to verify the limit condition of a perfect reflection at the interface  $z = 0$ . This indicates our plasma mirror is represented by a perfect conductor with absolute optical flatness. However, the experimental observation of surface plasmons on plasma mirror (section 6.1, [165]) for uncontrolled gradient length is an indication that the perfect reflector approximation becomes false when increasing the gradient scale length.

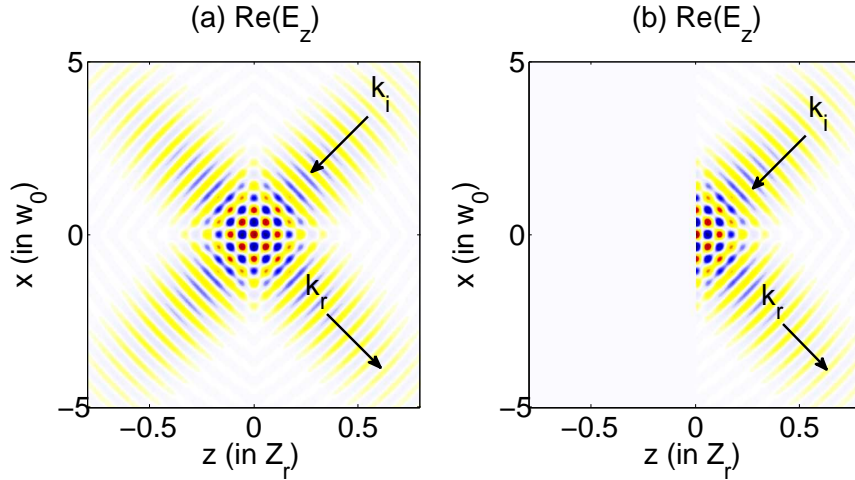


Figure 7.11 – (a) Incident and reflected pulses are propagating in directions respectively  $k_i$  and  $k_r$  with respective intensities  $a_{01}$  and  $a_{02}$ . We then impose the field to be equal to zero in the region  $z < 0$ .

Once this field has been constructed, we can inject test particles into the interference field from the plane  $z = 0$  at any given time  $t_{in}$  and calculate their trajectories in order

to evaluate to possible influence of the interferences ( $a_{02} \neq 0$ ) on both the spatial and spectral properties of the electron beam. In particular, we wonder whether (i) electrons can gain energy in the laser pulse (ii) if electrons can get trapped into the field to be efficiently accelerated.

Note that for the reflected field only, injecting test electrons at a constant phase  $\phi_r$  of the reflected laser beam corresponds to:

$$\mathbf{k}_r \mathbf{r} - \omega_0 t = \phi_r$$

and for the incident beam:

$$\mathbf{k}_i \mathbf{r} - \omega_0 t = \phi_i$$

Therefore, injecting electrons at a given time into the interference pattern, we have  $\phi_i - \phi_r = (\mathbf{k}_i - \mathbf{k}_r) \mathbf{r}$ . In the case of perfect reflection, this implies  $\phi_i = \phi_r$  on a surface parallel to the target, which means a constant phase of the reflected beam is also a constant phase of the incident beam.

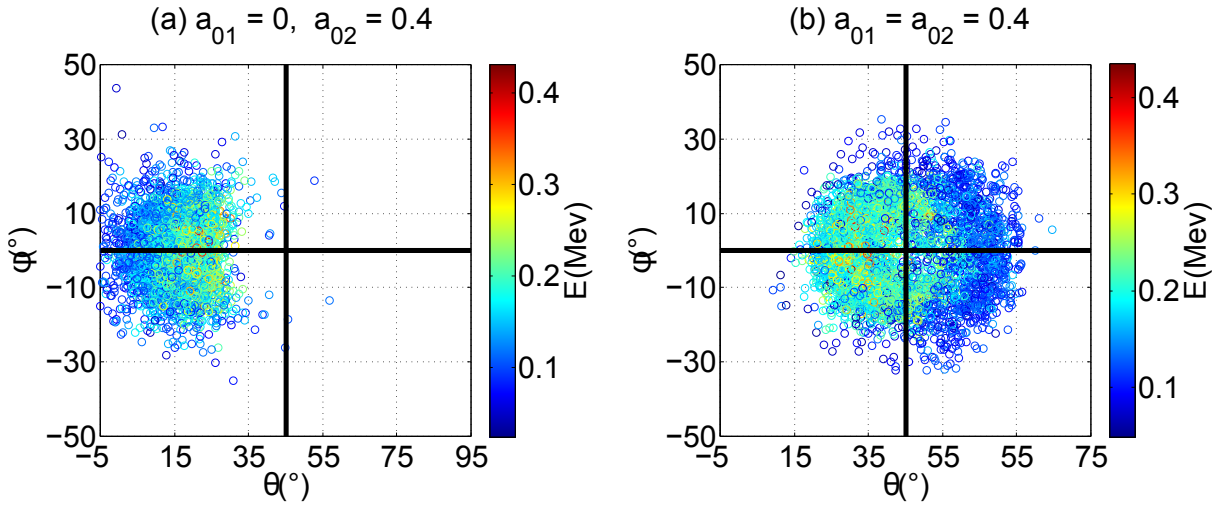


Figure 7.12 – Final angular distribution of electrons for  $a_0 = 0.4$  with (b) and without (a) incident field

The ejected electrons are much closer to the specular direction when taking into account the incident laser. This can be well understood for the case of perfect reflection on the surface  $z = 0$ , where the electric field is along the target normal only, thereby reducing the initial canonical momentum of the electron in the direction  $x$  along the target surface. When taking into account the incident field, the components  $E_x$  and  $B_z$  vanish in the plane of reflection  $z = 0$  because of the perfect reflector hypothesis. This is equivalent to reducing the initial canonical momentum towards  $\theta < 0$  values. We expect the electron angular profile closer to the specular direction, which is indeed the case in our experiment.

## 7.2.5 Non-axis-symmetrical components of the interference field

In section 6.3.3, we mentioned the appearance of  $\phi = 0$  as a plane of symmetry for the electron angular emission profile. In particular, this profile is shown in Fig 7.13 for laser intensities of respectively  $a_0 = 0.7$  and  $a_0 = 1$ .

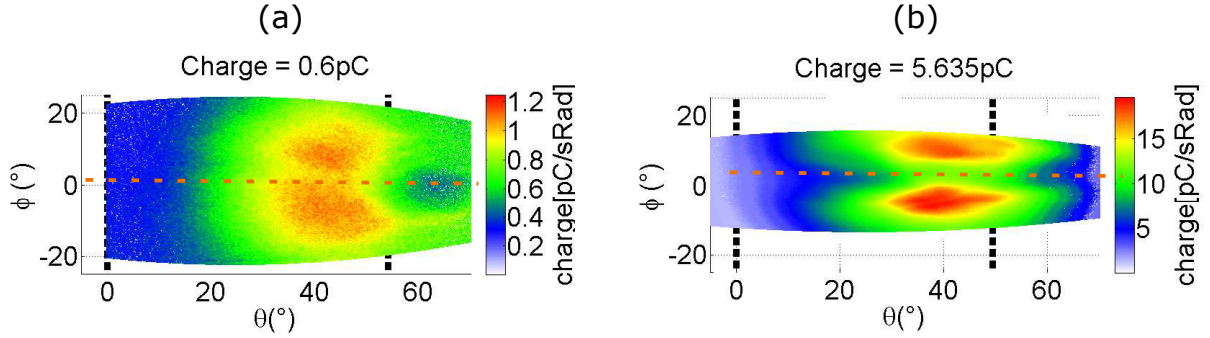


Figure 7.13 – Experimental angular emission profile (a)  $a_0 \sim 0.7$  (b)  $a_0 \sim 1$

The appearance of the depletion line indicated by the dotted orange line in Fig 7.13 can be understood by looking at the symmetry of the  $B_x$  component still remaining from the interference field, represented in Fig 7.14(b). Indeed, in the target plane, the upper part ( $y > 0$ ) of the electrons "feel" a magnetic field  $B_x$  of opposite sign from that of the lower part ( $y < 0$ ). Considering the  $-e\mathbf{v}_z \times \mathbf{B}_x = -ev_z B_x \mathbf{u}_y$  component, and assuming  $v_z > 0$ , the force is directed upward when  $B_x < 0$  and downward when  $B_x > 0$ . This symmetry argument could explain why we observe, at high intensity and in a tight focusing configuration (Fig 7.13(b)), a depletion line in the angular profile rather than a simple ponderomotive hole. Note that without the first-order decomposition of the field with respect to parameter  $\epsilon = \frac{\lambda_0}{2\pi w_0}$ , we would have  $B_x$  rigorously equal to 0, and we could thus not explain our observations.

Based on Fig 7.14, and considering only the zeroth order term of the electromagnetic field (paraxial approximation), the equation of motion in the laboratory referential is written (the component which have disappeared because of the interference field are indicated in red color):

$$\left\{ \begin{array}{l} \frac{d}{dt}[\gamma v_x] = -\frac{e}{m_e} \mathbf{E}_x + \frac{e}{m_e} v_z B_y = -\frac{e}{m_e} \frac{E_0}{\sqrt{2}} (1 - 2\sqrt{2} \frac{v_z}{c}) \\ \frac{d}{dt}[\gamma v_z] = -\frac{e}{m_e} E_z - \frac{e}{m_e} v_x B_y = -\frac{e}{m_e} \frac{2E_0}{\sqrt{2}} (1 + \sqrt{2} \frac{v_x}{c}) \end{array} \right. \quad (7.27a)$$

$$\left\{ \begin{array}{l} \frac{d}{dt}[\gamma v_x] = -\frac{e}{m_e} \mathbf{E}_x + \frac{e}{m_e} v_z B_y = -\frac{e}{m_e} \frac{E_0}{\sqrt{2}} (1 - 2\sqrt{2} \frac{v_z}{c}) \\ \frac{d}{dt}[\gamma v_z] = -\frac{e}{m_e} E_z - \frac{e}{m_e} v_x B_y = -\frac{e}{m_e} \frac{2E_0}{\sqrt{2}} (1 + \sqrt{2} \frac{v_x}{c}) \end{array} \right. \quad (7.27b)$$

Which, using the normalizing conventions of Appendix A we have:

$$\begin{cases} \frac{d}{dt}[\gamma v_x] = -\frac{1}{\sqrt{2}} \frac{\omega_{ce}}{\omega_0} (1 - 2\sqrt{2}v_z) = 2\frac{\omega_{ce}}{\omega_0} v_z & (7.28a) \\ \frac{d}{dt}[\gamma v_z] = -\frac{2}{\sqrt{2}} \frac{\omega_{ce}}{\omega_0} (1 + \sqrt{2}v_x) & (7.28b) \end{cases}$$

FTraject

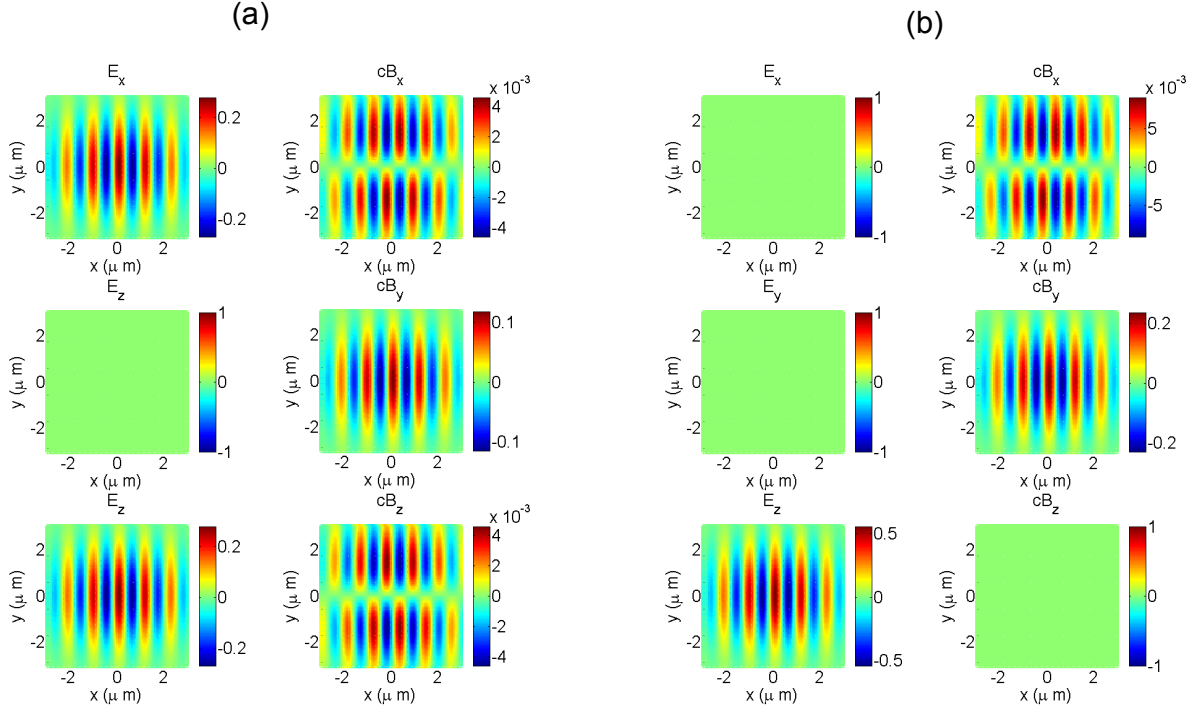


Figure 7.14 – Fields on plane  $z = 0$  at  $t = 0$ , with  $a_0 = 0.4$ ,  $w_0 = 2$  with (a) and without (b) incident field at  $45^\circ$  incident angle

The cancellation of the **electric term** relative to the magnetic term in equation 7.28 leads to the well-described gyromagnetic effect [181], already introduced in section 6.3.4. Indeed, since the magnetic field does not work, its dominant action will force particles to remain in orbits of constant energy, that is to stay closed orbits near the surface. This effect is all the more pronounced as the intensity is high. This is illustrated by the comparison of Fig 7.15 (b) and (c), where test electrons are injected at a node of the magnetic field along a vertical line  $x = 0$ , with or without interference field. we clearly see in Fig 7.15 (b) that electrons initially located in the center  $y \sim 0$  do not escape the surface.

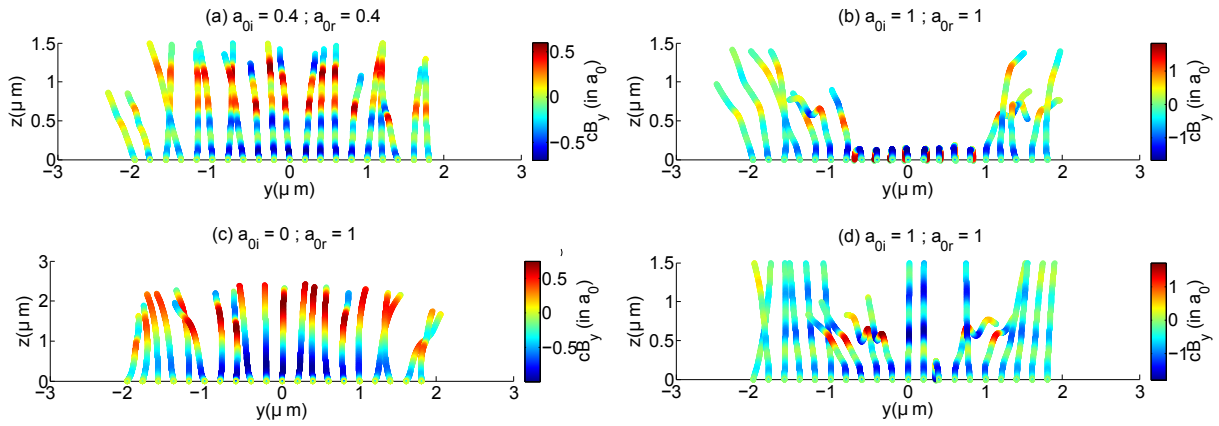


Figure 7.15 – Trajectories over 4 optical cycles of 20 test electrons injected when  $B_y$  becomes negative. The color scale indicates the magnetic field  $B_y$  felt by the electron over time. Test electrons are positioned along a vertical line  $y \in [-w_0 ; w_0]$ . (a) Low-intensity case  $a_0 = 0.4$ ; (b) high-intensity case  $a_0 = 1$  (c) No interference field,  $a_{0r} = 0$  (d) Similar conditions as in (b) when  $p_{0z}$  is doubled for all electrons

### 7.3 Conclusion

We have presented two regimes of acceleration, which we call respectively "ponderomotive" and "non-ponderomotive" regimes. In the first case, electrons are expelled by the laser through the ponderomotive force, and a hole is visible in the final electron angular profile. This regime is dominant at sub-relativistic intensities. When the laser intensity is clearly relativistic, as demonstrated in the literature, electrons can be "trapped" in the laser where they are efficiently accelerated. However, we have observed other singular patterns in the electron angular emission profile such as the appearance of a depletion line along the polarization plane. Using a 3D particle code which accounts for the high-order components of the fields in focus, and taking into account the reflection of the field (mostly valid for short gradient scale length) on a planar surface, it was possible to qualitatively reproduce the electron angular emission profiles obtained experimentally. Indeed, the  $j \times B$  force is oriented differently depending of the initial position of the electron with respect to the polarization plane. Provided that electrons are confined because of the gyromagnetic effect, this depletion line becomes visible. This experiment will be reproduced at 5 fs in the near future, and further investigations still need to be made to fully understand the dynamic of the electron-laser interaction in vacuum.

# Chapter 8

## Conclusion and perspectives

### Conclusion:

Several key experimental results have been obtained during this PhD. First, after a brief introduction of the Brunel mechanism and Coherent Wake Emission, we have presented a series of experiments related to high-order-harmonic generation from plasma mirrors. In particular, we saw how a variation of the consecutive emission times inside an attosecond pulse train has a direct influence on the spectral and spatial properties of the harmonic emission (spectral broadening, spatial modulations and divergence). Since most of those properties have already been described in the literature, we chose to present only experimental results bringing new insight into the understanding of the plasma dynamics.

For instance, we confirmed the drop in HHG signal at very short gradient scale length ( $\ll \lambda/100$ ) and attribute this effect to Landau damping effects due to strong inhomogeneities. Still on HHG emission, we investigated the possible use of FROG-type retrieval algorithms for the temporal reconstruction of the attosecond train emitted in the presence of laser wavefront rotation. On the one hand, we have demonstrated that it was possible to perform a time-to-space mapping of the harmonic emission, and observed an increase in the harmonic femtosecond chirp with increasing plasma scale lengths. This was manifested by a tilt of the angularly-resolved harmonic line spectra. In addition, we successfully implemented a FROG-like algorithm on the numerically generated attosecond traces. However, those traces were generated making the strong hypothesis that they can be written as the product of a space dependent function times a spectral dependent function. This property is a priori not true for the experimental traces, which, in addition to strong noise and signal clipping on the MCP, made the actual reconstruction impossible with experimental data.

Other experimental results presented in this manuscript concern the simultaneous detection of electrons and HHG as a function of the gradient scale length. It was already known that the HHG emission drops and that electron ejection increases with increasing

plasma scale lengths. Here we show for the first time that their relative variation have opposite dependence with respect to the gradient. This transition is due to a modification of the electronic structure at the surface of the plasma mirror where space-charge effects play an increasing role.

Finally, we discussed the spatial profile of the ejected electron beam. We observed the ponderomotive hole formed by the laser and how it disappears when  $L$  increases. We attribute this to a complete destruction of the laser reflected phase front. We have also discussed the gyromagnetic effect, which we believe prevents electrons from escaping the target at high intensity and for short gradient scale lengths. In strong focusing geometries and at high laser intensities, we have shown that the electron profile exhibits a new symmetry with respect to the plane of polarization of the incident laser.

### **Future directions:**

All our experiments have been conducted with a  $\sim 30$  fs laser pulse with sub-relativistic intensities. The laser is currently being upgraded to produce 5 fs pulses on target with the same energy. This will allow us to investigate electron acceleration and ROM-HHG emission from plasma mirrors at relativistic intensities. In addition, the non-linear interactions will be sensitive to the Carrier Envelope Phase (CEP) of the few-cycle pulse, which should allow us to separate attosecond pulses with higher photon energy content, and simultaneously generate electrons with energy of a few MeV.

We already mentioned in the introduction the existence of XFEL sources, which can provide short radiation pulses from UV to hard X-rays (few keV) of few  $\sim$ mJ energy. HHG from plasma mirrors are far from replacing these type of sources today, because the pulses are only on the  $\sim$ nJ level. However, it can be regarded as complementary and low-cost compared to XFELs. Here are some of the advantages we can stress in favor of ultrashort X-UV pulses generation from plasma mirrors:

- **Source tunability:** HHG on plasma mirrors can easily be tuned both spatially and temporally [186] because the generated X-UV inherits the coherence properties of the IR pulse used to drive the interaction. In other words, instead of using XUV optics, which are difficult to find in general, one can for instance shape the laser spatial properties to "mark" the harmonics. Note that this tunability is also true for the HHG in gases. One example of this is the generation of harmonics with orbital angular momentum [187].
- **Separation of attosecond pulses:** Another demonstration of the XUV tunability is the possibility of separating attosecond pulses from one another using STCs on the IR pulse. So far, the attosecond lighthouse has only been demon-

strated in the CWE regime [68]. In future experiments, we will try to isolate XUV pulses from ROM emission and perform XUV-XUV pump-probe experiments with attosecond resolution.

- **Ultrafast XUV non-linear optics:** Two-photon ionization experiments in the X-UV region with high temporal resolution have been performed [188–190]. However, they remain challenging because of low signal-to-noise ratio. If we manage to significantly increase the energy per pulse of the generated ultrashort XUV pulses, we will be able to study the two-photon ionization process on subfemtosecond time scales.
- **High spatial resolution:** Strong focusing of X-UV light for highly resolved imaging is very challenging and relies mostly on the conception of aberration-free demagnification optics [191, 192]. One advantage of HHG from PM over HHG in gases is the possibility of generating X-UV light with focal spot sizes reaching the diffraction limit of the driving laser. The X-UV source has a very small focal spot size itself, and therefore can be tightly refocused using a simple 2f-2f imaging system. This will allow us to perform ultrafast time-resolved experiments with high spatial resolution.

In addition, the PM is an efficient source of fast electrons bunches. In the work presented in this PhD,  $\sim$ pC effective charge per bunch were measured, compared to  $\sim$ fC [193] in the same experimental conditions, but shooting in a Nitrogen gas jet. In future experiments, we will investigate in more details the fine conditions required for efficient trapping of electrons inside the reflecting laser, and therefore the tunability of the electron angular emission profile and final energy spectra with the driving laser. Knowing to what extent we can control the properties of these electrons is crucial to know if they can be used as an actual source to perform time-resolved ( $\sim$ fs resolution) application experiments.

Indeed, electrons escaping the target have a duration comparable to the driving laser pulse duration of the order of a few fs. Ultrafast Electron Diffraction using plasma-generated electrons [194] requires electrons between 1 and 10 MeV, spread over a few  $\mu$ m. After propagation, the electron bunch duration increases because of the initial energy spread. However, each monoenergetic region of the pulse conserves its initial temporal extent [195], which makes it suitable for the study of ultrafast crystalline dynamics through electron diffraction [196].

# List of Figures

1.1	Examples of plasmas sorted by density and temperature . . . . .	12
1.2	Critical density as a function of wavelength . . . . .	16
1.3	(a) Incident laser pulse with degraded temporal contrast on anti-reflection coated wafer (b) Same laser pulse after reflection on the PM. Energy before the main pulse has been lost in the process of ionization . . . . .	17
1.4	Illustration of HHG for a 30fs laser pulse with intensity $I = 10^{18}$ W/cm <sup>2</sup> on a PM with a density of $200n_c$ . The percentage of energy of the incident laser contained in the harmonics is given in yellow colors . . . . .	20
2.1	Artistic representation of resonant absorption for a 1-dimensional electron density distribution $n_e(x)$ . $\mathbf{k}$ is the incident wave vector and $\theta$ is the incident angle. The field is reflected at the critical surface $n_c$ , which coincides with purely normal $\mathbf{E}$ component. This illustration is largely inspired by Figure 2.5 found in [74]. . . . .	28
2.2	Integration of Brunel's equation for an electric field of intensity $a_0 = 1$ ( $a_0$ convention described in AppendixA) and duration $\tau_{fwhm} = 20$ fs. Vacuum is located on the side $x < 0$ and a different color scale is used for electrons emitted from different laser cycles. . . . .	32
2.3	Phase plot comparison between the system of equations 2.16 (right) and its linearized equivalent (left). The trajectories of $\delta\bar{n} = \bar{n} - 1$ and $\nabla\bar{v}$ are integrated and represented for initials perturbation represented by solid circles from $\bar{t} = 0$ to $\bar{t} = 100$ . Final positions are marked with black solid squares. . . . .	35
2.4	Density gradient representation defined by Eq. 2.23, $L = \lambda/40$ and $n_{max} = 250n_c$ . . . . .	36
2.5	Representation of plasma oscillations over one laser period for gradients with $L = \lambda/15$ and $L = \lambda/40$ , where $n_{max} = 250n_c$ . The position where $n_e = 100n_c$ is represented by a solid red line on the left-hand-side figures, and the corresponding plasma oscillation is plotted on the right-hand-side figure . . . . .	37

2.6	1D pic simulation of plasma oscillations over time triggered by an electronic perturbation. The maximum density is $n_e = 100n_c$ the gradients are $\lambda/40$ (left) and $\lambda/300$ (right) respectively. The very short gradient shows damping effect due to strong inhomogeneities of the plasma. The electronic perturbation $\Delta_n = n_c/100$ and propagates at $v_p \approx c$ towards the plasma. The plasma initial temperature is $T_e = 0$ eV . . . . .	41
3.1	Layout of "Salle Noire" laser . . . . .	45
3.2	Principle of XPW (Cross Polarization Wave mixing): a S polarized 30fs pulse propagates non-linearly ( $\chi^{(3)}$ ) in BaF <sub>2</sub> crystals and coherently generates a crossed polarized beam (called XPW) with an efficiency proportional to $(I/I_{max})^3$ . The XPW pulse has an improved contrast and is selected with a Glan polarizer . . . . .	46
3.3	Contrast measurement after XPW contrast cleaning. $\alpha$ is the polarizer angle. $\alpha = 0$ corresponds to optimal alignment. . . . .	47
3.4	SEQUOIA contrast measurement for different angles of the polarizer after XPW. The dotted horizontal line represents an ionization threshold for fused silica arbitrarily set to $10^{12}$ W/cm <sup>2</sup> as an indicator (for $I_{max} = 10^{18}$ W/cm <sup>2</sup> ) . . . . .	47
3.5	SEQUOIA contrast measurement using sequoia after the double CPA with or without is apodization by the dazzler (respectively 30fs and 23fs FTL). (*) beam is blocked to show detector noise level . . . . .	48
3.6	Comparative temporal contrast measurement: removal of optics prior to the second CPA which induce post-pulses, and hence prepulses after the second CPA . . . . .	49
3.7	Block diagram describing the operations performed on the initial pulse leading to prepulse generation. The first three blocks are contained in Eq 3.1 and Eq 3.2. The pulse is compressed by imposing a negative chirp opposite to that induced by the stretcher. . . . .	50
3.8	Spectrum and phase prior to pulse stretching (continuous lines) and after compression (dotted lines) with a postpulse of $\eta = 1\%$ relative intensity added prior to stretching. The chirp factor introduced by the stretching is $\xi = \pm 5$ . When $\xi > +5$ (left), higher phase modulations appear in the blue part of the spectrum. When $\xi < -5$ (right) higher phase modulations appear in the red part of the spectrum. . . . .	51
3.9	Influence of SPM on prepulse generation. The left column represents the chirped pulses temporal profile for $\xi = 0, 0.5, 2.5$ and $5$ before SPM takes place. The right column shows the temporal profile of the pulses after SPM, and after compression (performed by adding $-\xi$ in spectral domain) on a logarithmic scale. For $\xi = 5$ a prepulse is generated at $t = -\tau$ . . .	52

3.10	Result using simulation code <i>Miró</i> . . . . .	53
3.11	(a) Hollow core fiber setup with active stabilization (b) Prepulse generation using a zero-order broadband beamsplitter reflecting 5 to 10% of the main pulse. The pump/probe delay is adjusted by translation of a motorized delay stage with sub - $\mu\text{m}$ resolution. (c) Final compression chamber under vacuum ( $\sim 10^{-5}$ mBar). We compress both main pulse and prepulse on a set of 2 times 4 chirped mirrors introducing $\phi^{(2)} = -250 \text{ fs}^2/\text{bounce}$ ( <i>Ultrafast Innovation</i> ). The main pulse can then be attenuated by translating a home-made optical block from a mirror coated to an uncoated surface with $< 1\%$ transmission. The main pulse is sent to a 2x telescope and the prepulse 0.5x telescope and both collimated pulses are sent to the experimental chamber to be focused on target . . . . .	54
3.12	Attenuator optic: one surface-enhanced Ag-coated ( <i>Femtolaser</i> ), one uncoated bare fused silica surface. Corresponding reflection and GDD are represented . . . . .	55
3.13	Experimental setup of pump/probe experiment on solid target at a 1kHz laser repetition rate . . . . .	56
3.14	Profile recorded at the focus of the parabola (a) Beam expander in the compression chamber (b) Bypassing the beam expander (c) Prepulse profile	57
3.15	Wizzler measurement before the interaction for compressed 24fs pulse (blue curve) and when apodizing the spectrum to improve the laser contrast (red curve), resulting in an increase to 30fs. On left caption, we represent the square of the real part modulus of the field in both cases. . . . .	58
3.16	Solid-target surface after an experiment visualized with an optical microscope (a) Shots on fused silica where shot overlap is due to the low target rotation velocity (b) Shots on fused silica with correct spacing (c) Shots on plastic with correct spacing where different impact sizes correspond to different laser energies . . . . .	59
3.17	Target stabilization setup (a) Reference fringes when the target is not rotating (b) Effect of horizontal phase corresponding to angle $\alpha_x$ variation resulting in fringes spacing (c) Effect of vertical phase corresponding to angle $\alpha_y$ variations resulting in a tilt of the fringes (d) Effect of constant phase shift corresponding to depth fluctuations: translation of the fringes (e) Retrieved $\alpha_x$ , $\alpha_y$ and depth $d$ when target is rotating . . . . .	60
4.1	(a) Experimental setup for HHG detection (b) spherical grating ( <i>Hitachi</i> 001-0639) for home-made spectrometer. The MCP is placed in the spectral plane and imaged using a triggered CCD. . . . .	62

4.2	Trajectories of Brunel electrons in vacuum for a 30 fs Gaussian pulse, $a_0 = 1$ and a gradient length $L = \lambda/100$ . Each laser period, electrons are pulled out of and back into the plasma where trajectories cross. The "crossing" time is represented by the red caustics in the $x < 0$ region ( $x = 0$ defines the critical surface). . . . .	64
4.3	CWE emission time calculated using 1D Brunel model for harmonics 5 to 10, a Gaussian pulse of 30 fs duration, a gradient length $L = \lambda/100$ and laser intensities of $a_0 = 0.2$ and $a_0 = 1$ respectively. . . . .	65
4.4	CWE emission spectral and temporal profile for a 30 fs Gaussian pulse, a gradient length $L = \lambda/100$ and an intensity of $a_0 = 0.4$ . . . . .	66
4.5	CWE experimental spectra for a compressed 26 fs pulse with $a_0 = 0.4$ (left caption) and with a normalized order chirp of $\xi = 0.6$ (right panel) . . .	67
4.6	Gaussian beam representation for X-UV pulse generated at the focus of a driving IR femtosecond pulse. The "generation plane" refers to the solid-target surface. . . . .	68
4.7	A transmission mask (a) is inserted into the collimated IR driving laser prior to the parabola. At focus, the main focal spot (c) splits into 3 replicas (b) relatively separated out by $4 \mu\text{m}$ as a result of diffraction. . .	69
4.8	Retrieved spatial separation $r_1$ between individual HHG sources generated on target as a function of laser defocusing. The result is given for three different harmonic orders (H10, H11 and H12). The $0^{\text{th}}$ order was intentionally saturated to highlight the side bands. . . . .	70
4.9	(a) Experimental harmonic spectra integrated along the vertical direction at different prepulse delays indicated in the colorscale. (b) Corresponding relative intensity of harmonics 9 to 12. Experimental conditions: 30 fs laser pulse with $a_0 = 0.35$ . The prepulse intensity is $1.3 \times 10^{14} \text{ W/cm}^2$ . . . . .	71
4.10	2D PIC simulation using Epoch: Influence of gradient length on CWE efficiency for $a_0 = 0.4$ and gradient scale lengths of respectively $L = \lambda/5, \lambda/10, \lambda/20, \lambda/40$ and $\lambda/80$ . The peak at $\omega/\omega_0 = 15$ corresponds to a numerical resonance and is non-physical; the efficiency is plotted on a log scale. . . . .	71
4.11	Modelling of CWE emission spectra between H7 and H20 for a pulse of 30 fs, a gradient length $L = \lambda/100$ for laser intensity of $a_0 = 0.4$ and a waist $w_0 = 2.5 \mu\text{m}$ . . . . .	72
4.12	(a) CWE temporal emission along $y$ direction for a 30 fs Gaussian pulse, a gradient length $L = \lambda/100$ . The laser intensity of $a_0 = 0.4$ and its waist $w_0 = 2.5$ . (b) Zoom on one attosecond pulse over one laser period. . . . .	73

4.13 (a) Effect of propagation direction for different laser wavelengths when two wedges are parallel (b) One of the wedges is tilted: the propagation direction for each wavelength is tilted by $\theta(\lambda)$ with respect to the initial case. . . . .	74
4.14 Influence of spatial chirp at focus in artistic view. Top: no WFR when all wavelengths are spatially overlapped. Bottom: WFR because low frequencies are shifted towards the $y > 0$ region and high frequencies towards the $y < 0$ region. . . . .	75
4.15 Experimental setup: Wedges are introduced in the main beam path in a parallel configuration (a). WFR is obtained by turning one of the wedges with respect to the other (b) . . . . .	78
4.16 Imaging spectrometer at $0^{th}$ order with an open slit (left) after setting the calibration $0.09 \mu\text{m}/\text{px}$ . The measured focal spot is $4 \mu\text{m}$ (FWHM). Comparison to an image given by our standard imaging camera (right) . . . . .	78
4.17 Comparison of model to experimental measurement of vertically resolved pulse spectra with WFR at focus, where $y$ is given in $\mu\text{m}$ . In the model (left) we considered a 30 fs pulse with the spatial dimension as measured experimentally. The spectra $S(\omega, y)$ is obtained by shearing the coordinate as described in 4.2.2. The experimental measured spectra are obtained by rotating the wedges of $\theta = 0^\circ$ (top), $15^\circ$ , $30^\circ$ , $40^\circ$ , $50^\circ$ , $60^\circ$ and $70^\circ$ (bottom) in order. . . . .	79
4.18 Evaluation of $V_{rot}$ with respect to angular dispersion $\beta$ calculated for each angular position of the wedges using the analytical model described in 4.2.2	80
4.19 Simulated (top) and experimental (bottom) influence of WFR on harmonic spectra for $a_0 = 0.1$ . . . . .	81
4.20 Angularly-resolved harmonic spectra recorded on the MCP with WFR. The prepulse intensity is $\sim 10^{14} \text{ W}/\text{cm}^2$ . . . . .	82
4.21 Result of iterative SVD FROG algorithm for input trace generated using $V_{rot} = -2 \text{ mrad}/[T_0]$ , where the residual error is $< 0.5\%$ . The initial harmonic field is represented in blue (top right), where we superimposed in red the retrieved field after 500 iterations. The corresponding gate is represented in the bottom right plot. . . . .	84
4.22 Experimental attosecond FROG traces for $a_0 = 0.15$ . Top: Laser spectrum is apodized which yields to a compressed pulse of 30 fs, Bottom: compressed laser to 23 fs (see Chapter 3 for description of apodisation method) . . . . .	85

5.1	SDI principle applied to ultrafast plasma mirror imaging: the probe field $E(x, y)$ is diffracted by a transmission mask $T_M$ (a) onto a plasma mirror in the focusing plane (b). The phase shift, $\Delta\phi$ , of the central diffraction spot induced by the plasma expansion leads to a modulation of the far-field spatial intensity profile(c) of the reflected probe with respect to $\Delta\phi$ . . . . .	89
5.2	Illustration of gradient expansion with $c_s = 10$ nm/ps for a prepulse delay of respectively $t = 0, 2$ and 10ps. The initial gradient scale length is taken $\delta L = \lambda/100$ . The IR probe pulse is shown to reflect on the critical density at respectively 2 and 10ps. . . . .	91
5.3	(a) Entrance slit for XUV generation (b) Silver mirror for prepulse (c) Holed mirror for main pulse (probe) (d) Transmission mask (e) Off-axis $f/1.2$ focusing parabola (f) Camera placed under vacuum imaging the entrance slit. . . . .	93
5.4	Simulated and experimental far-field probe beam intensity profile inversions at respectively 0 ps(a) 6 ps(b), 12 ps(c) and 20 ps(d) pump-probe delay. The simulations are performed using the measured pump beam profile and assuming the plasma expansion velocity $c_s \propto \sqrt{I_p}$ . . . . .	94
5.5	Measurement of plasma relative expansion for a prepulse intensity of $I_{p,1} = 3.5 \times 10^{14}$ W/cm <sup>2</sup> as a function of pump-probe delay. Each experimental point corresponds to a $\pi$ inversion in the intensity profile of the reflected probe. The corresponding linear fit allows one to retrieve a plasma expansion velocity of $c_s \approx 10.8$ nm/ps . . . . .	94
5.6	Definition of the variables $a$ : mask spacing, $T$ : plasma transfer function on target, $E_{ref}$ : field on target when $T = 1$ , $E_{ref,0}$ : 0 <sup>th</sup> order diffracted spot on target, $E_{exp}$ : field on target for arbitrary $T$ , $r$ : distance from center to first diffraction order, $\Sigma$ : reflected far-field conjugate to mask holes, $\bar{\Sigma}$ : reflected far-field conjugate to mask . . . . .	96
5.7	Image recorded on the glass diffuser positioned in the specular direction of the probe beam as represented in (a). Superimposed pump and probe spatial profiles for a mask spacing of $a = 0.8$ mm (b) and $a = 1.7$ mm mask (c). Profile on diffuser integrated over 50 consecutive shots with no prepulse for $a = 0.8$ mm (d) and $a = 1.7$ mm (e). The probe intensity is high enough to induce ionization on several diffracted orders. . . . .	97
5.8	Contrast evolution of the far-field for 3 different prepulse energies $E = 90, 220$ and $385 \mu\text{J}$ , respectively (corresponding to prepulse intensity $I_p = 4, 10$ and $18 \times 10^{14}$ , W/cm <sup>2</sup> , respectively). $\bar{\Sigma}$ (top), $\Sigma$ (bottom). . . . .	98
5.9	Image over $\bar{\Sigma}$ for a prepulse energy on target of $385 \mu\text{J}$ and a pump-probe delay of 30ps. In the case where prepulse and probe are misaligned on target: tilted fringes indicating a break in symmetry . . . . .	99

5.10	Simulated effect of beam misalignment on reflected far-field intensity of pump-probe for a maximum phase shift $\pi$ induced by the prepulse. (b)(c)(d) where both beams are superimposed at focus (left captions). Corresponding far fields are obtained by Fourier transform (right captions). (a): reference in case of no prepulse . . . . .	100
5.11	Experimental screen shot obtained by Adrien Denoeud during SDI measurements performed with UHI100 laser at CEA Saclay. . . . .	100
5.12	Evolution of the reflectivity as a function of chirp for an energy on target of 0.1mJ. Each data point corresponds to the integration of 50 consecutive shots. . . . .	101
5.13	Fienup phase retrieval principle . . . . .	102
5.14	Construction of object $f$ : The central Gaussian source $E_{ref,\sigma}$ is multiplied by the plasma complex transfer function $T$ without affecting the other sources positioned symmetrically around $x = 0$ , which we define as $E_{ref,\bar{\sigma}}$	103
5.15	Phase reconstruction (a): initial modulus and phase of object on $\sigma$ (plain) and reconstructed object using Fienup algorithm (dotted). (b): constraint modulus in Fourier space (black plain) and reconstructed modulus (green dotted) after 200 iterations. . . . .	104
5.16	Amplitude and phase reconstructions . . . . .	106
5.17	Phase reconstruction error for a symmetric reference field on $\bar{\sigma}$ (blue) and when this symmetry is broken (red) . . . . .	107
5.18	Amplitude and phase reconstructions for non symmetric reference field on $\bar{\sigma}$	108
5.19	Result of central object phase reconstruction after 20 iterations using non symmetrically distributed sources. The residual reconstruction error measured in the Fourier modulus is $e = 5 \times 10^{-4}$ . . . . .	110
6.1	Experimental setup: Main pulse and prepulse are focused on a rotating fused silica target with an off-axis parabola. The HHG signal is detected in the specular direction and the electronic emission with a LANEX screen placed normal to the target. Both signals are recorded simultaneously for each firing sequence (integration over $\sim 100$ laser shots). Prepulse intensity on target: $\sim 10^{14}$ W/cm <sup>2</sup> , Main laser intensity on target $\sim 10^{18}$ W/cm <sup>2</sup> . . . . .	117
6.2	LANEX response based on Monte Carlo simulations [173] . . . . .	117
6.3	Experimental results comparing simultaneous harmonic and electron emission for a prepulse (pump) intensity of (a) $I_p = 1.2 \times 10^{15}$ W/cm <sup>2</sup> and (b) $I_p = 3.5 \times 10^{14}$ W/cm <sup>2</sup> . In both cases, the main (probe) laser intensity is $a_0 = 0.85$ . The LANEX detection range in the horizontal plane is $\theta \in [-20^\circ \ 35^\circ]$ . The azimuthal spread was artificially extended to show the specular angle of $49.3^\circ$ indicated by the green dotted line . . . . .	118

6.4	Artistic representation of HHG/electron anticorrelated behavior of plasma mirrors. (a) Efficient CWE generation for $L/\lambda < 0.05$ (b) Efficient electron ejection for $L/\lambda \sim 0.1$ . . . . .	119
6.5	Integrated counts on MCP and LANEX measuring respectively the harmonic and electron generation efficiencies with respect to focus position in $\mu m$ . The focal spot size is $3.5 \mu m$ FWHM. . . . .	121
6.6	<b>Scan-a0-0.8</b> simulations.(a) HHG emission spectrum in log scale for initial plasma scale length $L_g/\lambda \in [1/80 \ 1/2.5]$ (b) Ejected charge in $pC/\mu m$ for respectively $8\lambda$ (probe 2) and $9\lambda$ (probe1) from plasma edge ( $n_c/5$ ) . . . .	122
6.7	<b>Scan-a0-0.4</b> simulations. (a) HHG emission spectrum in log scale for initial plasma scale length $L_g/\lambda \in [1/80 \ 1/5]$ (b) Ejected charge in $pC/\mu m$ for respectively $8\lambda$ (probe 1) and $9\lambda$ (probe2) from plasma edge ( $n_c/5$ ) . .	123
6.8	2D PIC simulation using the simulation code EPOCH comparing the $a_0 = 0.4$ and $a_0 = 0.8$ simulation cases. (a) and (b) HHG spectral emission integrated along its divergence as a function of initial plasma scale length. (c) and (d): electron angular emission as a function of plasma scale length. The laser specular direction at $45^\circ$ is indicated by the dotted green line. .	124
6.9	Ejected charge retrieved from 2D PIC simulations for density of $250n_c$ and $a_0 = 0.4$ as function of gradient scale length $L_g$ . . . . .	124
6.10	(a) Spherical parametrization of the coordinates (b) Top view . . . . .	125
6.11	Projection on the LANEX plane $\mathcal{L}$ of an isotropic ballistic emission for respectively $\mathcal{L} : y = -10$ (bottom left) and $\mathcal{L} : y = -x - 10$ (bottom right) . . . . .	127
6.12	(a) Layout of the experiment: the electron signal is recorded along a given plane for different positions of the CCD (illustrated by blue and orange colors). (b) Simulation of the effect due to LANEX Lambertian emission. A Gaussian distribution is represented by the dotted line. Each successive color lines correspond to this signal intensity for a displacement of $\Delta x$ . Each color corresponds to a displacement of 1cm. (c) Experimental results obtained by translating the LANEX along $\mathcal{L} : y = -0.46x + 10$ (cm) as a comparison. CCD counts are integrated in the vertical direction. . . . .	128
6.13	(a) R reconstruction: average over 20 sequences of 100 shots each (b) Corresponding polynomial fit of LANEX response as a function of incident angle on camera objective . . . . .	129
6.14	Projection on the LANEX (indicated with black solid line) of the electron angular distribution. One can clearly see the loss of information due to the geometrical position of the LANEX and its non-isotropic emission response	130

6.15	Experimental setup for electron detection in the specular direction. Pre-pulse: $I \sim 10^{14} \text{ W/cm}^2$ and main pulse: $I \sim 10^{18} \text{ W/cm}^2$ . The laser incidence angle is $50^\circ$ . . . . .	131
6.16	Image of HHG entrance slit with (a) or without (b) prepulse . . . . .	133
6.17	Influence of laser contrast on electron angular distribution. LANEX plane $\mathcal{L} : y = -0.51x + 7.7(\text{cm})$ . Both normal and specular directions are indicated by back dotted lines at respectively $0^\circ$ and $54^\circ$ . Laser intensity is $a_0 = 0.6$ , focal spot size $2.5 \mu\text{m}$ FWHM. . . . .	135
6.18	Experimental electron angular distribution in the plane of laser polarization for an intensity on target $a_0 = 0.77$ for a waist of $2.5 \mu\text{m}$ FWHM. Prepulse intensity is $I_p = 2 \times 10^{14} \text{ W/cm}^2$ . . . . .	136
6.19	Laser focus z-scan $\Delta z$ while measuring the electron angular emission profile. The pulse duration is 30 fs with $a_0 = 0.6$ (the left column) and 23 fs with $a_0 \sim 0.7$ (right column). Laser focal spot size is $2.2 \mu\text{m}$ FWHM . . .	138
6.20	Electron spectrometer setup . . . . .	139
6.21	Electron spectra normal to target. Signal is recorded when no prepulse is added, for a pump-probe delay $\delta t$ corresponding to an optimum on the LANEX, and for long pump/probe delays . . . . .	140
6.22	Electron spectra for various angles $\theta \in [0^\circ \ 40^\circ]$ . $a_0 = 0.7$ , $L/\lambda \sim 0.1$ . Pump/probe delay is 6 ps with a prepulse intensity of $3 \times 10^{14} \text{ W/cm}^2$ .	141
7.1	63 test electron trajectories in a Gaussian beam. All particles are injected at time $t = 0$ when the laser is at focus. Particles are initially at rest and located in the domain $x_{i0} \in [-w_0 \ w_0]$ , $z_{i0} \in [-Z_r \ Z_r]$ . The laser is 30 fs FWHM and the simulation performed from $t = 0$ to $t = 30$ fs. Laser parameters: (a) $w_0 = 3 \mu\text{m}$ , $a_0 = 0.1$ , (b) $w_0 = 3 \mu\text{m}$ , $a_0 = 1$ , (c) $w_0 = 0.4 \mu\text{m}$ , $a_0 = 0.1$ , (d) $w_0 = 0.4 \mu\text{m}$ , $a_0 = 1$ , . . . . .	146
7.2	Final energy distribution after $t = 30$ fs at $a_0 = 1$ for $w_0 = 0.4$ (red) and $w_0 = 3$ (blue) for 2500 test particles . . . . .	147
7.3	$E_x(x, y, z = 0)$ is a Gaussian beam of waist $w_0$ . $E_z(x, y)$ calculated with Eq 7.21 for $w_0 = 100\lambda$ and $w_0 = 0.5\lambda$ All images are normalized by the maximum value of $ E_x $ . . . . .	150
7.4	Schematic view of the 3D particle code: $z$ is the direction of propagation and $x$ the direction of the zero order Gaussian beam $E_x^{(0)}$ . $\theta$ : angle in the (x,z) plane with the conventions $\theta < 0$ toward the target normal, and $\phi$ the angle in vertical plane . . . . .	151

7.5	Result of 3D particle code showing final electron angular distribution with final kinetic energy $E_c = (\gamma - 1)m_e c^2$ in color scale. 5041 test particles initially at rest are randomly injected in the cylinder defined by $z_0 \in [-Z_R \ Z_R]$ , $r_0 \in [0 \ w_0]$ in a $\tau_{fwhm} = 30$ fs, $a_0 = 1$ focused laser beam polarized in the plane $\phi = 0$ with a waist of respectively $w_0 = 3$ (left) and $w_0 = 0.4$ (right).	152
7.6	$Z_{eff}$ as a function of $a_0$ and initial momentum $p_{z0}/mc$ from Fig 7.7 for relativistic case $a_0 \sim 2.5$ . Here, $\lambda = 0.8 \mu m$	153
7.7	(a) Initial conditions of injected electrons (screen shot from Reference [67]) extracted from 1D PIC simulation. Particles are injected when the magnetic field $B_y$ switches to positive values with random distribution $t_0 \in [-0.33$ fs ; $0.33$ fs] Laser conditions: $a_0 = 2.5$ , $\tau_{FWHM} = 15$ fs, $w_0 = 5 \mu m$ and $\lambda = 0.8 \mu m$ . (b) Angular distribution of ejected electrons were (each point corresponds to an electron). The colorbar indicates the final energy in MeV.	154
7.8	$Z_{eff}$ as a function of $a_0$ and initial momentum $p_{z0}/mc$	155
7.9	Injecting conditions retrieved from 1D PIC simulations with parameters $a_0 = 0.4$ , $L = \lambda/10$ The dotted line of the right-hand-side figure correspond to initial Gaussian fit used for the 3D particle simulation code	155
7.10	(a) Final electron angular profile. The final energy is indicated by the colorbar. The solid cross indicates the direction of propagation (b) Field $E_x$ felt by 25 test electrons from the moment they are injected into the propagating laser at position $(0,0)$ . (c) Trajectories of these 25 test electrons. The laser characteristics are $a_0 = 0.4$ , $w_0 = 2$ .	156
7.11	(a) Incident and reflected pulses are propagating in directions respectively $k_i$ and $k_r$ with respective intensities $a_{01}$ and $a_{02}$ . We then impose the field to be equal to zero in the region $z < 0$ .	157
7.12	Final angular distribution of electrons for $a_0 = 0.4$ with(b) and without(a) incident field	158
7.13	Experimental angular emission profile (a) $a_0 \sim 0.7$ (b) $a_0 \sim 1$	159
7.14	Fields on plane $z = 0$ at $t = 0$ , with $a_0 = 0.4$ , $w_0 = 2$ <b>with</b> (a) and without (b) incident field at $45^\circ$ incident angle	160
7.15	Trajectories over 4 optical cycles of 20 test electrons injected when $B_y$ becomes negative. The color scale indicates the magnetic field $B_y$ felt by the electron over time. Test electrons are positioned along a vertical line $y \in [-w_0 ; w_0]$ . (a) Low-intensity case $a_0 = 0.4$ ; (b) high-intensity case $a_0 = 1$ (c) No interference field, $a_{0r} = 0$ (d) Similar conditions as in (b) when $p_{0z}$ is doubled for all electrons	161
D.1	Representation of a Gaussian pulse	XVI

D.2	Representation in the plane $(r, z)$ where $z$ indicates the direction of the resulting intensity where $w_{0i} = 400 \text{ nm}$ , $z_{0i} = 0$ , $r_{01} = -r_{03} = 2.4 \mu\text{m}$ , $r_{02} = 0$ and $\lambda = 80 \text{ nm}$ . . . . .	XVIII
D.3	Fourier transform of intensity interference pattern for harmonic H10 ( $\lambda = 80 \text{ nm}$ ). Initial conditions are $z_{0i} = 0$ , $w_{0i} = \lambda_0$ and $r_{01} = 5\lambda_0$ . We then vary one parameter: (a) influence of central source defocus (b) influence of central source waist (c) influence of global waist variation (d) influence of satellite sources distance $r_{01}$ . . . . .	XIX

# List of Tables

1.1	Example of different laser performances . . . . .	15
6.1	EPOCH input . . . . .	121

# Appendix A

## Normalization conventions

When posing and solving a differential equation, one should always begin by adimensioning the system in order to neglect irrelevant terms depending on the parameter scaling. Let's define a normalizing convention for all physical variables:

$$\left\{ \begin{array}{l} \bar{t} = \omega_0 t \\ \bar{v} = \frac{v}{V_e} \\ \bar{r} = \frac{r}{L_0} \\ \bar{n} = \frac{n}{n_{e0}} \\ \bar{\rho} = \frac{\rho}{en_{e0}} \\ \bar{j} = \frac{j}{en_{e0}V_e} \\ \bar{E} = E/E_0 \quad \bar{B} = B/B_0 \end{array} \right. \quad (\text{A.1})$$

where  $\omega_0$  is a frequency,  $V_e$  a velocity,  $L_0$  a length,  $n_{e0}$  a density,  $e$  is the elementary electric charge, and  $E_0$  and  $B_0$  are an electric and a magnetic field.

### A.0.1 Constant and physical parameters

All these adimensioning constants are “a priori” independent from one another. However, in many physical systems (example or light propagating in vacuum) they can be strongly coupled. Here we define other normalizing variables which will be necessary depending on the physical system of equations we study.

**Definition:**


---

Plasma frequency	$\omega_P = \sqrt{\frac{e^2 n_{e0}}{\epsilon_0 m_e}}$
Critical density	$n_c = \frac{\epsilon_0 m_e \omega_0^2}{e^2}$
Electron quiver velocity	$v_{osc} = \frac{e E_0}{m_e \omega_0}$
Cyclotron pulsation	$\omega_{ce} = \frac{e B_0}{m_e}$
Debye length	$\lambda_D = \sqrt{\frac{\epsilon_0 k_b T_e}{e^2 n_{e0}}} = \frac{1}{\omega_p} \sqrt{\frac{k_b T_e}{m_e}}$
Fermi Temperature	$T_F = \frac{1}{8} \left(\frac{3}{\pi}\right)^{2/3} \frac{\hbar^2 n_e^{2/3}}{k_b m_e}$
Thermal de Broglie wavelength	$\lambda_B = \frac{\hbar}{m_e v}$
Coulomb Logarithm	$\ln(\Lambda) = \ln\left(\frac{\lambda_D}{\lambda_C}\right)$
Electron collision time scale	$\nu_{ee} = \frac{e^4 \ln(\Lambda) n_{e0}}{4\pi \epsilon_0^2 m_e^{1/2} T_e^{3/2}} = 3 \times 10^{-6} n_e (cm^{-3}) \ln(\Lambda) [T_e (eV)]^{(-3/2)}$

---

**Adimensionned parameters:**


---

Normalized intensity	$a_0 = \frac{v_{osc}}{c} = \frac{e E_0}{m_e \omega_0 c}$
Electron coupling parameters	$\Gamma_{ee} = \left(\frac{1}{\lambda_D n_{e0}^{1/3}}\right)^2 \approx 14.4 \left[\frac{n_e (m^{-3})}{10^{30}}\right]^{1/3} \frac{1}{T (eV)}$

---

**Physical constants:**


---

$\epsilon_0$	$8.854 \times 10^{-12} F/m$
$\mu_0$	$4\pi \times 10^{-7} N/A^2$
$k_b$	$8.617 \times 10^{-5} eV/K$
$m_e$	$9.1 \times 10^{-31} kg$
$e$	$1.6 \times 10^{-19} C$

---

**A.1 Maxwell's equations****A.1.1 General Maxwell's equations**

The most general formulation of Maxwell's equations is:

$$\left\{ \begin{array}{l} \nabla \times \mathbf{H}(\mathbf{r}, t) = \partial_t \mathbf{D}(\mathbf{r}, t) + \mathbf{j}(\mathbf{r}, t) \\ \nabla \cdot \mathbf{D}(\mathbf{r}, t) = \rho(\mathbf{r}, t) \\ \nabla \times \mathbf{E}(\mathbf{r}, t) = -\partial_t \mathbf{B}(\mathbf{r}, t) \\ \nabla \cdot \mathbf{B}(\mathbf{r}, t) = 0 \end{array} \right. \quad (\text{A.2})$$

with by definition:

$$\left\{ \begin{array}{l} \mathbf{B} = \mu_0 \mathbf{H} + \mathbf{M}(\mathbf{H}) \\ \mathbf{D} = \epsilon_0 \mathbf{E} + \mathbf{P}(\mathbf{E}) \end{array} \right. \quad (\text{A.3})$$

Electric and magnetic fields have used to calculate the Lorentz force felt by a single charge  $q$  of velocity  $\mathbf{v}$ , which expression is given by:

$$\mathbf{F}(\mathbf{r}, t) = q(\mathbf{E}(\mathbf{r}, t) + \mathbf{v} \times \mathbf{B}(\mathbf{r}, t))$$

$\mathbf{M}$  and  $\mathbf{P}$  are related to external fields  $\mathbf{E}$  and  $\mathbf{H}$  with the use of phenomenological laws.

### A.1.2 Energy conservation

Taking  $\mathbf{E}$  et  $\mathbf{H}$  as real functions, we can derive from Sytem A.2:

$$\partial_t \left[ \frac{\epsilon_0 |\mathbf{E}|^2}{2} + \mu_0 \frac{|\mathbf{H}|^2}{2} \right] = -\nabla \cdot [\mathbf{E} \times \mathbf{H}] - \mathbf{E} \partial_t \mathbf{P} - \mathbf{j} \cdot \mathbf{E} - \mathbf{H} \partial_t \mathbf{M} \quad (\text{A.4})$$

This equation clearly outlines the different sources of energy transfer:

- The kinetic energy of a charged particle:  $\partial_t [E_{kin}] = \partial_t [\frac{1}{2} m \mathbf{v}^2] = m \mathbf{v} \dot{\mathbf{v}} \propto \mathbf{j} \cdot \mathbf{E}$ . Charges in motion absorb the electromagnetic energy from an electric field which translates into kinetic energy.
- The terms  $\mathbf{E} \partial_t \mathbf{P}$  and  $\mathbf{H} \partial_t \mathbf{M}$  are potential energies due to dipole respectively electric and magnetic dipole interactions. For a linear response of the dipoles:  $\mathbf{P} = \epsilon_0 \chi \mathbf{E}$  et  $\mathbf{M} = \mu_0 \chi_m \mathbf{H}$ .
- The term  $\nabla \cdot [\mathbf{E} \times \mathbf{H}]$  corresponds to an energy flux.  $\mathbf{E} \times \mathbf{H}$  is commonly called the Poynting vector, and is collinear to the momentum of the electromagnetic wave.

### A.1.3 Maxwell's equations in vacuum

Maxwell's equation in vacuum are given :

$$\left\{ \begin{array}{l} \nabla \times \mathbf{B}(r, t) = \mu_0 \epsilon_0 \partial_t \mathbf{E}(r, t) \quad \text{Maxwell-Ampère} \\ \nabla \cdot \mathbf{E}(r, t) = 0 \quad \text{Maxwell-Gauss} \\ \nabla \times \mathbf{E}(r, t) = -\partial_t \mathbf{B}(r, t) \quad \text{Maxwell-Faraday} \\ \nabla \cdot \mathbf{B}(r, t) = 0 \quad \text{Maxwell-Thomson} \end{array} \right. \quad (\text{A.5})$$

Note that in order to define the electromagnetic completely, we need the full expression of  $(E_x, E_y, E_z) \in \mathcal{L}^2(\mathbb{C})^3$  and  $(B_x, B_y, B_z) \in \mathcal{L}^2(\mathbb{C})^3$ . For a monochromatic beam of frequency  $\omega$ , the temporal dependence vanishes from Eq A.5 to give:

$$\begin{cases} \nabla \times \mathbf{B}(\mathbf{r}) = -i\frac{\omega}{c^2}\mathbf{E}(\mathbf{r}) & \text{(A.6a)} \\ \nabla \cdot \mathbf{E}(\mathbf{r}) = 0 & \text{(A.6b)} \\ \nabla \times \mathbf{E}(\mathbf{r}) = i\omega\mathbf{B}(\mathbf{r}) & \text{(A.6c)} \\ \nabla \cdot \mathbf{B}(\mathbf{r}) = 0 & \text{(A.6d)} \end{cases}$$

From Eq A.6, it becomes quite straightforward that if  $\mathbf{B}(\mathbf{r})$  is fully known,  $\mathbf{E}(\mathbf{r})$  is immediately derived using Eq A.6a. Moreover, Eq A.6d implies that the components of  $\mathbf{B}$  can not be chosen independently from one another but that only 2 degrees of freedom are allowed. The same demonstration can be performed for  $\mathbf{E}$  since  $\mathbf{E}/c$  and  $\mathbf{B}$  are completely interchangeable in the equations. As a conclusion, only two components ( $(E_x, E_y)$ , or  $(E_x, E_z)$ , or  $(E_x, B_x)$ , or...) are necessary to completely determine the field  $(\mathbf{E}, \mathbf{B})$  (all constant fields are considered equal to zero).

### A.1.4 Intensity profile of a Gaussian pulse

The intensity on a given plane is defined by:

$$I[\text{W/cm}^2] = \underbrace{\frac{2e_0}{w_0^2\pi}}_{\text{spatial factor}} \underbrace{\frac{2\sqrt{\ln(2)}}{\tau_{fwhm}\sqrt{\pi}}}_{\text{temporal factor}} \exp\left(-\frac{4\ln(2)t^2}{\tau_{fwhm}^2}\right) \exp\left(-\frac{2r^2}{w_0^2}\right) \quad \text{(A.7)}$$

where  $w_0$  is the laser waist,  $\tau_{fwhm}$  the temporal Full Width at Half Maximum and  $e_0$  the pulse energy. In laser plasma interaction, the expression of the normalized intensity  $a_0$  is given by the relation:

$$a_0 = 0.855\lambda[\mu\text{m}]I^{1/2}[10^{18}\text{W/cm}^2] \quad \text{(A.8)}$$

The intensity is said to be relativistic when  $a_0 > 1$ .

### A.1.5 Maxwell's equations in plasmas

We suppose  $\mathbf{P} = \mathbf{0}$  and  $\mathbf{M} = \mathbf{0}$ .

$$\begin{cases} \nabla \times \mathbf{B}(\mathbf{r}, t) = \mu_0\epsilon_0\partial_t\mathbf{E}(\mathbf{r}, t) + \mu_0\mathbf{j}(\mathbf{r}, t) & \text{Maxwell-Ampère} \\ \nabla \cdot \mathbf{E}(\mathbf{r}, t) = \rho(\mathbf{r}, t)/\epsilon_0 & \text{Maxwell-Gauss} \\ \nabla \times \mathbf{E}(\mathbf{r}, t) = -\partial_t\mathbf{B}(\mathbf{r}, t) & \text{Maxwell-Faraday} \\ \nabla \cdot \mathbf{B}(\mathbf{r}, t) = 0 & \text{Maxwell-Thomson} \end{cases} \quad \text{(A.9)}$$

### A.1.6 Charge conservation

$$\partial_t \rho + \nabla \cdot \mathbf{j} = 0 \quad (\text{A.10})$$

## A.2 Equation and scaling laws

### A.2.1 Propagation of the electromagnetic fields

From system A.9, we can derive the equations of propagation for  $\bar{\mathbf{E}}$  and  $\bar{\mathbf{B}}$ , which we write using the normalizing conventions defined in A.1:

$$\left\{ \begin{array}{l} \nabla_{\bar{\mathbf{r}}}^2 \bar{\mathbf{E}} - \nabla_{\bar{\mathbf{r}}} (\nabla_{\bar{\mathbf{r}}} \cdot \bar{\mathbf{E}}) - \frac{L_0^2 \omega_0^2}{c^2} \partial_t^2 \bar{\mathbf{E}}(\bar{\mathbf{r}}, t) - \frac{L_0^2 \mu_0 \omega_0}{E_0} (en_{e0} V_e) \partial_t \bar{\mathbf{j}} = 0 \\ \nabla_{\bar{\mathbf{r}}}^2 \bar{\mathbf{B}}(\bar{\mathbf{r}}, t) - \frac{L_0^2 \omega_0^2}{c^2} \partial_t^2 \bar{\mathbf{B}}(\bar{\mathbf{r}}, t) + \frac{L_0^2 \mu_0 (en_{e0} V_e)}{B_0 L_0} \nabla_{\bar{\mathbf{r}}} \times \bar{\mathbf{j}} = 0 \end{array} \right. \quad (\text{A.11a})$$

$$\left\{ \begin{array}{l} \nabla_{\bar{\mathbf{r}}}^2 \bar{\mathbf{E}} - \nabla_{\bar{\mathbf{r}}} (\nabla_{\bar{\mathbf{r}}} \cdot \bar{\mathbf{E}}) - \frac{L_0^2 \omega_0^2}{c^2} \partial_t^2 \bar{\mathbf{E}}(\bar{\mathbf{r}}, t) - \frac{L_0^2 \mu_0 \omega_0}{E_0} (en_{e0} V_e) \partial_t \bar{\mathbf{j}} = 0 \\ \nabla_{\bar{\mathbf{r}}}^2 \bar{\mathbf{B}}(\bar{\mathbf{r}}, t) - \frac{L_0^2 \omega_0^2}{c^2} \partial_t^2 \bar{\mathbf{B}}(\bar{\mathbf{r}}, t) + \frac{L_0^2 \mu_0 (en_{e0} V_e)}{B_0 L_0} \nabla_{\bar{\mathbf{r}}} \times \bar{\mathbf{j}} = 0 \end{array} \right. \quad (\text{A.11b})$$

As a result, neglecting of the current term (or plasma response) in A.11a is equivalent to:

$$\frac{L_0^2 \mu_0 \omega_0}{E_0} (en_{e0} V_e) \ll \frac{L_0^2 \omega_0^2}{c^2}$$

that is to say after simplification:

$$\underbrace{\frac{\omega_P^2}{\omega_0^2}}_{\text{Plasma resonance}} \underbrace{\frac{1}{a_0}}_{\text{Field strength}} \underbrace{\frac{V_e}{c}}_{\text{Electron velocity}} \ll 1$$

In practice,  $\mathbf{j}$  depends on  $\mathbf{E}$ , which reduces the number of independent normalizing parameters. Using A.16 in a non-relativistic approximation, we have for instance the trivial relation:

$$\frac{V_e}{c} = a_0$$

As a consequence, neglecting of the plasma response in Eq A.11a leads to the relation:

$$\underbrace{\frac{\omega_P^2}{\omega_0^2}}_{\text{Plasma resonance}} \ll 1$$

This means that the high-frequency components of an electromagnetic field propagate as if they were in a dielectric material: electrons do not have time to oscillate and the plasma becomes “transparent”.

Similarly, to neglect the current term in Eq A.11b we impose:

$$\underbrace{\frac{\omega_P^2}{\omega_0^2}}_{\text{Plasma resonance}} \underbrace{\frac{V_e/L_0}{\omega_{ce}}}_{\text{electron motion}} \ll 1$$

where the electron velocity has to be compared to the characteristic cyclotron velocity.

## A.2.2 Charge screening

One can also derive Poisson's equation from Maxwell's equations using the normalizing conventions defined in A.1:

$$\frac{E_0}{L_0} \nabla^2 \bar{\Phi} = \frac{en_{e0}}{\epsilon_0} \bar{\rho}(r, t) \quad (\text{A.12})$$

where we immediately have the condition for a plasma screening:

$$L_0 \gg \frac{a_0 \omega_0 c}{\omega_p^2} = 127 nm$$

The numerical calculation is done for  $\lambda_0 = 800 nm$ ,  $a_0 = 1$  and  $\omega_p = \omega_0$  (at critical density).

In reality, there is another screening length which we can evaluate by developing  $\bar{\rho}$  as a function of  $\phi$  when the plasma is "thermalized". Indeed, the statistical approach leads to a Fermi-Dirac distribution of electrons in the potential  $\phi$  depending on the temperature  $T_e$ . When the temperature exceeds the Fermi temperature  $T_F$ , the distribution tends to a Maxwellian distribution and:

$$\frac{E_0}{L_0} \nabla^2 \bar{\Phi} = \frac{en_{e0}}{\epsilon_0} [-\delta(r) + 1 - \exp(-\frac{e^2 n_{e0} \bar{\phi}}{k_b T})] \quad (\text{A.13})$$

By using a series decomposition of the function above, and the scaling relation  $\Phi_0 = E_0 L_0$  this can also be written:

$$\frac{E_0}{L_0} \nabla^2 \bar{\Phi} = \frac{en_{e0}}{\epsilon_0} [-\delta(r) + \sum_{n=1}^{\infty} \frac{1}{n!} (\frac{e E_0 L_0 \bar{\phi}}{k_b T_e})^n] \quad (\text{A.14})$$

For a weakly correlated plasma, only the first term of that decomposition is significant, such that a second screening length can be identified:

$$L_0 \gg \sqrt{\frac{k_b T_e \epsilon_0}{e^2 n_{e0}}} = \lambda_D = 1.78 nm$$

The numerical calculation is done for  $\lambda_0 = 800 nm$ ,  $\omega_p = \omega_0$  and  $k_b T_e = 100 eV$

### A.2.3 Charge conservation

$$\partial_{\bar{t}}\bar{\rho} + \frac{V_e}{\omega_0 L_0} \nabla(\bar{j}) = 0 \quad (\text{A.15})$$

This equation is never violated, which implies:

$$L_0 = \frac{V_e}{\omega_0}$$

This relation a priori simple has important implications. Indeed, if the plasma is confined in space, and at the same time exposed to an intense electromagnetic field, space charge effects can quickly become important.

## A.3 Electron equation of motion

$$\gamma_e^3 \frac{d\bar{\mathbf{v}}_e(\bar{t})}{d\bar{t}} = -\frac{a_0}{(V_e/c)} \bar{\mathbf{E}}(\bar{\mathbf{r}}_e, \bar{t}) - \frac{\omega_{ce}}{\omega_0} \bar{\mathbf{v}}_e(\bar{t}) \times \bar{\mathbf{B}}(\bar{\mathbf{r}}_e(\bar{t}), \bar{t}) \quad (\text{A.16})$$

where the adimensioned terms are interpreted:

- $\gamma_e \approx 1$ : non-relativistic approximation. Perturbations propagate instantaneously in the scope of the approximation. It is equivalent to  $V_e/c \ll 1$ .
- $\omega_{ce}/\omega_0$ : electronic response to a magnetic field which tends to generate electron cycotronic orbitals. It is easy to calculate that this factor  $\approx 1$  for magnetic fields reaching  $B_0 \approx 10^4 T$ . This value can be reached for strong laser fields with so called "relativistic intensities".

In order to neglect the magnetic force in front of the electric force, we need:

$$\frac{1}{a_0} \frac{V_e}{c} \frac{\omega_{ce}}{\omega_0} \ll 1$$

Note that the parameters  $\omega_{ce}$  and  $a_0$  are of course not independent when one considers Maxwell's equation of propagation. For example, we could impose  $E_0 = cB_0$  (true in vacuum), which implies  $\omega_{ce}/\omega_0 = a_0$ . In this condition, the relation for neglecting the magnetic component of field is reduced to:

$$V_e \ll c$$

However, it is important to note that both the equation of motion and the equation of propagation are vectorial equations. So far, we have only considered one scaling parameter for a vector (for example  $E_0$  for  $\mathbf{E}$ ) when in reality, there should be one for each component along  $x, y$  and  $z$  after the equation has been projected into 3 scalar equations.

## A.4 Vlasov equation

Since we are working with plasmas only, we clearly see that so far we have no equation involving the electron temperature. Indeed, it is common to describe the motion of electrons using a fluid model. Such fluid is given a temperature  $T_e$ , a pressure  $P_e$  and a density  $n_e$ . This approach is necessary because the relativistic equation of motion applies to one electron only, but as electrons become numerous and move in random directions because of the intrinsic temperature (natural gain of entropy for a fermion population), it becomes impossible to describe each electron individually.

As demonstrated by Cedric Villani [197], this Vlasov equation [84, 198] can be derived by taking the average response of each individual electron following the non-relativistic ( $\gamma_e = 1$ ) equation of motion and adding to it the electron-electron interaction. This consists in “scaling” differently our physical system by looking at fictive particles made of multiple electrons. Attributing a temperature to each of these particles is done through an averaging of their kinetic energy. The system is described by the distribution function  $f_e(\mathbf{r}, \mathbf{v}, t)$  :

$$\begin{cases} \partial_{\bar{t}} f_e + \bar{\mathbf{v}}_e \nabla_{\mathbf{r}} f_e + \bar{\mathbf{F}}(\bar{v}_e) \cdot \nabla_{\mathbf{v}} f_e = (\partial_{\bar{t}} f_e)_{coll} \\ \bar{\mathbf{F}}(\bar{v}_e) = -a_0 \bar{\mathbf{E}}(\mathbf{r}, t) - \frac{\omega_{ce}}{\omega_0} (\bar{\mathbf{v}}_e \times \bar{\mathbf{B}}) \end{cases} \quad (\text{A.17})$$

where we then define several quantities such as:

— **Current:**

$$\mathbf{j}(\mathbf{r}, t) = \int_{\mathbf{v} \in \mathbb{R}} \mathbf{v} f_e(\mathbf{r}, \mathbf{v}, t) d\mathbf{v}$$

— **Electrostatic Coulomb field:**

$$\nabla_{\mathbf{r}} \mathbf{E}(\mathbf{r}, t) = \frac{-e}{\epsilon_0} \int_{\mathbf{v} \in \mathbb{R}} f_e(\mathbf{r}, \mathbf{v}, t) d\mathbf{v}$$

The term  $(\partial_{\bar{t}} f_e)_{coll}$  takes into account the thermalization of the electron fluid, and therefore only plays a significant role on time scales much longer than the average collision time between electrons. There is no absolute theory that would give the correct evolution of that term. Therefore, one should turn to Boltzmann equation and solve:

$$(\partial_{\bar{t}} f_e)_{coll} = R(f_e) \quad (\text{A.18})$$

Different expressions can be found for this term which refer to different physical schemes:

— Non-collisional Vlasov :

$$(\partial_{\bar{t}} f_e)_{coll} = 0 \quad (\text{A.19})$$

— Fokker-Planck :

$$(\partial_{\bar{t}} f_e)_{coll} = D \Delta_p f_e - A \nabla_p [f_e \bar{v}_e] \quad (\text{A.20})$$

The collisions are modeled using a diffusion and a drift term. This can be derived supposing the velocity diffusion follows a Markov process (Chandrasekhar, 1943). The electrons undergo multi-body interactions such that the coefficients can be retrieved within the scope of binary Coulomb interactions.

— Bhatnagar-Gross-Krook (BGK) :

$$(\partial_t f_e)_{coll} = -\frac{\nu_e}{\omega_0}(f_e - f_{e0}) \quad (\text{A.21})$$

with  $f_{m0}$  the Maxwellian distribution of electron at temperature  $T_e$ , and  $\nu_e$  the electron collision rate.

# Appendix B

## Green function

The Green function is an elementary solution to a differential equation with given constraints. Since the idea is not to be exhaustive from the mathematical point of view, we will directly apply it to the Poisson equation in a static case ( $\partial_t \Phi = 0$ ):

$$\nabla^2 \Phi(\mathbf{r}) = -\frac{\rho(\mathbf{r})}{\epsilon_0} \quad (\text{B.1})$$

where  $\mathbf{r} \in \mathbb{R}^n$  and  $\phi(\cdot) \in \mathcal{L}(\mathbb{R}^n)$ ,  $n$  being the dimension of the problem. In most physical problems,  $1 \leq n \leq 4$  (3 spatial dimensions and one temporal). Note that in the case  $n = 4$ , the Laplacian operator is called a 4-Laplacian and is equal to  $\nabla^2 = \partial_x^2 + \partial_y^2 + \partial_z^2 - \frac{1}{c^2} \partial_t^2$ .

The solutions of the problem are the  $\Phi(\cdot)$  functions, defined as distributions [199]. In general, we choose functions which can be Fourier transformed ("tempered distribution"), which is more restrictive from a mathematical point of view, but always true from a physical point of view.

The Green function is the solution to the following equation:

$$\nabla^2 G(\mathbf{r}) = \delta(\mathbf{r}) \quad (\text{B.2})$$

which will be different whether the problem is posed in 1, 2 or 3 dimensions. Since the  $\delta$  function has a spherical symmetry, it is convenient to express the Laplacian in the spherical coordinate system, such that:

$$\nabla^2 \Phi = \frac{1}{r^{n-1}} \partial_r [r^{n-1} \partial_r \Phi]$$

where  $n$  is the dimension of the problem. The solution of B.1 is given by the convolution:

$$\Phi(\mathbf{r}) = \int_{\mathbf{r}' \in \mathbb{R}^n} G(\mathbf{r} - \mathbf{r}') \rho(\mathbf{r}') d\mathbf{r}' = \int_{\mathbf{r}' \in \mathbb{R}^n} \underbrace{G(|\mathbf{r} - \mathbf{r}'|)}_{\text{spherical sym.}} \rho(\mathbf{r}') d\mathbf{r}'$$

To solve Eq B.2 one should first solve it on  $\mathbb{R}^n \setminus \{0\}$ . The solution of Eq B.2 when  $r \neq 0$  is trivial:

$$\begin{array}{l|l|l|l} n = 1 & G(r) = \lambda r + \mu & \lambda \neq 0 & \mu = 0 \\ n = 2 & G(r) = \lambda \log_e(r) + \mu & \lambda \neq 0 & \mu = 0 \\ n = 3 & G(r) = \frac{\lambda}{r} + \mu & \lambda \neq 0 & \mu = 0 \end{array}$$

Note that  $\mu$  is a simple additive constant which can be taken equal to 0. This means that the final solution  $\Phi(\cdot)$  is unique up to a constant added value. Finally, we use the theory of distributions to completely solve the problem by integration over a sphere of unit radius  $B_n$  centered on the origin. The volume integration is reduced to a surface integration using Stokes' Theorem:

$$\int_{dV \in B_{n-1}} \nabla^2[G]dV \underset{\text{Stokes' Th.}}{=} \int_{dS \in S_{n-1}} \nabla[G]_{r=1} \mathbf{n} d\mathbf{S}_n = \int_{dV \in B_{n-1}} \delta(\mathbf{r})dV = 1 \quad (\text{B.3})$$

The integration of the second term of that equality yields the relation:

$$|S_{n-1}| \partial_r [r^n \partial_r G]_{r=1} = -1 \quad (\text{B.4})$$

where  $|S_{n-1}| = 2, 2\pi, 4\pi$  for  $n = 1, 2, 3$  respectively. This implies that we can calculate  $\lambda$  for each dimension, such that *in-fine* we can write:

**For  $n = 1$ :**

$$\left\{ \begin{array}{l} G(r) = -\frac{1}{2}|r| \end{array} \right. \quad (\text{B.5a})$$

$$\left\{ \begin{array}{l} \Phi(r) = \frac{1}{2\epsilon_0} \int_{\mathbb{R}} \rho(r') |r - r'| dr' \end{array} \right. \quad (\text{B.5b})$$

**For  $n = 2$ :**

$$\left\{ \begin{array}{l} G(\mathbf{r}) = -\frac{1}{2\pi} \log_e |\mathbf{r}| \end{array} \right. \quad (\text{B.6a})$$

$$\left\{ \begin{array}{l} \Phi(\mathbf{r}) = \frac{1}{2\pi\epsilon_0} \int_{\mathbb{R}} \rho(\mathbf{r}') \log_e |\mathbf{r} - \mathbf{r}'| dr' \end{array} \right. \quad (\text{B.6b})$$

**For  $n = 3$ :**

$$\left\{ \begin{array}{l} G(\mathbf{r}) = -\frac{1}{4\pi|\mathbf{r}|} \end{array} \right. \quad (\text{B.7a})$$

$$\left\{ \begin{array}{l} \Phi(\mathbf{r}) = \frac{1}{4\pi\epsilon_0} \int_{\mathbb{R}} \frac{\rho(\mathbf{r}')}{|\mathbf{r} - \mathbf{r}'|} dr' \end{array} \right. \quad (\text{B.7b})$$

Note that the case  $n = 4$  is somewhat different than in the previous demonstration because of the temporal variable. The spherical Green equation would be written:

$$\nabla^2[G] - \frac{1}{c^2}\partial_t^2 G = \delta(r)\delta(t) \quad (\text{B.8})$$

The resolution on  $\mathbb{R}^4 \setminus \{0\}$  implies:

$$G(\mathbf{r}, t) = f_1(t - |\mathbf{r}|/c) + f_2(t + |\mathbf{r}|/c)$$

where  $f_1, f_2$  are two functions of one single variable corresponding to two counter propagating waves.  $f_1$  and  $f_2$  are a priori arbitrary tempered distributions.

If we now impose the solution to be equal to the static solution when  $t$  tends to infinity, we see that  $f_1$  and  $f_2$  are no longer arbitrary and must fulfill the relation:

$$G(\mathbf{r}, t) = \delta(t - |\mathbf{r}|/c) + \delta(t + |\mathbf{r}|/c) \quad (\text{B.9})$$

Therefore, the solution obtained by convolution with the Green function is:

$$\Phi(\mathbf{r}) = \frac{1}{4\pi\epsilon_0} \int_{t \in \mathbb{R}} \int_{\mathbb{R}} \frac{\rho(\mathbf{r}', t')}{|\mathbf{r} - \mathbf{r}'|} G(\mathbf{r} - \mathbf{r}', t - t') d\mathbf{r}' dt' \quad (\text{B.10})$$

Using the property of the Dirac distribution for integration, we finally have:

**For  $n = 4$ :**

$$\Phi(\mathbf{r}, t) = \frac{1}{4\pi\epsilon_0} \int_{\mathbb{R}} \frac{\rho(\mathbf{r}', t - |\mathbf{r} - \mathbf{r}'|/c)}{|\mathbf{r} - \mathbf{r}'|} d\mathbf{r}' + \frac{1}{4\pi\epsilon_0} \int_{\mathbb{R}} \frac{\rho(\mathbf{r}', t + |\mathbf{r} - \mathbf{r}'|/c)}{|\mathbf{r} - \mathbf{r}'|} d\mathbf{r}' \quad (\text{B.11})$$

# Appendix C

## Relativistic formulations

A detailed description of relativistic field theory can be found in [75]. Here, we remind the reader about some useful relations and definitions.

### C.1 A few definitions

- **Four-vector(4-vector):**  $R$  et  $R'$  designate two Galilean referentials, a four-vector  $v_R$  is by definition a vector which expression from  $R$  to  $R'$  is given by the Lorentz transformation  $v_{R'} = L'_\mu v_R$ .
- **Four-scalar(4-scalar):** Scalar invariant from  $R$  to  $R'$ . Example of 4-scalars: electric charge, phase  $(\omega t - kr)$  of electromagnetic radiation, proper time.
- **Proper time  $\tau$ :** Time intrinsically linked to a particle in motion. If  $t$  is the time in  $R$  we have  $dt = \gamma d\tau$ , with  $\gamma = (1 - \frac{v(t)^2}{c^2})^{-1/2}$ . An expression of  $\tau(t)$  is obtain with the equation of motion. However, since  $\gamma > 0$ ,  $\tau$  is necessarily strictly increasing with  $t$ , which means we can invert the expression to express  $t(\tau)$ .

Examples of 4-vectors:

4-vector	Einstein notation	Normal notation
<b>4-position</b>	$x^\mu(t)$	$(ct, \mathbf{r}(t))$
<b>4-current</b>	$j^i = \rho \frac{dx^i}{dt}$	$(\rho c, \rho \mathbf{v})$
<b>4-current</b>	$j^i = \rho \frac{dx^i}{dt}$	$(\rho c, \rho \mathbf{v})$
<b>4-wavevector</b>	$k^i$	$(\frac{\omega}{c}, \mathbf{k})$
<b>4-vector potential</b>	$\mathcal{A}^\mu(x^\mu)$	$(V(x^\mu)/c, \vec{A}(x^\mu))$

The **4-velocity**: obtained by the derivation of the 4-position relative to proper time. This way, we simply have:

$$u^\mu = \frac{dx^\mu(t(\tau))}{d\tau} = \left( \frac{dt(\tau)}{d\tau} c, \frac{d\mathbf{r}(t(\tau))}{d\tau} \right) = \left( \gamma c, \gamma \frac{d\mathbf{r}(t)}{dt} \right)$$

Note that since the 4-position is a 4-vector:

$$x^\mu(t)' = \mathcal{L}_\nu^\mu(t)x^\nu(t)$$

and therefore, the 4-velocity is also a 4-vector:

$$u'^\mu = \gamma \frac{dx'^\mu}{dt} = \gamma \frac{d(\mathcal{L}_\nu^\mu(t)x^\nu(t))}{dt} \equiv \gamma \frac{d(\mathcal{L}_\nu^\mu(t))}{dt} x^\nu(t) + \gamma \mathcal{L}_\nu^\mu(t) \frac{d(x^\nu(t))}{dt} = \mathcal{L}_\nu^\mu u^\nu$$

This demonstration is only valid for a Galilean referential (ie  $\frac{d(\mathcal{L}_\nu^\mu(t))}{dt} = 0$ ). One should be careful that " $\gamma$ " has two implicit definitions: First, the most common, is used in the definition of the proper time, where  $v$  denotes the particle velocity. Second, the analytical expression if the same, but  $\mathbf{v}$  now corresponds to the (constant !) velocity of the Galilean referential used in the definition of  $\mathcal{L}_\nu^\mu$ .

The **4-acceleration** is obtained by derivation of the 4-velocity relative to proper time:

$$\Gamma^\mu(t) = \frac{du^\mu}{d\tau} = (c\gamma \frac{d\gamma}{dt}, \gamma \frac{d\gamma}{dt} \vec{v} + \gamma^2 \vec{a})$$

## C.2 Relativistic equation of motion for a charged particle

The derivation of the equation is properly done in [75] using a principle of least action applied on a charge  $q$  of mass  $m$  in an electromagnetic field. In many publications [200, 201], it is given using tensorial Einstein notation:

$$\frac{du^i}{d\tau} = \frac{q}{mc} (\partial_{x^i} A^k - \partial_{x^k} A^i) u_k \quad (\text{C.1})$$

Which is equivalent to:

$$\left\{ \begin{array}{l} \frac{d}{dt} [\gamma \mathbf{v} + \frac{q}{m} \mathbf{A}] = \frac{q}{m} (\mathbf{v} \nabla) \mathbf{A} + \frac{q}{m} \mathbf{v} \times (\nabla \times \mathbf{A}) + q \nabla \phi \end{array} \right. \quad (\text{C.2a})$$

$$\left\{ \begin{array}{l} \frac{dE_{kin}}{dt} = \frac{d}{dt} (\gamma mc^2) = q \mathbf{E} \cdot \mathbf{v} \end{array} \right. \quad (\text{C.2b})$$

With the relation  $(\mathbf{v} \cdot \nabla) \mathbf{A} + \mathbf{v} \times (\nabla \times \mathbf{A}) = (\mathbf{v} \times \nabla) \times \mathbf{A} + (\nabla \cdot \mathbf{A}) \mathbf{v}$ , Eq C.2a can also be transformed into:

$$\left\{ \begin{array}{l} \frac{d}{dt} [\gamma v_x + \frac{q}{m} A_x] = \frac{q}{m_e} \mathbf{v} \partial_x \mathbf{A} + q \partial_x \phi \end{array} \right. \quad (\text{C.3a})$$

$$\left\{ \begin{array}{l} \frac{d}{dt} [\gamma v_y + \frac{q}{m} A_y] = \frac{q}{m_e} \mathbf{v} \partial_y \mathbf{A} + q \partial_y \phi \end{array} \right. \quad (\text{C.3b})$$

$$\left\{ \begin{array}{l} \frac{d}{dt} [\gamma v_z + \frac{q}{m} A_z] = \frac{q}{m_e} \mathbf{v} \partial_z \mathbf{A} + q \partial_z \phi \end{array} \right. \quad (\text{C.3c})$$

If on the contrary we develop the left-hand side of Eq C.2a, and use the relation  $\frac{d\mathbf{A}}{dt} = \partial_t \mathbf{A} + (\mathbf{v} \nabla) \mathbf{A}$ , we find the well-known equation:

$$\frac{d}{dt}[\gamma\mathbf{v}] = \frac{q}{m}\mathbf{E} + \frac{q}{m}\mathbf{v} \times \mathbf{B} \quad (\text{C.4})$$

### C.3 Gauge invariance

The 4-vector  $A_k = (\phi/c, A_x, A_y, A_z)$  contains all information about the electromagnetic fields ( $E, B$ ) at play in the equation of motion. Choosing the gauge consists in imposing a condition on  $A_k$  which has no impact on the equation of motion, but could simplify the analytical resolution of the equation. The ( $E, B$ ) fields are expressed by:

$$\begin{cases} \mathbf{B} = \nabla \times (\mathbf{A} + \nabla f(r, t)) = \nabla \times \mathbf{A} \\ \mathbf{E} = -\nabla (\phi - \partial_t f(r, t)) - \partial_t (\mathbf{A} + \nabla f(r, t)) = -\nabla \phi - \partial_t \mathbf{A} \end{cases} \quad (\text{C.5})$$

Therefore, one can choose an additional scalar equation verified by the components  $(\phi/c, A_x, A_y, A_z)$ , which is equivalent to choosing a function  $f$ . For example if  $F$  is a linear partial differential equation verified by  $A_k$  (i.e.  $F(A_k) = 0$ ), the corresponding gauge will be a solution of the differential system:

$$F((\partial_t f, \nabla f)) = -F(A_k) \quad (\text{C.6})$$

Lorenz Gauge	$\nabla \mathbf{A} + \frac{1}{c^2} \partial_t \phi = 0$
Coulomb Gauge	$\nabla \mathbf{A} = 0$

# Appendix D

## Interferences between coherent sources

A Gaussian beam is fully characterized by its waist and phase (radius of curvature  $R$  in Gaussian beam theory) in a given plane. When varying  $R$  in the plane  $z = 0$ , where the waist is  $w$ , the "focus" is no longer located at  $z = 0$ , but at position  $z_0$ , with a corresponding waist  $w_0$ . The question we ask is: is it possible to reach arbitrary values of  $z_0$  when changing  $R$ ?

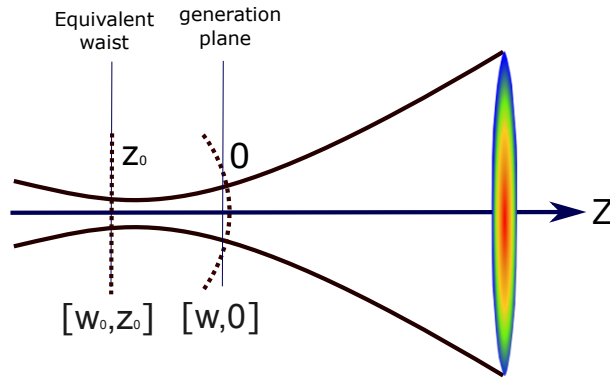


Figure D.1 – Representation of a Gaussian pulse

In Gaussian beam theory, the phase radius of curvature is defined by:

$$R = -z_0 - \frac{Z_r^2}{z_0}$$

Where  $Z_R = \frac{\pi w_0^2}{\lambda}$  is the Rayleigh length.

That first relation does not provide enough information because two different values of  $z_1$  (one very small, one very big) can lead to the same  $R$ . In other words, this  $z_0 \rightarrow R$  relation does not constitute a bijection of  $\mathbb{R}^*$  in  $\mathbb{R}$ . We use another relation on the waists:

$$w = w_0 \sqrt{1 + \frac{z_0^2}{Z_R^2}} \quad (\text{D.1})$$

Replacing  $Z_R$  by its definition in D.1, we derive the following equation:

$$(w_0^2)^2 - w^2(w_0^2) + z_0^2 \frac{\lambda^2}{\pi^2} = 0 \quad (\text{D.2})$$

The discriminant  $\Delta$  of that equation should be positive in order to find a solution for  $w_0$ , which ever value we impose on  $w_0$ . Moreover, the minimum waist is always at the position of flat phase such that we will always keep the smallest (positive) solution of that equation. A solution for  $(w_0^2)$  exists if, and only if:

$$\Delta = w^4 - 4z_0^2 \frac{\lambda^2}{\pi^2} \geq 0 \quad (\text{D.3})$$

that is to say

$$|z_0| \leq \frac{w^2 \pi}{2\lambda}$$

This means that which ever the phase we associate with a source of given waist  $w$  and wavelength  $\lambda$ , the equivalent waist (within the theory of Gaussian beams) is always be in an interval  $[-\frac{w^2 \pi}{2\lambda}, \frac{w^2 \pi}{2\lambda}]$ . This means a harmonic source can not be equivalent to a Gaussian beam arbitrarily far from the focus position where the interaction takes place. Indeed,  $R$  can be extremely large if  $z \ll Z_R$  or  $z \gg Z_r$ , and will be smaller for intermediate values. Therefore, another approach is to say: if  $R$  would be arbitrarily large, the beam could be considered very far from the position of its waist. Therefore, it would be almost collimated. But a collimated beam with a very small waist should diverge extremely quickly, which is in contradiction with the collimation. Necessarily, if  $R$  is large this means the waist is located within the Rayleigh length.

### 3 sources in vertical plane:

In *Matlab*, we use the analytical expression of a Gaussian beam [202] and explore the interference pattern resulting from 3 sources positioned vertically along the  $r$  axis as represented in Fig D.2. Each Gaussian beam indexed by  $i$  is defined by the variables  $[w_{0i}, z_i]$  where  $w_{0i}$  is the waist at focus, and  $z_i$  the position of the focus.

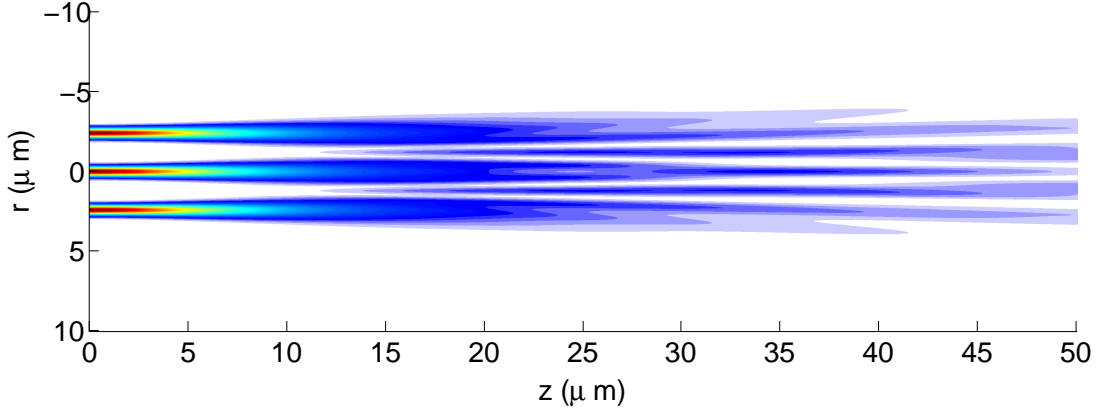


Figure D.2 – Representation in the plane  $(r, z)$  where  $z$  indicates the direction of the resulting intensity where  $w_{0i} = 400 \text{ nm}, z_{0i} = 0, r_{01} = -r_{03} = 2.4 \mu\text{m}, r_{02} = 0$  and  $\lambda = 80 \text{ nm}$

In this configuration where  $r_{01} = -r_{03}$ , the  $n^{\text{th}}$  diffracted interfringe is given by :

$$\Theta_n = n \frac{\lambda}{|r_{01}|} \quad (\text{D.4})$$

Using the analytical formulas at position  $z \gg Z_R$ , we can extract an interference pattern as the result of this 3 source configuration and the angular interfringe does correspond to that given by Eq D.4. The simplest way to retrieve the distance between the sources  $r_1$  is to Fourier transform the result. The main non-zero angular frequency will therefore correspond to:

$$f_\theta = \frac{r_{01}}{\lambda} \quad (\text{D.5})$$

It is therefore convenient to replace  $f_\theta$  by  $f_\theta \lambda$  after computing the Fourier signal to have the maximum at exactly  $r_{01}$ . In Fig D.3, we look at the influence of the intensity interference pattern on the Fourier transform when changing one parameter in this 3-source configuration. Here the beams  $i = 1$  and  $i = 3$  are taken symmetric. The dimensions are given in  $\lambda_0$  unit, where  $\lambda_0 = 800 \text{ nm}$  while each Gaussian beam is defined for the  $10^{\text{th}}$  harmonic ( $\lambda = 80 \text{ nm}$ )

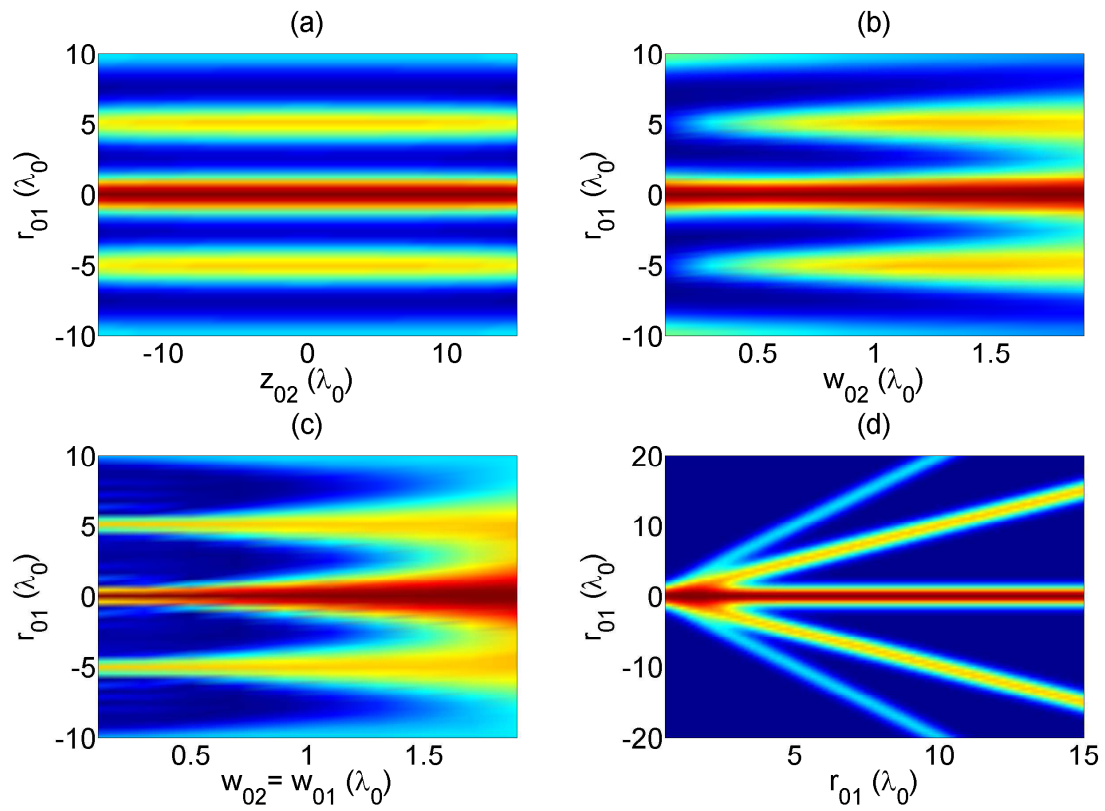


Figure D.3 – Fourier transform of intensity interference pattern for harmonic H10 ( $\lambda = 80$  nm). Initial conditions are  $z_{0i} = 0$ ,  $w_{0i} = \lambda_0$  and  $r_{01} = 5\lambda_0$ . We then vary one parameter: (a) influence of central source defocus (b) influence of central source waist (c) influence of global waist variation (d) influence of satellite sources distance  $r_{01}$

# Appendix E

## Publications

# Optics Letters

## Spatial-domain interferometer for measuring plasma mirror expansion

MAÏMOUNA BOCOUM,\* FREDERIK BÖHLE, ALINE VERNIER, AURÉLIE JULLIEN, JÉRÔME FAURE, AND RODRIGO LOPEZ-MARTENS

Laboratoire d'Optique Appliquée, École Nationale Supérieure de Techniques Avancées, Ecole Polytechnique CNRS UMR 7639, 91761 Palaiseau, France

\*Corresponding author: maimouna.bocoum@ensta-paristech.fr

Received 31 March 2015; revised 26 May 2015; accepted 27 May 2015; posted 29 May 2015 (Doc. ID 237168); published 18 June 2015

**We present a practical spatial-domain interferometer for characterizing the electronic density gradient of laser-induced plasma mirrors with sub-30-femtosecond temporal resolution. Time-resolved spatial imaging of an intensity-shaped pulse reflecting off an expanding plasma mirror induced by a time-delayed pre-pulse allows us to measure characteristic plasma gradients of 10–100 nm with an expansion velocity of 10.8 nm/ps. Spatial-domain interferometry (SDI) can be generalized to the ultrafast imaging of nm to  $\mu\text{m}$  size laser-induced phenomena at surfaces.** © 2015 Optical Society of America

**OCIS codes:** (120.5050) Phase measurement; (110.3175) Interferometric imaging; (070.7145) Ultrafast processing; (320.7100) Ultrafast measurements.

<http://dx.doi.org/10.1364/OL.40.003009>

Plasma mirrors constitute an ideal testbed for studying the interaction of ultrahigh-intensity laser light and solid-density plasmas [1]. However, the main challenge in such experiments is knowing and controlling the thin electronic density gradient that forms at the plasma–vacuum interface. High-order harmonic generation experiments performed with a controlled pre-pulse [2] have allowed direct observation of the transition to the relativistic oscillating-mirror regime for sharp density gradients  $L/\lambda \ll 1$ , where  $\lambda$  is the driving laser wavelength and  $L$  the density gradient length. Electron acceleration up to few-100-keV energies has been observed from plasma mirrors driven with density gradients increased up to a significant fraction of  $\lambda$  [3,4]. Short-pulse ion-acceleration experiments on thin foils have shown the rapid drop of signal that occurs for leading edge intensities  $\geq 10^{12}$  W/cm<sup>2</sup> already a few picoseconds (ps) before the pulse peak [5].

When a laser pulse of intensity  $\geq 10^{12-13}$  W/cm<sup>2</sup> interacts with a solid surface, multiphoton ionization quickly leads to the creation of a plasma of temperature typically around 10–100 eV [6]. The plasma inertia is dominated by its ionic constituents and its pressure by the free electrons that transmit their energy to the ions, resulting in plasma expansion velocities

of the order of several nm/ps. It is therefore essential to develop simple techniques for characterizing this expansion with both sub- $\mu\text{m}$  and sub-ps precision. The characteristic spatial and temporal expansion scale lengths ( $<10$  nm,  $<1$  ps, respectively) make femtosecond (fs) laser pulses the best candidates for performing accurate measurements using phase-sensitive detection schemes such as Frequency Domain Interferometry (FDI) [7]. Although FDI can reach  $\lambda/2000$  resolution, it is rather complex to implement on a running plasma mirror experiment. In this Letter, we demonstrate a new technique we call spatial domain interferometry (SDI), easy to implement experimentally, based on time-resolved spatial phase-shift imaging interferometry with sub-30-fs laser pulses. Similar to the fs pump-probe spatial imaging technique employed in [8,9], our time resolution is simply limited by the duration of the pulse used to probe the plasma expansion induced by the pump pulse.

The principle of SDI applied to fs plasma mirror imaging is shown on Fig. 1. An intensity mask is used to generate a diffraction pattern at the focus of a time-delayed probe pulse reflecting off the surface of a plasma mirror induced on a solid target by a pump pulse [Fig. 1(b)]. The temporal resolution of this spatial interferometer system is naturally limited by the laser pulse duration ( $<10$   $\mu\text{m}$  for 30-fs pulses at 800-nm wavelength). The reflection of the central diffraction spot by the peak of the plasma mirror surface induces a phase shift relative to the higher order diffraction spots around it, leading in turn to a clearly observable time-dependent spatial interference pattern in the far-field intensity profile of the reflected probe pulse. We designate  $T_M$  as the intensity masked introduced in the collimated probe beam prior to the focusing optic of focal length  $f$ . As a consequence, the probe focus spot splits into several smaller spots spaced by  $\Delta x = \frac{\lambda f}{a}$ , where  $a$  is the period of the mask. The probe field after the mask can be written as

$$E_M(x, y, \omega) = E(x, y, \omega) T_M(x, y). \quad (1)$$

Within the paraxial approximation, the spatial profile of the probe field in the focusing plane writes

$$E_1 = FT[E_M] = FT[E(x, y, \omega) T_M(x, y)]. \quad (2)$$

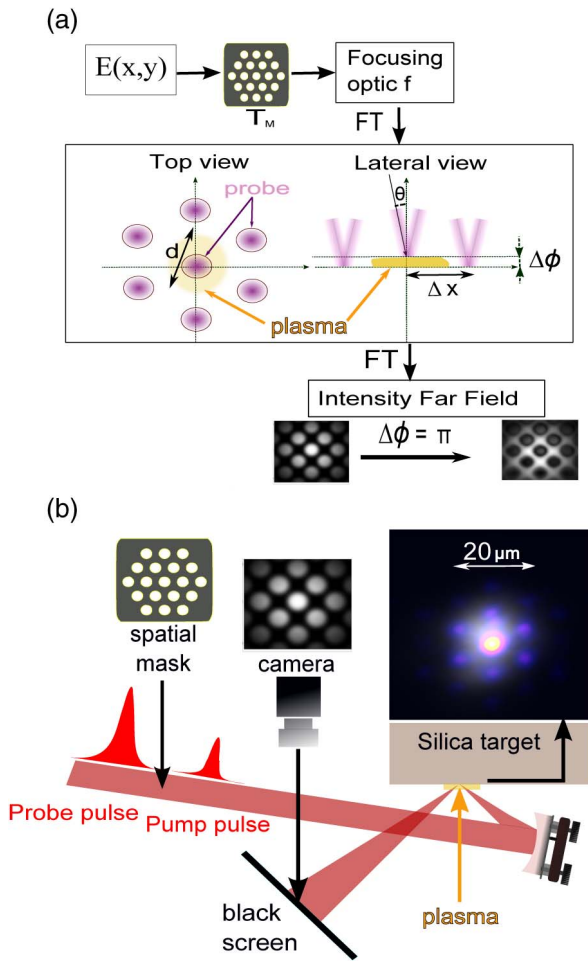


**Fig. 1.** (a) SDI principle applied to ultrafast plasma mirror imaging: the probe field  $E(x, y)$  is diffracted by an intensity mask  $T_M$  onto a plasma mirror in the focal plane. The phase shift,  $\Delta\phi$ , of the central diffraction spot induced by the plasma expansion leads to an inversion of the far-field spatial intensity profile of the reflected probe beam for  $\Delta\phi = \pi$ . (b) Experimental set-up: a 30 fs pump pulse is focused onto a solid target using an off-axis parabola in order to induce a plasma mirror. The far-field intensity profile of the time-delayed spatially shaped probe pulse reflected by the plasma mirror is imaged onto a CCD camera and recorded as a function of pump-probe delay. The far-right panel shows both pump (gray scale) and probe (color scale) beam profiles measured at focus on target.

As shown in Fig. 1(a), a plasma mirror of size  $d < 2\Delta x$  induces a phase shift  $\phi(x, y)$ , where the central spot of the diffracted beam gets reflected such that we can write

$$E_2 = E_1 T = FT[E(x, y, \omega) T_M(x, y)] T(x, y), \quad (3)$$

where  $T = |T|e^{i\phi}$  is the transfer function of the probed plasma surface. By Fourier transform of Eq. (3), we obtain the reflected far field  $E_F$ :

$$E_F = FT[FT[E(x, y, \omega) T_M(x, y)] |T| e^{i\phi(x, y)}]. \quad (4)$$

By doing a change of variables and using the relation  $FT(fg) = FT(f) * FT(g)$ , we can verify that the reflected intensity will be of the form

$$I(x, y) = \left| ET_M + \iint ET_M(x-x', y-y') b(x', y') dx' dy' \right|^2, \quad (5)$$

where

$$b(x, y) = FT(T-1) \left( \frac{x}{\lambda f}, \frac{y}{\lambda f} \right). \quad (6)$$

To estimate the effect of plasma mirror size on the reflected image, we can make the simple assumption that all diffracted spots are reflected equally by the plasma, and that the 0th-order alone is phase shifted by a spatially uniform  $\phi_0$ . Mathematically, this translates into  $|T| = 1$  and  $\phi(x, y) = \phi_0$  for  $|x|, |y| < \frac{\lambda f}{2a}$ . This allows us to express  $b$  by limiting the Fourier integration domain to  $[-\frac{\lambda f}{2a}, \frac{\lambda f}{2a}]$ , such that

$$b(x, y) = (e^{i\phi_0} - 1) \left( \frac{\lambda f}{a} \right)^2 \text{sinc} \left( \frac{x}{2a} \right) \text{sinc} \left( \frac{y}{2a} \right). \quad (7)$$

This particular solution shows that the convolution function,  $b$ , is periodic with  $\phi_0$  since the interference term in Eq. (5) leads to an inversion of the far-field for  $\phi_0 = \pi n$  where  $n$  is integer. Therefore, the monotonic expansion of the plasma mirror surface can be retrieved following each periodic inversion of the recorded interferogram. Our experiment is however different from this ideal case because the electronic-density gradient at the plasma mirror surface is better represented by an exponential decay rather than by a simple step function. This, however, does not prevent the inversions from being visible in the far-field intensity pattern, and each of them is associated with a  $\pi$  phase shift, as shown in Fig. 2, where we compare the theoretical and experimental probe beam profiles for different pump-probe delays.

Our experiment was conducted using the newly upgraded Salle Noire laser system of LOA, which delivers high-contrast, multi-mJ, 30-fs pulses at 1 kHz [10]. All beams used in the experiment are derived from the main 30 fs, 1 mJ, 15 mm pulses and focused using the same  $f/1.2$  off-axis parabola onto a rotating silica target at 1 kHz [11] repetition rate. 5% of the main beam is picked off as the prepulse, reduced in size by a factor of 3 with a reflecting telescope and sent through a variable delay stage prior to focusing. The remainder of the main pulse is used as the probe pulse that is sent through an  $a = 4$  mm periodic hexagonal mask with holes of 2.5 mm, leading to diffracted spots at the focus on target as shown in Fig. 1(b), which compares typically measured pump (gray scale) and probe (color scale) beam profiles. The central diffracted probe spot intensity is  $\sim 10^{16}$  W/cm<sup>2</sup> which is about 2 orders of magnitude less than without the mask such that the laser contrast plays a negligible role in the plasma dynamic. This allows to keep the set-up still for high field experiments by simply removing the mask. The peak intensity of the pump pulse is  $I_{p,1} = 3.5 \times 10^{14}$  W/cm<sup>2</sup> where it overlaps with the central diffraction spot and on average  $I_{p,2} = 8.7 \times 10^{13}$  W/cm<sup>2</sup> where it overlaps with the first order diffraction spots.

We image the far-field spatial profile of the reflected probe beam with a CCD camera, integrated over 100 shots for every pump-probe delay to compensate for a low individual signal shot, on an anodized black screen placed in the specular direction. The results for four different pump-probe delays are displayed in the right column of Fig. 2. We take the intensity profile recorded at zero pump-probe delay as our reference.

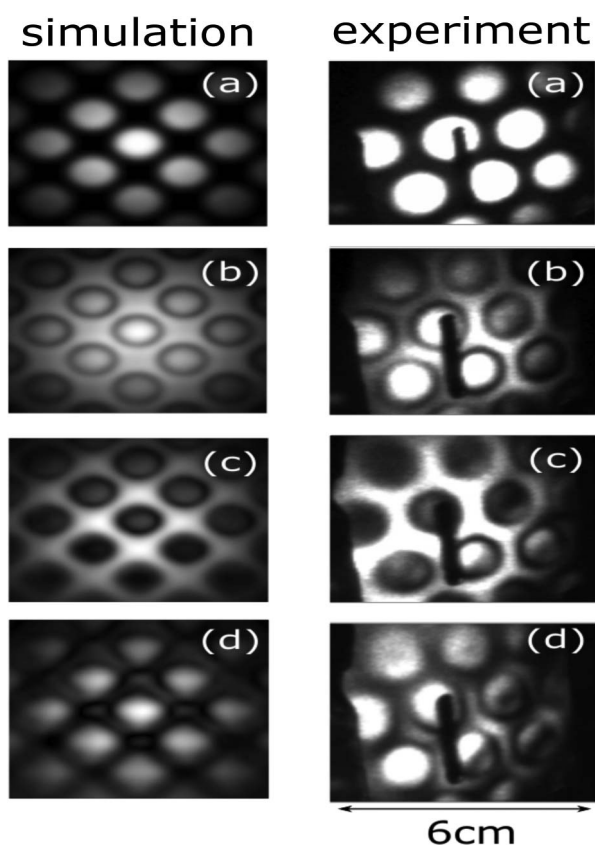


**Fig. 2.** Simulated (left column) and experimental (right column) far-field probe beam intensity profile inversions at, respectively, 0 ps (a), 6 ps (b), 12 ps (c), and 20 ps (d) pump-probe delay. The visible shadow is an experimental artifact. The simulations are performed using the measured pump beam profile and assuming the plasma expansion velocity to be proportional to the square root of the pump pulse intensity. The corresponding phase shifts in Rad are, respectively, 0 (a),  $\pi/2$  (b),  $\pi$  (c), and  $2\pi$  (d)

The first inversion of the intensity profile appears at 12 ps and the second inversion occurs at  $\approx 20$  ps. The profile inversion patterns are well reproduced by the simulations shown on the left column of Fig. 2 where we used the actual experimental pump pulse profile to simulate the phase shift due to the plasma expansion. We describe hereafter the model used to simulate the plasma expansion dynamics and extract the density gradient and its expansion velocity.

The electron density gradient is commonly derived from the self-similar solution of the isothermal equation of state for the electron [6] and is expressed by a decreasing exponential:

$$n_e(x) = n_c \exp\left(-\frac{x - x_c(t)}{c_s t}\right), \quad (8)$$

where  $c_s = (Zk_b T_e / m_i)^{1/2}$  is the ion sound velocity and  $n_c = (\omega_0^2 m_e \epsilon_0) / e^2$  the critical density. In these expressions,  $Z$  is the ion charge state,  $e$  is the electron charge,  $k_b$  the Helmholtz constant,  $T_e$  the electron temperature,  $m_e$  and  $m_i$ , respectively the electron and ion mass, and  $\omega_0$  is the carrier frequency of the probe pulse. We define  $L(t) = c_s t$  as the gradient length, proportional to the coordinate of critical density  $x_c(t)$ . For a

fully ionized silica target, the maximum density is about  $300n_c$ , such that  $x_c(t) = \ln(300) \times L(t) \approx 5.7 \times L(t)$ .

Assuming the electron temperature,  $T_e$ , depends linearly on the energy deposited on target when the plasma is created, i.e., on the pump pulse intensity  $I_p$ , we can write, according to its definition, that  $c_s \propto \sqrt{I_p}$ . The pump intensity is considered to be constant for each isolated diffracted probe spot in order to define a single corresponding plasma expansion velocity. The pump intensity is  $I_{p,1}$  at the center and  $I_{p,2}$  at the location of the first-order diffracted spots. This means that the center of the plasma expands nearly twice as fast as its edges. Taking into account the angle of incidence of  $\theta = 49.3$  deg from the target normal, we express the phase difference  $\Delta\phi$  as a function of the relative difference in position of the critical surface  $\Delta x_c$ :

$$\Delta\phi(t) = \frac{4\pi}{\lambda} \Delta x_c(t) \cos(\theta) = \frac{4\pi}{\lambda} 0.7 \Delta x_c(t), \quad (9)$$

where

$$\Delta x_c(t) = c_s \left(1 - \sqrt{\frac{I_{p,2}}{I_{p,1}}}\right) t. \quad (10)$$

A linear fit of each inversion data point is performed in Fig. 3, resulting in a measured expansion velocity  $c_s = 10.8 \text{ nm/ps} \pm 1.1 \text{ nm/ps}$  for a pump intensity of  $I_{p,1} = 3.5 \times 10^{14} \text{ W/cm}^2$ . This order of magnitude matches other measurements obtained by FDI [2], assuming the plasma expansion velocity scales as  $c_s \propto \sqrt{I_p}$  and does not vary with time. The price to pay for such a simple measurement technique is an increasing error bar on the inversion as pump-probe delay increases. In order to probe longer gradients, one idea would be to decrease the period  $a$  of the diffraction mask in order to increase the distance between the different diffracted spots on target and therefore be less sensitive to the first-order linear phase induced by the slope of the critical plasma surface distribution. In our case, we focused on the early stages of plasma expansion ( $L < \lambda$ ), since this is the regime where ultrafast nonlinear dynamics of interest can occur.

In conclusion, we demonstrate that simple imaging of a spatially shaped probe pulse reflecting off an expanding plasma mirror induced by a time-delayed pump pulse yields the electronic density gradient of the plasma mirror with sub- $\mu\text{m}$

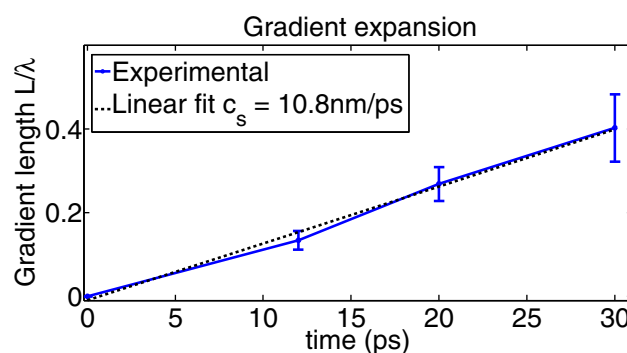


**Fig. 3.** Measured relative plasma expansion velocity for a pump pulse intensity of  $I_{p,1} = 3.5 \times 10^{14} \text{ W/cm}^2$  as a function of pump-probe delay. Each experimental point corresponds to an inversion in the far-field probe beam intensity profile induced by the expanding critical surface of the plasma formed at the surface of the solid target. Inversions are defined by  $\Delta\phi = n\pi$  with here  $n = 0, 1, 2, 3$ .

and sub-ps accuracy. The only assumption made here is that the plasma expansion velocity is proportional to the pump intensity [6]. As a consequence, experimental plasma expansion velocities of  $\approx 10.8$  nm/ps were measured for a peak pump pulse intensity of  $3.5 \times 10^{14}$  W/cm<sup>2</sup>. This is possible because of clearly visible far-field probe beam pattern inversions for every  $\pi$  phase shift for short pump-probe delays. This is no longer the case at longer delays ( $\gg 10$  ps, [12]), where we reach the spatial coherence length ( $\sim 6$   $\mu$ m) of our interferometer. However, our approach is accurate for very steep gradients  $< \lambda$ , for which efficient high-order harmonic generation and electron acceleration is typically observed from plasma mirrors. We emphasize the simplicity of the SDI technique, which only requires inserting a spatial mask into the main beam used to drive nonlinear plasma mirror dynamics. In principle, SDI can be used for ultrafast imaging of any nm to  $\mu$ m size moving phase objects in a configuration suited to multiple-beam reflection interferometry [13]. We are currently working on a phase retrieval algorithm that would allow single-shot retrieval of the full complex probe pulse field transmitted by the plasma mirror optical system, whatever its state. This would allow 2D mapping of both the reflectivity and phase of the expanding plasma mirror without the need for any assumption on its expansion dynamics.

Agence Nationale pour la Recherche (ANR-11-EQPX-005-ATTOLAB); European Research Council (306708, ERC Starting Grant FEMTO- ELEC).

## REFERENCES

1. C. Thauray, F. Quéré, J. P. Geindre, A. Levy, T. Ceccotti, P. Monot, M. Bougeard, F. Réau, P. D'Oliveira, P. Audebert, R. Marjoribanks, and P. Martin, *Nat. Phys.* **3**, 424 (2007).
2. S. Kahaly, S. Monchocé, H. Vincenti, T. Dzelzainis, B. Dromey, M. Zepf, P. Martin, and F. Quéré, *Phys. Rev. Lett.* **110**, 175001 (2013).
3. S. Bastiani, A. Rousse, J. P. Geindre, P. Audebert, C. Quoi, G. Hamoniaux, A. Antonetti, and J.-C. Gauthier, *Phys. Rev. E* **56**, 7179 (1997).
4. A. G. Mordovanakis, J. Easter, N. Naumova, K. Popov, P.-E. Masson-Laborde, B. Hou, I. Sokolov, G. Mourou, I. V. Glazyrin, W. Rozmus, V. Bychenkov, J. Nees, and K. Krushelnick, *Phys. Rev. Lett.* **103**, 235001 (2009).
5. A. Flacco, F. Sylla, M. Veltcheva, M. Carrié, R. Nuter, E. Lefebvre, D. Batani, and V. Malka, *Phys. Rev. E* **81**, 036405 (2010).
6. W. L. Kruer, *The Physics of Laser Plasma Interactions* (Addison-Wesley, 1988), vol. **73**.
7. J. P. Geindre, A. Mysyrowicz, A. Dos Santos, P. Audebert, A. Rousse, G. Hamoniaux, A. Antonetti, F. Fallières, and J. C. Gauthier, *Opt. Lett.* **19**, 1997 (1994).
8. M. C. Downer, R. L. Fork, and C. V. Shank, *J. Opt. Soc. Am. B* **2**, 595 (1985).
9. V. V. Temnov, K. Sokolowski-Tinten, P. Zhou, and D. von der Linde, *J. Opt. Soc. Am. B* **23**, 1954 (2006).
10. A. Jullien, A. Ricci, F. Böhle, J.-P. Rousseau, S. Grabielle, N. Forget, H. Jacqmin, B. Mercier, and R. Lopez-Martens, *Opt. Lett.* **39**, 3774 (2014).
11. A. Borot, D. Douillet, G. Iaquaniello, T. Lefrou, P. Audebert, J. P. Geindre, and R. Lopez-Martens, *Rev. Sci. Instrum.* **85**, 013104 (2014).
12. T. Kiefer, T. Schlegel, and M. C. Kaluza, *Phys. Rev. E* **87**, 043110 (2013).
13. J. Holden, *Proc. Phys. Soc. B* **62**, 405 (1949).



## Anticorrelated Emission of High Harmonics and Fast Electron Beams From Plasma Mirrors

Maimouna Bocoum,\* Maxence Thévenet, Frederik Böhle, Benoît Beaurepaire, Aline Vernier, Aurélie Jullien, Jérôme Faure, and Rodrigo Lopez-Martens  
*Laboratoire d'Optique Appliquée, ENSTA ParisTech, CNRS, Ecole polytechnique, Université Paris-Saclay, 828 bd des Maréchaux, 91762 Palaiseau cedex, France*

(Received 17 December 2015; revised manuscript received 4 March 2016; published 5 May 2016)

We report for the first time on the anticorrelated emission of high-order harmonics and energetic electron beams from a solid-density plasma with a sharp vacuum interface—plasma mirror—driven by an intense ultrashort laser pulse. We highlight the key role played by the nanoscale structure of the plasma surface during the interaction by measuring the spatial and spectral properties of harmonics and electron beams emitted by a plasma mirror. We show that the nanoscale behavior of the plasma mirror can be controlled by tuning the scale length of the electron density gradient, which is measured *in situ* using spatial-domain interferometry.

DOI: 10.1103/PhysRevLett.116.185001

Over the past 30 years, solid-density plasmas driven by intense femtosecond pulses, so-called plasma mirrors, have been successfully tested as a source of high-order harmonics and attosecond extreme ultraviolet (XUV) pulses in a number of experiments [1–10], where the laser intensity typically exceeds a few  $10^{14}$  W/cm<sup>2</sup>. Other experiments have shown it is also possible to accelerate energetic electrons from plasma mirrors for intensities above  $10^{16}$  W/cm<sup>2</sup> [11–13]. Attempting to understand each of these experimental observations invariably points to the key role played by the plasma-vacuum interface during the interaction both on the nanoscale spatially and on the sub-laser-cycle scale temporally [14,15].

It is commonly assumed that the electron density at the plasma mirror surface decreases exponentially from solid to vacuum over a distance  $L_g$ , also called the density gradient. When the laser pulse reflects on this plasma mirror, for every oscillation of the laser field, some electrons are driven towards vacuum and sent back to the plasma [16,17]. These bunches of so-called Brunel electrons [18] impulsively excite collective high-frequency plasma oscillations in the density gradient that lead to the emission of XUV radiation through linear mode conversion [19]. As illustrated in Fig. 1(a), each position  $x$  of the plasma behaves as a nanoscale oscillator of frequency  $\omega_p(x) = \omega_0 \sqrt{n_e(x)/n_c}$ , where  $\omega_0$  is the driving laser angular frequency,  $n_e$  is the local electron density at position  $x$ , and  $n_c$  is the critical density. This periodic mechanism, called coherent wake emission (CWE), leads to efficient high-harmonics generation for very short plasma scale lengths, typically  $L_g \sim \lambda/100$  [19], even for subrelativistic intensities  $a_0 < 1$ , where  $a_0 = eA_0/mc$  is the normalized vector potential,  $e$  and  $m$  are the electron charge and mass, and  $c$  is the speed of light. However, the efficiency significantly drops for  $L_g \gg \lambda/20$  [4,5,19,20]. At higher intensities

$a_0 \gg 1$ , the relativistic oscillating mirror (ROM) becomes the dominant mechanism for harmonic generation [16,21].

A fraction of electrons do not follow Brunel-like trajectories: they are accelerated in the density gradient towards vacuum and escape the plasma, as illustrated in Fig. 1(b). Depending on the interaction conditions, the final energy and angular spread of these electrons can be influenced by plasma waves below the critical surface [11], interference fields created by the incident and reflected laser beams [13,22,23], betatronlike motion at the plasma surface [24], or even direct laser acceleration in vacuum [25]. Here again, the plasma scale length plays a critical role: enhanced electron generation is observed typically for  $0.1 < L_g/\lambda < 1$  [11,13,26] or sometimes even for  $L_g/\lambda > 1$  [27–29]. To our knowledge, the anticorrelated

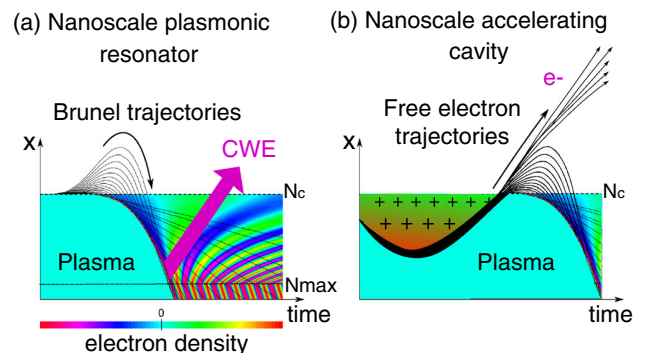


FIG. 1. Diagrams of nanoscale plasma mirror surface structures leading to (a) CWE, where electrons are pulled toward the vacuum and are sent back to the plasma where they excite high-frequency plasma waves, which radiate high-order harmonics (b) electron acceleration on the sub-laser-cycle time scale, where electrons are accelerated in the density gradient and escape from the plasma.

emission of harmonics and fast electrons from plasma mirrors has never been investigated experimentally. In this Letter, through a controlled pump-probe experiment using subrelativistic femtosecond laser pulses, we directly observe the transition from a confined plasma that can efficiently emit laser harmonics to an extended plasma structure that accelerates fast electrons into vacuum up to a few hundred keV energies, where the laser interference field only plays a second role.

The experiment was carried out using the ‘‘Salle Noire’’ laser system at the Laboratoire d’Optique Appliquée (LOA) delivering up to 3 mJ energy, 30 fs pulses at 1 kHz repetition rate with high temporal contrast ( $>10^{10}$ ) [30]. The  $p$ -polarized pulses are focused down to 1.7  $\mu\text{m}$  FWHM spot size onto an optically flat fused silica target ( $\sim 250n_c$ ), leading to peak intensities on target  $\approx 10^{18}$  W/cm $^2$  ( $a_0 \approx 0.7$ ) for an incidence angle  $\theta_L = 49.3^\circ$ , with high repeatability at 1 kHz [31]. Five percent of the main beam is picked off and focused down to 5 times the main beam spot size on target in order to induce homogeneous plasma expansion at the surface (see also Supplemental Material [32]). The plasma scale length  $L_g$  can then be varied by changing the relative delay between this prepulse and the main high-intensity pulse. We use spatial domain interferometry [33] to estimate the plasma expansion velocity  $c_s$  and find  $c_s = dL_g/dt = 10.8 \pm 1.1$  nm/ps for a prepulse intensity of  $\approx 3.5 \times 10^{14}$  W/cm $^2$  ( $a_0 \approx 0.013$ ).

Harmonics emitted in the specular direction are sent into a homemade XUV spectrometer where the harmonic spectrum is resolved in the horizontal plane and the harmonic beam divergence in the vertical direction using a coupled micro-channel plate and phosphor screen detector. At the same time, a  $6 \times 17$  cm Lanex screen was positioned 10 cm away, parallel to the target surface without blocking the specular direction. The angular electron emission profile in this geometry was recorded as a function of  $\theta \in [-20^\circ 30^\circ]$ , the angle with respect to target normal in the plane of incidence, and  $\phi \in [-20^\circ 20^\circ]$ , the angle with respect to target normal in the tangential plane. Note that the Lanex screen only detects electrons with energies larger than 150 keV [34]. The Lanex screen could also be replaced by an electron spectrometer for characterizing the electron energy distribution.

Figure 2(a) shows the harmonic spectrum and the electron signal as a function of pump-probe delay, hence the gradient length. The harmonic signal was integrated along the divergence angle. The plasma scale length calculated from the plasma expansion velocity is indicated on the bottom axis. The first striking result is that harmonics are generated efficiently for pump-probe delays below 4 ps, corresponding to  $L_g \leq 0.05\lambda$ . The spectrum extends up to the plasma frequency cutoff  $\omega_c/\omega_0 = 16$  and its divergence is about 1/10 that of the driving laser beam, which is the typical signature of CWE [20]. The plasma frequency cutoff confirms that Brunel electrons can

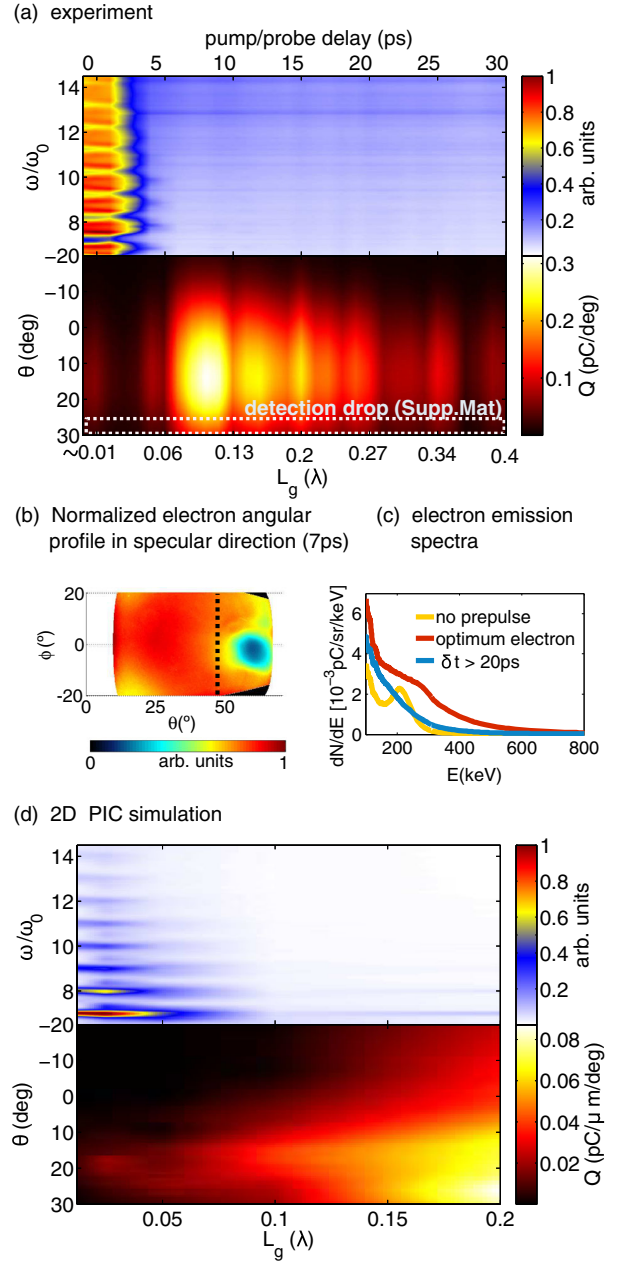


FIG. 2. (a) Experimental harmonic spectra and electron angular emission profiles as a function of pump-probe delay (top axis) between the prepulse and the main pulse. The electron signal was integrated along the tangential coordinate  $\phi$ . The corresponding plasma scale length  $L_g$  (bottom axis) was extracted from the plasma expansion velocity  $c_s = 10.8$  nm/ps measured by spatial domain interferometry [33]. (b) Electron angular distribution when the Lanex is placed perpendicular to the specular direction and after deconvolution (see Supplemental Material [32]). (c) Electron energy spectra for three typical delays. (d) Same as (a) for 2D PIC simulations with  $a_0 = 0.4$  and gradient length  $L_g \in [0.01\lambda 0.2\lambda]$ .

efficiently excite collective plasma oscillations and therefore that the initial plasma scale length should be on the order of  $L_g \sim 0.01\lambda$  [19] rather than rigorously  $0\lambda$ . This also indicates that the temporal contrast close to the pulse peak

does not allow us to explore arbitrarily small plasma scale lengths. The drop in CWE efficiency with increasing density gradient has already been observed experimentally and is theoretically predicted to be in the range  $0.02 < L_g/\lambda < 0.1$  [20,36], depending on laser intensity [19]. This can be explained with 1D considerations: the minimum time required to excite plasma waves from the critical surface  $x = x_c$  to the location of maximum density  $x = x_{\max}$  is  $\Delta t = (L_g/c) \log(n_{\max}/n_c)$ , which should be less than the laser period in order to prevent cycle-to-cycle destructive interferences. For traveling electrons, this limit reads  $L_g \leq 0.17\lambda$ . In our case, the drop in efficiency occurs at much lower values around  $L_g \sim 0.05\lambda$  because the electron perturbation propagates at less than  $c$  and the initial perturbation strength (i.e., amplitude of plasma waves) decreases with  $L_g$  [19]. The second striking result is that a maximum electron signal is reached for a delay of 8 ps ( $L_g \sim 0.1\lambda$ ), where harmonic emission is negligible. The ejected electrons form a large spot between  $10^\circ$  and  $20^\circ$  and drop at the edge of the Lanex at  $\sim 30^\circ$ . This drop in signal is a geometrical artifact due to the anisotropic emission of the Lanex screen [34] (see Supplemental Material for details [32]). Figure 2(b) shows the full electron angular distribution for a delay of  $\sim 7$  ps, obtained by moving the Lanex screen perpendicular to the specular direction. The distribution displays a hole close to the specular direction, presumably formed by the ponderomotive force of the reflected laser pulse [13,22,25,37]. Using the Lanex calibration [34], we estimate that the ejected charge reaches a maximum of  $\sim 11$  pC compared to  $\sim 2$  pC at zero delay. Figure 2(c) shows electron spectra respectively without prepulse, for the optimal delay for electron emission, and after 20 ps. Hence, electrons can be effectively accelerated up to  $\sim 600$  keV at the optimal density gradient.

To summarize, we observe that the emission of harmonics and electrons is anticorrelated when changing the gradient scale length. These experimental results were confronted to 2D particle-in-cell (PIC) simulations, in which a  $\lambda = 800$  nm, 30 fs pulse is focused onto an overdense plasma ( $n_{\max} = 250n_c$ ) with immobile ions. The plasma density decreases exponentially with various scale lengths, from  $L_g = 0.01\lambda$  to  $0.2\lambda$ . The plasma density is cut at  $n_b = n_c/5$ , so that the plasma boundary is defined by  $x_b = -\log 5 L_g$ . The laser amplitude is  $a_0 = 0.4$  and the incidence angle is  $45^\circ$ . A good spatial resolution is required for simulating CWE harmonics, so we use  $\delta x = \lambda/420$ . In the simulations, electrons are detected at  $9\lambda$  away from the critical surface and only electrons with energies  $> 150$  keV are detected (as in the experiment). As illustrated in Fig. 2(d), the PIC simulations qualitatively reproduce our experimental observations: the CWE emission efficiency decreases for  $L_g > 0.05\lambda$  and the effective ejected electron charge increases up to  $\sim 3$  pC  $\cdot \mu\text{m}^{-1}$  for  $L_g = 0.2\lambda$  compared to  $0.12$  pC  $\cdot \mu\text{m}^{-1}$  when  $L_g = 0.01\lambda$  (i.e.,  $\approx 10$

and  $0.7$  pC, respectively, for a  $3.4 \mu\text{m}$  spot size FWHM). The electron angular distribution was plotted over the range  $\theta \in [-20^\circ 30^\circ]$  for a direct comparison with experiment. Here again, there is a very good agreement with the experiment, with a large divergence  $10$  pC beam ejected at  $\sim 30^\circ$  when  $L_g \sim 0.2\lambda$ . Note that PIC simulations were first performed with the experimental vacuum laser amplitude  $a_0 = 0.8$ , but a strong harmonic emission attributed to the ROM emission mechanism [20] persisted for longer gradients. These simulations at high intensities suggested a correlation between ROM harmonics and electron ejection, as opposed to the anticorrelation that we observed. In our experiment, ROM emission does not occur and the harmonics are due to CWE. This indicates that the laser intensity at focus is not high enough to support ROM emission [14]. Therefore, in the simulations, the beam spot size was doubled without changing the pulse energy; i.e.,  $a_0$  was decreased to  $0.4$ , to reproduce the anticorrelated behavior. Note that our overestimation of the experimental intensity on target may be due to a slight defocusing of the laser on target or debris reducing the overall transmission of the focusing optic, a standard problem with high repetition rate laser-plasma interaction experiments using tight focusing.

Figure 3 shows a comparison of 2D PIC simulations with a gradient length optimized for harmonic emission ( $L_g = \lambda/40$ ) and electron emission ( $L_g = \lambda/5$ ), respectively. In Figs. 3(a) and 3(b), one can clearly see oscillations of the electron surface at the laser period. Strong harmonic generation can be seen in Fig. 3(a). The corresponding electron trajectories are shown in Fig. 3(c), where the  $x$  coordinate (normal to the target) of electrons is plotted along time. For clarity, a single bunch of electrons is represented here, which interacts with the laser around its temporal maximum ( $t = 22T$ , where  $T$  is the optical period) in the center of the interference pattern. One can clearly see Brunel-like trajectories: electrons make a short excursion in vacuum before being driven back to the plasma where they trigger plasma waves. In Fig. 3(b), the amplitude of these oscillations is greater and layers of electrons are ejected from the plasma surface. The corresponding electron trajectories are plotted in Fig. 3(d). Once again, a bunch of electrons was selected for clarity. A fraction of these electrons (in red) escape from the plasma and propagate into vacuum in the interference pattern with a velocity  $\approx c/2$ .

For each laser cycle, the ejection mechanism can be described as follows: (i) the laser electric field pushes electrons inside the plasma, while the heavy ions stay in place, creating a charge separation electrostatic field, i.e., a plasma capacitor which can give potential energy to electrons; (ii) half a cycle later, the laser field changes sign and both the capacitor and the laser electric force pull and accelerate electrons towards vacuum. Assuming that all the electrons originating from  $x < 0$  (where  $n = n_c$ )

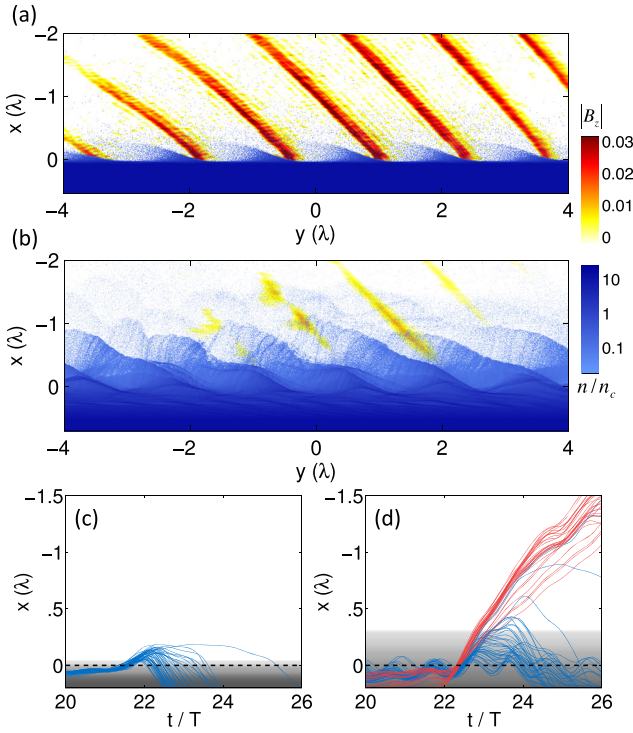


FIG. 3. (a) Snapshot from the 2D PIC simulation for  $L_g = \lambda/40$ . Blue, electron density (log scale). Yellow-red, reflected harmonic field (a Fourier filter was applied to keep only harmonic orders  $\geq 5\omega_0$ ). The harmonic field comes out as a train of attosecond pulses. (b) Same as (a) for  $L_g = \lambda/5$  (same instant, same color scale). (c),(d) Typical electron trajectories for  $L_g = \lambda/40$  and  $L_g = \lambda/5$ , respectively.  $x$  is the coordinate normal to the plasma. The gray scale stands for the plasma initial density and the black dotted line ( $x = 0$ ) shows the position of the critical density. The electrons represented here interact with the laser around its maximum ( $t = 22T$ ). Red trajectories stand for ejected electrons.

are pushed towards  $x \geq 0$ , the electrostatic potential of the remaining ions can be calculated using Poisson's equation  $\Delta V_P = -n_c/\epsilon_0 e^{x/L_g}$ , and reads  $V_P = -n_c L_g^2/\epsilon_0$ . Therefore, electrons are expected to gain more energy from the plasma for longer gradients. Figure 4(a) shows the spectrum of ejected electrons when they cross the plasma boundary at  $x_b$ . The average energy is much higher for longer gradients, thus confirming our predictions. Hence, the plasma serves as an injector of electrons into the reflecting laser [25]. In order to determine whether the electrons are mainly accelerated in the plasma or in the interference pattern, we plot the simulated electron spectra at the plasma border, at  $3.3\lambda$  and  $9\lambda$  away from the plasma in Fig. 4(b). Within this range, no net energy gain can be observed from the electromagnetic wave in vacuum; we conclude that the energy gain is mostly due to acceleration inside the plasma gradient. However, farther away from the plasma at  $9\lambda$ , the electron spectrum broadens and the tail of the distribution reaches 400 keV, which could be the signature of ponderomotive [13,23] and/or stochastic

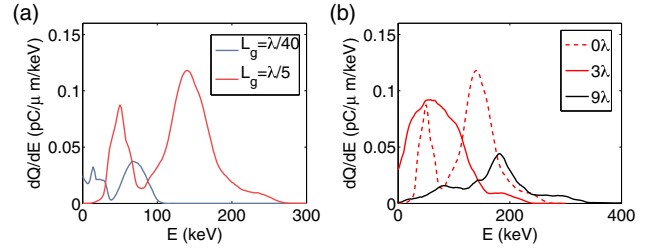


FIG. 4. Simulated ejected electron spectra at the plasma boundary  $x_b$  for  $L_g = \lambda/40$  (gray line) and  $L_g = \lambda/5$  (red line) as they cross the plasma critical surface. (b) Ejected electron spectra for  $L_g = \lambda/5$  as they cross the plasma critical surface (dotted line),  $3\lambda$  and  $9\lambda$  away from the plasma surface (red and black solid line, respectively).

heating in the interference pattern [38]. The formation of a hole in the experimental electron angular emission profile [see Fig. 2(b)] and the absence of a beaming as seen in Ref. [25] are more evidence that the interaction between the accelerated electrons and the laser is purely ponderomotive. Finally, from simulations and experiments, we also conclude that for  $a_0 < 1$  and  $L_g \sim 0.1\lambda$  electrons cannot be accelerated by plasma waves related to the CWE mechanism, as suggested in Ref. [11], otherwise, electron and harmonic emission would be optimal simultaneously.

To conclude, we observe for the first time the transition from high-harmonic emission to fast electron ejection as the electron density gradient increases at the surface of a plasma mirror driven at subrelativistic laser intensity. Our measurements reveal that both processes cannot occur simultaneously for the same density gradient. For sharp gradients ( $L_g < 0.05\lambda$ ), electrons drive oscillations in a confined plasma, leading to efficient coherent harmonic emission in their wake. For softer gradients, electrons can be efficiently accelerated out of the plasma by the space-charge field created for  $L_g \sim 0.1\lambda$ . Although the interaction with the reflected laser field thermalizes the electron population and reshapes the spatial emission profile via ponderomotive interactions, most of the acceleration occurs inside the plasma density gradient. As the gradient length increases by  $\sim 40$  nm, the plasma mirror behavior switches from a collection of efficient XUV resonators to a nano-scale electron accelerator.

We thank N. Naumova for useful discussions. This work was funded by the Agence Nationale pour la Recherche (under Contracts No. ANR-11-EQPX-005-ATTOLAB and No. ANR-14-CE32-0011-03 APERO), the European Research Council (under Contract No. 306708, ERC Starting Grant FEMTOELEC) and the Région Ile-de-France (under Contract No. SESAME 2012-ATTOLITE). Access was granted to the HPC resources of CINES under allocation 2015-056057 made by GENCI. Simulations were run using EPOCH, which was developed as part of the UK EPSRC funded Project No. EP/G054940/1.

- \*Corresponding author.  
maimouna.bocoum@ensta-paristech.fr
- [1] N. Burnett, H. Baldis, M. Richardson, and G. Enright, *Appl. Phys. Lett.* **31**, 172 (1977).
- [2] R. L. Carman, C. K. Rhodes, and R. F. Benjamin, *Phys. Rev. A* **24**, 2649 (1981).
- [3] D. von der Linde, T. Engers, G. Jenke, P. Agostini, G. Grillon, E. Nibbering, A. Mysyrowicz, and A. Antonetti, *Phys. Rev. A* **52**, R25 (1995).
- [4] A. Tarasevitch, A. Orisch, D. Von der Linde, P. Balcou, G. Rey, J.-P. Chambaret, U. Teubner, D. Klöpfel, and W. Theobald, *Phys. Rev. A* **62**, 023816 (2000).
- [5] F. Quéré, C. Thauray, P. Monot, S. Dobosz, P. Martin, J.-P. Geindre, and P. Audebert, *Phys. Rev. Lett.* **96**, 125004 (2006).
- [6] Y. Nomura, R. Hörlein, P. Tzallas, B. Dromey, S. Rykovanov, Z. Major, J. Osterhoff, S. Karsch, L. Veisz, M. Zepf *et al.*, *Nat. Phys.* **5**, 124 (2009).
- [7] J. H. Easter, A. G. Mordovanakis, B. Hou, A. G. Thomas, J. A. Nees, G. Mourou, and K. Krushelnick, *Opt. Lett.* **35**, 3186 (2010).
- [8] A. Borot, A. Malvache, X. Chen, D. Douillet, G. Iaquaniello, T. Lefrou, P. Audebert, J.-P. Geindre, G. Mourou, F. Quéré *et al.*, *Opt. Lett.* **36**, 1461 (2011).
- [9] P. Heißler, R. Hörlein, J. M. Mikhailova, L. Waldecker, P. Tzallas, A. Buck, K. Schmid, C. Sears, F. Krausz, L. Veisz *et al.*, *Phys. Rev. Lett.* **108**, 235003 (2012).
- [10] J. A. Wheeler, A. Borot, S. Monchocé, H. Vincenti, A. Ricci, A. Malvache, R. Lopez-Martens, and F. Quéré, *Nat. Photonics* **6**, 829 (2012).
- [11] S. Bastiani, A. Rousse, J. P. Geindre, P. Audebert, C. Quoix, G. Hamoniaux, A. Antonetti, and J.-C. Gauthier, *Phys. Rev. E* **56**, 7179 (1997).
- [12] F. Brandl, B. Hidding, J. Osterholz, D. Hemmers, A. Karmakar, A. Pukhov, and G. Pretzler, *Phys. Rev. Lett.* **102**, 195001 (2009).
- [13] A. G. Mordovanakis, J. Easter, N. Naumova, K. Popov, P.-E. Masson-Laborde, B. Hou, I. Sokolov, G. Mourou, I. V. Glazyrin, W. Rozmus *et al.*, *Phys. Rev. Lett.* **103**, 235001 (2009).
- [14] C. Thauray, F. Quéré, J.-P. Geindre, A. Levy, T. Ceccotti, P. Monot, M. Bougeard, F. Réau, P. d'Oliveira, P. Audebert *et al.*, *Nat. Phys.* **3**, 424 (2007).
- [15] A. Borot, A. Malvache, X. Chen, A. Jullien, J.-P. Geindre, P. Audebert, G. Mourou, F. Quéré, and R. Lopez-Martens, *Nat. Phys.* **8**, 416 (2012).
- [16] R. Lichters, J. Meyer-ter-Vehn, and A. Pukhov, *Phys. Plasmas* **3**, 3425 (1996).
- [17] T. Liseykina, P. Mulser, and M. Murakami, *Phys. Plasmas* **22**, 033302 (2015).
- [18] F. Brunel, *Phys. Rev. Lett.* **59**, 52 (1987).
- [19] C. Thauray and F. Quéré, *J. Phys. B* **43**, 213001 (2010).
- [20] S. Kahaly, S. Monchocé, H. Vincenti, T. Dzelzainis, B. Dromey, M. Zepf, P. Martin, and F. Quéré, *Phys. Rev. Lett.* **110**, 175001 (2013).
- [21] S. V. Bulanov, N. Naumova, and F. Pegoraro, *Phys. Plasmas* **1**, 745 (1994).
- [22] Y. Tian, J. Liu, W. Wang, C. Wang, A. Deng, C. Xia, W. Li, L. Cao, H. Lu, H. Zhang *et al.*, *Phys. Rev. Lett.* **109**, 115002 (2012).
- [23] N. Naumova, I. Sokolov, J. Nees, A. Maksimchuk, V. Yanovsky, and G. Mourou, *Phys. Rev. Lett.* **93**, 195003 (2004).
- [24] M. Chen, Z.-M. Shenga, J. Zheng, Y.-Y. Ma, M. A. Bari, Y.-T. Li, and J. Zhang, *Opt. Express* **14**, 3093 (2006).
- [25] M. Thévenet, A. Leblanc, S. Kahaly, H. Vincenti, A. Vernier, F. Quéré, and J. Faure, *Nat. Phys.* **12**, 355 (2015).
- [26] J. P. Geindre, R. S. Marjoribanks, and P. Audebert, *Phys. Rev. Lett.* **104**, 135001 (2010).
- [27] W. Wang, J. Liu, Y. Cai, C. Wang, L. Liu, C. Xia, A. Deng, Y. Xu, Y. Leng, R. Li *et al.*, *Phys. Plasmas* **17**, 023108 (2010).
- [28] D. F. Cai, Y. Q. Gu, Z. J. Zheng, W. M. Zhou, X. D. Yang, C. Y. Jiao, H. Chen, T. S. Wen, and S. T. Chunyu, *Phys. Rev. E* **70**, 066410 (2004).
- [29] W. Yu, V. Bychenkov, Y. Sentoku, M. Y. Yu, Z. M. Sheng, and K. Mima, *Phys. Rev. Lett.* **85**, 570 (2000).
- [30] A. Jullien, A. Ricci, F. Böhle, J.-P. Rousseau, S. Grabielle, N. Forget, H. Jacqmin, B. Mercier, and R. Lopez-Martens, *Opt. Lett.* **39**, 3774 (2014).
- [31] A. Borot, D. Douillet, G. Iaquaniello, T. Lefrou, P. Audebert, J.-P. Geindre, and R. Lopez-Martens, *Rev. Sci. Instrum.* **85**, 013104 (2014).
- [32] See Supplemental Material at <http://link.aps.org/supplemental/10.1103/PhysRevLett.116.185001> for Experimental setup and Lanex signal deconvolution, which includes Refs [25,33,34,35].
- [33] M. Bocoum, F. Böhle, A. Vernier, A. Jullien, J. Faure, and R. Lopez-Martens, *Opt. Lett.* **40**, 3009 (2015).
- [34] Y. Glinec, J. Faure, A. Guemnie-Tafo, V. Malka, H. Monard, J. Larbre, V. De Waele, J. Marignier, and M. Mostafavi, *Rev. Sci. Instrum.* **77**, 103301 (2006).
- [35] A. Jullien, C. Durfee, A. Trisorio, L. Canova, J.-P. Rousseau, B. Mercier, L. Antonucci, G. Cheriaux, O. Albert, and R. Lopez-Martens, *Appl. Phys. B* **96**, 293 (2009).
- [36] A. Tarasevitch, K. Lobov, C. Wünsche, and D. von der Linde, *Phys. Rev. Lett.* **98**, 103902 (2007).
- [37] B. Quesnel and P. Mora, *Phys. Rev. E* **58**, 3719 (1998).
- [38] Z.-M. Sheng, K. Mima, Y. Sentoku, M. S. Jovanović, T. Taguchi, J. Zhang, and J. Meyer-ter-Vehn, *Phys. Rev. Lett.* **88**, 055004 (2002).

## Effect of the Laser Wave Front in a Laser-Plasma Accelerator

B. Beaufrepaire, A. Vernier, M. Bocoum, F. Böhle, A. Jullien, J-P. Rousseau, T. Lefrou, D. Douillet,  
G. Iaquaniello, R. Lopez-Martens, A. Lifschitz, and J. Faure

*Laboratoire d'Optique Appliquée, UMR 7639, ENSTA-CNRS-Ecole Polytechnique,  
91761 Palaiseau, France*

(Received 10 December 2014; published 31 July 2015)

A high-repetition rate electron source is generated by tightly focusing kHz, few-mJ laser pulses into an underdense plasma. This high-intensity laser-plasma interaction leads to stable electron beams over several hours but with strikingly complex transverse distributions even for good quality laser focal spots. We find that the electron beam distribution is sensitive to the laser wave front via the laser midfield distribution rather than the laser focal spot itself. We are able to measure the laser wave front around the focus and include it in realistic particle-in-cell simulations demonstrating the role of the laser wave front on the acceleration of electrons. Distortions of the laser wave front cause spatial inhomogeneities in the midfield laser intensity and, consequently, the laser pulse drives an inhomogeneous transverse wakefield whose focusing and defocusing properties affect the electron distribution. These findings explain the experimental results and suggest the possibility of controlling the electron spatial distribution in laser-plasma accelerators by tailoring the laser wave front.

DOI: [10.1103/PhysRevX.5.031012](https://doi.org/10.1103/PhysRevX.5.031012)

Subject Areas: Optics, Plasma Physics

### I. INTRODUCTION

Laser-plasma accelerators [1,2] currently provide 100 MeV to few GeV electron beams in short distances [3,4], owing to their very high accelerating gradients  $\approx 100$  GV/m. In these experiments, an intense laser pulse drives a large amplitude plasma wave in which plasma electrons can be trapped and accelerated to relativistic energies in millimeter distances. These laser-driven electron sources are also of great interest because the generated electron bunches can be extremely short, with durations reaching down to a few femtoseconds only [5]. In general, laser-plasma accelerators operate using 100-TW, joule-level laser systems. In this case, the laser power exceeds the critical power for relativistic self-focusing [6,7],  $P/P_c > 1$ , and the laser pulses are self-focused over several Rayleigh lengths. Injection and acceleration of electrons occur in the region where the laser is self-focused, corresponding to the region where the plasma wave amplitude is high. In many experiments, the laser wave front is corrected in order to obtain the best laser spot in the focal plane and little attention is given to the laser transverse distribution outside the focal plane.

Recently, several groups have been developing laser-plasma accelerators operating at high-repetition rate, using kHz lasers with energies  $< 10$  mJ [8,9]. Such developments are particularly important for applications as the

high-repetition rate improves the beam stability and permits data accumulation. Indeed, kHz electron beams with femtosecond duration and energies in the MeV range are of great interest for ultrafast electron diffraction [10,11], a powerful technique for investigating structural dynamics in matter with femtosecond resolution. Recent experiments have shown the possibility of generating 100-keV electron bunches at kHz repetition rate [8]. Electron bunches from a kHz laser-plasma source were successfully used to obtain clear diffraction patterns on single crystal gold foils [12]. In these high-repetition rate experiments, the laser pulse has to be focused very tightly in order to reach intensities in excess of  $10^{18}$  W/cm<sup>2</sup>, as required to drive large amplitude plasma waves. Therefore, the Rayleigh range of the laser beam is extremely short, typically on the order of  $z_R \approx 10$   $\mu$ m. In addition, self-focusing does not occur because the power is not high enough,  $P/P_c < 1$ . Consequently, the interaction region extends outside the focal region and one expects that experimental results should also depend critically on the laser distribution in the intermediate field.

In this article, we show results from a laser-plasma accelerator operating at kHz repetition rate. The interaction region is large compared to the Rayleigh range,  $L \gg z_R$ , so that the laser distribution outside the focal region plays an important role in the physics of electron injection and acceleration. We demonstrate that the spatial distribution of the electron beam originates from the inhomogeneity of the laser distribution outside the focal region, due to an imperfect laser wave front. Particle-in-cell (PIC) simulations show that an inhomogeneous laser pulse drives an inhomogeneous transverse wakefield, which affects the

---

*Published by the American Physical Society under the terms of the Creative Commons Attribution 3.0 License. Further distribution of this work must maintain attribution to the author(s) and the published article's title, journal citation, and DOI.*

electron beam quality through its focusing and defocusing properties. Our work emphasizes the influence of the laser wave front over wake excitation as well as on the electron beam spatial distribution.

## II. EXPERIMENT

A schematic of the experiment is shown in Fig. 1. The experiment is performed using 1-kHz, 800-nm laser pulses with  $\tau = 22$  fs duration at FWHM. The energy on target is in the range 2.5–3 mJ. The laser system provides high-contrast laser pulses and good beam quality through the use of spatial filtering in a hollow core fiber [13]. The laser pulses are focused down to a spot size of  $\lesssim 2$   $\mu\text{m}$  FWHM using a  $f\#1.5$ ,  $90^\circ$  off-axis parabolic mirror, thus leading to a peak intensity of  $I = (2.5\text{--}3) \times 10^{18}$  W/cm<sup>2</sup> and a measured Rayleigh range of  $\approx 20$   $\mu\text{m}$ . The gas target consists of a 100- $\mu\text{m}$  diameter gas jet operating in continuous flow so as to make kHz operation possible. The electron beam profile is measured using a CsI(Tl) phosphor screen imaged onto a 14-bit CCD camera. The electron energy distribution is measured by inserting a magnetic electron spectrometer. Information on laser propagation in the gas jet is obtained by imaging the transmitted laser mode at the exit of the plasma. Finally, the electron density is monitored *in situ* by transverse interferometry with a 22-fs probe laser pulse. The experiment is run at kHz repetition rate and all data shown in this paper are averaged over 500–1000 shots.

The data are taken using nitrogen as we are limited by the evacuation of the gas fed into the jet. Gas evacuation is a critical issue in this experiment since we need, on the one hand, a continuous gas flow to make full use of the high-repetition rate of the laser, and, on the other hand, a fairly high electron density ( $n_e > 10^{19}$  cm<sup>-3</sup>). The required electron density is reached with nitrogen for a backing pressure about 5 times lower than with helium, and considering the inefficiency of the pumping of helium

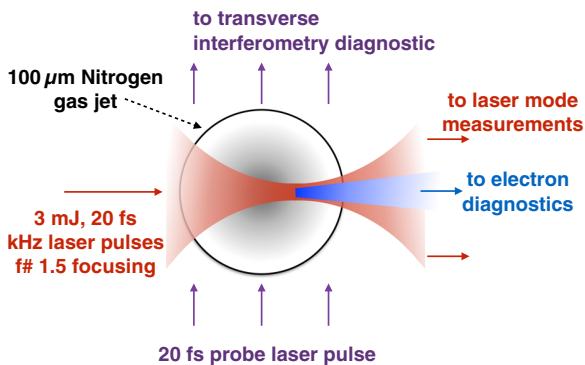


FIG. 1. Top view schematic of the experimental setup. A laser pulse is tightly focused into a gas jet. Strong focusing with a  $f\#1.5$  optics results in a short Rayleigh length compared to the gas jet length of 100  $\mu\text{m}$ .

compared to nitrogen, using the latter allows us to get the most complete data set.

In nitrogen, the first five electrons are ionized at intensities  $I \lesssim 10^{16}$  W/cm<sup>2</sup>, so that ionization-induced defocusing [14,15] does not significantly affect the laser pulse propagation for  $I \approx 10^{18}$  W/cm<sup>2</sup>. However, away from focus ( $L \gg z_R$ ), the laser intensity in the gas jet can decrease down to the  $10^{16}$  W/cm<sup>2</sup> range and ionization might affect propagation. By measuring the transmitted laser mode, we check that the laser pulse does not undergo filamentation and that ionization-induced defocusing [14,15] does not significantly affect the position and size of the focal spot (see Supplemental Material [16]). Therefore, even in the presence of ionization, the laser pulse reaches intensities in excess of  $10^{18}$  W/cm<sup>2</sup>, as required for generating large amplitude plasma waves.

The green curve in Fig. 2(a) represents a typical longitudinal electron density profile when the laser is focused 150  $\mu\text{m}$  above the gas jet. Here, the density reaches  $n_e = 3 \times 10^{19}$  cm<sup>-3</sup> and the density gradients are on the order of 50  $\mu\text{m}$ . The blue curve in Fig. 2(a) represents the measured accelerated charge as a function of the position of the laser focus. We find that the amount of accelerated electrons depends critically on the position of the focal plane, and that a charge as high as 20 fC/shot (i.e., 20 pC/s) can be obtained when the laser is focused in the density down ramp. In Fig. 2(b), the accelerated charge is plotted as a function of  $\omega_p(z)\tau$ , where  $\omega_p(z) = \sqrt{n_e(z)e^2/m_e\epsilon_0}$  is the local plasma frequency along the propagation axis. The green curve represents the plasma wave amplitude  $\Delta\phi$  obtained from a 1D nonlinear fluid model of plasma wave excitation [17]. The experimental data peak at  $\omega_p\tau \approx 2.6$ , which is very close to the theoretical estimate of resonant plasma wave excitation; i.e., for a 22-fs laser pulse, the resonant density is  $n_e^{\text{res}} \approx 5 \times 10^{18}$  cm<sup>-3</sup>. This last result indicates that electrons are produced preferentially when the resonant condition is satisfied, suggesting electron acceleration by plasma waves. In addition, electrons are produced only when the laser is focused in the density down ramp, pointing toward density gradient injection [18–22], as reported previously in a similar experiment in Ref. [8]. Thus, the experimental evidence tends to show that the excitation of a large amplitude plasma wave in the density gradient results in trapping and subsequent acceleration. This interpretation is confirmed by the simulations shown Sec. III.

Comparable results were obtained using helium instead of nitrogen, excluding ionization injection [23,24] as a possible injection mechanism. Finally, we measure that the accelerated electrons have a large energy distribution extending to about 100 keV; see Fig. 2(f). Note that electrons below 50 keV are not detected because our CsI(Tl) detector has a very small response below 50 keV.

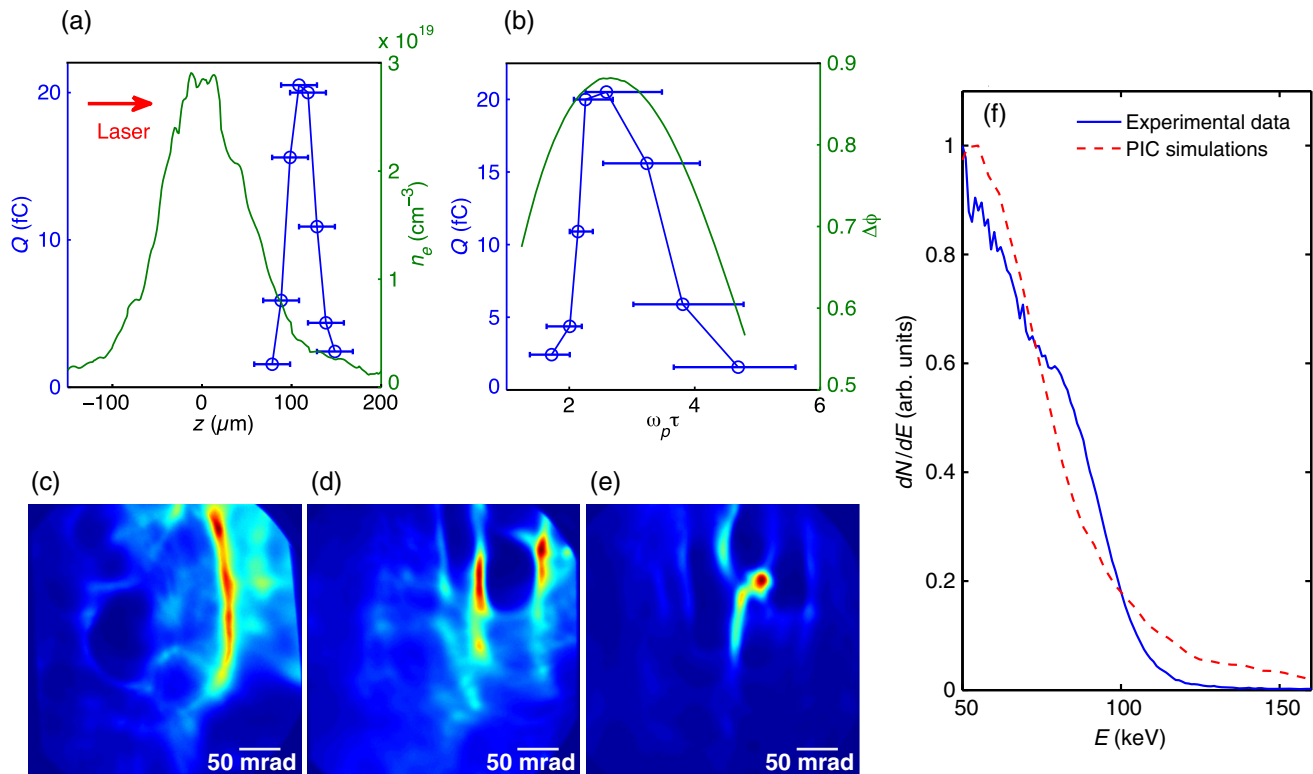


FIG. 2. Experimental results. (a) Green curve, measured longitudinal electron density profile; blue curve, charge or shot of the accelerated electrons for different positions of the laser focus. (b) Beam charge as a function of  $\omega_p(z)\tau$ , where  $\omega_p(z)$  is estimated using the experimental plasma density at the focal plane. The green curve is the theoretical plasma wave amplitude  $\Delta\phi$ . Horizontal error bars originate from a  $\pm 20 \mu\text{m}$  uncertainty on the position of the focus. (c)–(e) Typical images of electron beam profiles. (f) Electron energy distribution. Blue line, experimental result; red line, distribution from the 3D PIC simulation.

Figures 2(c)–2(e) show typical electron beam transverse distributions obtained during different experimental runs. Each image is obtained by averaging over about 1000 shots. These beams have complex structures that are not random and are remarkably stable over the course of several hours. In these kHz experiments, the electron beam parameters vary very little for a given set of experimental conditions (see also Ref. [12]): the charge fluctuations are on the order of 7% rms and the energy and divergence fluctuate at the percent level [25]. The shape of the beam does, however, change from run to run. Depending on the experimental conditions, it can exhibit various complex patterns [see Figs. 2(c) and 2(d)] or a low-divergence beam  $< 10 \text{ mrad}$  and containing  $\approx 20 \text{ fC}$ , as in Fig. 2(e). Such electron distributions are quite different from those emerging from high-energy laser-plasma accelerators. Similar beams were obtained in Ref. [8], but no explanation was given for the observed complex structures.

Experimentally, we notice that the electron beam spatial structures are correlated to the laser distribution in the intermediate field rather than to the laser distribution at focus. Indeed, similar focal spots produce very different

electron beams when the mid-field laser distribution changes significantly. For instance, Figs. 3(a) and 3(b) show the laser beam at focus for two different runs that result in different electron beams. Both laser beams have a  $\sim 2 \mu\text{m}$  diameter FWHM, and the laser intensity is similar. In contrast, the differences between the laser distributions at an intermediate plane [ $z = 2z_R$ , Fig. 3(c)] are conspicuous. The strong degradation of the beam quality far from the focal plane indicates the presence of significant wave front distortions, which can vary from run to run.

The wave front is reconstructed numerically from the laser intensity distribution at the two planes shown in Fig. 3 ( $z = 0$  and  $z = 2z_R = 40 \mu\text{m}$ ) using the Gerchberg-Saxton algorithm [26]. To test the accuracy of the result, the obtained phase is used to reconstruct the intensity distribution before the focal plane (at  $z = -2z_R$ ). The extrapolated intensity is in good agreement with the experimentally measured laser distribution in this plane. The wave fronts obtained at the focal plane are shown in Figs. 3(e) and 3(f). They exhibit complex structures, which are quite different for the two runs. These data suggest that the variation of the laser wave front has a direct influence over the electron beam distribution.

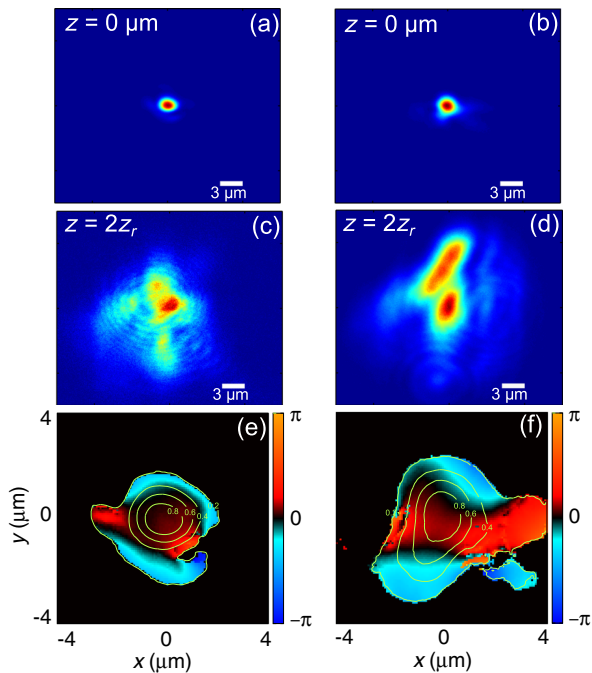


FIG. 3. Laser focal spots and wave fronts. (a),(b) Laser focal spots for two different runs. (c),(d) Corresponding mid-field laser transverse distribution at  $z = 2z_r$ . (e),(f) Corresponding reconstructed laser phase at the focal plane.

### III. PIC SIMULATIONS

To understand how the wave front distortions actually affect the electron acceleration, we perform PIC simulations including realistic laser wave fronts. We use the code CALDER-CIRC [27], a fully electromagnetic 3D code based on cylindrical coordinates  $(r, z)$  and Fourier decomposition in the poloidal direction. The simulations are performed using a mesh with  $\Delta z = 0.3k_0^{-1}$  and  $\Delta r = 1.5k_0^{-1}$  (where  $k_0$  is the laser wave vector) and the seven first Fourier modes. The neutral gas density profile is taken from the experimental data. The simulations start with pure neutral nitrogen, which is ionized via tunnel ionization. The number of macroparticles per cell before ionization is 2000, which corresponds to  $2000 \times 5 = 10\,000$  macro-electrons per cell in the region of full ionization of the  $L$  shell of nitrogen. We perform simulations on two test cases. In the first one, the laser focal spot is taken from the experimental data and the wave front is reconstructed using the Gerchberg-Saxton algorithm. In the second one, the same experimental focal spot is used, but the wave front is assumed to be perfectly flat. The wave front quality has a dramatic effect on the mid-field intensity distribution (see also Supplemental Material for more details [16]).

PIC simulations show that electrons are injected in the wakefield generated in the downward density gradient. This can be seen in Fig. 4, which shows the map of the electron density in the plane  $y = 0$  and the electron distribution in phase space  $(z, v_z)$  for two times,

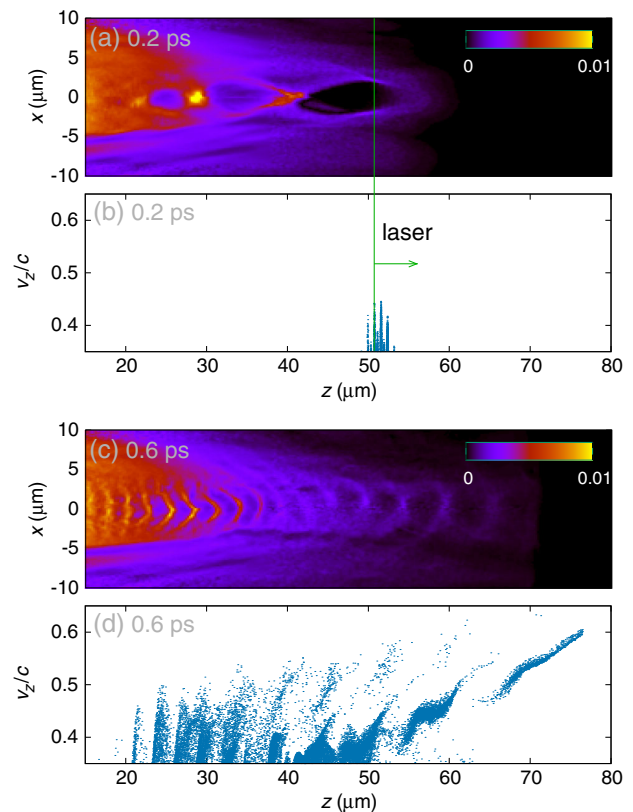


FIG. 4. Results of 3D PIC simulations with reconstructed laser wave front. Electron density  $n_e/n_c$  in the downward density ramp at the exit of the gas jet at (a) 0.2 and (c) 0.6 ps. (b), (d) Corresponding electron longitudinal phase space showing electron trapping and acceleration in the wakefield.

corresponding to the simulation with the reconstructed wave front. The figure displays only the region at the exit of the gas jet ( $z = 0$  is the center of the jet). The laser pulse, whose focal plane is at  $z \sim 43 \mu\text{m}$ , is close to resonance in this region, and therefore it excites a large amplitude wakefield [Fig. 4(a)]. In addition, comparing the density maps at 0.2 and 0.6 ps, Figs. 4(a) and 4(c), clearly shows that the wavelength of the plasma wave decreases with time. This reduction of the plasma wavelength (i.e., increase of the plasma wave vector) is a known feature of plasma wave excitation in a density gradient. It leads to the decrease of the phase velocity  $v_p$ , which eventually leads to the trapping and injection of electrons in the wakefield [19,21] (see also the Appendix for more details).

The analysis of the simulations confirms that electrons are injected when the phase velocity is sufficiently low. At early times,  $v_p \approx c$ , and there are no longitudinally accelerated electrons in the wakefield buckets closest to the laser pulse, as can be seen in the phase space for  $t = 0.2$  ps [Fig. 4(b)]. The only electrons with large longitudinal velocity are those oscillating in the high-frequency laser field. The simulation shows that trapping occurs later, when the phase velocity reaches  $v_p/c \approx 0.45$ ; see Fig. 4(d).

This low phase velocity explains why electrons are accelerated in the 100-keV energy range. Note also that trapping occurs after the laser pulse has passed; i.e., the electron bunch sits  $\approx 70 \mu\text{m}$  behind the laser pulse and never interacts with the laser field. Electrons are trapped in several buckets of the wakefield, as shown in the phase space snapshot at 0.6 ps [Fig. 4(d)]. Finally, the energy distribution at the exit of the plasma agrees very well with the experiment [see Fig. 2(f)], which confirms the trapping and acceleration mechanism.

The trends described above are also found in the simulations using a flat wave front. However, differences are dramatic when inspecting the shape of the electron transverse distribution obtained in each case. We now focus on the impact of the transverse wakefield  $E_{\perp} = \sqrt{E_x^2 + E_y^2}$  on the electron distribution. When the experimental laser spot and the reconstructed wave front are used [Fig. 5(a)],

the cross sections of the transverse wakefield  $E_{\perp}$  are highly asymmetric and the electron distribution is complex, with hot spots and regions without electrons. This computed electron distribution is similar to the experimental ones [Figs. 2(c) and 2(d)]. For the case with a flat wave front, Fig. 5(b), the cross section of the transverse wakefield is more rotationally symmetric, and as a result, the electron bunch is much more collimated. This flat phase case resembles the measured electron beam image shown in Fig. 2(e), indicating that on that particular experimental run the wave front is less distorted.

The total charge ( $\sim 40 \text{ fC}$ , close to the experimental result) is similar when a flat or distorted wave front is used, but the crucial difference is that a flat wave front yields an electron beam contained within a small solid angle  $\lesssim 0.05 \text{ sr}$ , compared to  $\sim 0.6 \text{ sr}$  for the experimental wave front. Note that in both cases the intensity distributions at the focal plane are the same, only the wave front differs.

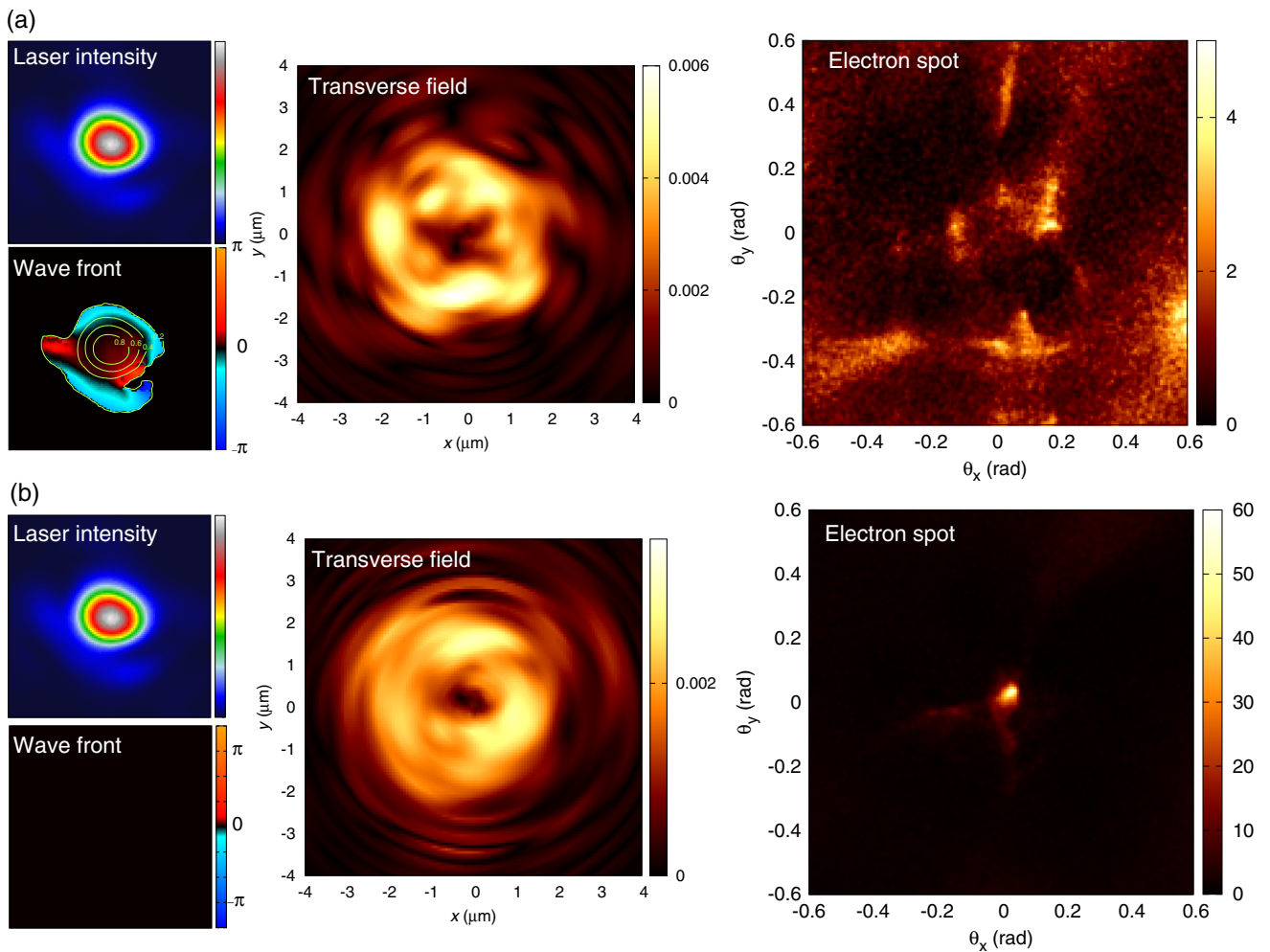


FIG. 5. Simulations results for a laser pulse with both focal spot and wave front reconstructed from experimental data (a) and with the same experimental focal spot but with a flat wave front (b) Left column: input intensity distribution and wave front at the focal plane. Central column: cross-sections of the transverse field  $E_{\perp}/E_0$  ( $E_0 = m_e c \omega_p / e$  is the cold wave breaking field) at 0.6 ps and for  $z = 28 \mu\text{m}$ . Right column: electron spot far from the gas jet.

These results indicate that the transverse wakefield inhomogeneities act as focusing or defocusing electron optics, resulting in the observed complex patterns. A good electron beam quality can be obtained when the transverse inhomogeneities are reduced over the acceleration length, i.e., a few Rayleigh lengths.

We find that the transverse inhomogeneities originate mostly from the distorted laser wave front, and not from ionization-induced nonlinear propagation effects. Indeed, both our experimental measurements (see Supplemental Material [16]) and simulations show that the laser pulse and the wakefield do not undergo any significant distortion associated with ionization. However, it is quite clear that the phase distortion at the focal plane greatly affects the midfield intensity profile of the laser beam (see Fig. 3), and therefore the shape of the wakefield. The structured electron distribution and the structure of the wakefield thus come as a result of the midfield inhomogeneities induced by the distorted wave front. This interpretation is also supported by the fact that our simulations with a flat wave front and the same focal spot yield a much more collimated and symmetric electron beam, even though ionization is present. Another effect that we can rule out is beam-plasma filamentation [28], as the structures in the electron beam disappear when using the flat laser wave front. Thus, the laser wave front has a direct effect on the electron beam distribution. This suggests that tailoring the wave front permits the control of the focusing properties of the transverse wakefield. This also explains the results of Refs. [8,29], where a deformable mirror was used in order to modify the wave front and optimize the electron beam quality.

In conclusion, we observe and explain the complex electron distributions in a high-repetition rate laser-plasma accelerator. PIC simulations indicate that these complex distributions are related to distortions of the laser wave front, which cause inhomogeneities in the laser distribution and the transverse wakefield. Our work emphasizes the importance of using realistic laser distributions in simulations in order to understand and reproduce experimental results quantitatively. In addition, while our experiment operates in an extreme regime where the interaction length is large compared to the Rayleigh length, it demonstrates the importance of controlling the laser wave front over several Rayleigh lengths in laser-plasma interaction experiments. These results might also be relevant to the case of higher energy laser-plasma accelerators, even when self-focusing governs the laser propagation: recent work mentions the importance of the laser intensity in the midfield [30,31]. Finally, our results suggest that the laser wave front is a knob for actively tuning the electron beam distribution, which can be achieved with a deformable mirror, for instance [8,29]. This fact, along with the stability and the kHz repetition rate make this electron source attractive for applications such as time-resolved electron diffraction [10,12].

## ACKNOWLEDGMENTS

This work was funded by the European Research Council under Contract No. 306708, ERC Starting Grant FEMTOELEC, and the Agence Nationale pour la Recherche under Contract No. ANR-11-EQPX-005-ATTOLAB

## APPENDIX: WAKEFIELD PHASE VELOCITY IN A DENSITY GRADIENT

Our experimental data and PIC simulations indicate that electrons are injected in the wakefield in the downward density ramp, at the exit of the gas jet. The trapping and the acceleration of electrons in a density down ramp were studied theoretically in Ref. [19], where it was shown that the local wave number of the wakefield increases over time:

$$k(z, t) = k_p(z) + (z - ct) \frac{dk_p}{dz}, \quad (\text{A1})$$

where  $z$  is the longitudinal coordinate,  $c$  is the speed of light,  $k_p(z) = \omega_p(z)/c$ , and  $\omega_p(z) = \sqrt{n_e(z)e^2/\epsilon_0 m_e}$  is the  $z$ -dependent plasma frequency in the density gradient. It is important to note that, contrary to the wave vector  $k(z, t)$ ,  $\omega_p(z)$  does not evolve with time. As a result of this time-varying wave vector, the phase velocity  $v_p(z, t) = \omega_p/k(z, t)$  of the wakefield generated by a laser focused in a density down ramp decreases with time as

$$v_p(z, t) = c \frac{1}{1 + (z - ct) \frac{1}{k_p} \frac{dk_p}{dz}}. \quad (\text{A2})$$

Indeed, for a downward density ramp,  $dk_p/dz < 0$ , and behind the laser pulse  $z - ct < 0$ , so that the denominator in this equation is larger than 1. Consequently, as the wave vector increases with time, the phase velocity decreases. Injection occurs behind the laser pulse when the wakefield becomes slow enough to trap plasma background electrons.

- 
- [1] E. Esarey, P. Sprangle, J. Krall, and A. Ting, *Overview of Plasma-Based Accelerator Concepts*, *IEEE Trans. Plasma Sci.* **24**, 252 (1996).
  - [2] E. Esarey, C. B. Schroeder, and W. P. Leemans, *Physics of Laser-Driven Plasma-Based Electron Accelerators*, *Rev. Mod. Phys.* **81**, 1229 (2009).
  - [3] J. Faure, C. Rechatin, A. Norlin, A. Lifschitz, Y. Glinec, and V. Malka, *Controlled Injection and Acceleration of Electrons in Plasma Wakefields by Colliding Laser Pulses.*, *Nature (London)* **444**, 737 (2006).
  - [4] W. P. Leemans, B. Nagler, A. J. Gonsalves, Cs. Tòth, K. Nakamura, C. G. R. Geddes, E. Esarey, C. B. Schroeder, and S. M. Hooker, *GeV Electron Beams from a Centimetre-Scale Accelerator*, *Nat. Phys.* **2**, 696 (2006).

- [5] O. Lundh, J. Lim, C. Rechatin, L. Ammoura, A. Ben-Ismaïl, X. Davoine, G. Gallot, J.-P. Goddet, E. Lefebvre, V. Malka, and J. Faure, *Few Femtosecond, Few Kiloampere Electron Bunch Produced by a Laser-Plasma Accelerator*, *Nat. Phys.* **7**, 219 (2011).
- [6] G. Sun, E. Ott, Y. C. Lee, and P. Guzdar, *Self-Focusing of Short Intense Pulses in Plasmas*, *Phys. Fluids* **30**, 526 (1987).
- [7] A. B. Borisov, A. V. Borovskiy, O. B. Shiryayev, V. V. Korobkin, A. M. Prokhorov, J. C. Solem, T. S. Luk, K. Boyer, and C. K. Rhodes, *Relativistic and Charge Displacement Self-Channeling of Intense Ultrashort Laser Pulses in Plasmas*, *Phys. Rev. A* **45**, 5830 (1992).
- [8] Z.-H. He, B. Hou, J. H. Easter, J. Faure, K. Krushelnick, J. A. Nees, and A. G. R. Thomas, *High Repetition-Rate Wakefield Electron Source Generated by Few-Millijoule, 30 Femtosecond Laser Pulses on a Density Downramp*, *New J. Phys.* **15**, 053016 (2013).
- [9] B. Beaufrepaire, A. Lifschitz, and J. Faure, *Electron Acceleration in Sub-Relativistic Wakefields Driven by Few-Cycle Laser Pulses*, *New J. Phys.* **16**, 023023 (2014).
- [10] G. Sciaïni and R. J. D. Miller, *Femtosecond Electron Diffraction: Heralding the Era of Atomically Resolved Dynamics*, *Rep. Prog. Phys.* **74**, 096101 (2011).
- [11] P. Musumeci, J. T. Moody, C. M. Scoby, M. S. Gutierrez, and M. Westfall, *Laser-Induced Melting of a Single Crystal Gold Sample by Time-Resolved Ultrafast Relativistic Electron Diffraction*, *Appl. Phys. Lett.* **97**, 063502 (2010).
- [12] Z.-H. He, A. G. R. Thomas, B. Beaufrepaire, J. A. Nees, B. Hou, V. Malka, K. Krushelnick, and J. Faure, *Electron Diffraction Using Ultrafast Electron Bunches from a Laser-Wakefield Accelerator at kHz Repetition Rate*, *Appl. Phys. Lett.* **102**, 064104 (2013).
- [13] A. Jullien, A. Ricci, F. Böhle, J.-P. Rousseau, S. Grabielle, N. Forget, H. Jacqmin, B. Mercier, and R. Lopez-Martens, *Carrier-Envelope-Phase Stable, High-Contrast, Double Chirped-Pulse-Amplification Laser System*, *Opt. Lett.* **39**, 3774 (2014).
- [14] R. Rankin, C. E. Capjack, N. H. Burnett, and P. B. Corkum, *Refraction Effects Associated with Multi-Photon Ionisation and Ultra-Short Pulse Laser Propagation in Plasma Waveguides*, *Opt. Lett.* **16**, 835 (1991).
- [15] P. Chessa, E. De Wispelaere, F. Dorchies, V. Malka, J.-R. Marquès, G. Hamoniaux, P. Mora, and F. Amiranoff, *Temporal and Angular Resolution of the Ionization-Induced Refraction of a Short Laser Pulse in a Helium Gas*, *Phys. Rev. Lett.* **82**, 552 (1999).
- [16] See Supplemental Material at <http://link.aps.org/supplemental/10.1103/PhysRevX.5.031012> for information concerning the laser beam propagation in the plasma and the reconstruction of the laser wave front.
- [17] D. Teychenné, G. Bonnaud, and J.-L. Bobin, *Wave-Breaking Limit to the Wake-Field Effect in an Underdense Plasma*, *Phys. Rev. E* **48**, R3248 (1993).
- [18] S. Bulanov, N. Naumova, F. Pegoraro, and J. Sakai, *Particle Injection into the Wave Acceleration Phase due to Nonlinear Wake Wave Breaking*, *Phys. Rev. E* **58**, R5257 (1998).
- [19] A. V. Brantov, T. Zh. Esirkepov, M. Kando, H. Kotaki, V. Yu. Bychenkov, and S. V. Bulanov, *Controlled Electron Injection into the Wake Wave Using Plasma Density Inhomogeneity*, *Phys. Plasmas* **15**, 073111 (2008).
- [20] C. G. R. Geddes, K. Nakamura, G. R. Plateau, Cs. Tóth, E. Cormier-Michel, E. Esarey, C. B. Schroeder, J. R. Cary, and W. P. Leemans, *Plasma-Density-Gradient Injection of Low Absolute-Momentum-Spread Electron Bunches*, *Phys. Rev. Lett.* **100**, 215004 (2008).
- [21] J. Faure, C. Rechatin, O. Lundh, L. Ammoura, and V. Malka, *Injection and Acceleration of Quasimonoenergetic Relativistic Electron Beams Using Density Gradients at the Edges of a Plasma channel*, *Phys. Plasmas* **17**, 083107 (2010).
- [22] K. Schmid, A. Buck, C. M. S. Sears, J. M. Mikhailova, R. Tautz, D. Herrmann, M. Geissler, F. Krausz, and L. Veisz, *Density-Transition Based Electron Injector for Laser Driven Wakefield Accelerators*, *Phys. Rev. ST Accel. Beams* **13**, 091301 (2010).
- [23] C. McGuffey, A. G. R. Thomas, W. Schumaker, T. Matsuoka, V. Chvykov, F. J. Dollar, G. Kalintchenko, V. Yanovsky, A. Maksimchuk, K. Krushelnick, V. Yu. Bychenkov, I. V. Glazyrin, and A. V. Karpeev, *Ionization Induced Trapping in a Laser Wakefield Accelerator*, *Phys. Rev. Lett.* **104**, 025004 (2010).
- [24] A. Pak, K. A. Marsh, S. F. Martins, W. Lu, W. B. Mori, and C. Joshi, *Injection and Trapping of Tunnel-Ionized Electrons into Laser-Produced Wakes*, *Phys. Rev. Lett.* **104**, 025003 (2010).
- [25] These statistics were obtained by analyzing a sequence of data where each point was the result of an average over 500–1000 shots.
- [26] R. W. Gerchberg and W. O. Saxton, *A Practical Algorithm for the Determination of the Phase from Image and Diffraction Plane Pictures*, *Optik (Stuttgart)* **35**, 237 (1972).
- [27] A. F. Lifschitz, X. Davoine, E. Lefebvre, J. Faure, C. Rechatin, and V. Malka, *Particle-in-Cell Modelling of Laser-Plasma Interaction Using Fourier Decomposition*, *J. Comput. Phys.* **228**, 1803 (2009).
- [28] M.-C. Firpo, A. F. Lifschitz, E. Lefebvre, and C. Deutsch, *Early Out-of-Equilibrium Beam-Plasma Evolution*, *Phys. Rev. Lett.* **96**, 115004 (2006).
- [29] Z.-H. He, B. Hou, V. Lebailly, J. A. Nees, K. Krushelnick, and A. G. R. Thomas, *Coherent Control of Plasma Dynamics*, *Nat. Commun.* **6**, 7156 (2015).
- [30] X. Wang *et al.*, *Quasi-Monoenergetic Laser-Plasma Acceleration of Electrons to 2 GeV*, *Nat. Commun.* **4**, 1988 (2013).
- [31] W. P. Leemans, A. J. Gonsalves, H.-S. Mao, K. Nakamura, C. Benedetti, C. B. Schroeder, Cs. Tóth, J. Daniels, D. E. Mittelberger, S. S. Bulanov, J.-L. Vay, C. G. R. Geddes, and E. Esarey, *Multi-GeV Electron Beams from Capillary-Discharge-Guided Subpetawatt Laser Pulses in the Self-Trapping Regime*, *Phys. Rev. Lett.* **113**, 245002 (2014).

# Carrier-envelope phase stability of hollow fibers used for high-energy few-cycle pulse generation

William A. Okell,<sup>1,\*</sup> Tobias Witting,<sup>1</sup> Davide Fabris,<sup>1</sup> Dane Austin,<sup>1</sup> Maimouna Bocoum,<sup>2</sup> Felix Frank,<sup>1</sup>  
Aurélien Ricci,<sup>2</sup> Aurélie Jullien,<sup>2</sup> Daniel Walke,<sup>1</sup>  
Jonathan P. Marangos,<sup>1</sup> Rodrigo Lopez-Martens,<sup>2</sup> and John W. G. Tisch<sup>1</sup>

<sup>1</sup>Blackett Laboratory, Imperial College London, Prince Consort Road, London SW7 2AZ, UK

<sup>2</sup>Laboratoire d'Optique Appliquée, Ecole Nationale Supérieure de Techniques Avancées-ParisTech,  
Ecole Polytechnique-CNRS, 91761 Palaiseau Cedex, France

\*Corresponding author: william.okell09@imperial.ac.uk

Received July 19, 2013; revised August 27, 2013; accepted September 2, 2013;  
posted September 3, 2013 (Doc. ID 194215); published September 30, 2013

We investigated the carrier-envelope phase (CEP) stability of hollow-fiber compression for high-energy few-cycle pulse generation. Saturation of the output pulse energy is observed at 0.6 mJ for a 260  $\mu\text{m}$  inner-diameter, 1 m long fiber, statically filled with neon. The pressure is adjusted to achieve output spectra supporting sub-4-fs pulses. The maximum output pulse energy can be increased to 0.8 mJ by either differential pumping (DP) or circularly polarized input pulses. We observe the onset of an ionization-induced CEP instability, which saturates beyond input pulse energies of 1.25 mJ. There is no significant difference in the CEP stability with DP compared to static-fill. © 2013 Optical Society of America

OCIS codes: (320.0320) Ultrafast optics; (320.5520) Pulse compression; (320.7090) Ultrafast lasers; (320.7100) Ultrafast measurements; (320.7110) Ultrafast nonlinear optics; (320.7140) Ultrafast processes in fibers.  
<http://dx.doi.org/10.1364/OL.38.003918>

High-energy few-cycle pulses can be generated with millijoule-level 20–30 fs pulses from a Ti:sapphire chirped pulse amplifier (CPA) using hollow-fiber pulse compression [1]. Sub-4-fs pulses [2–4], and pulses with up to 5 mJ of energy in somewhat longer pulses of 5 fs duration [5], have been generated using this technique. For a typical fiber inner-diameter of 250  $\mu\text{m}$ , there is a trade-off between spectral broadening and energy transmission because ionization and self-focusing become increasingly important issues when the input pulse energy exceeds  $\sim 1$  mJ. To combine a high throughput with a large broadening factor, differential pumping (DP) [6,7] or circularly polarized (CP) input pulses [8,9], can be used to mitigate the impact of these unwanted nonlinear effects. The continuing development of hollow-fiber technology toward single-cycle pulses with  $>1$  mJ energy is particularly important for relativistic laser-matter studies [10] and for the generation of more intense attosecond pulses. While larger-diameter fibers are also a promising route to higher-energy few-cycle pulses [5,11,12], the looser focusing conditions demand a significantly increased laboratory space for the apparatus in order to minimize nonlinear effects in the entrance and exit windows.

Although stabilization of the carrier-envelope phase (CEP) is crucial to many experiments requiring few-cycle pulses with higher energies, the effect that energy scaling of hollow-fiber pulse compression has on the CEP stability of the output pulses is yet to be investigated systematically. Through self-phase modulation (SPM), the main spectral broadening process occurring in the fiber, pulse energy fluctuations induce a CEP instability in the output pulses [13]. At high-input pulse energies, ionization within the fiber becomes significant and will also contribute to the CEP fluctuations. Furthermore, the possibility of an additional instability caused by gas flow in differentially pumped fibers has not yet been explored.

In this letter, we examine the energy scaling of the hollow-fiber compression technique in three commonly used modes of operation: statically filled using linearly polarized pulses (SFLP), differentially pumped using linearly polarized pulses (DPLP), and statically filled using CP pulses (SFCP). We also investigate the CEP stability of the fiber as a function of the input energy.

In our experiment, 28 fs pulses with up to 2.5 mJ energy at a 1 kHz repetition rate are generated by a commercial CPA laser system (Femtolasers GmbH, Femtopower HE CEP). The fast CEP fluctuations of the oscillator are stabilized by modulating the pump power with an acousto-optic modulator (AOM). The feedback signal to the AOM is generated using a photonic crystal-fiber-based  $f$ -to- $2f$  interferometer and locking electronics. The amplified pulses were delivered to a 260  $\mu\text{m}$  inner diameter, 1 m long fiber filled with neon. The experimental setup is shown in Fig. 1. To statically fill the fiber, the entrance and exit tubes are filled with neon. DP is achieved by evacuating the entrance tube, which is typically held at  $\sim 10^{-1}$  mbar when the exit tube is filled with 3 bar of neon. An  $f = 1.5$  m focusing mirror couples the beam into the fiber, and the output beam is recollimated using an  $f = 87.5$  cm mirror. The spectrally broadened pulses are compressed using 10 reflections from double-angle technology chirped-mirrors (UltraFast Innovations GmbH) and through fine-tuning of the group delay dispersion (GDD) with fused silica wedges. The pulse can be converted to circular polarization for propagation through the fiber by introducing a quarter-wave plate into the beam. A broadband achromatic quarter-wave plate (Femtolasers GmbH, OA229) converts the pulses back to linear polarization after the fiber.

The beam reflected from the front face of the wedges enters an  $f$ -to- $2f$  interferometer, which is used to measure the CEP stability after the fiber. Since the spectrum from the hollow fiber spans more than an octave, no additional spectral broadening is required within the

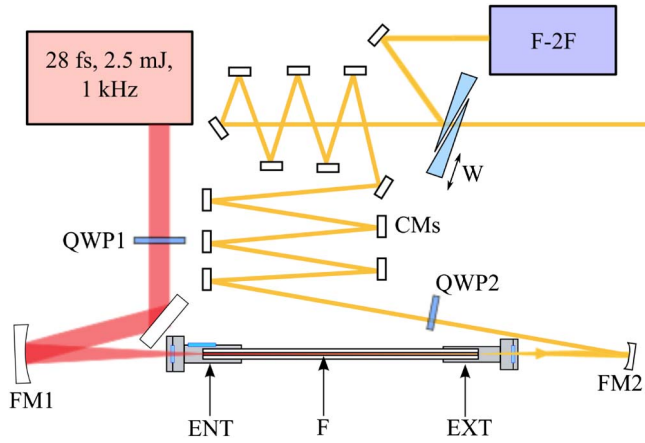


Fig. 1. Experimental setup. QWP1,2: quarter-wave plates; FM1,2: focusing and re-collimating mirrors, respectively; F: hollow fiber; ENT, EXT: entrance and exit tubes, respectively; CMs: chirped mirrors; W: fused silica wedges; F-2F: slow-loop  $f$ -to- $2f$  interferometer.

interferometer. The pulses are focused into a beta-barium borate (BBO) crystal to double the long wavelength part of the spectrum. A polarizing beam-splitter cube is used to interfere overlapping regions of the second harmonic and fundamental spectra around 520 nm. Feedback is achieved by applying a DC offset to the fast-loop locking electronics.

The input pulse energy was varied using a half-wave plate and polarizer before the compressor in the CPA laser. The neon pressure was adjusted to maintain a spectrum with a sub-4-fs Fourier transform limit (FTL) at the output of the fiber, i.e., a constant broadening factor  $F = \Delta\omega/\Delta\omega_0$ , where  $\Delta\omega_0$  and  $\Delta\omega$  are the initial and final pulse bandwidths, respectively. The output pulse energy is shown as a function of the input pulse energy in Fig. 2(a). Below an input pulse energy of 0.6 mJ, the energy transmission for all configurations is close to the transmission at low energy, with the fiber evacuated (68%). At input pulse energies above 1.5 mJ, the output energy for SFLP saturates at 0.6 mJ. Both SFCP and DPLP permit significantly higher-output pulse energies of up to 0.8 mJ, but also show deviation from the transmission of the fiber under vacuum conditions at high-input pulse energies and appear to be approaching saturation. Figure 2(b) shows the experimental and theoretical neon pressure in the exit tube as a function of the input pulse energy. The theoretical curves were calculated using the approach in [14], which leads to gas pressure given by

$$p = \frac{cA_{\text{eff}}}{2\kappa_2\omega_0 P_0 L_{\text{eff}}} \left[ 3\sqrt{3}(F^2 - 1) \right]^{1/2}, \quad (1)$$

where  $c$  is the speed of light in a vacuum,  $A_{\text{eff}} \approx 0.48\pi a^2$  is the effective area of the fiber of inner-radius  $a$ ,  $\kappa_2 = 7.4 \times 10^{-25} \text{ m}^2 \text{ W}^{-1} \text{ bar}^{-1}$  is the neon nonlinear coefficient per unit pressure [15],  $\omega_0$  is the laser central frequency, and  $P_0$  is the laser peak power. The effective fiber lengths,  $L_{\text{eff}}$ , for SFLP, SFCP, and DPLP are

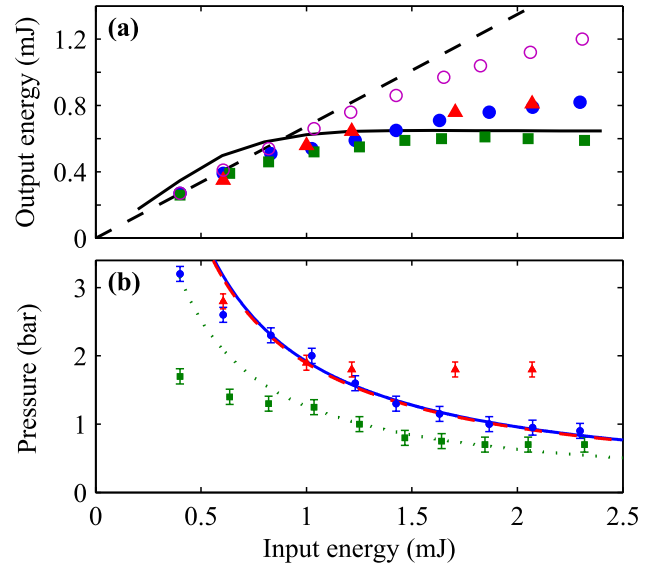


Fig. 2. (a) Output pulse energy with evacuated fiber and LP (purple open circles), and for a sub-4-fs FTL output spectrum for SFLP (green squares), DPLP (blue circles), and SFCP (red triangles). The black-dashed line represents 68% transmission. The black solid line is the transmission predicted by our model. (b) Corresponding experimental neon pressure in the exit tube (data points), and theoretical pressure for SFLP (dotted green curve), DPLP (solid blue curve), and SFCP (dashed red curve).

$$L_{\text{eff}}^{\text{SFLP}} = \frac{1 - e^{-\alpha L}}{\alpha}, \quad L_{\text{eff}}^{\text{SFCP}} = \frac{2}{3} \left( \frac{1 - e^{-\alpha L}}{\alpha} \right),$$

$$L_{\text{eff}}^{\text{DPLP}} \approx \frac{2}{3} \left( \frac{1 - e^{-1.21\alpha L}}{1.21\alpha} \right), \quad (2)$$

respectively, where  $L$  is the fiber length and  $\alpha$  is the mode attenuation constant defined in [14]. For our experimental parameters,  $L_{\text{eff}}^{\text{SFLP}} = 0.94 \text{ m}$ ,  $L_{\text{eff}}^{\text{SFCP}} = 0.63 \text{ m}$ , and  $L_{\text{eff}}^{\text{DPLP}} = 0.62 \text{ m}$ .

The saturation of the output energy is an indication that physical processes other than SPM start to play a significant role. Therefore we investigate the CEP stability as a function of input energy. During the propagation of a laser pulse through a medium, the CEP will change due to the difference between the group and phase velocities by an amount proportional to the derivative of the refractive index with respect to angular frequency [16]. For a plasma with a free electron density  $\rho_e$ , the CEP shift is  $\varphi \approx e^2 \rho_e z / m_e \epsilon_0 c \omega_0$  over a distance  $z$ , where  $\omega_0$  is the laser central frequency,  $c$  is the speed of light,  $\epsilon_0$  is the permittivity of free-space, and  $e$  and  $m_e$  are the electronic charge and mass, respectively. Modern CPA laser systems typically have output pulse energy fluctuations of around 1%, which will cause fluctuations in the plasma density in the fiber. The CEP fluctuations induced as a consequence are given by

$$\delta\varphi = \frac{e^2 z}{m_e \epsilon_0 \omega_0 c} \frac{\partial \rho_e(I_0, p)}{\partial I_0} \delta I_0, \quad (3)$$

where  $I_0$  is the peak intensity of the laser pulse,  $\delta I_0$  is a small change in the pulse peak intensity, and  $p$  is the gas pressure. Pulse energy fluctuations can also induce a

CEP instability associated with SPM through the mechanism described in [13]. In order to model the CEP fluctuations induced by the fiber, we have simulated our experiments using a coupled-mode, split-step technique incorporating modal dispersion and loss, the Kerr effect including self-steepening, and ionization. The ionization rate was calculated using the Ammosov, Delone, and Krainov theory [17]. The initial conditions were the experimentally measured laser temporal profile and a Gaussian spatial profile with an optimal  $1/e^2$  diameter of  $0.64 \times 260 \mu\text{m}$ . The gas pressure was varied with input energy in order to maintain a constant broadening factor, as prescribed by Eq. (1). The input pulses were assumed to have 1% energy fluctuations and  $\sim 150$  mrad CEP fluctuations, which is the typical performance of our laser system. The experimental output pulse energy fluctuations from the fiber are also 1%. Pulse energy fluctuations were measured single-shot with a photodiode and digital storage oscilloscope. Our simulations were performed for DPLP, where in-coupling effects due to ionization and self-focusing of the beam can be neglected due to the low gas pressure ( $<10^{-1}$  mbar).

Figure 3 shows the standard deviation of the CEP measured after the fiber using DPLP and SFLP, with constant  $F$ . The overall trend for both DPLP and SFLP is a degradation in the CEP stability as the input pulse energy is increased, suggesting the onset of an ionization-induced CEP instability. The results of the simulation are also shown in Fig. 3 and show excellent agreement with the experimental data. The simulation confirms that the decrease in the CEP stability as the input energy is increased from 0.5 to 1.25 mJ is a consequence of ionization in the fiber. Above 1 mJ, switching off SPM does not change the CEP fluctuations, showing that ionization is the dominant contribution. Above 1.25 mJ, further degradation in the CEP stability is prevented by energy losses caused by ionization. Without direct ionization losses (which include the acceleration of ionized electrons), this roll-off remains present and can therefore be attributed to ionization defocusing causing energy losses by coupling energy into higher-order modes of the fiber.

The experimental results show no significant difference in the CEP stability using DPLP compared to SFLP, demonstrating for the first time that gas flow in differentially pumped fibers does not degrade the CEP stability. However, in a DP fiber, the highest gas density is at the

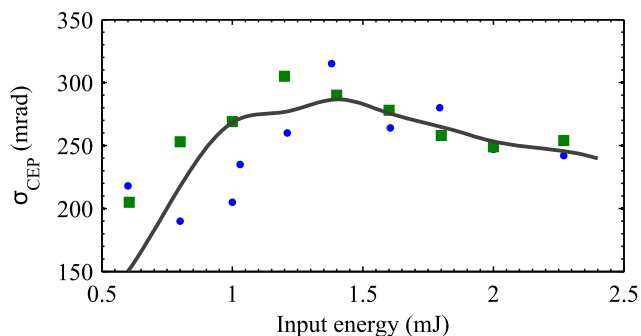


Fig. 3. Experimental single-shot standard deviation of CEP fluctuations,  $\sigma_{\text{CEP}}$ , measured after the fiber using DPLP (blue circles) and SFLP (green squares) and theoretical CEP fluctuations predicted by propagation simulations (black line).

fiber exit. At the exit, mode attenuation will have decreased the peak intensity of the pulse. Since the ionization-induced CEP instability is linear with pressure, but extremely nonlinear with intensity, one might expect a CEP stability improvement when using DPLP compared to SFLP in parameter regimes where the ionization-induced CEP instabilities are not prevented by propagation losses.

For CEP sensitive experiments in day-to-day operation, we avoid operating the fiber at the maximum of CEP fluctuations. Using, e.g.,  $\sim 1$  mJ input pulse energy and DPLP, we can achieve excellent long-term CEP stability after the fiber, as shown in Fig. 4. The residual CEP fluctuations have a standard deviation of 206 mrad, again confirming that the CEP stability of differentially pumped fibers is sufficient for attosecond experiments. Indeed, the full characterization of these pulses in Fig. 4(c) was achieved through attosecond streaking, which requires excellent CEP stability. Attosecond streaking using the few-cycle infrared (IR) pulses and isolated attosecond extreme ultraviolet (XUV) pulses was performed in a neon-gas jet, using the setup described in detail in [18]. The 0.4 mJ compressed pulses have a duration of 3.5 fs and were fully characterized using the vector potential retrieved from the FROG-CRAB trace, as described in [19].

In conclusion, we have demonstrated that the output pulse energy from a  $260 \mu\text{m}$  inner-diameter hollow-fiber saturates at 0.6 mJ with the fiber statically filled with neon, and that the output pulse energy can be increased to 0.8 mJ by using either DP or CP pulses. We observe an overall degradation in the CEP stability as the input pulse energy is increased, which is the consequence of increased ionization within the fiber. For our experimental parameters, ionization losses prevent further degradation of the CEP stability above 1.25 mJ input pulse

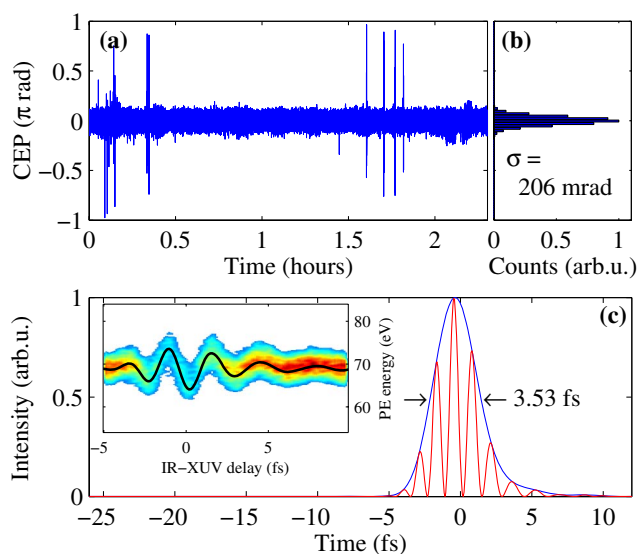


Fig. 4. CEP stability and temporal characterization of pulses generated using DPLP. (a) CEP data. (b) Histogram of CEP data, with 206 mrad single-shot standard deviation. (c) Full temporal characterization of 0.4 mJ pulses; square of the retrieved electric field (red), intensity envelope (blue); FWHM duration is 3.53 fs. Inset: experimental FROG-CRAB trace; retrieved vector potential of the IR pulse (black line).

energies. However, this instability should be carefully considered when scaling hollow-fiber pulse compression to multimillijoule energies. If the peak intensity is held constant by increasing the fiber inner diameter, the highly nonlinear scaling of tunnel ionization with intensity can be avoided. Finally, we have presented the first direct evidence that the CEP stability performance of differentially pumped fibers can be equivalent to that of statically filled fibers. We have generated 0.4 mJ, 3.5 fs pulses with a CEP stability of  $\sim 200$  mrad over  $>2$  h using a differentially pumped fiber, showing that the long-term CEP stability of differentially pumped fibers is sufficient for attosecond experiments. We expect this work to aid in the design of multimillijoule hollow-fiber systems where CEP stability is required.

This work was financially supported by the EPSRC through grants EP/I032517/1 and EP/F034601/1 and by Laserlab Europe (project LOA001657). We acknowledge technical support from Andrew Gregory and Peter Ruthven.

#### References

1. M. Nisoli, S. de Silvestri, and O. Svelto, *Appl. Phys. Lett.* **68**, 2793 (1996).
2. E. Goulielmakis, M. Schultze, M. Hofstetter, V. S. Yakovlev, J. Gagnon, M. Uiberacker, A. L. Aquila, E. M. Gullikson, D. T. Attwood, R. Kienberger, F. Krausz, and U. Kleineberg, *Science* **320**, 1614 (2008).
3. J. Park, J. Lee, and C. H. Nam, *Opt. Lett.* **34**, 2342 (2009).
4. T. Witting, F. Frank, C. A. Arrell, W. A. Okell, J. P. Marangos, and J. W. G. Tisch, *Opt. Lett.* **36**, 1680 (2011).
5. S. Bohman, A. Suda, T. Kanai, S. Yamaguchi, and K. Midorikawa, *Opt. Lett.* **35**, 1887 (2010).
6. A. Suda, M. Hatayama, K. Nagasaka, and K. Midorikawa, *Appl. Phys. Lett.* **86**, 111116 (2005).
7. J. S. Robinson, C. A. Haworth, H. Teng, R. A. Smith, J. P. Marangos, and J. W. G. Tisch, *Appl. Phys. B* **85**, 525 (2006).
8. S. Ghimire, B. Shan, C. Wang, and Z. Chang, *Laser Phys.* **15**, 838 (2005).
9. X. Chen, A. Jullien, A. Malvache, L. Canova, A. Borot, A. Trisorio, C. G. Durfee, and R. Lopez-Martens, *Opt. Lett.* **34**, 1588 (2009).
10. A. Borot, A. Malvache, X. Chen, A. Jullien, J.-P. Geindre, P. Audebert, G. Mourou, F. Quéré, and R. Lopez-Martens, *Nat. Phys.* **8**, 416 (2012).
11. T. Nagy, V. Pervak, and P. Simon, *Opt. Lett.* **36**, 4422 (2011).
12. W. Schweinberger, A. Sommer, E. Bothschafter, J. Li, F. Krausz, R. Kienberger, and M. Schultze, *Opt. Lett.* **37**, 3573 (2012).
13. H. Wang, M. Chini, E. Moon, H. Mashiko, C. Li, and Z. Chang, *Opt. Express* **17**, 12082 (2009).
14. C. Vozzi, M. Nisoli, G. Sansone, S. Stagira, and S. de Silvestri, *Appl. Phys. B* **80**, 285 (2005).
15. M. Nisoli, S. Stagira, S. De Silvestri, O. Svelto, S. Sartania, Z. Cheng, G. Tempea, C. Spielmann, and F. Krausz, *IEEE J. Sel. Top. Quantum Electron.* **4**, 414 (1998).
16. G. G. Paulus, F. Lindner, H. Walther, A. Baltuka, and F. Krausz, *J. Mod. Opt.* **52**, 221 (2005).
17. M. V. Ammosov, N. B. Delone, and V. P. Krainov, *J. Exp. Theor. Phys.* **64**, 1191 (1986).
18. F. Frank, C. Arrell, T. Witting, W. A. Okell, J. McKenna, J. S. Robinson, C. A. Haworth, D. Austin, H. Teng, I. A. Walmsley, J. P. Marangos, and J. W. G. Tisch, *Rev. Sci. Instrum.* **83**, 071101 (2012).
19. T. Witting, F. Frank, W. A. Okell, C. A. Arrell, J. P. Marangos, and J. W. G. Tisch, *J. Phys. B* **45**, 074014 (2012).

# Bibliography

- [1] I. Langmuir, “Positive ion currents from the positive column of mercury arcs,” *Science*, vol. 58, no. 1502, pp. 290–291, 1923. 13
- [2] L. Tonks and I. Langmuir, “Oscillations in ionized gases,” *Phys. Rev.*, 1929. 13
- [3] E. Atkinson, “Atomic synthesis and stellar energy,” *Astrophysical Journal*, 1931. 13
- [4] H. A. Bethe, “Nuclear physics b. nuclear dynamics, theoretical,” *Reviews of Modern Physics*, vol. 9, no. 2, p. 69, 1937. 13
- [5] H. A. Bethe, “Energy production in stars,” *Physical Review*, vol. 55, no. 5, p. 434, 1939. 13
- [6] L. Artsimovich and I. Pomeranchuk, “Radiation of fast electrons in a magnetic field, jetp, 16 1946, 379,” *J. Phys. USSR*, vol. 9, p. 267, 1945. 13
- [7] A. Akhiezer and Y. B. Fainberg, “About interaction of charged particle beam with electron plasma,” *DAN SSSR*, vol. 69, no. 4, pp. 555–556, 1949. 13
- [8] J.-M. Rax, *Physique des tokamaks*. Editions Ecole Polytechnique, 2011. 13
- [9] J. M. Dawson, “On the production of plasma by giant pulse lasers,” *Physics of Fluids (1958-1988)*, vol. 7, no. 7, pp. 981–987, 1964. 13
- [10] N. Basov and O. Krokhin, “Conditions for heating up of a plasma by the radiation from an optical generator,” *Sov. Phys. JETP*, vol. 19, pp. 123–125, 1964. 13
- [11] J. Daiber, A. Hertzberg, and C. Wittliff, “Laser-generated implosions,” *Physics of Fluids (1958-1988)*, vol. 9, no. 3, pp. 617–619, 1966. 13
- [12] K. A. Brueckner and S. Jorna, “Laser-driven fusion,” *Reviews of modern physics*, vol. 46, no. 2, p. 325, 1974. 13, 25
- [13] L. Rayleigh, “On the instability of jets,” *Proceedings of the London mathematical society*, vol. 1, no. 1, pp. 4–13, 1878. 13
- [14] M. H. Emery, J. H. Gardner, and J. P. Boris, “Rayleigh-taylor and kelvin-helmholtz instabilities in targets accelerated by laser ablation,” *Physical Review Letters*, vol. 48, no. 10, p. 677, 1982. 13
- [15] R. Betti, V. Goncharov, R. McCrory, and C. Verdon, “Growth rates of the ablative rayleigh–taylor instability in inertial confinement fusion,” *Physics of Plasmas (1994-present)*, vol. 5, no. 5, pp. 1446–1454, 1998. 13

- [16] W. L. Kruer *et al.*, *The physics of laser plasma interactions*, vol. 70. Addison-Wesley New York, 1988. 14, 35
- [17] P. Maine, D. Strickland, P. Bado, M. Pessot, and G. Mourou, “Generation of ultrahigh peak power pulses by chirped pulse amplification,” *Quantum electronics, IEEE Journal of*, vol. 24, no. 2, pp. 398–403, 1988. 14
- [18] J. M. Mikhailova, A. Buck, A. Borot, K. Schmid, C. Sears, G. D. Tsakiris, F. Krausz, and L. Veisz, “Ultra-high-contrast few-cycle pulses for multipetawatt-class laser technology,” *Optics letters*, vol. 36, no. 16, pp. 3145–3147, 2011. 14
- [19] A. Dubietis, G. Jonušauskas, and A. Piskarskas, “Powerful femtosecond pulse generation by chirped and stretched pulse parametric amplification in bbo crystal,” *Optics Communications*, vol. 88, no. 4, pp. 437–440, 1992. 14
- [20] N. Burnett, H. Baldis, M. Richardson, and G. Enright, “Harmonic generation in co2 laser target interaction,” *Applied Physics Letters*, vol. 31, no. 3, pp. 172–174, 1977. 15, 19, 61
- [21] R. Carman, C. Rhodes, and R. Benjamin, “Observation of harmonics in the visible and ultraviolet created in c o 2-laser-produced plasmas,” *Physical Review A*, vol. 24, no. 5, p. 2649, 1981. 15, 61
- [22] A. Tarasevitch, A. Orisch, D. Von der Linde, P. Balcou, G. Rey, J.-P. Chambaret, U. Teubner, D. Klöpfel, and W. Theobald, “Generation of high-order spatially coherent harmonics from solid targets by femtosecond laser pulses,” *Physical Review A*, vol. 62, no. 2, p. 023816, 2000. 15
- [23] P. Monot, G. Doumy, S. Dobosz, and al., “High-order harmonic generation by nonlinear reflection of an intense high-contrast laser pulse on a plasma,” *Optics letters*, vol. 29, no. 8, pp. 893–895, 2004. 15
- [24] C. Thaury, *Generation d’harmoniques d’ordres elevees sur miroir plasma*. PhD thesis, Universite de Paris 11, 2008. 15, 33, 36, 61, 63, 64, 67
- [25] A. Borot, A. Malvache, X. Chen, D. Douillet, G. Iaquianniello, T. Lefrou, P. Audebert, J.-P. Geindre, G. Mourou, F. Quéré, *et al.*, “High-harmonic generation from plasma mirrors at kilohertz repetition rate,” *Optics letters*, vol. 36, no. 8, pp. 1461–1463, 2011. 15, 59, 61
- [26] W. M. Manheimer, “Plasma reflectors for electronic beam steering in radar systems,” *Plasma Science, IEEE Transactions on*, vol. 19, no. 6, pp. 1228–1234, 1991. 16
- [27] A. Robson, R. Morgan, and R. Meger, “Demonstration of a plasma mirror for microwaves,” *Plasma Science, IEEE Transactions on*, vol. 20, no. 6, pp. 1036–1040, 1992. 16

- [28] D. Bach, D. Casperson, D. Forslund, S. Gitomer, P. Goldstone, A. Hauer, J. Kephart, J. Kindel, R. Kristal, G. Kyrala, *et al.*, “Intensity-dependent absorption in 10.6- $\mu\text{m}$  laser-illuminated spheres,” *Physical review letters*, vol. 50, no. 26, p. 2082, 1983. 16, 32, 112
- [29] H. C. Kapteyn, A. Szoke, R. W. Falcone, and M. M. Murnane, “Prepulse energy suppression for high-energy ultrashort pulses using self-induced plasma shuttering,” *Optics letters*, vol. 16, no. 7, pp. 490–492, 1991. 16, 17
- [30] M. Nantel, J. Itatani, A.-C. Tien, J. Faure, D. Kaplan, M. Bauvier, T. Buma, P. Van Rompay, J. Nee, P. P. Pronko, *et al.*, “Temporal contrast in ti: sapphire lasers, characterization and control,” *Selected Topics in Quantum Electronics, IEEE Journal of*, vol. 4, no. 2, pp. 449–458, 1998. 16, 17, 45
- [31] J. Mathew, R. Fernsler, R. Meger, J. Gregor, D. Murphy, R. Pechacek, and W. Manheimer, “Generation of large area, sheet plasma mirrors for redirecting high frequency microwave beams,” *Physical review letters*, vol. 77, no. 10, p. 1982, 1996. 16
- [32] G. Doumy, F. Quéré, O. Gobert, M. Perdrix, P. Martin, P. Audebert, J. Gauthier, J.-P. Geindre, and T. Wittmann, “Complete characterization of a plasma mirror for the production of high-contrast ultraintense laser pulses,” *Physical Review E*, vol. 69, no. 2, p. 026402, 2004. 16, 18, 45
- [33] B. Dromey, S. Kar, M. Zepf, and P. Foster, “The plasma mirror- a subpicosecond optical switch for ultrahigh power lasers,” *Review of Scientific Instruments*, vol. 75, no. 3, pp. 645–649, 2004. 16
- [34] W. L. Kruer, “The physics of laser plasma interactions((book)),” *Reading, MA, Addison-Wesley Publishing Co.(Frontiers in Physics.*, vol. 73, 1988. 16, 35, 91, 115
- [35] W. Yan-Hai, P. Xue, L. Xue-Chun, and L. Zun-Qi, “Optimization of pulse temporal contrast in optical parametric chirped pulse amplification,” *Chinese Physics Letters*, vol. 26, no. 2, p. 024211, 2009. 17
- [36] M. M. Murnane, H. C. Kapteyn, M. D. Rosen, and R. W. Falcone, “Ultrafast x-ray pulses from laser-produced plasmas,” *Science*, vol. 251, no. 4993, pp. 531–536, 1991. 18
- [37] R. Schoenlein, S. Chattopadhyay, H. Chong, T. Glover, P. Heimann, C. Shank, A. Zholents, and M. Zolotarev, “Generation of femtosecond pulses of synchrotron radiation,” *Science*, vol. 287, no. 5461, pp. 2237–2240, 2000. 18
- [38] J. M. Madey, “Stimulated emission of bremsstrahlung in a periodic magnetic field,” *Journal of Applied Physics*, vol. 42, no. 5, pp. 1906–1913, 1971. 18
- [39] P. Emma, R. Akre, J. Arthur, R. Bionta, C. Bostedt, J. Bozek, A. Brachmann, P. Bucksbaum, R. Coffee, F.-J. Decker, *et al.*, “First lasing and operation of an

- ångström-wavelength free-electron laser,” *nature photonics*, vol. 4, no. 9, pp. 641–647, 2010. 18
- [40] P. R. Ribic and G. Margaritondo, “Status and prospects of x-ray free-electron lasers (x-fels): a simple presentation,” *Journal of Physics D: Applied Physics*, vol. 45, no. 21, p. 213001, 2012. 18
- [41] S. Corde, K. T. Phuoc, G. Lambert, R. Fitour, V. Malka, A. Rousse, A. Beck, and E. Lefebvre, “Femtosecond x rays from laser-plasma accelerators,” *Reviews of Modern Physics*, vol. 85, no. 1, p. 1, 2013. 18
- [42] G. Geloni, E. Saldin, L. Samoylova, E. Schneidmiller, H. Sinn, T. Tschentscher, and M. Yurkov, “Coherence properties of the european xfel,” *New Journal of Physics*, vol. 12, no. 3, p. 035021, 2010. 18
- [43] W. Helml, A. Maier, W. Schweinberger, I. Grguraš, P. Radcliffe, G. Doumy, C. Roedig, J. Gagnon, M. Messerschmidt, S. Schorb, *et al.*, “Measuring the temporal structure of few-femtosecond free-electron laser x-ray pulses directly in the time domain,” *Nature photonics*, vol. 8, no. 12, pp. 950–957, 2014. 19
- [44] N. Sarukura, K. Hata, T. Adachi, R. Nodomi, M. Watanabe, and S. Watanabe, “Coherent soft-x-ray generation by the harmonics of an ultrahigh-power krf laser,” *Physical Review A*, vol. 43, no. 3, p. 1669, 1991. 19
- [45] J. Macklin, J. Kmetec, and C. Gordon III, “High-order harmonic generation using intense femtosecond pulses,” *Physical review letters*, vol. 70, no. 6, p. 766, 1993. 19
- [46] A. L Huillier and P. Balcou, “High-order harmonic generation in rare gases with a 1-ps 1053-nm laser,” *Physical review letters*, vol. 70, no. 6, p. 774, 1993. 19
- [47] K. Zhao, Q. Zhang, M. Chini, Y. Wu, X. Wang, and Z. Chang, “Tailoring a 67 attosecond pulse through advantageous phase-mismatch,” *Optics letters*, vol. 37, no. 18, pp. 3891–3893, 2012. 19
- [48] E. Goulielmakis, M. Schultze, M. Hofstetter, V. S. Yakovlev, J. Gagnon, M. Uiberacker, A. L. Aquila, E. Gullikson, D. T. Attwood, R. Kienberger, *et al.*, “Single-cycle nonlinear optics,” *Science*, vol. 320, no. 5883, pp. 1614–1617, 2008. 19
- [49] F. Quéré, C. Thaury, P. Monot, S. Dobosz, P. Martin, J.-P. Geindre, and P. Audebert, “Coherent wake emission of high-order harmonics from overdense plasmas,” *Physical review letters*, vol. 96, no. 12, p. 125004, 2006. 20
- [50] L. Plaja, L. Roso, K. Rzazewski, and M. Lewenstein, “Generation of attosecond pulse trains during the reflection of a very intense laser on a solid surface,” *JOSA B*, vol. 15, no. 7, pp. 1904–1911, 1998. 20
- [51] C. Thaury and F. Quéré, “High-order harmonic and attosecond pulse generation on plasma mirrors: basic mechanisms,” *Journal of Physics B: Atomic, Molecular and Optical Physics*, vol. 43, no. 21, p. 213001, 2010. 20, 31, 34, 36, 38, 40, 41, 61, 64, 86, 122

- [52] C. Thaury, F. Quéré, J.-P. Geindre, A. Levy, T. Ceccotti, P. Monot, M. Bougeard, F. Réau, P. d'Oliveira, P. Audebert, *et al.*, “Plasma mirrors for ultrahigh-intensity optics,” *Nature Physics*, vol. 3, no. 6, pp. 424–429, 2007. 20, 33
- [53] N. Naumova, I. Sokolov, J. Nees, A. Maksimchuk, V. Yanovsky, and G. Mourou, “Attosecond electron bunches,” *Physical review letters*, vol. 93, no. 19, p. 195003, 2004. 20, 61
- [54] E. Rutherford and A. Wood, “Xliiii. long-range alpha particles from thorium,” *The London, Edinburgh, and Dublin Philosophical Magazine and Journal of Science*, vol. 31, no. 184, pp. 379–386, 1916. 20
- [55] J. Cockcroft and E. Walton, “Experiments with high velocity positive ions,” *Proceedings of the Royal Society of London. Series A, Containing Papers of a Mathematical and Physical Character*, vol. 129, no. 811, pp. 477–489, 1930. 20
- [56] J. Cockcroft and E. Walton, “Experiments with high velocity positive ions. ii. the disintegration of elements by high velocity protons,” in *Proceedings of the Royal Society of London A: Mathematical, Physical and Engineering Sciences*, vol. 137, pp. 229–242, The Royal Society, 1932. 20
- [57] D. Kerst, “Acceleration of electrons by magnetic induction,” *Physical Review*, vol. 58, no. 9, p. 841, 1940. 21
- [58] T. Tajima and J. Dawson, “Laser electron accelerator,” *Physical Review Letters*, vol. 43, no. 4, p. 267, 1979. 21
- [59] M. Tabak, J. Hammer, M. E. Glinsky, W. L. Kruer, S. C. Wilks, J. Woodworth, E. M. Campbell, M. D. Perry, and R. J. Mason, “Ignition and high gain with ultrapowerful lasers\*,” *Physics of Plasmas (1994-present)*, vol. 1, no. 5, pp. 1626–1634, 1994. 21, 22, 26
- [60] J. J. Honrubia and J. Meyer-ter Vehn, “Three-dimensional fast electron transport for ignition-scale inertial fusion capsules,” *Nuclear fusion*, vol. 46, no. 11, p. L25, 2006. 22, 112
- [61] F. Brunel, “Not-so-resonant, resonant absorption,” *Physical Review Letters*, vol. 59, no. 1, p. 52, 1987. 22, 26, 29, 30, 112
- [62] P. Gibbon and A. Bell, “Collisionless absorption in sharp-edged plasmas,” *Physical review letters*, vol. 68, no. 10, p. 1535, 1992. 22, 112
- [63] G. Askar Yan, G. Yan, S. Bulanov, F. Pegoraro, and A. Pukhov, “Magnetic interaction of self-focusing channels and fluxes of electromagnetic radiation: their coalescence, the accumulation of energy, and the effect of external magnetic fields on them,” *JETP Letters*, vol. 60, no. 4, pp. 251–257, 1994. 22, 113
- [64] A. Pukhov and J. Meyer-ter Vehn, “Relativistic magnetic self-channeling of light in near-critical plasma: three-dimensional particle-in-cell simulation,” *Physical review letters*, vol. 76, no. 21, p. 3975, 1996. 22, 113

- [65] Z.-M. Sheng, K. Mima, Y. Sentoku, M. Jovanović, T. Taguchi, J. Zhang, and J. Meyer-ter Vehn, “Stochastic heating and acceleration of electrons in colliding laser fields in plasma,” *Physical review letters*, vol. 88, no. 5, p. 055004, 2002. 22, 115
- [66] A. G. Mordovanakis, J. Easter, N. Naumova, K. Popov, P.-E. Masson-Laborde, B. Hou, I. Sokolov, G. Mourou, I. V. Glazyrin, W. Rozmus, *et al.*, “Quasimonoe-nergetic electron beams with relativistic energies and ultrashort duration from laser-solid interactions at 0.5 khz,” *Physical review letters*, vol. 103, no. 23, p. 235001, 2009. 22, 115, 131, 132, 133
- [67] M. Thévenet, A. Leblanc, S. Kahaly, H. Vincenti, A. Vernier, F. Quéré, and J. Faure, “Vacuum laser acceleration of relativistic electrons using plasma mirror injectors,” *Nat. Phys.*, p. 3597, 2015. 22, 115, 132, 133, 152, 153, 154, 174
- [68] J. A. Wheeler, A. Borot, S. Monchocé, H. Vincenti, A. Ricci, A. Malvache, R. Lopez-Martens, and F. Quéré, “Attosecond lighthouses from plasma mirrors,” *Nature Photonics*, vol. 6, no. 12, pp. 829–833, 2012. 23, 62, 73, 81, 164
- [69] J. Nuckolls and L. Wood, “Laser compression of matter to super-high densities: Thermonuclear (ctr),” *Nature*, vol. 239, p. 139, 1972. 25
- [70] W. L. Kruer and K. E. Estabrook, “Laser light absorption due to self-generated magnetic fields,” 1976. 25
- [71] W. Priedhorsky, D. Lier, R. Day, and D. Gerke, “Hard-x-ray measurements of 10.6- $\mu\text{m}$  laser-irradiated targets,” *Physical Review Letters*, vol. 47, no. 23, p. 1661, 1981. 25, 32
- [72] J. Freidberg, R. Mitchell, R. L. Morse, and L. Rudsinski, “Resonant absorption of laser light by plasma targets,” *Physical Review Letters*, vol. 28, no. 13, p. 795, 1972. 26, 29, 112
- [73] J. Albritton and P. Koch, “Cold plasma wavebreaking: Production of energetic electrons,” *Physics of Fluids (1958-1988)*, vol. 18, no. 9, pp. 1136–1139, 1975. 26, 112
- [74] A. Borot, *Generation d’impulsion attosecond sur miroir plasma a tres haute ca-dence*. PhD thesis, Ecole Polytechnique, 2012. 28, 36, 43, 64, 73, 86, 165
- [75] L. . E. Lifchitz, *Fields Theory*. ellipses, 1989. 28, 37, XIII, XIV
- [76] H. P. Vincenti, *Generation d’impulsions attosesondes sur mirror plasma relativiste*. PhD thesis, Ecole Polytechnique, 2012. 30, 73, 80, 81, 86, 122
- [77] A. A. Gonoskov, A. V. Korzhimanov, A. V. Kim, M. Marklund, and A. M. Sergeev, “Ultrarelativistic nanoplasmonics as a route towards extreme-intensity attosecond pulses,” *Physical Review E*, vol. 84, no. 4, p. 046403, 2011. 30, 61

- [78] G. Enright, M. Richardson, and N. Burnett, “Superthermal x-ray emission from CO<sub>2</sub>-laser-produced plasmas,” *Journal of Applied Physics*, vol. 50, no. 6, pp. 3909–3914, 1979. 32
- [79] A. Malvache, *Optique non-lineaire a haute intensite : Compression d’impulsion laser Interaction laser-plasma*. PhD thesis, Ecole Polytechnique, 2011. 33, 34, 36, 50, 61, 63, 64, 65, 67, 86, 122
- [80] P. Chen, J. Dawson, R. W. Huff, and T. Katsouleas, “Acceleration of electrons by the interaction of a bunched electron beam with a plasma,” *Physical review letters*, vol. 54, no. 7, p. 693, 1985. 34
- [81] P. Mora, “Plasma expansion into a vacuum,” *Physical Review Letters*, vol. 90, no. 18, p. 185002, 2003. 35
- [82] P. Mora, “Introduction aux plasmas créés par laser,” *Cours Ecole Polytechnique, chapitre*, vol. 2, 2011. 38
- [83] A. Vlasov, “On the theory of the solid state,” *Journal of Physics*, vol. 9, pp. 130–138, 1945. 39
- [84] L. D. Landau, “On the vibrations of the electronic plasma,” *Zh. Eksp. Teor. Fiz.*, vol. 10, p. 25, 1946. 39, 40, VIII
- [85] V. Karpman and D. Shklyar, “Nonlinear landau damping in an inhomogeneous plasma,” tech. rep., Inst. of Terrestrial Magnetism, Ionosphere, and Radio-Wave Propagation, Moscow, 1974. 40
- [86] E. Asseo, G. Laval, R. Pellat, R. Welti, and A. Roux, “Effect of the plasma inhomogeneity on the nonlinear damping of monochromatic waves,” *Journal of Plasma Physics*, vol. 8, no. 03, pp. 341–355, 1972. 40
- [87] B. Dromey, S. Rykovanov, D. Adams, R. Hörlein, Y. Nomura, D. Carroll, P. Foster, S. Kar, K. Markey, P. McKenna, *et al.*, “Tunable enhancement of high harmonic emission from laser solid interactions,” *Physical review letters*, vol. 102, no. 22, p. 225002, 2009. 41
- [88] Y. Nomura, R. Hörlein, P. Tzallas, B. Dromey, S. Rykovanov, Z. Major, J. Osterhoff, S. Karsch, L. Veisz, M. Zepf, *et al.*, “Attosecond phase locking of harmonics emitted from laser-produced plasmas,” *Nature Physics*, vol. 5, no. 2, pp. 124–128, 2009. 41
- [89] A. Jullien, A. Ricci, F. Böhle, J.-P. Rousseau, S. Grabielle, N. Forget, H. Jacqmin, B. Mercier, and R. Lopez-Martens, “Carrier-envelope phase stable, high-contrast, double-cpa laser system,” 43
- [90] V. Yanovsky, V. Chvykov, G. Kalinchenko, P. Rousseau, T. Planchon, T. Matsuoka, A. Maksimchuk, J. Nees, G. Cheriaux, G. Mourou, *et al.*, “Ultra-high intensity-300-tw laser at 0.1 hz repetition rate,” *Optics Express*, vol. 16, no. 3, pp. 2109–2114, 2008. 43

- [91] V. Malka, S. Fritzler, E. Lefebvre, M.-M. Aleonard, F. Burgy, J.-P. Chambaret, J.-F. Chemin, K. Krushelnick, G. Malka, S. Mangles, *et al.*, “Electron acceleration by a wake field forced by an intense ultrashort laser pulse,” *Science*, vol. 298, no. 5598, pp. 1596–1600, 2002. 43
- [92] B. Loupiau, M. Koenig, N. Ozaki, A. Benuzzi-Mounaix, M. R. le Goahec, E. Falize, S. Bouquet, C. Michaut, W. Nazarov, C. Courtois, *et al.*, “Plasma jet experiments using luli 2000 laser facility,” in *High Energy Density Laboratory Astrophysics*, pp. 103–107, Springer, 2007. 43
- [93] F. Quéré, C. Thauray, J. Geindre, G. Bonnaud, P. Monot, and P. Martin, “Phase properties of laser high-order harmonics generated on plasma mirrors,” *Physical review letters*, vol. 100, no. 9, p. 095004, 2008. 43
- [94] A. Ricci, *Développement d’une source laser ultra-brève, stabilisée en phase et haut contraste, pour l’optique relativiste haute cadence*. PhD thesis, Ecole Polytechnique, 2013. 44
- [95] A. Trisorio, *Développement d’une source laser femtoseconde de quelques cycles optique pour la génération d’harmoniques sur cible solide*. PhD thesis, Ecole Polytechnique, 2008. 44
- [96] L. Canova, *Generation of high contrast, ultra-short pulses for high-repetition-rate relativistic optics*. PhD thesis, Ecole Polytechnique, 2009. 44, 61
- [97] P. F. Moulton, “Spectroscopic and laser characteristics of ti:al<sub>2</sub>O<sub>3</sub>,” *JOSA B*, vol. 3, no. 1, pp. 125–133, 1986. 44
- [98] A. Jullien, O. Albert, F. Burgy, G. Hamoniaux, J.-P. Rousseau, J.-P. Chambaret, F. Augé-Rochereau, G. Chériaux, J. Etchepare, N. Minkovski, *et al.*, “10<sup>10</sup> temporal contrast for femtosecond ultraintense lasers by cross-polarized wave generation,” *Optics letters*, vol. 30, no. 8, pp. 920–922, 2005. 44, 45
- [99] F. Verluise, V. Laude, Z. Cheng, C. Spielmann, and P. Tournois, “Amplitude and phase control of ultrashort pulses by use of an acousto-optic programmable dispersive filter: pulse compression and shaping,” *Optics letters*, vol. 25, no. 8, pp. 575–577, 2000. 44
- [100] N. Bloembergen *et al.*, “Fundamentals of damage in laser glass,” *National Materials Advisory Board Publication NMAB*, vol. 271, 1970. 45
- [101] B. Stuart, M. Feit, A. Rubenchik, B. Shore, and M. Perry, “Laser-induced damage in dielectrics with nanosecond to subpicosecond pulses,” *Physical review letters*, vol. 74, no. 12, p. 2248, 1995. 45
- [102] E. G. Gamaly, A. V. Rode, B. Luther-Davies, and V. T. Tikhonchuk, “Ablation of solids by femtosecond lasers: Ablation mechanism and ablation thresholds for metals and dielectrics,” *Physics of Plasmas (1994-present)*, vol. 9, no. 3, pp. 949–957, 2002. 45

- [103] D. Homoelle, A. L. Gaeta, V. Yanovsky, and G. Mourou, "Pulse contrast enhancement of high-energy pulses by use of a gas-filled hollow waveguide," *Optics letters*, vol. 27, no. 18, pp. 1646–1648, 2002. 45
- [104] J.-L. Tapié and G. Mourou, "Shaping of clean, femtosecond pulses at 1.053  $\mu\text{m}$  for chirped-pulse amplification," *Optics letters*, vol. 17, no. 2, pp. 136–138, 1992. 45
- [105] H. C. Kapteyn, A. Szoke, R. W. Falcone, and M. M. Murnane, "Prepulse energy suppression for high-energy ultrashort pulses using self-induced plasma shuttering," *Optics letters*, vol. 16, no. 7, pp. 490–492, 1991. 45
- [106] C. Ziener, P. Foster, E. Divall, C. Hooker, M. Hutchinson, A. Langley, and D. Neely, "Specular reflectivity of plasma mirrors as a function of intensity, pulse duration, and angle of incidence," *Journal of applied physics*, vol. 93, no. 1, pp. 768–770, 2003. 45
- [107] J. P. Oakley and B. L. Satherley, "Improving image quality in poor visibility conditions using a physical model for contrast degradation," *Image Processing, IEEE Transactions on*, vol. 7, no. 2, pp. 167–179, 1998. 49
- [108] H. Ren, L. Qian, H. Zhu, D. Fan, and P. Yuan, "Pulse-contrast degradation due to pump phase-modulation in optical parametric chirped-pulse amplification system," *Optics express*, vol. 18, no. 12, pp. 12948–12959, 2010. 49
- [109] J. Bromage, C. Dorrer, and R. Jungquist, "Temporal contrast degradation at the focus of ultrafast pulses from high-frequency spectral phase modulation," *JOSA B*, vol. 29, no. 5, pp. 1125–1135, 2012. 49
- [110] N. Didenko, A. Konyashchenko, A. Lutsenko, and S. Y. Tenyakov, "Contrast degradation in a chirped-pulse amplifier due to generation of prepulses by postpulses," *Optics express*, vol. 16, no. 5, pp. 3178–3190, 2008. 49
- [111] M. Kalashnikov, A. Andreev, and H. Schönagel, "Limits of the temporal contrast for cpa lasers with beams of high aperture," in *Ultrafast Nonlinear Optics 2009*, pp. 750104–750104, International Society for Optics and Photonics, 2009. 49
- [112] S. Kahaly, S. Monchocé, H. Vincenti, T. Dzelzainis, B. Dromey, M. Zepf, P. Martin, and F. Quéré, "Direct observation of density-gradient effects in harmonic generation from plasma mirrors," *Physical review letters*, vol. 110, no. 17, p. 175001, 2013. 59
- [113] R. Lichters, J. Meyer-ter Vehn, and A. Pukhov, "Short-pulse laser harmonics from oscillating plasma surfaces driven at relativistic intensity," *Physics of Plasmas (1994-present)*, vol. 3, no. 9, pp. 3425–3437, 1996. 61
- [114] D. Von der Linde, T. Engers, G. Jenke, P. Agostini, G. Grillon, E. Nibbering, A. Mysyrowicz, and A. Antonetti, "Generation of high-order harmonics from solid surfaces by intense femtosecond laser pulses," *Physical Review A*, vol. 52, no. 1, p. R25, 1995. 61

- [115] L. Roos, E. Constant, E. Mével, P. Balcou, D. Descamps, M. B. Gaarde, A. Valette, R. Haroutunian, and A. L’Huillier, “Controlling phase matching of high-order harmonic generation by manipulating the fundamental field,” *Physical Review A*, vol. 60, no. 6, p. 5010, 1999. 61
- [116] A. Malvache, A. Borot, F. Quéré, and R. Lopez-Martens, “Coherent wake emission spectroscopy as a probe of steep plasma density profiles,” *Physical Review E*, vol. 87, no. 3, p. 035101, 2013. 64
- [117] C. Thaury, H. George, F. Quéré, R. Loch, J.-P. Geindre, P. Monot, and P. Martin, “Coherent dynamics of plasma mirrors,” *Nature physics*, vol. 4, no. 8, pp. 631–634, 2008. 68, 86
- [118] T. D. Arber, K. Bennett, C. S. Brady, A. Lawrence-Douglas, M. G. Ramsay, N. J. Sircombe, P. Gillies, R. G. Evans, H. Schmitz, A. R. Bell, and C. P. Ridgers, “Contemporary particle-in-cell approach to laser-plasma modelling,” *Plasma Physics and Controlled Fusion*, vol. 57, pp. 1–26, Nov. 2015. 70
- [119] S. Aktürk, X. Gu, P. Gabolde, and R. Trebino, “First-order spatiotemporal distortions of gaussian pulses and beams,” in *Ultrafast Optics V*, pp. 233–239, Springer, 2007. 73
- [120] S. Akturk, X. Gu, P. Gabolde, and R. Trebino, “The general theory of first-order spatio-temporal distortions of gaussian pulses and beams,” in *Lasers and Applications in Science and Engineering*, pp. 61080E–61080E, International Society for Optics and Photonics, 2006. 73
- [121] H. Vincenti and F. Quéré, “Attosecond lighthouses: how to use spatiotemporally coupled light fields to generate isolated attosecond pulses,” *Physical review letters*, vol. 108, no. 11, p. 113904, 2012. 73
- [122] M. M. Wefers and K. A. Nelson, “Space-time profiles of shaped ultrafast optical waveforms,” *Quantum Electronics, IEEE Journal of*, vol. 32, no. 1, pp. 161–172, 1996. 76
- [123] S. Monchocé, *Contrôle et métrologie de la génération d’harmoniques sur miroir plasma*. PhD thesis, Ecole Doctoral Ondes et Matière, 2014. 81, 86
- [124] R. Trebino and D. J. Kane, “Using phase retrieval to measure the intensity and phase of ultrashort pulses: frequency-resolved optical gating,” *JOSA A*, vol. 10, no. 5, pp. 1101–1111, 1993. 81, 82
- [125] D. J. Kane, “Principal components generalized projections: a review [invited],” *JOSA B*, vol. 25, no. 6, pp. A120–A132, 2008. 83, 102
- [126] M. Miranda, M. Kotur, P. Rudawski, C. Guo, A. Harth, A. L Huillier, and C. L. Arnold, “Spatiotemporal characterization of ultrashort laser pulses using spatially resolved fourier transform spectrometry,” *Optics letters*, vol. 39, no. 17, pp. 5142–5145, 2014. 84

- [127] G. Pariente, V. Gallet, O. Gobert, and F. Quéré, “Measuring ultra-high power femtosecond lasers in space-time,” in *The European Conference on Lasers and Electro-Optics*, p. CH\_8\_4, Optical Society of America, 2015. 84
- [128] J. Geindre, A. Mysyrowicz, A. D. Santos, P. Audebert, A. Rousse, G. Hamoniaux, A. Antonetti, F. Fallières, and J. Gauthier, “Frequency-domain interferometer for measuring the phase and amplitude of a femtosecond pulse probing a laser-produced plasma,” *Optics letters*, vol. 19, no. 23, pp. 1997–1999, 1994. 88
- [129] R. Evans, A. Badger, F. Fallies, M. Mahdieh, T. Hall, P. Audebert, J.-P. Geindre, J.-C. Gauthier, A. Mysyrowicz, G. Grillon, *et al.*, “Time-and space-resolved optical probing of femtosecond-laser-driven shock waves in aluminum,” *Physical review letters*, vol. 77, no. 16, p. 3359, 1996. 88
- [130] C. Quiox, G. Hamoniaux, A. Antonetti, J.-C. Gauthier, J.-P. Geindre, and P. Audebert, “Ultrafast plasma studies by phase and amplitude measurements with femtosecond spectral interferometry,” *Journal of Quantitative Spectroscopy and Radiative Transfer*, vol. 65, no. 1, pp. 455–462, 2000. 88
- [131] P. Audebert, J.-P. Geindre, S. Rebibo, and J.-C. Gauthier, “Direct observation of the ponderomotive force effects in short-scale-length laser plasmas by frequency-domain interferometry,” *Physical Review E*, vol. 64, no. 5, p. 056412, 2001. 88
- [132] J.-P. Geindre, P. Audebert, S. Rebibo, and J.-C. Gauthier, “Single-shot spectral interferometry with chirped pulses,” *Optics Letters*, vol. 26, no. 20, pp. 1612–1614, 2001. 88
- [133] M. Downer, R. L. Fork, and C. V. Shank, “Femtosecond imaging of melting and evaporation at a photoexcited silicon surface,” *JOSA B*, vol. 2, no. 4, pp. 595–599, 1985. 95
- [134] M. H. Hayes and T. F. Quatieri, “Recursive phase retrieval using boundary conditions,” *JOSA*, vol. 73, no. 11, pp. 1427–1433, 1983. 102
- [135] G.-z. Yang, B.-z. Dong, B.-y. Gu, J.-y. Zhuang, and O. K. Ersoy, “Gerchberg–saxton and yang–gu algorithms for phase retrieval in a nonunitary transform system: a comparison,” *Applied optics*, vol. 33, no. 2, pp. 209–218, 1994. 102
- [136] R. Trebino, *FROG*. Springer, 2000. 102
- [137] D. J. Kane and R. Trebino, “Single-shot measurement of the intensity and phase of an arbitrary ultrashort pulse by using frequency-resolved optical gating,” *Optics letters*, vol. 18, no. 10, pp. 823–825, 1993. 102
- [138] J. R. Fienup, “Reconstruction of a complex-valued object from the modulus of its fourier transform using a support constraint,” *JOSA A*, vol. 4, no. 1, pp. 118–123, 1987. 102, 104

- [139] T. Crimmins and J. Fienup, “Uniqueness of phase retrieval for functions with sufficiently disconnected support,” *J. Opt. Soc. Am.*, vol. 73, no. 2, pp. 218–221, 1983. 105
- [140] Y. M. Bruck and L. Sodin, “On the ambiguity of the image reconstruction problem,” *Optics Communications*, vol. 30, no. 3, pp. 304–308, 1979. 105, 109
- [141] M. H. Hayes, “The reconstruction of a multidimensional sequence from the phase or magnitude of its fourier transform,” *Acoustics, Speech and Signal Processing, IEEE Transactions on*, vol. 30, no. 2, pp. 140–154, 1982. 105
- [142] J. R. Fienup, “Holographic reconstruction with latent reference points (a),” *Journal of the Optical Society of America (1917-1983)*, vol. 73, p. 1861, 1983. 105
- [143] J. Fienup, “Experimental evidence of the uniqueness of phase retrieval from intensity data,” in *Indirect Imaging. Measurement and Processing for Indirect Imaging*, vol. 1, p. 99, 1984. 105
- [144] C. Fienup and J. Dainty, “Phase retrieval and image reconstruction for astronomy,” *Image Recovery: Theory and Application*, pp. 231–275, 1987. 109
- [145] J. Fienup, “Diffraction-limited imaging of space objects ii.,” tech. rep., DTIC Document, 1984. 109
- [146] P. Napier and R. Bates, “Inferring phase information from modulus information in two-dimensional aperture synthesis,” *Astronomy and Astrophysics Supplement Series*, vol. 15, p. 427, 1974. 109
- [147] J. Rosenblatt, “Phase retrieval,” *Communications in Mathematical Physics*, vol. 95, no. 3, pp. 317–343, 1984. 109
- [148] R. Barakat and G. Newsam, “Necessary conditions for a unique solution to two-dimensional phase recovery,” *Journal of mathematical physics*, vol. 25, no. 11, pp. 3190–3193, 1984. 109
- [149] D. E. Dudgeon, “The existence of cepstra for two-dimensional rational polynomials,” *Acoustics, Speech and Signal Processing, IEEE Transactions on*, vol. 23, no. 2, pp. 242–243, 1975. 109
- [150] N. K. Bose, *Applied multidimensional systems theory*. Van Nostrand Reinhold Company, 1982. 109
- [151] S. Tzafestas, “State-feedback control of three dimensional systems,” in *Multidimensional Systems, Techniques and Applications*, pp. 161–232, Marcel Denner New York and Basel, 1986. 109
- [152] L. Schlessinger and J. Wright, “Inverse-bremsstrahlung absorption rate in an intense laser field,” *Physical Review A*, vol. 20, no. 5, p. 1934, 1979. 112
- [153] T. W. Johnston and J. M. Dawson, “Correct values for high-frequency power absorption by inverse bremsstrahlung in plasmas,” *Physics of Fluids (1958-1988)*, vol. 16, no. 5, pp. 722–722, 1973. 112

- [154] T. Liseykina, P. Mulser, and M. Murakami, “Collisionless absorption, hot electron generation, and energy scaling in intense laser-target interaction,” *Physics of Plasmas (1994-present)*, vol. 22, no. 3, p. 033302, 2015. 112
- [155] P. Gibbon, “Efficient production of fast electrons from femtosecond laser interaction with solid targets,” *Physical review letters*, vol. 73, no. 5, p. 664, 1994. 112
- [156] M. Chen, Z.-M. Sheng, J. Zheng, Y.-Y. Ma, M. Bari, Y.-T. Li, and J. Zhang, “Surface electron acceleration in relativistic laser-solid interactions,” *Optics express*, vol. 14, no. 7, pp. 3093–3098, 2006. 112, 113, 115, 131
- [157] A. Getz and V. Krainov, “Vacuum heating of large atomic clusters by a superintense femtosecond laser pulse,” *Journal of Experimental and Theoretical Physics*, vol. 101, no. 1, pp. 80–87, 2005. 112
- [158] W. Kruer and K. Estabrook, “ $J \times b$  heating by very intense laser light,” *Physics of Fluids (1958-1988)*, vol. 28, no. 1, pp. 430–432, 1985. 113
- [159] S. C. Wilks and W. L. Kruer, “Absorption of ultrashort, ultra-intense laser light by solids and overdense plasmas,” *Quantum Electronics, IEEE Journal of*, vol. 33, no. 11, pp. 1954–1968, 1997. 113
- [160] J. Denavit, “Absorption of high-intensity subpicosecond lasers on solid density targets,” *Physical review letters*, vol. 69, no. 21, p. 3052, 1992. 113
- [161] S. Baton, J. Santos, F. Amiranoff, H. Popescu, L. Gremillet, M. Koenig, E. Martignoli, O. Guilbaud, C. Rousseaux, M. R. Le Gloahec, *et al.*, “Evidence of ultrashort electron bunches in laser-plasma interactions at relativistic intensities,” *Physical review letters*, vol. 91, no. 10, p. 105001, 2003. 113, 115
- [162] A. Pukhov, Z.-M. Sheng, and J. Meyer-ter Vehn, “Particle acceleration in relativistic laser channels,” *Physics of Plasmas (1994-present)*, vol. 6, no. 7, pp. 2847–2854, 1999. 113
- [163] W. Douglas and J. Ritchie, “On excitation of non-medullated afferent fibres in the vagus and aortic nerves by pharmacological agents,” *The Journal of physiology*, vol. 138, no. 1, pp. 31–43, 1957. 114
- [164] R. Ritchie, E. Arakawa, J. Cowan, and R. Hamm, “Surface-plasmon resonance effect in grating diffraction,” *Physical Review Letters*, vol. 21, no. 22, p. 1530, 1968. 114
- [165] L. Fedeli, A. Sgattoni, G. Cantono, D. Garzella, F. Réau, I. Prencipe, M. Passoni, M. Raynaud, M. Květoň, J. Proška, *et al.*, “Electron acceleration by relativistic surface plasmons in laser-grating interaction,” *arXiv preprint arXiv:1508.02328*, 2015. 114, 157
- [166] T. Ceccotti, V. Floquet, A. Sgattoni, A. Bigongiari, O. Klimo, M. Raynaud, C. Riconda, A. Heron, F. Baffigi, L. Labate, *et al.*, “Evidence of resonant surface-wave

- excitation in the relativistic regime through measurements of proton acceleration from grating targets,” *Physical review letters*, vol. 111, no. 18, p. 185001, 2013. 114
- [167] J. Mendonca and F. Doveil, “Stochasticity in plasmas with electromagnetic waves,” *Journal of Plasma Physics*, vol. 28, no. 03, pp. 485–493, 1982. 115
- [168] R. Kodama, K. Tanaka, Y. Sentoku, T. Matsushita, K. Takahashi, H. Fujita, Y. Kitagawa, Y. Kato, T. Yamanaka, and K. Mima, “Long-scale jet formation with specularly reflected light in ultraintense laser-plasma interactions,” *Physical review letters*, vol. 84, no. 4, p. 674, 2000. 115
- [169] L. Chen, J. Zhang, Y. Li, H. Teng, T. Liang, Z. Sheng, Q. Dong, L. Zhao, Z. Wei, and X. Tang, “Effects of laser polarization on jet emission of fast electrons in femtosecond-laser plasmas,” *Physical review letters*, vol. 87, no. 22, p. 225001, 2001. 115
- [170] W. Wang, J. Liu, Y. Cai, C. Wang, L. Liu, C. Xia, A. Deng, Y. Xu, Y. Leng, R. Li, *et al.*, “Angular and energy distribution of fast electrons emitted from a solid surface irradiated by femtosecond laser pulses in various conditions,” *Physics of Plasmas (1994-present)*, vol. 17, no. 2, p. 023108, 2010. 115, 132
- [171] L. Chen, J. Zhang, Q. Dong, H. Teng, T. Liang, L. Zhao, and Z. Wei, “Hot electron generation via vacuum heating process in femtosecond laser–solid interactions,” *Physics of Plasmas (1994-present)*, vol. 8, no. 6, pp. 2925–2929, 2001. 115
- [172] Y. Li, J. Zhang, Z. Sheng, H. Teng, T. Liang, X. Peng, X. Lu, Y. Li, and X. Tang, “Spatial distribution of high-energy electron emission from water plasmas produced by femtosecond laser pulses,” *Physical review letters*, vol. 90, no. 16, p. 165002, 2003. 115
- [173] Y. Glinec, J. Faure, A. Guemnie-Tafo, V. Malka, H. Monard, J. Larbre, V. De Waele, J. Marignier, and M. Mostafavi, “Absolute calibration for a broad range single shot electron spectrometer,” *Review of scientific instruments*, vol. 77, no. 10, p. 103301, 2006. 117, 127, 171
- [174] J. Geindre, R. Marjoribanks, and P. Audebert, “Electron vacuum acceleration in a regime beyond brunel absorption,” *Physical review letters*, vol. 104, no. 13, p. 135001, 2010. 119
- [175] M. Bocoum, M. Thévenet, F. Böhle, B. Beaurepaire, A. Vernier, A. Jullien, J. Faure, and R. Lopez-Martens, “Anticorrelated emission of high harmonics and fast electron beams from plasma mirrors,” *Physical review letters*, vol. 116, no. 18, p. 185001, 2016. 119
- [176] T. Arber, K. Bennett, C. Brady, A. Lawrence-Douglas, M. Ramsay, N. Sircombe, P. Gillies, R. Evans, H. Schmitz, A. Bell, *et al.*, “Contemporary particle-in-cell approach to laser-plasma modelling,” *Plasma Physics and Controlled Fusion*, vol. 57, no. 11, p. 113001, 2015. 121

- [177] S. Bastiani, A. Rousse, J. Geindre, P. Audebert, C. Quoix, G. Hamoniaux, A. Antonetti, and J.-C. Gauthier, “Experimental study of the interaction of subpicosecond laser pulses with solid targets of varying initial scale lengths,” *Physical Review E*, vol. 56, no. 6, p. 7179, 1997. 131, 133
- [178] Y. Li, J. Zhang, L. Chen, Y. Mu, T. Liang, Z. Wei, Q. Dong, Z. Chen, H. Teng, S. Chun-Yu, *et al.*, “Hot electrons in the interaction of femtosecond laser pulses with foil targets at a moderate laser intensity,” *Physical Review E*, vol. 64, no. 4, p. 046407, 2001. 131
- [179] Y. Li, X. Yuan, M. Xu, Z. Zheng, Z. Sheng, M. Chen, Y. Ma, W. Liang, Q. Yu, Y. Zhang, *et al.*, “Observation of a fast electron beam emitted along the surface of a target irradiated by intense femtosecond laser pulses,” *Physical review letters*, vol. 96, no. 16, p. 165003, 2006. 131
- [180] Y. Tian, J. Liu, W. Wang, C. Wang, A. Deng, C. Xia, W. Li, L. Cao, H. Lu, H. Zhang, *et al.*, “Electron emission at locked phases from the laser-driven surface plasma wave,” *Physical review letters*, vol. 109, no. 11, p. 115002, 2012. 132
- [181] J. Geindre, P. Audebert, and R. Marjoribanks, “Relativistic a c gyromagnetic effects in ultraintense laser-matter interaction,” *Physical review letters*, vol. 97, no. 8, p. 085001, 2006. 136, 160
- [182] L. Schächter, *Beam-wave interaction in period and quasi-static structures*. Springer. 142
- [183] P. Mora and T. M. Antonsen Jr, “Electron cavitation and acceleration in the wake of an ultraintense, self-focused laser pulse,” *Physical Review E*, vol. 53, no. 3, p. R2068, 1996. 144
- [184] B. Quesnel, *Effet relativistes dans l’interaction laser-plasma haut flux : instabilités paramétriques électroniques et force ponderomotrice*. PhD thesis, Ecole Polytechnique, 1989. 149
- [185] B. Quesnel and P. Mora, “Theory and simulation of the interaction of ultraintense laser pulses with electrons in vacuum,” *Physical Review E*, vol. 58, no. 3, p. 3719, 1998. 149, 150
- [186] A. Borot, A. Malvache, X. Chen, A. Jullien, J.-P. Geindre, P. Audebert, G. Mourou, F. Quéré, and R. Lopez-Martens, “Attosecond control of collective electron motion in plasmas,” *Nature Physics*, vol. 8, no. 5, pp. 416–421, 2012. 163
- [187] R. Généaux, A. Camper, T. Auguste, O. Gobert, J. Caillat, R. Taeïb, and T. Ruchon, “Attosecond light and electronic vortices,” *arXiv preprint arXiv:1509.07396*, 2015. 163
- [188] N. Miyamoto, M. Kamei, D. Yoshitomi, T. Kanai, T. Sekikawa, T. Nakajima, and S. Watanabe, “Observation of two-photon above-threshold ionization of rare gases

- by xuv harmonic photons,” *Physical review letters*, vol. 93, no. 8, p. 083903, 2004. 164
- [189] X. Guan, K. Bartschat, and B. Schneider, “Dynamics of two-photon double ionization of helium in short intense xuv laser pulses,” *Physical Review A*, vol. 77, no. 4, p. 043421, 2008. 164
- [190] N. Papadogiannis, L. Nikolopoulos, D. Charalambidis, G. D. Tsakiris, P. Tzallas, and K. Witte, “Two-photon ionization of he through a superposition of higher harmonics,” *Physical review letters*, vol. 90, no. 13, p. 133902, 2003. 164
- [191] L. Poletto, F. Frassetto, F. Calegari, A. Trabattoni, and M. Nisoli, “Micro-focusing of xuv attosecond pulses by grazing-incidence toroidal mirrors,” in *Lasers and Electro-Optics Europe (CLEO EUROPE/IQEC), 2013 Conference on and International Quantum Electronics Conference*, pp. 1–1, IEEE, 2013. 164
- [192] C. Valentin, D. Douillet, S. Kazamias, T. Lefrou, G. Grillon, F. Augé, G. Mullot, P. Balcou, P. Mercère, and P. Zeitoun, “Imaging and quality assessment of high-harmonic focal spots,” *Optics letters*, vol. 28, no. 12, pp. 1049–1051, 2003. 164
- [193] B. Beaurepaire, A. Vernier, M. Bocoum, F. Böhle, A. Jullien, J. Rousseau, T. Lefrou, D. Douillet, G. Iaquaniello, R. Lopez-Martens, *et al.*, “Effect of the laser wavefront in a laser-plasma accelerator,” *arXiv preprint arXiv:1501.05797*, 2015. 164
- [194] G. Sciaini and R. D. Miller, “Femtosecond electron diffraction: Heralding the era of atomically resolved dynamics,” *Reports on Progress in Physics*, vol. 74, no. 9, p. 096101, 2011. 164
- [195] J. Faure, B. van der Geer, B. Beaurepaire, G. Gallé, A. Vernier, and A. Lifschitz, “Concept of a laser-plasma based electron source for sub-10 fs electron diffraction,” *arXiv preprint arXiv:1510.04119*, 2015. 164
- [196] S. Tokita, M. Hashida, S. Inoue, T. Nishoji, K. Otani, and S. Sakabe, “Single-shot femtosecond electron diffraction with laser-accelerated electrons: experimental demonstration of electron pulse compression,” *Physical review letters*, vol. 105, no. 21, p. 215004, 2010. 164
- [197] C. Villani, “Limite de champ moyen. cours de dea,” 2001. VIII
- [198] A. Vlasov, “The vibrational properties of an electron gas,” *Physics-Uspekhi*, vol. 10, no. 6, pp. 721–733, 1968. VIII
- [199] R. S. Strichartz, *A guide to distribution theory and Fourier transforms*. World Scientific, 2003. X
- [200] T. Kibble, “Mutual refraction of electrons and photons,” *Physical Review*, vol. 150, no. 4, p. 1060, 1966. XIV
- [201] G. Schmidt and T. Wilcox, “Relativistic particle motion in nonuniform electromagnetic waves,” *Physical Review Letters*, vol. 31, no. 23, p. 1380, 1973. XIV

[202] S. Forget, “Optique des lasers et faisceaux gaussiens,” in *Cours, exercices et exemple d’applications*, Université Paris Nord/13. XVII

**Titre :** Génération d'harmoniques et de faisceaux d'électrons sur miroir plasma

**Mots clés :** laser femtoseconde, plasma, électrons

**Résumé :** Dans cette thèse expérimentale, nous nous intéressons à la réponse non-linéaire d'un miroir plasma sous l'influence d'un laser d'intensité sous-relativiste ( $\sim 10^{18} W/cm^2$ ), et de très courte durée ( $\sim 30 fs$ ). Nous avons en particulier étudié la génération d'impulsions attosecondes ( $1 as = 10^{-18} s$ ) et de faisceaux d'électrons en effectuant des expériences dites de « pompe-sonde » contrôlées. Un premier résultat important est l'observation d'une anticorrélation entre l'émission X-UV attoseconde et l'accélération d'électrons lorsque l'on change la longueur caractéristique du plasma, résultats confirmés par des simulations numériques.

Un second résultat important concerne le diagnostic de l'expansion du plasma sous vide par « interférométrie en domaine spatial » (SDI),

technique élaborée dans le cadre de cette thèse. Enfin nous discutons à deux reprises l'utilisation d'algorithmes de reconstruction de phase dans le domaine spatial ou temporel.

De manière plus générale, nous avons cherché à replacer ce travail de thèse dans un contexte scientifique plus général. En particulier, nous tentons de convaincre le lecteur qu'à travers l'interaction laser-miroir plasma, il devient concevable de fournir un jour aux utilisateurs des sources peu onéreuses d'impulsions X-UV et de faisceaux d'électrons de résolutions temporelles inégalées.

**Title :** High-order harmonics and electron beams from plasma mirrors

**Keywords :** femtosecond lasers, plasmas, electrons

**Abstract :** The experimental work presented in this manuscript focuses on the non-linear response of plasma mirrors when driven by a sub-relativistic ( $\sim 10^{18} W/cm^2$ ) ultra-short ( $\sim 30 fs$ ) laser pulse. In particular, we studied the generation of attosecond pulses ( $1 as = 10^{-18} s$ ) and electron beams from plasma mirror generated in controlled pump-probe experiment. One first important result exposed in this manuscript is the experimental observation of the anticorrelated emission behavior between high-order harmonics and electron beams with respect to plasma scale length. The second important result is the presentation

of the « spatial domain interferometry » (SDI) diagnostic, developed during this PhD to measure the plasma expansion in vacuum. Finally, we will discuss the implementation of phase retrieval algorithms for both spatial and temporal phase reconstructions.

From a more general point of view, we replace this PhD in its historical context. We hope to convince the reader that through laser-plasma mirror interaction schemes, we could tomorrow conceive cost-efficient X-UV and energetic electron sources with unprecedented temporal resolutions.

